UNIVERSIDAD DE GRANADA

Doctoral Thesis

Design of new radiating systems and phase shifters for 5G communications at millimeter-wave frequencies

---

Author:
Ángel Palomares Caballero

Thesis supervisors:
Dr. Juan F. Valenzuela Valdés
Dr. Pablo Padilla de la Torre

Department of Signal Theory, Telematics and Communications
University of Granada
Programa de Doctorado en Tecnologías de la Información y la Comunicación

Granada, February, 2023

Editor: Universidad de Granada. Tesis Doctorales
Autor: Angel Palomares Caballero
ISBN: 978-84-1117-846-4
URI: https://hdl.handle.net/10481/82002

"Things that people learn purely out of curiosity can have a revolutionary effect on human affairs."

Frederick Seitz

Preface

This is an article-based thesis submitted in fulfillment of the requirements requested by the University of Granada (Spain) to obtain the International PhD degree in the Doctoral Programme in Information and Communications Technologies. Prof. Juan F. Valenzuela Valdés and Prof. Pablo Padilla de la Torre have supervised the research presented in this document. The research results were mainly developed at the University of Granada.

The development of this thesis was mainly supported by the Spanish Ministry of Universities through the predoctoral grant FPU18/01965 and its international mobility program.

Acknowledgements

Al término de este camino llamado tesis, he tenido la suerte de conocer a muchas personas con un enorme talento y entusiasmo que me han transmitido por este campo de investigación. Quiero agredecer a todas estas personas que de alguna manera han puesto su granito de arena en esta tesis.

De manera especial, me gustaría comenzar agradeciendo a mis amigos y directores de tesis, Juanfra y Pablo, por enseñarme tanto a nivel de investigación como a nivel personal. Su experiencia y conocimientos han sido un faro para llegar al final de este camino. Siempre han estado ahí para cualquier problema que me surgiera o para darme los consejos que fueran necesarios. Estoy profudamente agradecido de la confianza que depositaron en mí desde el minuto cero, a aquel chaval que entró en su despacho queriendo saber de antenas y radiofrecuencia. De igual manera, todo lo anterior también lo podría decir de Paco Luna, quien también me brindó su ayuda desde los inicios y su pasión por los temas de optimización.

También quiero dar las gracias todos mis compañeros de despacho/laboratorio (o que algún día lo fueron): Alex, Cleo, Carmelo, Salva, Nacho, Migue, Natalia, Sohrab, Jesús, Jonathan, Óscar, Zapata. Gracias por todo vuestro apoyo, buen sentido humor y por hacer que el día a día sea más llevadero. Gracias también a Antonio Alex, mi primer compañero del grupo SWAT. Gran parte de mi conocimiento científico se lo debo a las largas conversaciones sobre artículos "del Marca" que he tenido con él y a las re-

visiones que hemos hecho codo con codo. También quiero dar las gracias a Carlos Molero por su sabiduría científica, humildad y gran compañerismo.

Quiero hacer un agradecimiento especial también a mi familia, en particular a mis padres, Jose María y Pepi, y mi hermano Carlos, por entender que esta tesis ha requerido de un gran esfuerzo y dedicación. Su amor y apoyo incondicional a lo largo del transcurso de esta tesis han sido esenciales para poder estar aquí y no sé cómo podría haberlo hecho sin ellos.

Por último, quiero agradecer a mi pareja y compañera de vida, Pilar, por su amor y apoyo incondicional en todos los momentos de este camino. Su cariño, comprensión y paciencia han sido una fuente de energía para mí. Sin ella, esta tesis no hubiera sido posible.

¡Gracias de corazón a todos!

Abstract

With the arrival of the new generation of communications, known as 5G, the systems that constitute it must offer better performance in terms of data speed, latency and connection density than the previous generation of communications. For 5G, an allocation of the frequency ranges that will support future wireless communications has been established. This allocation is formed by a range of frequencies corresponding to bands below 6 GHz and the other range of frequencies includes bands above 24 GHz. In the latter frequency range, which includes part of the millimeter-wave frequency band (from 30 GHz to 300 GHz), the development of new radio frequency (RF) components is necessary because their design and manufacture is a technological challenge.

As the frequency that supports wireless communications increases, propagation losses also increase. Therefore, these losses must be compensated by the radiating systems in 5G to make these communications possible. The RF devices that make up these new systems must provide high antenna gain, be power efficient and offer spatial reconfigurability of the radiated signal.

In this thesis, the main objective is the design of both guided and radiating RF devices to provide design solutions for future 5G systems at millimeter-wave frequencies. In particular, the contributions made have been to the design of phase shifters and antenna arrays. To improve efficiency at millimeter-wave frequencies, these devices have been designed in waveguide technology.

Phase shifters are essential RF devices to control the phase shift of the electromagnetic wave that will be radiated to a certain spatial direction by an antenna array. The design of beamforming networks requires the implementation of phase shifters that produce a fixed or variable phase shift value. However, the design and fabrication of these devices at millimeter-wave frequencies is a complex task. In this thesis, four designs of waveguide phase shifters that produce both fixed and variable phase shift are presented. For phase shifters that provide a fixed phase shift, the value of this phase shift along the frequency is tuned in a desired manner by using periodic structures with higher symmetries. These types of configurations provide both flexibility in the design process and improved electromagnetic performance such as greater operating bandwidth. All the phase shifters have been implemented in gap-waveguide technology to demonstrate its effectiveness in these devices for millimeter-wave frequencies.

Regarding the radiating systems, two feeding strategies have been considered in the design process. First, the design of a 70 GHz centered antenna array implemented in gap-waveguide technology combined with the use of separate waveguides in E-plane is proposed. In this design, the feed is guided through a waveguide corporate-feed network. Second, the design of a reflectarray whose unit cells are formed using three-dimensional geometries is presented. In this case, the feeding is done in free space by radiation from a source antenna. In the previous designs, the fabrication of the prototypes was done by 3D printing based on stereolithography. Finally, using unit cells with three-dimensional geometries, the design of radiating devices with more complex functionalities such as reflection/transmission with high directivity and reconfiguration of the reflected radiation by means of graphene structures are proposed.

Keywords: 3D geometry, 3D printing, antenna array, gap-waveguide technology, glide symmetry, metal-only, millimeter-wave frequencies, phase shifter, reconfigurable intelligent surface, reconfigurability, reflectarray, reflect-transmit-array, unit cell.

Resumen

Con la llegada de la nueva generación de comunicaciones, denominada 5G, los sistemas que la conforman deben ofrecer unas mejores prestaciones en términos de velocidad de datos, latencia y densidad de conexiones respecto a la generación de comunicaciones anterior. Para 5G se ha establecido una asignación de los rangos de frecuencia que van a soportar las futuras comunicaciones inalámbricas. Esta asignación se compone por un rango de frecuencias correspondiente a las bandas por debajo de los 6 GHz y el otro rango de frecuencias engloba a las bandas por encima de los 24 GHz. En este último rango de frecuencias, en el cual están incluidas parte de la banda de las frecuencias milimétricas (desde 30 GHz a 300 GHz), es necesario el desarrollo de nuevos componentes de radiofrecuencia (RF) ya que su diseño y fabricación supone un reto tecnológico.

Al aumentar la frecuencia que soporta las comunicaciones inalámbricas, las pérdidas por propagación también aumentan. Es por ello por lo que estas pérdidas deben ser compensadas por los sistemas radiantes en 5G para que las comunicaciones sean posibles. Los dispositivos de RF que componen estos nuevos sistemas deben proporcionar una alta ganancia de antena, ser eficientes en términos de potencia y ofrecer reconfigurabilidad espacial de la señal radiada.

En esta tesis, el objetivo principal es el diseño de dispositivos de RF tanto guiados como radiantes para ofrecer soluciones de diseño a los futuros sistemas 5G en frecuencias milimétricas. De manera particular, las contribuciones realizadas han sido al diseño de desfasadores y agrupaciones de antenas. Para mejorar la eficiencia en frecuencias milimétricas, estos dispositivos han sido diseñados en tecnología en guía de ondas.

Los desfasadores son dispositivos RF esenciales para controlar el desfase de la onda electromagnética que será radiada hacia una cierta dirección espacial por una agrupación de antenas. Las redes de *beamforming* tienen la necesidad de implementar en su diseño desfasadores que producen un valor de desfase fijo o variable. Sin embargo, el diseño y fabricación de estos dispositivos en frecuencias milimétricas resulta una tarea de alta dificultad. En esta tesis se presenta cuatro diseños de desfasadores en guía de onda que producen un desfase tanto fijo como variable. Para los desfasadores que proporcionan un desfase fijo, el valor de este desfase a lo largo de la frecuencia es ajustado de manera deseada mediante el uso de estructuras

periódicas con simetrías superiores. Este tipo de configuraciones proporcionan tanto flexibilidad en el proceso de diseño como una mejora de las características electromagnéticas como puede ser un mayor ancho de banda de operación. Todos los desfasadores realizados han sido implementados en tecnología *gap waveguide* para demostrar su efectividad en estos dispositivos para frecuencias milimétricas.

Respecto a los sistemas radiantes, se han considerado dos estrategias de alimentación en el proceso diseño. En primer lugar, se propone el diseño de un array centrado a 70 GHz implementado en tecnología *gap waveguide* combinado con el uso de guías de onda separadas en plano E. En este diseño, la alimentación es guiada a través de una red de alimentación corporativa en guía de onda. En segundo lugar, se presenta el diseño de un *reflectarray* cuyas celdas unitarias son formadas mediante geometrías tridimensionales. En este caso, la alimentación se hace en el espacio libre mediante la radiación de una antena fuente. En los anteriores diseños, la fabricación de los prototipos se realizó mediante impresión 3D basado en estereolitografía. Finalmente, a través del uso de celdas unitarias con geometrías tridimensionales, se proponen el diseño de dispositivos radiantes con funcionalidades más complejas como la reflexión/transmisión con alta directividad y la reconfiguración de la radiación reflejada mediante estructuras con grafeno.

Palabras Clave: Geometría 3D, impresión 3D, agrupación de de antenas, tecnología *gap-waveguide*, simetría *glide*, sólo metal, frecuencias de ondas milimétricas, desfasador, superficie inteligente reconfigurable, reconfigurabilidad, *reflectarray*, *reflect-transmit-array*, celda unitaria.

Contents

Acronyms

1G First Generation.

3GPP 3rd Generation Partnership Project.

4G Fourth Generation.

5G Fifth Generation.

6G Sixth Generation.

BJ Binder Jetting.

CNC Computer Numerical Control.

DLP Digital Light Processing.

DMLS Direct Metal Laser Sintering.

DRIE Deep reactive-ion etching.

DUT Device Under Test.

EBG Electromagnetic Band-gap.

FDM Fused Deposition Modelling.

FR1 Frequency Range 1.

FR2 Frequency Range 2.

KPIs Key Performance Indicators.

LC Liquid Crystal.

MEMS microelectromechanical.

MJ Material Jetting.

NLOS Non Line of Sight.

PCB Printed Circuit Board.

PIN Positive Intrinsic Negative.

RF radiofrequency.

RIS Reconfigurable Intelligent Surface.

SIW Substrated Integrated Waveguide.

SLA Stereolithography.

SLM Selective Laser Melting.

SLS Selective Laser Sintering.

STAR Simultaneously Transmitting And Reflecting.

VNA Vector Network Analyzer.

Chapter 1

Introduction

1.1 Background and motivation

Since the First Generation (1G) of mobile communications in the 80's, new generations of mobile communications have taken place, each of them bringing new technological breakthroughs. Nowadays, we are facing the arrival of a new generation of communications, the Fifth Generation (5G), which is in its early stages of deployment. For the 5G, the capabilities offered by the previous generation, the Fourth Generation (4G), must be improved. Some of these improvements are related to peak data rate, latency or connection density [1]. In general, there is an order of magnitude improvement in all of these Key Performance Indicators (KPIs) compared to 4G. Achieving these KPIs is the major challenge and it requires a breakthrough in the current technology. One of the ways to achieve these improvements is through the use of frequency bands above 30 GHz [2], i.e., where the wavelength is in the order of millimeters and therefore, also known as millimeter-wave frequencies. In this frequency range whose limit is set at 300 GHz, more bandwidth is available with lower latency communications compared to the sub-6 GHz bands where spectrum is currently quite crowded. One of the first experimental demonstrations to check the feasibility of the millimeter-wave frequencies for 5G communications can be found in [3]. In this work done in 2013, the authors test a communications system at 28 GHz and 38 GHz with successful outcomes. A bit later, the propagation channel was again measured but at higher frequencies, specifically at 73 GHz, and its feasibility was also demonstrated [4]. This encouraged the scientific and standardization community to definitively establish this frequency range as the radio support for the new wireless communication technologies [5, 6]. The 3rd Generation Partnership Project (3GPP) has established the following division for the 5G frequency bands, Frequency Range 1 (FR1) for frequencies in the sub-6GHz band and Frequency Range 2 (FR2) for frequencies above 24 GHz, which correspond to the millimeter-wave frequencies [7]. For FR1, the

technology is now ready for the use in commercial 5G due to the advances inherited from the previous generations of communications while for FR2, the technology needs to be developed. One of the main key points for the evolution of the enabling technology in FR2 is related to the radiofrequency (RF) hardware devices. In the wireless infrastructures, the hardware for the RF frontends are the antennas. They are essential components that allows an efficient power transmission or reception of the radiated signal from free space. In the millimeter-wave frequency range, the propagation losses are higher with the distance according to the Friis formula. Therefore, to compensate for these undesired losses in the link budget, the antennas must have higher gain. If this solution is not adopted, the signal would arrive at the receiving equipment too attenuated and it would not be possible to identify it from the floor noise. This makes the use of high gain antennas crucial for 5G infrastructure [8, 9]. To meet the above-mentioned requirement (high gain), the radiating system must be as energy efficient as possible, i.e. the losses in the hardware components must be as low as possible. This is another of the objectives of 5G, since a greater number of antennas are expected in the wireless infrastructure to implement small cell networks [10, 11]. The infrastructure should be as energy efficient as possible. As a consequence of having high gain antennas, the beamwidth of these antennas is directly reduced [12]. This leads to a reduction of the wireless connection area in case the antennas are used to cover a specific region instead of being used for point-to-point backhaul link [6, 13]. This reduction in coverage area can be mitigated by the use of multibeam antennas with fixed or reconfigurable beams in the pointing direction [14]. These requirements presented for 5G radiating systems in FR2 are challenges that are currently open and are the focus of the scientific community's attention to try to solve them in the most optimal manner.

In the design of RF devices for millimeter-wave frequencies, the technology chosen for implementation is crucial as it will determine their electromagnetic performance. For FR1, a common choice is microstrip technology [15] as it allows compact, planar and low-cost solutions because conventional Printed Circuit Board (PCB) fabrication techniques can be used. In this frequency range, loss factors such as dielectric and radiation losses are of limited relevance. However, when a higher frequency design is needed, for example in the millimeter waves, the aforementioned loss factors start to become decisive for the efficiency of the system. In fact, these loss factors cause a reduction of the realized gain (defined in [16]), which includes all the efficiency factors of the system. This is the reason, as the operating frequency band increases, that other guiding technologies have to be used for the design of RF devices. In Table 1 of work [17], a comparison in different points of many of the transmission line technologies and waveguide structures can be read. The one that stands out for being the least lossy is the metallic waveguide since it does not use dielectric in its structure and is

fully shielded. On the contrary, the conventional manufacturing of waveguides at millimeter-wave frequencies becomes very expensive and sensitive to tolerances since there must be a perfect electrical contact between the parts that form the waveguide. If this electrical contact is imperfect (very likely to occur due to manufacturing tolerances), power leakage is generated through the gaps due to a discontinuity of the electrical currents generated on the surfaces which form the waveguide structure. As a solution to the problem described above, the gap-waveguide technology was developed [18], which avoids the requirement for perfect electrical contact. The removal of this harsh requirement, which had to be met by the parts forming the fabricated waveguide, is achieved by replacing the vertical walls of the waveguide with Electromagnetic Band-gap (EBG) structures [19]. As the name suggests, these periodic structures present an electromagnetic gap (also called stopband) in certain frequency bands that prevents the propagation of a wave through the EBG. Thus, by placing them on both sides of the waveguide, they prevent electromagnetic field leakage and thus, the associated losses. Usually, these EBGs are designed to produce a stopband regardless of whether or not there is separation between the layers that form it. This provides robustness in the manufacturing tolerance and not altering the device performance. This fact relieves to a great extent the constraints of waveguide fabrication at millimeter-wave frequencies and makes it a promising technology for future RF systems.

As mentioned above, one of the desirable features of the radiating systems in 5G is the ability to steer the main direction of radiation. For this purpose, there are many design configurations to achieve this requirement. One of the most popular is the adoption of beamforming networks such as Butler matrix [20, 21, 22]. Both in this type of beamforming networks and in other alternatively configuration [23, 24], in order to achieve the desired progressive phase requirements in the antenna elements, phase shifters with a determined performance along the frequency are needed. This type of beamforming networks perform the modification of the main beam pointing depending on the input port selection. This is because the components, which form the network, are not able to be tunable. As an alternative design strategy to achieve beamforming, there are the phased arrays. These often consist of only one input port and reconfigurable phase shifters, which are essential among the components that form the beamforming network. Some examples of these phased arrays in waveguide technology are presented in [25, 26, 27, 28, 29]. In all of them, reconfigurable phase shifters are implemented by some design strategy in waveguide technology. Thus, both fixed and variable phase shifters are key RF devices to meet the needs required by the beamforming networks.

Apart from the characteristics for 5G radiating systems to be efficient and can perform beamforming, another relevant feature aforementioned is that they must provide high gain which implies high directivity. For this aim,

for electromagnetic reasons, the physical aperture of the radiating system must be large compared to the wavelength [30], which is on the order of millimeters for frequencies above 30 GHz. This makes that one of the solutions generally adopted to achieve a larger physical aperture is the implementation of antenna arrays. These antenna arrays may be divided in two groups. The first group comprises the antenna arrays fed by means of guiding structures, as in the case of beamforming networks or corporate feeding networks [31]; and the second group is the one whose antenna arrays are fed by the radiation from an primary source antenna. Arrays corresponding to the latter group are named spatially-fed antennas. In this group of antenna arrays are includes lenses [32], transmitarrays [33] and reflectarrays [34]. If we compare both groups of antennas, network-fed or spatially-fed, both have their advantages and disadvantages. For example, in antenna arrays fed by feeding networks, the design with a lossless network, reflection-less components that form it and great operation bandwidth becomes difficult design tasks. However, if this is achieved, the aperture efficiency of the radiating system is very high. On the other hand, spatially-fed antennas have the advantage of not having to deal with the problems of implementing feeding networks but in return, the entire system must be precisely designed to be efficient and to avoid as many losses as possible. In the case of reflectarrays (they can also be extended to the rest of spatially-fed antennas), the illumination efficiency, spillover efficiency, element losses, phase efficiency, blockage and other efficiency factors have to be maximized. The selection of one of the two groups of antennas depends on the requirements of bandwidth, available physical space, electromagnetic polarization, maximum reachable directivity or number of radiated beams needed.

Recently, a new paradigm has emerged to complement the infrastructure of the future wireless communications based on reconfigurable metasurfaces controlled by software [35]. The main function of these metasurfaces is to dynamically improve the coverage area in situations where there is Non Line of Sight (NLOS) between the base stations and the users. In addition to this functionality, there is a general desire to extend the functionalities offered with the aim of controlling the wireless environment in a smart way [36]. The conception of this new use for reconfigurable metasurfaces originates from the pioneering work [37]. This work presents for the first time the coding metamaterials that are based on discretizing the phase responses produced by the unit cells. These unit cells compose the metamaterial or metasurface. In the experimental results presented in [37], a unit cell controlled by a Positive Intrinsic Negative (PIN) diode is employed, which produces two phase responses with a difference between them of 180^{o}. Because of this binary behavior, the unit cell is referred to as a 1-bit unit cell. The possible number of states of the reconfigurable unit cell determines its bit number. In general, such metasurfaces are used to reflect the incident waves in the desired direction(s). The electromagnetic theory for the design of these

reflection metasurfaces, also called Reconfigurable Intelligent Surface (RIS), is inherited from that used for reflectarrays with some assumptions for the phases available in the elements and the characteristics of the incident wave. Because RIS does not make use of RF chains in its implementation, lower cost design and lower power consumption are obtained compared to future 5G base stations. In this way, the use of RIS is a ground-breaking device for the sustainability and reconfigurability of future wireless communications.

This thesis is primarily devoted to contribute to the design of RF devices at millimeter-wave frequencies for future generations of communications. The thesis document has the following organization. In Chapter 1, it starts with a description of the role of millimeter-wave devices in 5G communications and the different design strategies proposed to obtain these devices with the target requirements. In the following subsections of Chapter 1, from subsection 1.1.1 to 1.1.6, a more detailed description of the state-of-the-art of the topics most related to the contributions presented in this thesis will be made. Section 1.2 describes the objectives achieved in this thesis. The research methodology followed along the thesis is described in Section 1.3. Section 1.4 lists the results produced by this thesis both in terms of publications and awards. Chapter 2 is devoted to the presentation of the publications comprising this thesis as well as a description of the contributions made in each publication. This chapter has been divided into two parts, the first one dedicated to the contributions made on the topic of millimeter-wave phase shifters. The other part of the chapter presents the publications and contributions made on the topic of millimeter-wave radiating systems. Finally, Chapter 4 lists the main conclusions of this thesis and envisions the future research lines based on the achieved contributions.

1.1.1 Gap-waveguide devices

The gap-waveguide technology emerged as an effective and low-cost solution for waveguides at millimeter-wave frequencies. In this frequency range, manufacturing tolerances are more significant and determinant in RF device performance. In [19] is described some of the most common implementations for gap-waveguide technology such as: groove gap waveguide, ridge gap waveguide, inverted microstrip gap waveguide and microstrip ridge gap waveguide. All of them consist of a zone where the fundamental mode of the waveguide propagates and on both sides of this zone are placed EBGs that can be of different types. The most popular EBG implementations are bed of pins or substrate with mushroom patch type. These EBG structures avoid the need for perfect electrical contact between the layers that make up the waveguide in this way, greatly alleviate the manufacturing requirements. From the use of different implementations of gap-waveguide technology, directive antenna arrays have been realized at millimeter-wave frequencies with high radiation efficiency. Some examples of groove and

ridge gap-waveguide antenna array designs are presented in the following works [31, 38, 39, 40]. Antenna array designs in inverted microstrip gap waveguide [41] and microstrip ridge gap waveguide [42, 43] have also been reported.

One of the disadvantages of gap-waveguide technology, which uses the pin bed as the EBG structure, is that as the design frequency increases, the pin dimensions become smaller and require more precise and consequently more costly manufacturing. In addition, small pin dimensions become more fragile in fabrication. In 2017, gap-waveguide technology based on holes with glide symmetry emerged as an alternative to the previously mentioned EBG structures [44]. This new type of EBG structure provides a large stopband in addition to a more robust fabrication at millimeter frequencies as smaller dimensions are not necessary as in the case of pin-based EBGs. Additionally, the holes are more robust in fabrication compared to the pin bed. In [45], the effectiveness of glide-symmetric holes as EBGs for gap waveguides was demonstrated. There are a few examples of RF devices using this type of gap-waveguide technology [46, 47]. Taking advantage of the benefit in terms of stopband provided by holes with glide symmetry, in [48] applied to waveguides formed by multiple layers. A low-cost prototype waveguide implemented with this gap-waveguide technology for frequencies above 100 GHz is shown in the previous work. Some designs based on this gap-waveguide technology are presented in [49, 50].

1.1.2 Higher symmetries

A periodic structure has a higher symmetry if it remains invariant to a translation and another geometric operator such as a reflection or a rotation [51]. The main higher symmetries are the glide symmetry and the p-fold screw symmetry [51]. The latter is also referred to as the twist symmetry [52]. The glide symmetry is composed of a half-period unit cell translation and a reflection against a plane called the glide plane. In the case of p-fold twist symmetry, this consists of a d/p-translation followed by a $2pi/p$-radian rotation along rotation or also called screw axis. Another type of higher symmetry related to glide symmetry is presented in [53], which is called polar glide symmetry. The term "polar" indicates that the glide plane is defined as a cylindrical plane around the screw axis. If a periodic structure has any type of higher symmetry, in general, it brings benefits to the dispersion diagram such as improving the linearity of the propagating modes, closing stopbands or increasing the maximum refractive index [54, 53, 55].

In the literature there are a greater number of designs with glide symmetry compared to those with twist symmetry. This is because glide symmetry can be applied in a more direct way in the design since twist symmetry involves implementing turns around a rotation axis in the RF device. This is less common to find in the design process. Some examples of designs with

twist symmetry can be seen in [56, 57, 58, 59]. On the other hand, examples of RF devices with glide symmetry can be found in [60, 61, 62, 63, 64, 65, 66].

1.1.3 Phase shifters in waveguide

Phase shifters are essential RF devices that are present in every beamforming network both passive and active [14]. The phase shift, when dealing with low frequencies, appears naturally in RF circuits based on lumped elements when using capacitors and inductors. However, when we work at higher frequencies, these RF circuits consider distributed elements [15]. These can implicitly synthesize the frequency behavior of the above reactive elements. If we focus on the design strategies followed to implement phase shifters in waveguide technology, one of the first phase shifter design appears in 1947 [67]. In this paper, several practical ways of introducing phase shift in a circular waveguide depending on the orientation of the propagating TE_{11} mode are presented. The proposals to introduce the phase shift are by means of slits, metallic rods or dielectric structures oriented in the same direction of the electric field oscillation. Other designs of phase shifters for rectangular waveguides can be found in [68, 69, 70]. In [68], a dielectric structure is inserted inside a waveguide. The ends of the piece of dielectric have a taper to maintain a low reflection coefficient. In [69, 70], phase shift is introduced in a rectangular waveguide by including carefully designed E-plane stubs. In general, for waveguide phase shifter designs, which provide a non-tunable phase shift, the way to introduce the phase shift is by including elements inside the waveguide. These are intended to modify the phase constant β of the waveguide and/or to synthesize the behavior of reactive elements. For instance, one of the design strategies to change the value of β is to use periodic structures such as small corrugations [71] or tiny pins [72]. Complementary or alternatively, reactive elements can be introduced in the form of discontinuities such as narrowing of the waveguide height [73, 74], E-plane stubs [70] or twists between waveguides aided by the gap-waveguide technology [75].

On the other hand, for waveguide tunable phase shifters, several designs have been presented in the literature. One of the first designs of a waveguide reconfigurable phase shifters was the phase shifter with ferrite [76]. Depending on the magnetic field strength provided externally to the ferrite, a phase shift occurs in the propagating mode of the waveguide. Other types of materials whose electrical properties are changed by electric or magnetic fields have also been used as a phase shift mechanism in waveguide. This is the case of Liquid Crystal (LC), which has been employed in several designs to make phase shifters in different waveguide technologies such as [77, 78, 79]. Depending on the strength of the electric or magnetic field used to orient the LC molecules, the electromagnetic wave passing through this material experiences a given permittivity included in the range offered by the LC

material. A waveguide phase shifter based on the photosensitivity of the silicon has also been reported in [80]. This characteristic of the silicon allows modifying its sheet resistance depending on the received light density. By modifying the conductivity value of a piece of silicon placed parallel to the sidewall of the waveguide, the propagation constant is in turn modified and thus, a phase shift is obtained. Other approaches to design variable phase shifters using materials can be found in [81, 82]. These works have used high permittivity materials and liquid metals, respectively. Nonetheless, both of them have used Substrated Integrated Waveguide (SIW)[17] as the guiding technology. Another common feature of the latest designs is that the reconfigurability is done mechanically, either by precisely moving the material [81] or by applying the pressure needed to move the liquid metal [82]. Designs of phase shifters based on mechanical reconfiguration have also been proposed in the literature. In [25], a reflection waveguide phase shifter is proposed by mechanically moving the short circuit at the end of the phase shifter. Following this design strategy, in [83], a hybrid waveguide coupler is presented where certain ports are short-circuited and loaded with a mechanically adjustable screw which provides a certain phase shift at the output port. Instead of mechanically reconfiguring the position of the short circuit at the end of the waveguide [25], a phase shifter can be realized by moving the sidewall constituting the rectangular waveguide as proposed in [84]. In [85], mechanical insertion of dielectrics into a waveguide is analyzed to obtain a tunable phase shifter. In order to ensure that the inclusion of the dielectric material inside the waveguide causes the least amount of losses, a longitudinal opening is made in the middle of the wide side of the rectangular waveguide.

1.1.4 Reflectarrays

Reflectarray combines features of phased arrays and reflectors to provide a spatially fed (as in reflectors) whose radiating elements are arranged in a plane and spaced a certain distance between them (as in phased arrays). Depending on the incident wave direction in the reflectarray and the desired direction of the main beam, the radiating elements must have certain responses for the reflected phase [86]. The reflectarray concept emerged in 1963 with the following paper [87]. The design developed as a proof of concept was an array of short-circuited waveguides with variable depth to obtain the desired phase reflection and in consequence the required phase distribution in the reflectarray plane. Later, with the development of PCB fabrication technology, reflectarrays based on microstrip patch antennas appeared. Following a phase shift mechanism based on the length of a shorted or open line attached to the reflectarray element, different phase values in reflection are obtained allowing the design of the reflectarray using patch antennas [88]. Since these early reflectarrays, a great diversity of reflectar-

rays have been proposed in the literature from different design strategies and technologies resulting in different electromagnetic performances [34, 89]. By the increasing of the operating frequency and the needing of communications with more directive beams to overcome propagation losses, reflectarrays have been proposed as a element to improve the communication channel [90, 91]. In addition, this increase in operating frequency leads to ensure that the electromagnetic performance is efficient in terms of losses so that it improves the link budget. To this end, the losses in the reflectarray structure must be minimized. A strategy followed in the design of reflectarrays at millimeter-wave frequencies is not to use dielectric structures since this material contributes to increase losses, specially in this frequency region. Therefore, the use of metal-only structures is preferred to get rid of dielectric losses in the reflectarray. Different designs have been presented in the literature for metal-only reflectarrays [92, 93, 94, 95].

Recently, the term reflectarray has evolved and been combined with the term transmitarray to produce the benefits of both in a single design. This has acquired the term of reflect-transmit-array [96]. In this way, radiation with high directivity can be obtained in both reflection and transmission, i.e., in full space. For the design of the reflect-transmit-array, the element that forms it must allow both reflection and transmission and for both operations it should be possible to select the phase shift introduced. For the case of [96], the phase shift is controlled by the length of the square-ring slot. Nevertheless, once the phase shift is set, it is the same for reflection and transmission. One of the design approach proposed to allow the independent main beam design for both transmission and reflection is the use of the sparse-array method [97]. An alternative to this method is that the element forming the reflect-transmit-array was sensitive to the incident polarization. In this way, each polarization is assigned a radiation region, either reflection or transmission. Thus, the independent adjustment of the phase shift in transmission and reflection is facilitated. This approach has been employed by the designs presented in [98, 99].

1.1.5 Reconfigurable Intelligent Surface

RIS can be viewed as reconfigurable reflectarray whose phase states are discretized by 2^n bits where n is the number of bits considered. This assumption in the RIS simplifies the design of the reconfigurable element, which does not have to provide a continuous phase range up to 360^o [100]. On the other hand, implementing a discretized phase distribution in a reflectarray causes phase errors decreasing the aperture efficiency. It is a good compromise to accept this performance disadvantage in exchange for having a low cost and reconfigurable device that improves the received signal in a wireless communications environment. With the RIS being the central element of the future wireless communications paradigm, different RIS designs

have been proposed such as those presented in [101, 102, 103, 104]. These works use PIN diodes or varactors for reconfigurability of the RIS elements and their operation frequency bands are located sub-6 GHz. If we increase the operating frequency, at the beginning of the millimeter-wave frequency range, we find a few proposed designs for RIS [105, 106]. The cause of this fact is the increased difficulty in making the RIS element reconfigurable as there are not many models of commercial varactors or diodes that operate well at millimeter-wave frequencies. In lasted works mentioned, the reconfiguration is done with PIN diodes and for 1-bit RIS. Revisiting the reconfiguration mechanisms of reconfigurable reflectarrays [107], there are more reconfiguration alternatives using other type of lumped element such as RF microelectromechanical (MEMS) or by tunable materials such as LC, ferroelectrics or graphene. Indeed, the electromagnetic behavior of the latter has been explored in more detail for its promising use in the microwave and millimeter-wave frequency range [108, 109, 110].

1.1.6 3D Printing for RF devices

In recent years, 3D printing technology has had a great development providing different manufacturing techniques available [111]. Depending on the material used in the additive manufacturing, we have different types of 3D fabrication techniques. In case the material is plastic or similar, we have mainly: Fused Deposition Modelling (FDM), Stereolithography (SLA), Selective Laser Sintering (SLS), Material Jetting (MJ) and Digital Light Processing (DLP). On the other hand, in case the material is metal, the main techniques are: Selective Laser Melting (SLM), Direct Metal Laser Sintering (DMLS) and Binder Jetting (BJ). The development of the above 3D fabrication techniques has made possible the consideration of their use for manufacturing RF devices for microwave and millimeter-wave frequencies [112]. In particular, there are some fabrication techniques that provide better precision and minimal print detail which makes them more suitable for the fabrication of antennas and other devices when the frequency increases. This is the case of SLA, which has demonstrated the feasibility of its use for millimeter-wave frequencies [113, 114, 115]. The disadvantage of this kind of fabrication technique based on printed plastic is that the subsequent metallization of the printed part/s is required in the case the design needs conductive parts such as a waveguide filter. This leads to an appropriate choice of a plating technique that provides the necessary conductivity, thickness and roughness to maintain the performance of the designed device, especially at millimeter-wave frequencies [116]. Regarding the 3D fabrication techniques directly in metal, several antenna designs have been presented for the millimeter-wave and submillimeter-wave range [115, 117]. In the last work, the feasibility of SLM and BJ techniques has been demonstrated but with the need to apply polishing and gold electroplating post-processing

to the resulting pieces. Therefore, with the advent of these 3D fabrication techniques, they become an effective and generally lower cost alternative [118] that makes it possible to bring to reality RF device designs which were impossible, or very expensive, to realize with traditional techniques such as Computer Numerical Control (CNC).

Being able to apply three-dimensional geometries to RF devices relatively easily using the aforementioned 3D printing techniques provides an additional degree of freedom in the design process. This 3D character brings new functionalities and potentials to the desired electromagnetic behavior[119, 120]. For example, in [121], period structures with 3D geometry are used to control the phase of the incident wave in both polarizations to achieve a metal-only polarizer. The proof of concept of the previous work is fabricated using SLM. Another example using 3D structures in the design process can be seen in [122]. In the design proposed in the previous work, the incident field is transmitted through a 3D periodic structure with a total power transfer to the cross-polarized component in a bandwidth determined by a bandpass filter, also implemented in the design. As can be seen, this degree of freedom offered by 3D structures allows to achieve complex behaviors in an efficient and direct way with the cost of making the design more bulky compared to the conventional metasurfaces, which lack this third dimension and therefore, offering less flexibility and higher complexity in the design process.

1.2 Objectives

The main objective of this thesis is the design of new radiating devices and phase shifters at millimeter-wave frequencies as they are essential components for the future wireless communication systems. The following is the subdivision of this principal objective in sub-objectives that allow its accomplishment.

- Design of both guiding and radiating devices in waveguide for efficient operation at millimeter-wave frequencies.
- Use of new design strategies in the design of millimeter-waves devices in order to achieve flexibility and improvement in terms of performance of the state-of-the-art designs.
- Development of directive radiating systems that allow in their design a flexible and reconfigurable radiation capability for future communication scenarios as well as active elements to fulfill their functionality.
- Use of new fabrication techniques for a feasible and effective prototyping of devices at millimeter-wave frequencies.

1.3 Research Methodology

In order to successfully achieve the above-referred sub-objectives, the following research methodology has been employed. First, a systematic review of the state-of-the-art has been carried out to identify the different types of technologies and solutions proposed for the design of millimeter-wave frequency devices. This literature review has been done periodically during the thesis. Once the opportunities for improving the state-of-the-art designs have been identified, the electromagnetic simulation software is used to perform the first tests of the conceived new designs. The electromagnetic software used has been *CST Studio Suite*, which allows the calculation of the useful electromagnetic results for the performance of the device under design. In *CST Studio Suite* software, different types of solver have been used according to the properties of the analyzed design. As an example, for the periodic structures, for which we are interested in calculating their dispersion diagram (relationship between frequency and phase constant), the solver used was the eigensolver. In this stage of design and optimization of the electromagnetic behavior of the device, in addition to *CST Studio Suite*, *Matlab* has been used for the calculation of some electromagnetic results in an efficient way to control more finely the application of optimization algorithms.

After having reached the design with the desired performance in simulation, we proceed to select the most appropriate fabrication technique. This technique will depend on the type of geometries that form the structures in the device and their orientation. In this thesis we have used both conventional manufacturing techniques such as CNC and more innovative manufacturing techniques such as 3D printing in plastic plus a subsequent metallization. With respect to the last technique, different options have been explored such as 3D printing plus electroplating (provided by the company Protolabs) and 3D printing with the Formlabs 3 (3D printer of Formlabs) plus a silver spray metallization provided by the company JetMetal. For the characterization and validation of the manufactured prototypes, the equipment and infrastructure of the SWT laboratory [123] of the University of Granada has been used. For the measurements of the guiding devices, only it is neccesary the use of the Vector Network Analyzer (VNA) from 10 MHz up to 67 GHz (model: ZVA67 from R&S), 1.85mm RF cables, coaxial-to-waveguide transitions and frequency extenders (model: ZVA-Z110E from R&S) if necessary to expand the frequency range. For the measurements of the radiating devices, in addition to the described equipment, the anechoic chamber has been used, which is a shielded enclosure covered on the inside by absorbent material. In addition, the anechoic chamber is equipped with software-controlled positioners that allow the automatic acquisition of 2D and 3D radiation patterns, gain and other antenna parameters of the Device Under Test (DUT). Once the measurements are acquired, they are

processed and compared with the results obtained in simulation to see their similarities and differences and, if the latter appear, to seek the origin of these differences in relation to the fabrication technique used.

1.4 Thesis Results

This is the list of **publications** in renowned journals and conferences that support the results achieved in this thesis:

- [P1] **Á. Palomares-Caballero**, A. Alex-Amor, P. Padilla, F. Luna and J. Valenzuela-Valdés, "Compact and Low-Loss V-Band Waveguide Phase Shifter Based on Glide-Symmetric Pin Configuration," in IEEE Access, vol. 7, pp. 31297-31304, 2019.
- [P2] **Á. Palomares-Caballero**, A. Alex-Amor, P. Padilla and J. F. Valenzuela-Valdés, "Dispersion and Filtering Properties of Rectangular Waveguides Loaded With Holey Structures," in IEEE Transactions on Microwave Theory and Techniques, vol. 68, no. 12, pp. 5132-5144, Dec. 2020.
- [P3] **Á. Palomares-Caballero**, C. Megías, C. Molero, A. Alex-Amor and P. Padilla, "Wideband Gap-Waveguide Phase Shifter Based on a Glide-Symmetric Ridge," in IEEE Microwave and Wireless Technology Letters, vol. 33, no. 1, pp. 27-30, Jan. 2023.
- [P4] **Á. Palomares-Caballero**, A. Alex-Amor, P. Escobedo, J. Valenzuela-Valdés and P. Padilla, "Low-Loss Reconfigurable Phase Shifter in Gap- Waveguide Technology for mm-Wave Applications," in IEEE Transactions on Circuits and Systems II: Express Briefs, vol. 67, no. 12, pp. 3058-3062, Dec. 2020.
- [P5] **Á. Palomares-Caballero**, A. Alex-Amor, J. Valenzuela-Valdés and P. Padilla, "Millimeter-Wave 3-D-Printed Antenna Array Based on Gap-Waveguide Technology and Split E-Plane Waveguide," in IEEE Transactions on Antennas and Propagation, vol. 69, no. 1, pp. 164-172, Jan. 2021.
- [P6] **Á. Palomares-Caballero**, C. Molero, P. Padilla, M. García-Vigueras and R. Gillard, "Metal-Only Reflectarray Unit Cell for Dual-Polarization Control," in 2022 16th European Conference on Antennas and Propagation (EuCAP), 2022.
- [P7] **Á. Palomares-Caballero**, C. Molero, P. Padilla, M. García-Vigueras and R. Gillard, "Wideband 3-D-Printed Metal-only Reflectarray for Controlling Orthogonal Linear Polarizations," in IEEE Transactions on Antennas and Propagation, doi: 10.1109/TAP.2023.3240583.

- [P8] **Á. Palomares-Caballero**, C. Molero, Juan F. Valenzuela-Valdés, P. Padilla, M. García-Vigueras and R. Gillard, "Metal-Only Reflect-Transmit-Array Unit Cell with Polarization-Dependent Performance," in 2023 17th European Conference on Antennas and Propagation (EuCAP), 2023.

- [P9] C. Molero, **Á. Palomares-Caballero**, A. Alex-Amor, I. Parellada-Serrano, F. Gamiz, P. Padilla, J. Valenzuela-Valdés, "Metamaterial-Based Reconfigurable Intelligent Surface: 3D Meta-Atoms Controlled by Graphene Structures," in IEEE Communications Magazine, vol. 59, no. 6, pp. 42-48, June 2021.

Other related papers that have been generated along the development of this thesis but have not been included:

- **Á. Palomares-Caballero**, P. Padilla, A. Alex-Amor, J. Valenzuela-Valdés, and O. Quevedo-Teruel, "Twist and glide symmetries for helix antenna design and miniaturization," in Symmetry, vol. 11, no. 3, p. 349, Mar. 2019.

- P. Padilla, **Á. Palomares-Caballero**, A. Alex-Amor, J. Valenzuela-valdés, J. M. Fernández-González and O. Quevedo-Teruel, "Broken Glide-Symmetric Holey Structures for Bandgap Selection in Gap-Waveguide Technology," in IEEE Microwave and Wireless Components Letters, vol. 29, no. 5, pp. 327-329, May 2019.

- Q. Chen, O. Zetterstrom, E. Pucci, **Á. Palomares-Caballero**, P. Padilla and O. Quevedo-Teruel, "Glide-Symmetric Holey Leaky-Wave Antenna With Low Dispersion for 60 GHz Point-to-Point Communications," in IEEE Transactions on Antennas and Propagation, vol. 68, no. 3, pp. 1925-1936, March 2020.

- C. Segura-Gómez, **Á. Palomares-Caballero**, A. Alex-Amor, J. Valenzuela-Valdés and P. Padilla, "Modular Design for a Stacked SIW Antenna Array at Ka-Band," in IEEE Access, vol. 8, pp. 158568-158578, 2020.

- B. Hammu-Mohamed, **Á. Palomares-Caballero**, C. Segura-Gómez, F. G. Ruiz, and P. Padilla, "SIW cavity-backed antenna array based on double slots for mmWave communications," in Applied Sciences, vol. 11, no. 11, p. 4824, May 2021.

- A. Alex-Amor, **Á. Palomares-Caballero** and C. Molero, "3-D Metamaterials: Trends on Applied Designs, Computational Methods and Fabrication Techniques," in Electronics, vol. 11, no. 3, p.410, Jan. 2022.

- S. Moreno-Rodríguez, M. A. Balmaseda-Márquez, J. Carmona-Murillo and **Á. Palomares-Caballero**, "Polarization-Insensitive Unit Cells for a Cost-Effective Design of a 3-D-Printed Fresnel-Lens Antenna," in Electronics, vol. 11, no. 3, p.338, Jan. 2022.

- C. Segura-Gómez, **Á. Palomares-Caballero** and P. Padilla, "A 1-to-8 Fully Modular Stacked SIW Antenna Array for Millimeter-Wave Applications," in IEEE Transactions on Antennas and Propagation, vol. 70, no. 11, pp. 11149-11154, Nov. 2022.

- A. Biedma-Pérez, P. Padilla, C. Segura-Gómez and **Á. Palomares-Caballero**, "Holey SIW Horn Antenna Based on an H-plane Lens-wise Wavefront Collimation," in IEEE Transactions on Antennas and Propagation, vol. 71, no. 1, pp. 1023-1028, Jan. 2023.

- O. Zetterstrom, M. Petek, P. Castillo-Tapia, **Á. Palomares-Caballero**, N. J. G. Fonseca and O. Quevedo-Teruel, "V-band Fully-Metallic Geodesic Luneburg Lens Antenna", in IEEE Transactions on Antennas and Propagation, vol. 71, no. 2, pp. 1965-1970, Feb. 2023.

Some of the research results of this thesis have received the following **awards**:

- Finalist of the Young Researchers Award at URSI 2018 (Granada, Spain) for the paper "V-band aperture array antenna using gap waveguide technology based on glide-symmetric structures".

- Best paper of the Young Researchers Award at URSI 2022 (Málaga, Spain) for the paper "Design of a Wideband Metal-only Reflectarray with Phase Control of Orthogonal Polarizations".

- Nominee for the Best Paper Award Competition in Antena Theory and Design at EuCAP 2023 for the paper "Metal-Only Reflect-Transmit-Array Unit Cell with Polarization-Dependent Performance".

During the realization of the thesis, the following **international stays** have been carried out in research centers of recognized prestige:

- Research stay for 2 months at KTH Royal Institute of Technology (Stockholm, Sweden) in 2019.

- Research stay for 3 months at L'Institut d'Electronique et des Technologies du numéRique (Rennes, France) in 2021.

Chapter 2

Publications

This chapter includes the publications that present and detail the research results developed during this thesis. There are 7 publications in JCR indexed journals and 2 publications in international conferences. The publications have been organized in two sections: phase shifters and radiating systems, which are the two main topics of the thesis. For each publication, the contributions included in the given publication have been discussed. Besides, information about the journal where it has been published and the quality indexes of the journal are also provided.

2.1 Phase Shifters

2.1.1 Compact and Low-Loss V-Band Waveguide Phase Shifter Based on Glide-Symmetric Pin Configuration

This paper presents a new waveguide phase shifter where the elements that introduce the phase shift are pins placed with glide symmetry. Through the use of this higher symmetry, the phase shifter can provide a higher phase shift compared to its counterpart design where the pins do not preserve this higher symmetry. This provides an improvement in compactness in the phase shifter design and a relaxation in fabrication requirements since the pins can be spaced a greater distance apart without losing performance. The prototype has been implemented in gap-waveguide technology based on glide-symmetric holes for ease of fabrication. The operating band of the proposed design ranges from 46 GHz to 60 GHz with an insertion loss low and no use of dielectrics in its structure. In addition, it improves the compactness of the waveguide phase shifters that make up the state-of-the-art.

THIS IS A POSTPRINT VERSION OF THE PAPER:

A. Palomares-Caballero, A. Alex-Amor, P. Padilla, F. Luna and J. Valenzuela-Valdes, "Compact and Low-Loss V-Band Waveguide Phase Shifter Based on Glide-Symmetric Pin Configuration," in *IEEE Access*, vol. 7, pp. 31297-31304, 2019.

- Journal Impact Factor (JIF) in JCR 2019: 3.745
- Category: COMPUTER SCIENCE, INFORMATION SYSTEMS. JIF Rank: 35/156 (Q1).
- Category: ENGINEERING, ELECTRICAL & ELECTRONIC. JIF Rank: 61/266 (Q1).
- Category: TELECOMMUNICATIONS. JIF Rank: 26/90 (Q2).

Disclaimer:
This work has been published on IEEE Access. DOI: 10.1109/ACCESS.2019.2903438

IEEE Access

Date of publication xxxx 00, 0000, date of current version xxxx 00, 0000.

Digital Object Identifier 10.1109/ACCESS.2017.DOI

Compact and Low-Loss V-band Waveguide Phase Shifter Based on Glide-Symmetric Pin Configuration

ANGEL PALOMARES-CABALLERO[1], ANTONIO ALEX-AMOR[1], PABLO PADILLA[2], FRANCISCO LUNA[1] AND JUAN VALENZUELA-VALDES[2]

[1]Departamento de Lenguajes y Ciencias de la Información, Universidad de Málaga, Málaga, Spain
[2]Departamento de Teoría de la Señal, Telematica y Comunicaciones, Universidad de Granada, Granada, Spain

Corresponding author: Angel Palomares-Caballero (e-mail: angelpc@uma.es).

This work has been supported by the Spanish Research and Development National Program and FEDER under the proyect TIN2016-75097-P, by Universidad de Málaga, under the grant PPIT.UMA.B1.2017/15, and by Universidad de Granada, under the project PPJI2017.15. Also, this work has been partially supported by the Universidad de Granada through the grant program "Becas de iniciación a la investigación" from Plan Propio de Investigación.

ABSTRACT

This paper presents a compact and low-loss V-band waveguide phase shifter based on glide-symmetric pin configuration. This kind of higher symmetry permits the control and improvement of the electromagnetic behavior or radiofrequency devices, as it is the case of the proposed phase shifter. The study of the dispersion diagram of the phase shifter unitary cell demonstrates that the pin configuration is a proper option for introducing phase shift in a waveguide-based system. There is significant increase in terms of phase shift when using a glide-symmetric pin distribution compared to its corresponding non-glide-symmetric configuration. Through this study, the key geometrical parameters are also determined. The complete phase shifter is composed of an optimized cascade of tailored unitary cells so that the desired final phase shift value is achieved. A prototype has been manufactured in order to validate the theoretical approach through the comparison of phased shifters with both non-glide-symmetric and glide-symmetric configurations. The measurement results demonstrate the higher performance and compactness of the glide-symmetric phase shifter. For the same distance, the glide-symmetric version of the phase shifter provides more than 60% of phase shifting compared to the non-glide-symmetric phase shifter. Both phase shifters have a good impedance matching between 46 to 60 GHz and an insertion loss lower than 1 dB, thus clearly enabled as a 5G technology.

INDEX TERMS phase shifter, millimeter-wave, glide symmetry, gap waveguide.

I. INTRODUCTION

Digital society is evolving faster and faster and new applications are being created that demand unprecedented performance from mobile communications, some of which are expected to require communication speeds of the order of Terabit/s. To satisfy these requirements, it is necessary to develop high data transfer communication systems allowing these speeds, which makes it is essential to perform communications in a frequency band above 50 GHz. Traditional radiofrequency solutions do not work for this frequency bands and new technologies have to be developed. In the first place it is necessary to develop very directive antennas to face the propagation losses that exist at those frequencies. In that way, beamforming is one of the major goals of the future generation of communication systems. The steering of the radiated beam in wireless communication links is possible by means of antenna arrays whose input signals are controlled in amplitude and phase. Beamforming networks [1]- [3] are typically used for this purpose. Millimeter-wave range is a challenging spectrum range in these next-generation systems. In this frequency ranges, the beamforming networks are needed for producing directive beams that overcome the undesired effect of the high propagation losses in this frequency range [4]- [7].

Beamforming networks make use of phase shifters that provide a different amount of phase shift depending on the

requirements. These phase shifters need to be lossless and compact in order to achieve the maximum efficiency and reduce the footprint of the beamforming network. Moreover, in the millimeter-wave frequency range the transmission technologies are decisive since they impose the level of propagation losses. Microstrip or coplanar waveguides present a high loss level at high frequencies due to the substrate and radiation losses. Substrate Integrated Waveguide (SIW) is another planar technological solution for high frequency since it reduces the transmission loss level. A variety of SIW phase shifters in high frequency range have been presented [8]- [10]. In waveguide-based designs, stretching the broad side of the waveguide by utilizing metallic posts or etching air holes in the upper layer are the usual techniques used to introduce signal phase shift. However, for SIW technology, the presence of dielectric material imposes a strong efficiency drawback. Hollow waveguide technology is the most suitable technology in this frequency range. Nevertheless, metallic contact between waveguide plates is needed for avoiding unwanted signal leakage. Recently, gap waveguide technology has arisen to overcome waveguide plate contact and shielding requirements [11], [12]. Different phase shifters using gap waveguide technology are presented in [13]- [15]. Dielectric material use and low compactness are the principal disadvantages in these designs. On the other hand, there are waveguide-based phase shifter solutions that have a good performance in millimeter-wave range but they are highly complex and have a high manufacturing cost [16], [17].

Metasurfaces can also provide signal phase shift. Tuning the design of the metasurface, the phase shift can be controlled. One of the best advantage for this kind of phase shifter is that, for the same size, the phase shift can be different, depending on the design [18]. In these terms, a recent study [19] presents a prototype made in groove gap waveguide technology that uses a pin lattice to get the desired phase shift. Compared to other previous designs that make use of corrugated ridges [20], it is demonstrated that a higher phase shift and a higher compactness can be achieved by using pin lattices.

Structures with higher symmetries make possible to tailor the signal propagation behavior [21]. Some intensive studies about structures that posses higher symmetries have been recently presented [22]- [24]. Based on higher symmetries, it is possible to widen stop-bands or to control the equivalent refractive index. Some examples such as lenses or filters in microwave and millimeter-wave range based on higher symmetries are [25], [26]. Thus, introducing higher symmetries in electromagnetic devices permits a new degree of freedom in the design process.

This work presents a waveguide phase shifter working in millimeter-wave and based on higher symmetries. Glide symmetry is the chosen type of higher symmetry to achieve a greater phase shift for the same waveguide length. A unit cell has glide symmetry configuration if it is generated by a translation of half unit cell period and a mirroring regarding to a symmetry plane [21].

The document is organized as follows: Section I introduces the phase shifter designs for the millimeter-wave range. In Section II, the phase shifting unitary cells are presented and studied by means of the dispersion diagrams. Section III provides the description and design of the glide-symmetric phase shifter, joined to its comparison with the non-glide-symmetric counterpart. Section IV introduces the manufactured prototype and presents the measurement results. Finally, the conclusions are drawn in section V.

II. GLIDE-SYMMETRIC PIN STRUCTURES

Glide symmetry is the most suitable higher symmetry for this kind of phase shifter structures. Through the application of glide symmetry to the pin lattice that composes the phase shifter, the electromagnetic performance can be significantly improved and controlled. In this section, the forming phase shifting unitary cells for the different configurations are presented and analyzed through dispersion diagram studies.

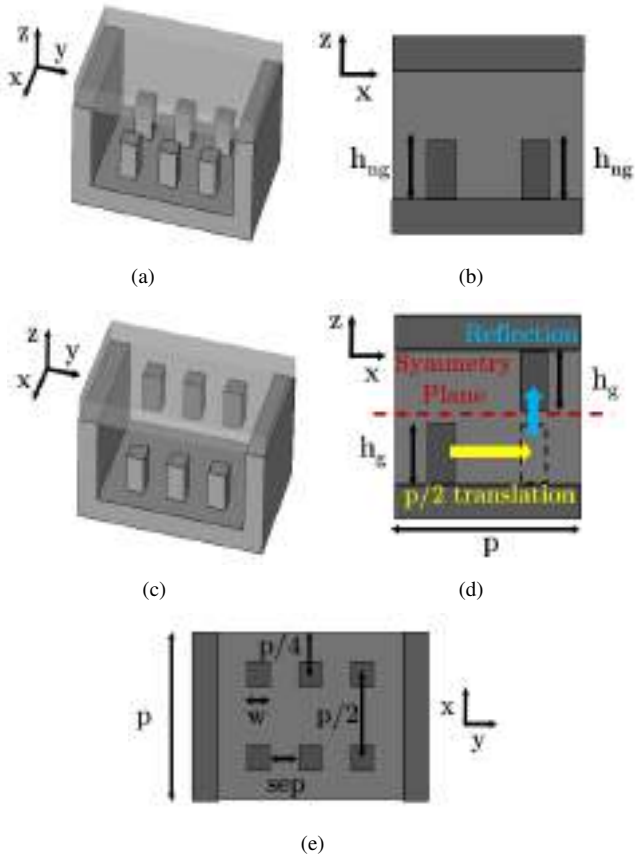

FIGURE 1: Phase shifting unitary cells: (a) non-glide-symmetric design, (b) its longitudinal cutting view, (c) glide-symmetric design, (d) its longitudinal cutting view, and (e) top view.

A. PHASE SHIFTING UNITARY CELLS

Phase shifter based on a cascade of pin rows located perpendicular to the propagation direction can be divided into unitary phase shifting cells, as it is illustrated in Figure 1. Two types of unitary cells are depicted in 3D, longitudinal

and top view. The non-glide-symmetric unitary cell (Figure 1(a)) corresponds to the unitary cell that forms the phase shifter state-of-art presented in [19].

The metallic pins that compose the phase shifter are placed only in one broad side of the waveguide. Glide symmetry is applied to each pair of pin rows that form the non-glide-symmetric cell, taking advantage of having free the upper broad side of the waveguide. This pin row displacement to impose a glide-symmetric configuration in the unitary cell is depicted in Figure 1(d). The reference symmetry plane for pin mirroring is located in the middle of the lateral waveguide side and perpendicular to it. Note that, in the pin displacement, the heights of the pins (*H*) are preserved, which means that $H_{ng} = H_g$.

The top view illustrated in Figure 1(e) is the same for both phase shifting unitary cells. Considering *p* as the fixed unitary cell length, the distance between pin rows is *p/2*. The separation between pins in the transversal direction is denoted as *sep*. The width (*W*) and height (*H*) of the pins are also the other geometric variables that have influence in the performance of the phase shifter.

The following subsection shows the comparison between both phase shifting unitary cells, glide and non-glide, presented by means of their dispersion diagrams.

B. PERFORMANCE AND DISPERSION DIAGRAM COMPARISON

Dispersion diagrams let accurately demonstrate the performance of a guiding structure through the study of the propagating modes and their distribution in frequency. The position of the first propagating mode is normally the one that defines the working range and the forward mode dispersion properties. The dispersion diagrams contained in this study have been carried out with the eigenmode solver of *CST Microwave Studio*. Each dispersion diagram shows the first propagating mode of the unitary cell for a parametric sweep. Figure 2 and Figure 3 illustrate the dispersion diagram comparison between both types of unitary cell, including height and width pin tuning, respectively. The reference line corresponds to the first propagating mode of the WR-15 standard waveguide. The sweeps of pin heights and pin widths are referred, in percentage, to the narrow and broad

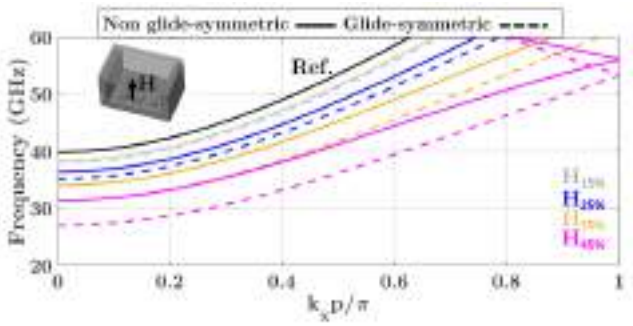

FIGURE 2: Dispersion diagram comparison modifying pin height. Dimensions are: p = 2.1 mm, w = 0.45 mm, sep = 0.6 mm and $H_{ng} = H_g$.

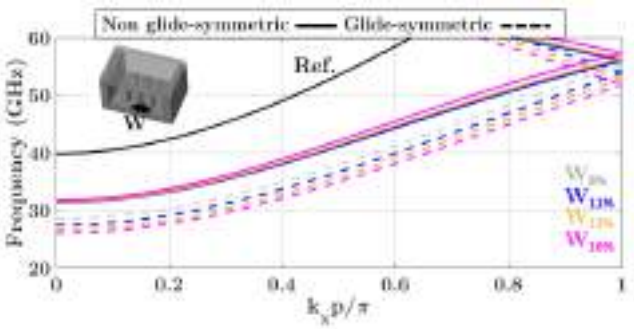

FIGURE 3: Dispersion diagram comparison modifying pin width. Dimensions are: p = 2.1 mm, sep = 0.6 mm and $H_{ng} = H_g$ = 0.85 mm.

waveguide side dimensions, respectively.

The height variation in the phase shifter pins have a higher influence in the dispersion behavior than the pin width variation. Both pin configurations, non-glide-symmetric and glide-symmetric, lower the first propagating mode regarding to the reference mode. This means that, for a given frequency, the propagation constant is increased. It can be identified that the glide-symmetric phase shifting unitary cell produces a higher propagation constant for any value of pin height and width than the non-glide case. This is directly translated into a higher phase shifting for the same waveguide length in the case of the glide-symmetric configuration. Therefore, the glide-symmetric unitary cell has a better performance in terms of phase shifting capacity compared to any other configuration. A remarkable propagation effect that appears in the mode distribution is the position of the initial propagation frequencies. The reference waveguide mode starts to propagate at approximately 40 GHz while the phase shifting unitary cell starts at 30 GHz in the case of $H_{45\%}$. This decrease in the cutoff frequency for the same waveguide size is useful for miniaturization and size reduction. This will be matter for further work since is not the scope of this document. Additionally, modifications in cell length (*p*) have been studied and illustrated in a dispersion diagram comparison in Figure 4. The normalization of the length, *p*, has been removed for a more realistic representation of the dispersion diagram and fair comparison between modes and their propagating properties.

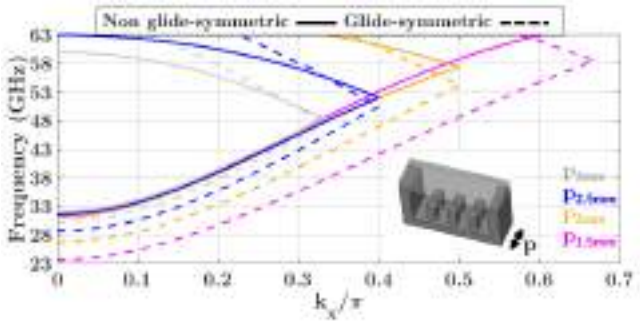

FIGURE 4: Dispersion diagram comparison modifying the cell length (*p*). Dimensions are: W = 0.45mm, sep = 0.6 mm and $H_{ng} = H_g$ = 0.85 mm.

From these results, two main conclusions can be drawn. First, the length of the phase shifting unit cell does not affect the locations of the modes for the non-glide-symmetric unitary cell. However, for glide-symmetric unit cell, the frequency position of the modes decreases as the cell length is reduced. Second, the position of the cutting frequency between the two types of cell configuration is different. It is also noticed that, for greater values of p in the glide configuration, the cutting frequency between modes is reduced. This effect is due to the reduction of electromagnetic coupling between pin rows placed in in the glide-symmetric configuration. Therefore, the length of the unitary cell strongly affects the mode distribution and has to be carefully chosen for a proper effect of the glide symmetry in the frequencies of interest.

III. PHASE SHIFTER PERFORMANCE

The design of a complete phase shifter consists of several phase shifting unitary cell in cascade along the direction of propagation. The pin heights and cell length have to be properly chosen according to the phase delay required and the working frequency band. In this section, 53 GHz is fixed as the central frequency, providing a phase shift of 180 degrees for the glide configuration. Once the glide-symmetric phase shifter is designed complying with this requirement, the same pins are considered, but placed in non-glide-symmetric configuration. Figure 5 illustrates both phase shifter designs, non-glide-symmetric and glide-symmetric configurations, and the parameter values of each constituting unitary cell introduced. For a proper impedance matching, incremental tailoring of the pin row heights at both ends of the phase shifter are needed.

The gap waveguide technology employed for manufacturing both phase shifters and a reference waveguide, is the glide-symmetric holey gap waveguide reported in [27], [28]. This technology provides very low manufacturing costs with a great waveguide propagation performance. The periodic glide-symmetric holey structure used provides a stop band from 36 to 70 GHz. The holey-glide-symmetric unit cell posses these dimensions: hole diameter $2r = 3.5$ mm, hole depth $h = 3.6$ mm, unit cell size $a = 5.36$ mm and gap $g = 0.05$ mm. Complete information regarding this manufacturing technology and design guidelines can be found in the referred work [28].

A. DESIGN AND SIMULATION RESULTS

In order to validate these results, a complete prototype is designed, shown in Figure 6. It is formed by three WR-15 gap waveguide, each one with a different configuration: reference waveguide (without pins), non-glide-symmetric phase shifter and glide-symmetric phase shifter. Glide-symmetric holes are included in both sides of each waveguide path for avoiding signal leakage and coupling.

The simulation results are illustrated in Figure 7. Both phase shifters achieve a great bandwidth, from 46 to 60 GHz with insertion losses below 0.5 dB.

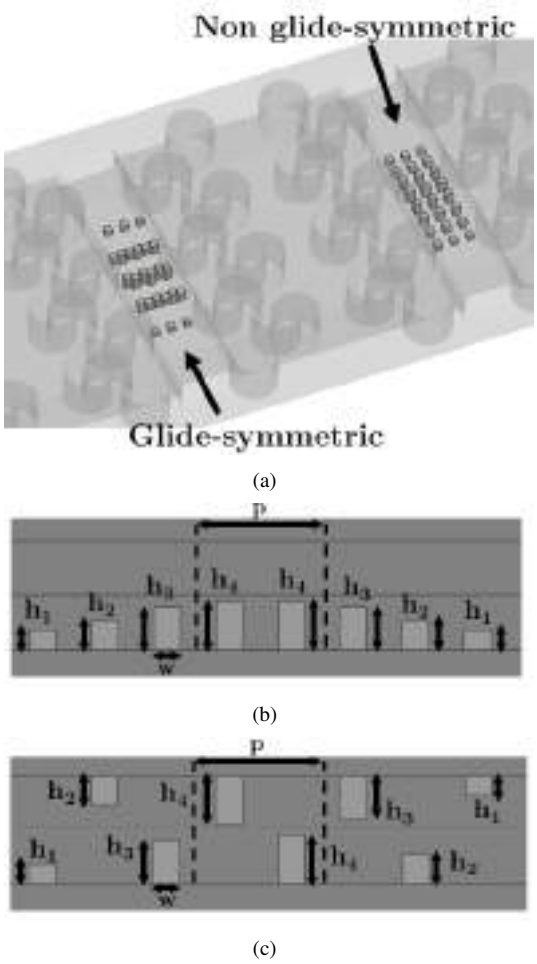

FIGURE 5: Phase shifter designs: (a) pin configurations integrated into the glide-symmetric holey gap waveguide (b) longitudinal cutting view of the non-glide-symmetric configuration, (c) longitudinal cutting view of the glide-symmetric configuration. Transversal separation *sep* = 0.6 mm.

Parameters	w	p	h_1	h_2	h_3	h_4
Values	0.45	2.1	0.35	0.5	0.75	0.85

TABLE 1: Dimensions of both phase shifters [mm].

Regarding to the phase behavior, both phase shifters have a higher phase shift than the reference waveguide. The glide-symmetric phase shifter provides a greater phase shift along the whole frequency band. Nevertheless, this difference in phase decreases as frequency increases.

Figure 7(c) illustrates the phase shift produced by each phase shifter regarding the reference waveguide phase. It is noticed that, at the center frequency, the phase shift provided by the glide-symmetric phase shifter is 40 degrees higher than its non-glide-symmetric version. This difference in phase shift was predicted in the previous dispersion diagram study. Moreover, the difference between both phase shift graphs decreases as frequency increases since they are approaching to the cutting frequency between modes.

Additionally, non-glide-symmetric phase shifter can be

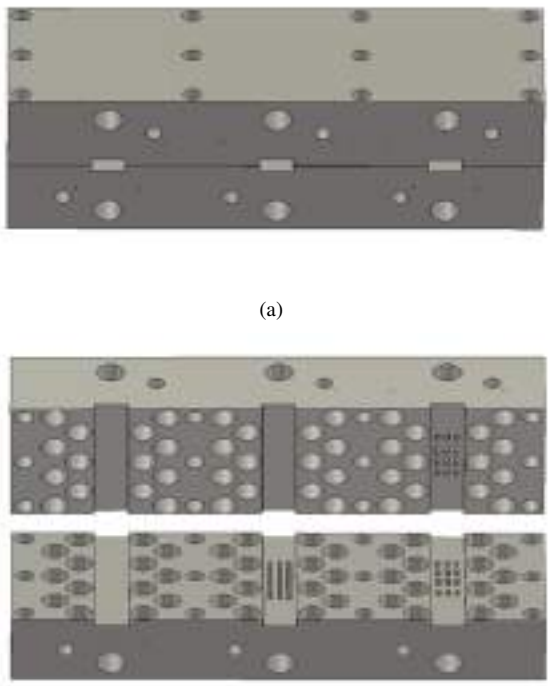

(a)

(b)

FIGURE 6: Phase shifter prototype design: (a) assembled (b) upper and lower parts.

designed to produce 180 degrees phase shift by means of enlarging the pins. However, its phase deviation with the same reference phase degree (180 degrees at 53 GHz) is bigger than the glide-symmetric phase shifter case as Figure 8 shows. This higher phase deviation in the non glide-symmetric case can be explained through linearity comparison in Figure 4. The glide-symmetric case provides a less dispersive propagating mode than the non-glide-symmetric case when the frequency increases. Table 2 shows the performance differences between both depicted phase shifter designs. Also, some aspects about manufacturing are listed.

Gap waveguide technology confines the propagation signal inside waveguides and avoids any coupling between paths. A clear vision of this fact and the difference between the field distribution for both phase shifters is illustrated in Figure 9, where the absolute E-field distribution in the gap plane is presented.

IV. PROTOTYPE MEASUREMENTS

Once designed, the prototype has been manufactured to validate the simulation results discussed above. For manufacturing, the technique used is CNC milling. The prototype is presented in Figure 10. Some screws are introduced between each row of glide-symmetric holes to achieve an accurate assembly.

The prototype has been measured from 46 to 60 GHz

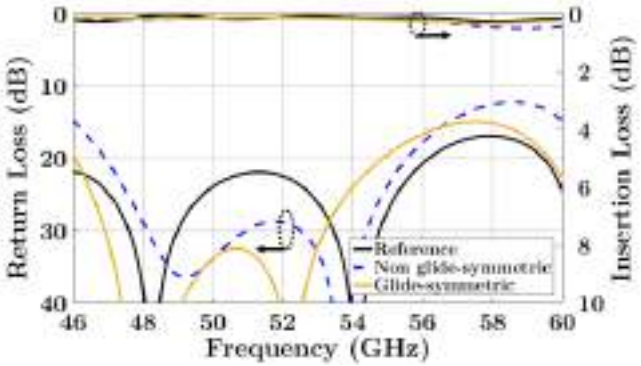

(a)

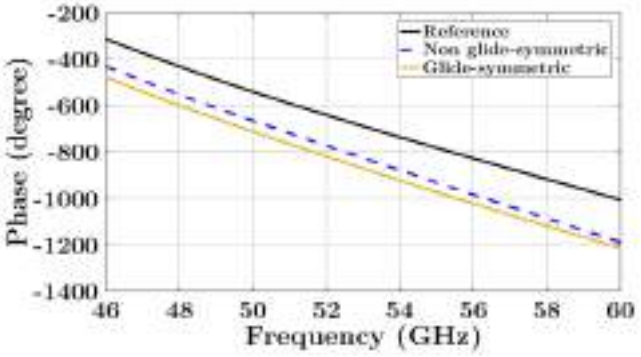

(b)

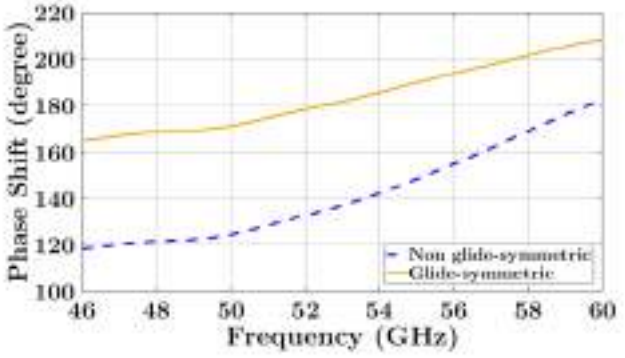

(c)

FIGURE 7: Simulated S-Parameters of the phase shifters and reference waveguide: (a)Return loss and Insertion loss (b) Unwrapped phase of S_{21} (c) Phase shift referred to the reference waveguide.

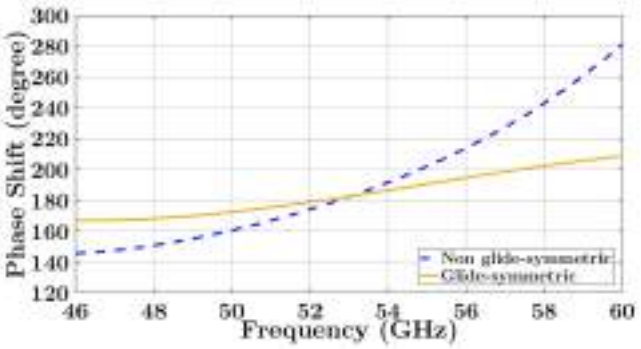

FIGURE 8: Phase shift referred to the reference waveguide when non-glide-symmetric is designed to produce 180 degrees at 53 GHz

TABLE 2: Comparison between non-glide-symmetric and glide-symmetric phase shifter designs

Phase Shifter design	Compactness (degree/mm) (Simulated Results)	Phase deviation (degree) regarding to Figure 8	Manufacturing
Non glide-symmetric	16.7	±65	Hard due to large and close pins
Glide-symmetric	22.1	±20	Easy due to small pins and bigger separation between pins

TABLE 3: Comparison between proposed and reported waveguide phase shifters

Ref.	Frequency (GHz)	Compactness (degree/mm)	Complexity	Use of Dielectric	Insertion Loss (dB)
[15]	44.5-61	7.56	Low	Yes	<1.5
[8]	26.5-40	4.63	Low	Yes	<0.4
[16]	85-115	7.08	High	No	<0.2
[17]	33-50	11.49	High	No	<9
This work	46-60	25	Low	No	<1

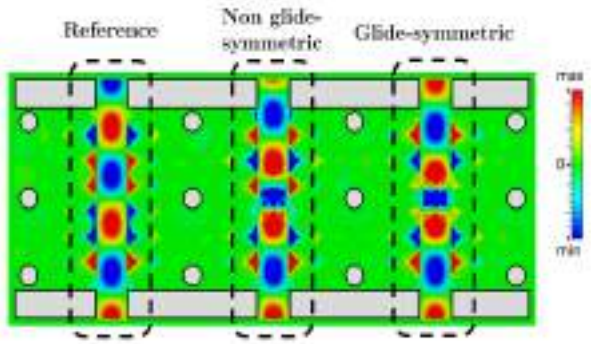

FIGURE 9: E-field distribution for the phase shifters and the reference waveguide at 53 GHz

FIGURE 10: CNC milling manufactured prototype.

with a R&S-ZVA67 VNA and the results are depicted in Figure 11(a). Regarding to the S-parameters, the return loss is higher than 10 dB in the whole frequency band for both phase shifters. On the other hand, the insertion loss of both phase shifters are very similar. The maximum is 1 dB of losses in the entire operational band. The slight increase of 0.5 dB of insertion losses compared to simulations are due to the manufacturing process, and are negligible for the phase behavior validation. Also, the ripple presented in all of the measured S-parameters are caused by the use of 1.85mm coaxial to WR-15 waveguide transitions in the measurement process. Nevertheless, there is an appropriate agreement between simulations and measurements. The comparison between the measured phase shift achieved for each phase shifter is illustred in the Figure 11(b). It is observed a difference in phase shift between the glide-symmetric and non-glide-symmetric pin configurations quite similar to the simulation results. The phase shift difference between both phase shifters is around 80 degrees. The phase shift provided by the glide-symmetric phase shifter is 40 degrees greater than the simulation results. The reason of this increment could be related to a higher height in the pins during the manufacturing process. Therefore, taking in to account the length of the phase shifter, a compactness of 25 degrees per millimeter can be achieved in comparison with the 15 degrees per millimeter provided by the non-glide-symmetric configuration. The table 3 presents a comparison with others reported works. This work presents a phase shifter design in a fully metallic structure with high compactness and low loss. Additionally, the phase shifter with the glide-symmetric pin configuration has an advantage in the pin manufacturing. The pins that compose the phase shifter are easier to manufacture since the distance between pins can be greater to achieve equal phase shift than in the non-glide-symmetric version.

V. CONCLUSIONS

In this work, we have presented a compact and low-loss V-band waveguide phase shifter design technique based on glide-symmetric pin configuration. This kind of higher symmetry permits the control and improvement of the electromagnetic behavior or radiofrequency devices. It has been demonstrated that the pin configuration is the proper option for introducing higher phase shifting effect in a waveguide-based system. There is significant increase in terms of phase shift when using a glide-symmetric pin distribution compared to its corresponding non-glide-symmetric configuration. A prototype has been manufactured in order to validate the theoretical approach through the comparison of phased shifters

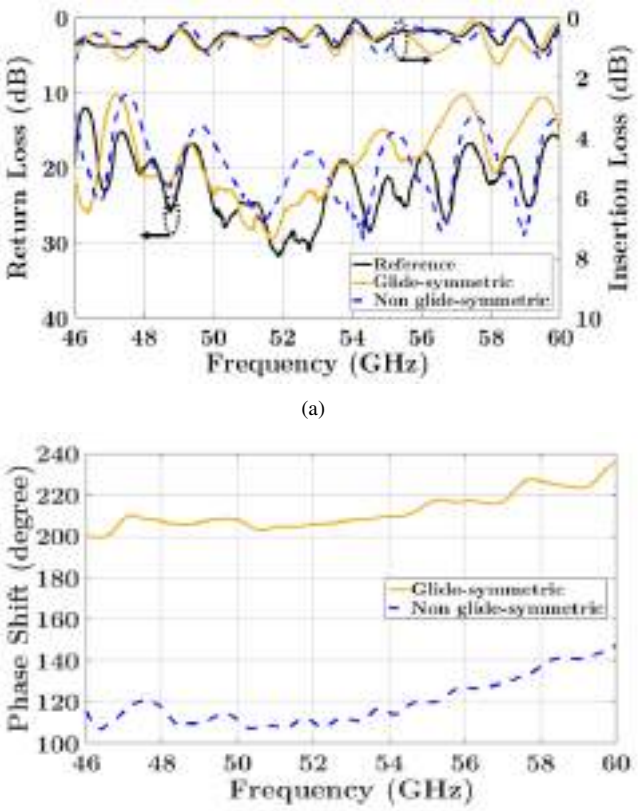

FIGURE 11: Measured S-Parameters of the phase shifters and the reference waveguide: (a) Return loss and Insertion loss (b) Phase shift referred to the reference waveguide.

with both non-glide-symmetric and glide-symmetric configurations. The measurement results demonstrate the higher performance and compactness of the glide-symmetric phase shifter. For the same distance, the glide-symmetric version of the phase shifter provides more than 60% of phase shifting compared to the non-glide-symmetric phase shifter. Both phase shifters have proper impedance matching between 46 to 60 GHz and insertion loss levels lower than 1 dB in the entire band.

REFERENCES

[1] W. Hong et al.,"Multibeam Antenna Technologies for 5G Wireless Communications," in *IEEE Transactions on Antennas and Propagation*, vol. 65, no. 12, pp. 6231-6249, Dec. 2017.

[2] T. Djerafi, N. J. G. Fonseca and K. Wu, "Broadband Substrate Integrated Waveguide 4x4 Nolen Matrix Based on Coupler Delay Compensation," in *IEEE Transactions on Microwave Theory and Techniques*, vol. 59, no. 7, pp. 1740-1745, July 2011.

[3] A. Tamayo-Dominguez, J. Fernandez-Gonzalez and M. S. Castaner, "Low-Cost Millimeter-Wave Antenna with Simultaneous Sum and Difference Patterns for 5G Point-to-Point Communications," in *IEEE Communications Magazine*, vol. 56, no. 7, pp. 28-34, July 2018.

[4] J. Lian, Y. Ban, Q. Yang, B. Fu, Z. Yu and L. Sun, "Planar Millimeter-Wave 2-D Beam-Scanning Multibeam Array Antenna Fed by Compact SIW Beam-Forming Network," in *IEEE Transactions on Antennas and Propagation*, vol. 66, no. 3, pp. 1299-1310, March 2018.

[5] J. Lian, Y. Ban, C. Xiao and Z. Yu, "Compact Substrate-Integrated 4 ÃŮ 8 Butler Matrix With Sidelobe Suppression for Millimeter-Wave Multibeam Application," in *IEEE Antennas and Wireless Propagation Letters*, vol. 17, no. 5, pp. 928-932, May 2018.

[6] K. Tekkouk, J. Hirokawa, R. Sauleau, M. Ettorre, M. Sano and M. Ando, "Dual-Layer Ridged Waveguide Slot Array Fed by a Butler Matrix With Sidelobe Control in the 60-GHz Band," in *IEEE Transactions on Antennas and Propagation*, vol. 63, no. 9, pp. 3857-3867, Sept. 2015.

[7] Q. Yang, Y. Ban, J. Lian, Z. Yu and B. Wu, "SIW Butler Matrix with Modified Hybrid Coupler for Slot Antenna Array," in *IEEE Access*, vol. 4, pp. 9561-9569, 2016.

[8] F. Parment, A. Ghiotto, T. Vuong, J. Duchamp and K. Wu, "Double Dielectric Slab-Loaded Air-Filled SIW Phase Shifters for High-Performance Millimeter-Wave Integration," in *IEEE Transactions on Microwave Theory and Techniques*, vol. 64, no. 9, pp. 2833-2842, Sept. 2016..

[9] T. Yang, M. Ettorre and R. Sauleau, "Novel Phase Shifter Design Based on Substrate-Integrated-Waveguide Technology," in *IEEE Microwave and Wireless Components Letters*, vol. 22, no. 10, pp. 518-520, Oct. 2012.

[10] I. Boudreau, K. Wu and D. Deslandes, "Broadband phase shifter using air holes in substrate integrated waveguide," 2011 IEEE MTT-S International Microwave Symposium, Baltimore, MD, 2011, pp. 1-1.

[11] P. Kildal, A. U. Zaman, E. Rajo-Iglesias, E. Alfonso and A. Valero-Nogueira, "Design and experimental verification of ridge gap waveguide in bed of nails for parallel-plate mode suppression," in *IET Microwaves, Antennas & Propagation*, vol. 5, no. 3, pp. 262-270, 21 Feb. 2011.

[12] H. Raza, J. Yang, P. Kildal and E. Alfonso, "Resemblance between gap waveguides and hollow waveguides," in *IET Microwaves, Antennas & Propagation*, vol. 7, no. 15, pp. 1221-1227, 10 December 2013.

[13] A. Algaba-Brazalez and E. Rajo-Iglesias, "Design of a Butler matrix at 60GHz in inverted microstrip gap waveguide technology," 2015 IEEE International Symposium on Antennas and Propagation & USNC/URSI National Radio Science Meeting, Vancouver, BC, 2015, pp. 2125-2126.

[14] M. A. Abdelaal, S. I. Shams and A. A. Kishk, "Compact RGW Differential Phase Shifter for Millimeter-Wave Applications," 2018 18th International Symposium on Antenna Technology and Applied Electromagnetics (ANTEM), Waterloo, ON, Canada, 2018, pp. 1-2.

[15] E. Rajo-Iglesias, M. Ebrahimpouri and O. Quevedo-Teruel, "Wideband Phase Shifter in Groove Gap Waveguide Technology Implemented With Glide-Symmetric Holey EBG," in *IEEE Microwave and Wireless Components Letters*, vol. 28, no. 6, pp. 476-478, June 2018.

[16] M. Chung, D. Je, S. Han and S. Kim, "Development of a 85-115 GHz 90-deg phase shifter using corrugated square waveguide," 2014 44th European Microwave Conference, Rome, 2014, pp. 1146-1149.

[17] E. Villa, B. Aja, J. Cagigas, E. Artal and L. de la Fuente, "Four-State Full Q-Band Phase Shifter Using Smooth-Ridged Waveguides," in *IEEE Microwave and Wireless Components Letters*, vol. 27, no. 11, pp. 995-997, Nov. 2017.

[18] Z. Qamar, S. Y. Zheng, W. S. Chan and D. Ho, "An Equal-Length Multiway Differential Metamaterial Phase Shifter," in *IEEE Transactions on Microwave Theory and Techniques*, vol. 65, no. 1, pp. 136-146, Jan. 2017.

[19] S. A. Razavi and A. U. Zaman, "A compact phase shifter in groove gap waveguide for millimeter-wave applications," 12th European Conference on Antennas and Propagation (EuCAP 2018), London, 2018, pp. 1-3.

[20] A. Tribak, A. Mediavilla, J. Zbitou, J. Cano, "Novel ridged waveguide differential phase shifter for satellite application," in *International Journal of Microwave and Optical Technology*, vol. 9, pp. 409-414, 2014.

[21] A. Hessel, Ming Hui Chen, R. C. M. Li and A. A. Oliner, "Propagation in periodically loaded waveguides with higher symmetries," in *Proceedings of the IEEE*, vol. 61, no. 2, pp. 183-195, Feb. 1973.

[22] G. Valerio, F. Ghasemifard, Z. Sipus and O. Quevedo-Teruel, "Glide-Symmetric All-Metal Holey Metasurfaces for Low-Dispersive Artificial Materials: Modeling and Properties," in *IEEE Transactions on Microwave Theory and Techniques*, vol. 66, no. 7, pp. 3210-3223, July 2018.

[23] O. Dahlberg, R. Mitchell-Thomas, and O. Quevedo-Teruel, "Reducing the dispersion of periodic structures with twist and polar glide symmetries," in *Scientific Reports*, vol. 7, 2017.

[24] F. Ghasemifard, M. Norgren, O. Quevedo-Teruel and G. Valerio, "Analyzing Glide-Symmetric Holey Metasurfaces Using a Generalized Floquet Theorem," in *IEEE Access*, vol. 6, pp. 71743-71750, 2018.

[25] P. Padilla, L. F. Herran, A. Tamayo-Dominguez, J. F. Valenzuela-Valdes and O. Quevedo-Teruel, "Glide Symmetry to Prevent the Lowest Stopband of Printed Corrugated Transmission Lines," in *IEEE Microwave and Wireless Components Letters*, vol. 28, no. 9, pp. 750-752, Sept. 2018.

[26] O. Quevedo-Teruel, J. Miao, M. Mattsson, A. Algaba-Brazalez, M. Johansson and L. Manholm, "Glide-Symmetric Fully Metallic Luneburg Lens

for 5G Communications at Ka-Band," in *IEEE Antennas and Wireless Propagation Letters*, vol. 17, no. 9, pp. 1588-1592, Sept. 2018.

[27] M. Ebrahimpouri, E. Rajo-Iglesias, Z. Sipus and O. Quevedo-Teruel, "Cost-Effective Gap Waveguide Technology Based on Glide-Symmetric Holey EBG Structures," in *IEEE Transactions on Microwave Theory and Techniques*, vol. 66, no. 2, pp. 927-934, Feb. 2018.

[28] M. Ebrahimpouri, O. Quevedo-Teruel and E. Rajo-Iglesias, "Design Guidelines for Gap Waveguide Technology Based on Glide-Symmetric Holey Structures," in *IEEE Microwave and Wireless Components Letters*, vol. 27, no. 6, pp. 542-544, June 2017.

ANGEL PALOMARES-CABALLERO was born in 1994 in Jaén, Spain. He received his B.Sc and M.Sc. in Telecommunication engineering from the University of Granada (UGR), Spain, in 2016 and 2018, respectively. Since 2017, he has been in the Department of Signal Theory, Telematics and Communications of University of Granada, where he is currently a Ph.D student. In 2018 he joined the Department of Language and Computer Science of Universidad de Málaga (UMA). His research interests include millimeter wave-antennas, gap waveguide, optimization algorithms and structures with higher symmetries.

ANTONIO ALEX-AMOR received the B.Sc. in Telecommunication Engineering from Universidad de Granada (UGR) in 2016 and the M.Sc. degree in Telecommunication engineering from Universidad Politécnica de Madrid (UPM) in 2018, where he is currently pursuing the Ph.D. degree. Since 2016 he has been with the Radiation Group of the Signal, Systems and Radiocommunications Department of UPM, and in 2018 he joined the Department of Language and Computer Science of Universidad de Málaga (UMA). His current research area covers the use of liquid crystal as tunable dielectric, radiofrequency (RF) energy harvesting systems and higher symmetry structures.

PABLO PADILLA was born in 1982 in Jaén, Spain. He received the Telecommunication Engineer degree from Technical University of Madrid (UPM), Spain, in 2005. Until September 2009, he was with the Radiation Group of the Signal, Systems and Radiocommunications Department of UPM, where he carried out his Ph.D. In 2007, he was with the Laboratory of Electromagnetics and Acoustics at the Ecole Polytechnique Fd́érale de Lausanne (EPFL), Switzerland, as an invited Ph.D. Student. In 2009 he carried out a postdoctoral stay at the Helsinki University of Technology (AALTO-TKK), and in September 2009, he gained an Assistant Professor position in the Signal Theory, Telematics and Communications Department at the University of Granada (UGR). Since 2012, he is Associate Professor. In 2017 he was visiting professor at the Royal Institute of Technology of Stockholm (KTH). He is author of more than sixty high-impact journal contributions and more than fifty contributions to international symposia. His research interests include a variety area of knowledge, related mainly to electromagnetism and communication topics (radiofrequency devices, antennas, propagation, etc.).

FRANCISCO LUNA received his degree in Engineering and PhD in Computer Science in 2002 and 2008, respectively, from the University of Málaga, Spain, where he was research assistant until 2012. In 2012, he joined Universidad Carlos III of Madrid with a postdoc position, and in 2013 the Universidad de Extremadura as Assistant Professor. Since 2015 he is an Associate Professor at the University of Málaga. His current research interests include the design and implementation of parallel and multi-objective meta-heuristics, and their application to solve complex problems arising in several domains, including telecommunications, finance, and structural design.

JUAN VALENZUELA-VALDES was born in Marbella, Spain. He received his degree in telecommunications engineering from the Universidad de Malaga, Spain, in 2003 and his Ph.D. from Universidad Politécnica de Cartagena, Spain, in May 2008. In 2004, he joined the Department of Information Technologies and Communications, Universidad Politécnica de Cartagena. In 2007, he joined EMITE Ing. as head of research. In 2011, he joined Universidad de Extremadura, and in 2015, he joined Universidad de Granada where he is currently an associate professor. His current research areas cover wireless communications and efficiency in wireless sensor networks. He has also been awarded several prizes, including a national prize to the Best Ph.D in Mobile Communications by Vodafone and the i-patentes award by Spanish Autonomous Region of Murcia for innovation and technology transfer excellence. He was cofounder of Emite Ing, a spin-off company. He also holds several national and international patents. His publication record is composed of more than 80 publications, including 40 JCR indexed articles, more than 30 contributions in international conferences and 7 book chapter.

2.1.2 Dispersion and Filtering Properties of Rectangular Waveguides Loaded With Holey Structures

In this publication, the potentials of rectangular waveguides with holey structures for millimeter-wave frequencies is presented. A comprehensive study of the propagation constant for different hole configurations inside the waveguide is performed. Hole configurations in glide symmetry, mirror symmetry and other intermediate ones are analyzed. Noting the benefits of glide symmetry and mirror symmetry for phase constant and attenuation constant, respectively, two millimeter-waves devices are designed. The first one is a phase shifter with a flat phase response in 180º from 56.5 GHz to 74.5 GHz. The second design corresponds to a filter with a 20-dB rejection band in the 63 GHz to 75 GHz band.

THIS IS A POSTPRINT VERSION OF THE PAPER:

Á. Palomares-Caballero, A. Alex-Amor, P. Padilla and J. F. Valenzuela-Valdés, "Dispersion and Filtering Properties of Rectangular Waveguides Loaded With Holey Structures," in *IEEE Transactions on Microwave Theory and Techniques*, vol. 68, no. 12, pp. 5132-5144, Dec. 2020.

- Journal Impact Factor (JIF) in JCR 2020: 3.599
- Category: ENGINEERING, ELECTRICAL & ELECTRONIC. JIF Rank: 81/273 (Q2).

Disclaimer:
This work has been published on IEEE Transactions on Microwave Theory and Techniques. DOI: 10.1109/TMTT.2020.3021087

Dispersion and Filtering Properties of Rectangular Waveguides Loaded with Holey Structures

Ángel Palomares-Caballero, Antonio Alex-Amor, Pablo Padilla, and Juan F. Valenzuela-Valdés

***Abstract*—This paper analyzes thoroughly the dispersion and filtering features of periodic holey waveguides in the millimeter-wave frequency range. Two structures are mainly studied depending on the glide and mirror symmetries of the holes. A parametric study of the dispersion characteristics of their unit cells is carried out. Glide-symmetric holey waveguides provide a higher propagation constant and a low dispersion over a wide frequency range regarding hollow waveguides. This property is particularly useful for the design of low-loss and low-dispersive phase shifters. We also demonstrate that glide-symmetric holey waveguides are less dispersive than waveguides loaded with glide-symmetric pins. Furthermore, we perform a Bloch analysis to compute the attenuation constants in holey waveguides with mirror and broken glide symmetries. Both configurations are demonstrated to be suitable for filter design. Finally, the simulation results are validated with two prototypes in gap-waveguide technology. The first one is a 180^o phase shifter based on a glide-symmetric holey configuration that achieves a flat phase shift response over a wide frequency range (27.5% frequency bandwidth). The second one is a filter based on a mirror-symmetric holey structure with 20-dB rejection from 63 GHz to 75 GHz.**

***Index Terms*—Filter, gap waveguide, glide symmetry, hollow waveguide, low dispersion, millimeter-wave, mirror symmetry, multi-modal (M-M) transfer matrix, periodic holey structures, phase shifter.**

I. Introduction

WAVEGUIDE technology is one of the preferred guiding structures technology for high-frequency applications due to the low losses produced in the field propagation [1]. Hollow waveguides are suitable for the design of electronic devices that operate at millimeter-wave and terahertz regimes [2], at the expense of the complexities in its manufacturing process that were lately relieved with the implementation of gap waveguides [3]–[7].

In communication systems, the implementation of filters and phase shifters is typically necessary [8]–[10]. A strategy to design these RF (radio-frequency) components is the inclusion of periodic structures inside the waveguide [11]–[13]. In the case of filters, the stopbands produced by the periodic configuration are utilized to tune rejection bands [14]–[21]. The design of phase shifters based on metallo-dielectric periodic structures allows to artificially modify the propagation constant in the waveguide with high tunability. In substrate integrate waveguide (SIW) technology, there are some designs that make use of periodic metallic posts [22], omega particles [23] or thin slots [24] to achieve the desired phase shift. Conversely, only a few phase shifters based on periodic structures are reported in hollow waveguides. Corrugations [25], [26] and structures based on pins [27]–[29] are commonly used.

Some previous works have already combined periodic structures with glide symmetry to enhance the properties of their devices: increase the propagation constant and reduce the dispersion over a wide frequency range [30]–[39]. Glide-symmetric holey structures [40] are of particular interest from a manufacturing point of view due to their cost-effective fabrication with milling techniques. For instance, glide-symmetric holes have been implemented in a parallel-plate waveguide [41] and in multilayer waveguide [42]. A similar periodic structure with a higher separation between plates is used in [43] to design a prism in order to decrease the beam squint of a leaky-wave antenna. Furthermore, it has been detailed in [44] that breaking the glide symmetry is a complementary tool for the design of filters, due to the creation of a stopband. The only reported work that uses glide-symmetric holey structures, namely braided glide symmetry, for the design of a filter device in waveguide is [45].

Most of the previously reported works are focused on the study of parallel-plate structures loaded with glide-symmetric holes. In this paper, we analyze the wave propagation when periodic holes possessing glide and mirror symmetries are inserted in the upper and lower plates of the rectangular waveguide. We characterize the influence of the geometrical parameters that define the holey structures on their dispersion curves. In particular, the variations of the cutoff frequencies in the holey waveguide are studied in detail. A comparison between waveguides loaded with glide-symmetric holes and pins [28] is also carried out, showing that holey waveguides are generally less dispersive than pin-loaded waveguides. In addition, the attenuation constant is computed to accurately characterize the stopbands that appear in both holey configurations. Finally, two prototypes are manufactured for validation purposes: a wideband and low-dispersive phase shifter based on a glide-symmetric holey configuration that operates in V-band, and a filter based on the a mirror-symmetric holey configuration with 20-dB rejection from 63 GHz to 75 GHz.

The paper is organized as follows. In Section II, the anal-

Manuscript received X, 2020; revised X, 2020. This work was supported in part by the Spanish Program of Research, Developmentand Innovation under Project TIN2016-75097-P, Project RTI2018-102002-A-I00 and, Project EQC2018-004988-P, in part by "Junta de Andalucía" under Project B-TIC-402-UGR18 and Project P18.RT.4830 and in part by the predoctoral grant FPU18/01965. *(Corresponding author: Ángel Palomares-Caballero.)*

Á. Palomares-Caballero, A. Alex-Amor, Juan Valenzuela-Valdés and P. Padilla are with the Departamento de Teoría de la Señal, Telemática y Comunicaciones, Universidad de Granada, 18071 Granada, Spain (e-mail: angelpc@ugr.es; aalex@ugr.es; juanvalenzuela@ugr.es; pablopadilla@ugr.es).

A. Alex-Amor is with the Information Processing and Telecommunications Center, Universidad Politécnica de Madrid, 28040 Madrid, Spain (e-mail: aalex@gr.ssr.upm.es).

ysis of the dispersion properties of the holey waveguide is carried out. We also elaborate a comparison with pin-loaded waveguides, as well as a discussion of the stopband properties for the mirror-symmetric and broken glide-symmetric cases. Section III presents the design, manufacturing and experimental results of a filter and a wideband phase shifter composed by the analyzed mirror-symmetric and glide-symmetric holey unit cells, respectively. Finally, the conclusions are drawn in Section IV.

II. Dispersion and Stopband Analysis of the Holey Waveguide

In this section, we study the wave propagation in periodic holey waveguides and analyze their dispersion and stopband features. The periodic holey waveguides under study are illustrated in Fig. 1(a) where perfect metallic boundary conditions are enforced on the lateral walls of the waveguide. In this figure, the air zones inside the periodic structures are depicted to observe the configurations of the holes inside the waveguide. A cut showing their longitudinal sections is also presented in Fig. 1(b). Two configurations are considered depending on the symmetry of the holes of the upper and lower waveguide plates. In the mirror-symmetric configuration, the upper and lower holes are aligned along the z-axis. In the glide-symmetric configuration, the lower holes are off-shifted half a period in x-direction in regard to the upper holes [31]. A reference waveguide is also considered in the study in order to compare the properties of the holey unit cells to it.

Fig. 1(c) illustrates the unit cells associated to the aforementioned periodic holey 1D structures. Both mirror-symmetric and glide-symmetric structures are periodic in x-direction. They have a waveguide height g and a waveguide width w whose size corresponds to the WR15 waveguide. All simulated results in this section are related to lossless structures. The computation of the dispersion diagrams is performed in commercial software *CST Microwave Studio* and an own code based on multi-modal analysis. Our reference unit cell has the following dimensions: height of the waveguide $g = 0.3$ mm, width of the waveguide $w = 3.76$ mm and period $p = 2.4$ mm. Moreover, for the sake of completeness, the first or fundamental and second propagating modes of the unit cell are represented in the dispersion diagrams.

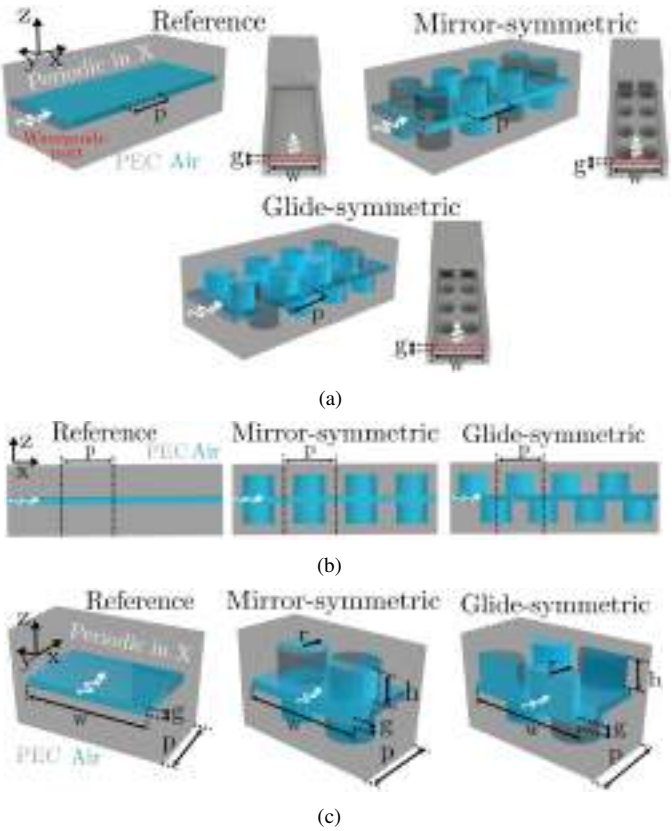

Fig. 1. Reference and holey waveguide periodic structures. (a) Formed by four unit cells where input waveguide is marked in red. (b) Longitudinal cut views and (c) Unit cells.

A. Dispersion Properties

In this subsection, the effect of the geometrical parameters in the holey unit cells is analyzed in detail. Both mirror-symmetric and glide-symmetric unit cells are studied in order to identify their dispersion behaviors and differences between them. The present results are computed with the Eigenmode solver of *CST*.

Fig. 2(a) presents the dispersion diagram of a holey waveguide whose lower holes are off-shifted a distance d_x with respect to the upper holes. Displacements of $d_x = 0$ and $d_x = p/2$ correspond to the mirror-symmetric and glide-symmetric configuration, respectively. A displacement different from the glide-symmetric one introduces stopbands. This effect is also appreciated for other kinds of unit cells [34], [38]. Another advantage provided by the glide-symmetric configuration is that the first mode is approximately parallel regarding the reference waveguide in a wide frequency range. This dispersive behavior will be used in Section III to design a low-dispersive phase shifter in waveguide. For the sake of completeness, Fig. 2(b) presents the comparison of the glide-symmetric unit cell with PEC (perfect electric conductor) and PMC (perfect magnetic conductor) lateral walls. In the case of placing a lateral PMC condition, a mode without cutoff frequency propagates. This mode corresponds to the TEM mode in a parallel-plate waveguide.

The influence of hole radius r on the dispersion diagram of the glide-symmetric and mirror-symmetric unit cells is illustrated in Fig. 3. As previously evidenced in Fig. 2, a stopband exists between the first and second propagating modes when the holes do not preserve glide symmetry. In both structures, an increase in the radius of the hole provokes a denser unit cell, in terms of propagation constant, due to a higher interaction between the propagating modes and the hole radius. Another important effect that is observed is the increase in the separation between the cutoff frequencies of the first and second propagating modes.

Fig. 4 illustrates the dispersion diagram for the glide-symmetric and mirror-symmetric structures when the depth of the hole h is modified. In both configurations, an increase

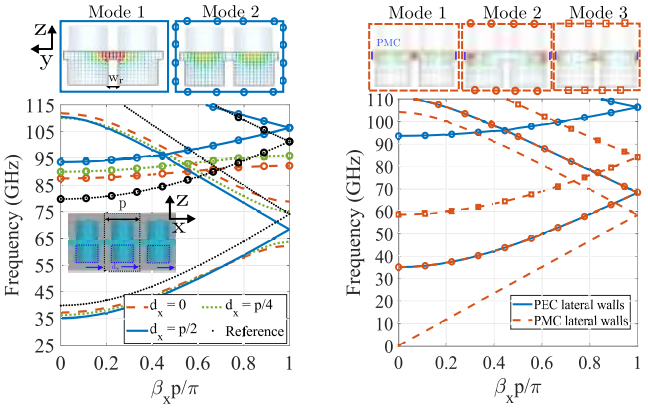

(a) (b)

Fig. 2. (a) Dispersion diagram of a glide-symmetric unit cell when the lower holes are displaced d_x in x-direction. (b) Dispersion diagram when PEC or PMC are placed at lateral walls in the glide-symmetric unit cell. First, second and third propagating modes are displayed in the figure. Holey waveguide unit cell has the following dimensions: $p = 2.4$ mm, $g = 0.3$ mm, $h = 1$ mm and $r = 0.75$ mm.

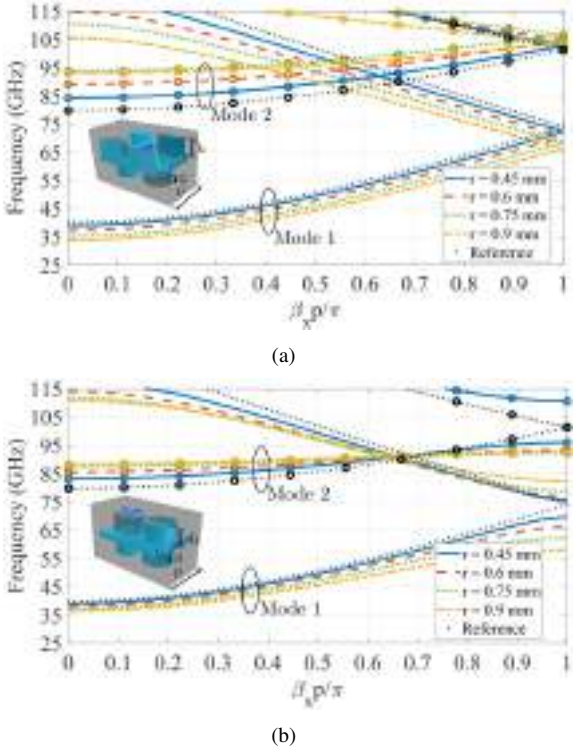

(a) (b)

Fig. 3. Dispersion diagrams of the (a) Glide-symmetric and (b) Mirror-symmetric holey waveguides when the radius of the holes is modified. First and second propagating modes are displayed in the figure. The geometrical parameters of the depicted unit cells are: $p = 2.4$ mm, $g = 0.3$ mm, $h = 1$ mm and $w = 3.76$ mm.

in the depth of the hole provokes a denser unit cell. Nevertheless, from certain hole depth, the dispersion diagram remains unchanged since the modes are evanescent inside the holes. This effect also occurs in holey metasurfaces [32], [35], [37], [40]. This enables an interesting cost-effective manufacturing of waveguide structures with holey unit cells by through holes if the selected hole depth is large enough. That is, the end of the hole does not need to be short-circuited if the hole is depth

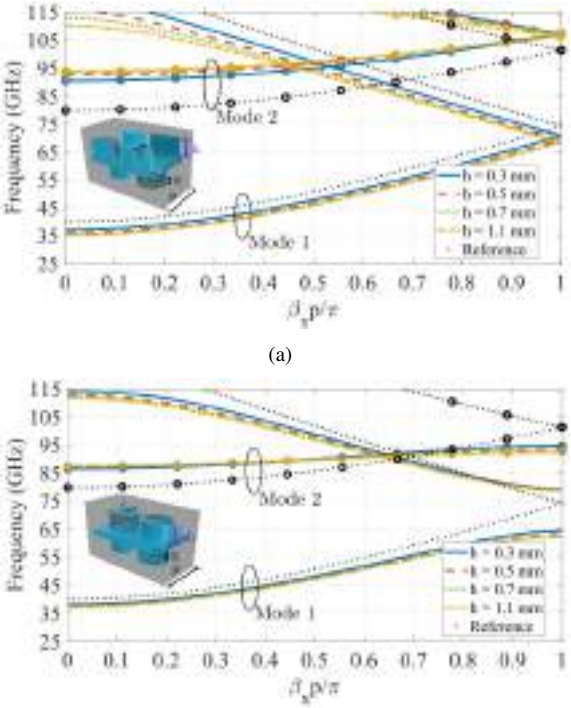

(a) (b)

Fig. 4. Dispersion diagrams of the (a) Glide-symmetric and (b) Mirror-symmetric holey waveguides when varying the depth of the holes. First and second propagating modes are displayed in the figure. The geometrical parameters of the unit cells are: p = 2.4 mm, g = 0.3 mm and r = 0.75 mm.

in terms of wavelength.

In Fig. 5, the influence of the height of the waveguide g is analyzed. It is observed that smaller values of g provide a higher propagation constant, since the top and bottom holes are closer and their interaction with the propagating mode is stronger. This fact makes the need of a waveguide height small enough in order to take into account the effect of the holes. An additional effect of reducing the height of the waveguide is the increase in the separation of the cutoff frequencies, similar to the one shown in Fig. 3. This is another possibility to extend the bandwidth of the fundamental mode.

The effect of the period p on the glide-symmetric and mirror-symmetric holey waveguides is shown in Fig. 6. Note that propagation constant β_x is normalized to k_0 in Fig. 6 to take into account that the period is varying. For both configurations, as the period increases, the holes are more distant and thus, their interaction decreases. For instance, the consequence in the mirror-symmetric case is the narrowing of the stopband region. Conversely, reducing the period, the stopband widens and displaces upwards in frequency.

The last parameter under study is the number of upper and lower holes that define the unit cell. The influence of the number of holes on the dispersion diagram is illustrated in Figs. 7(a) and 7(b) for the glide-symmetric and mirror-symmetric configurations, respectively. The cutoff frequencies of the first and second propagating modes vary according to the number of holes placed in the unit cell. Furthermore, both configurations present the same effects

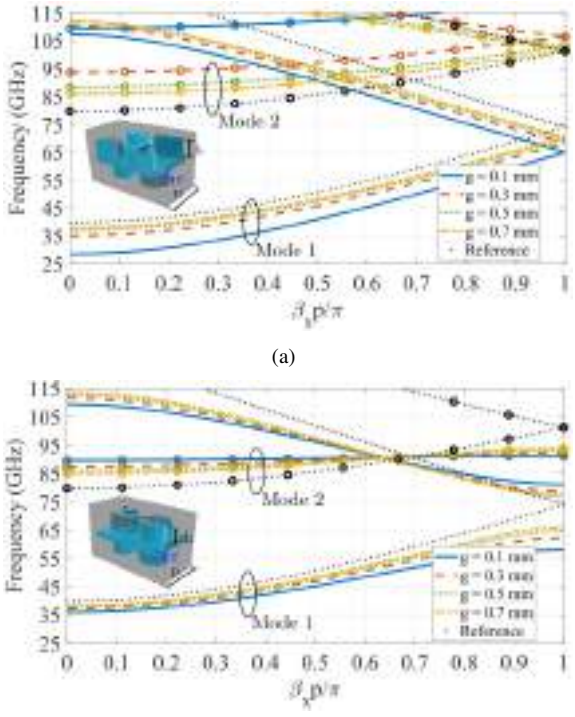

Fig. 5. Dispersion diagrams of the (a) Glide-symmetric and (b) Mirror-symmetric holey waveguides when varying the height of the waveguide. First and second propagating modes are displayed in the figure. The geometrical parameters of the unit cells are: p = 2.4 mm, r = 0.75 mm and h = 1 mm.

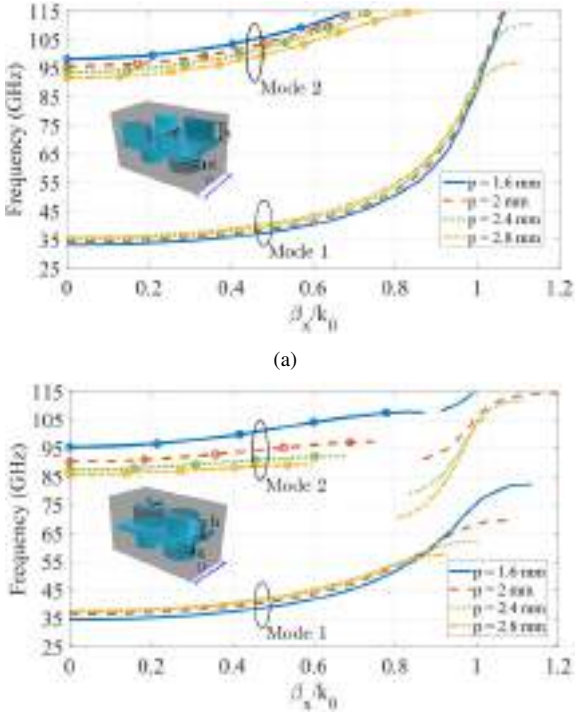

Fig. 6. Dispersion diagrams of the (a) Glide-symmetric and (b) Mirror-symmetric holey waveguides when varying the period of the unit cell. First and second propagating modes are displayed in the figure. The geometrical parameters of the unit cells are: g = 0.3 mm, r = 0.75 mm and h = 1 mm.

when the number of holes is varied with the difference of the appearance of stopbands in the mirror-symmetric unit cell.

The amplitude distributions of the different modes provide a physical rationale for understanding the cutoff frequencies for each unit cell case. Thus, Fig. 7(c) illustrates the electric field distributions of the propagating modes in the glide-symmetric unit cell as the number of holes is varied. For the sake of conciseness, the electric field of the mirror-symmetric unit cell has not been shown. In the case of a unit cell with a single hole (blue lines), the cutoff frequencies of the first and second modes are above and below the reference waveguide modes, respectively. The presence of a hole in the middle of the waveguide makes the TE_{10} splits in two quasi-TE_{10} modes that form the first mode (see blue box of Fig. 7(c)). The effective width of the quasi-TE_{10} mode is shorter than the width of the original TE_{10} and thus, the cutoff frequency for the first mode increases regarding the reference waveguide. The value of the cutoff frequency takes into account all the effective widths along the length of the unit cell since the size of the hole varies along the x-direction due to its circular geometry. However, it should be remarked that the illustrated transversal cut is shown at the center of the unit cell, that is, where the size of the hole is maximum and the effective width is minimum.

The second mode for the single-hole unit cell has a similar configuration that the TE_{20} of the reference waveguide. A lower cutoff frequency compared to the reference waveguide is obtained due to the increase of the separation in y-direction between amplitude maxima of the second mode, which means the increase of the effective width for the mode. If the radius of the hole is progressively smaller, the cutoff frequency of the second mode increases turning into the TE_{20} mode in the reference waveguide.

In the case of the unit cell with two holes in glide-symmetric configuration, the cutoff frequencies of the first and second modes are below and above the reference waveguide modes, respectively. Observing the electric field distributions of the modes, they resemble to the existing modes in a single ridged waveguide [46]. Comparing the mirror-symmetric and glide-symmetric unit cells, the differences in the cutoff frequencies are caused by the existence of transversal cuts without presence of holes, in the same manner that it occurs for the single-hole unit cell.

Lastly, the unit cell with three holes is analyzed. In this case, the electric fields for the first and second modes are similar to those observed in a double-ridged waveguide section [47]. In addition, it is evidenced in Figs. 7(a) and 7(b) that the phase constant for the first mode in the two-hole and three-hole unit cell are quite similar. This fact can be explained by the similarity between their electric field distributions (see red and green boxes in Fig. 7(c)).

B. Comparison between holey and pin-loaded unit cells

A dispersion comparison between the holey waveguide unit cell and its counterpart, the pin-loaded unit cell, is carried out in this subsection. The dispersion properties of

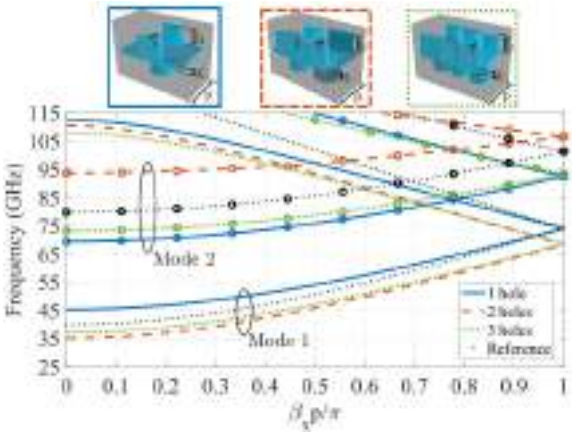

(a)

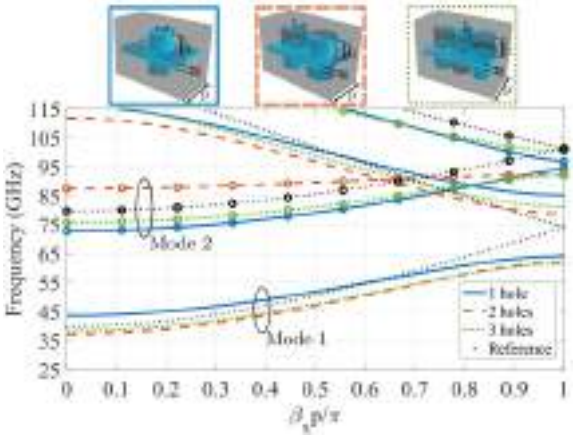

(b)

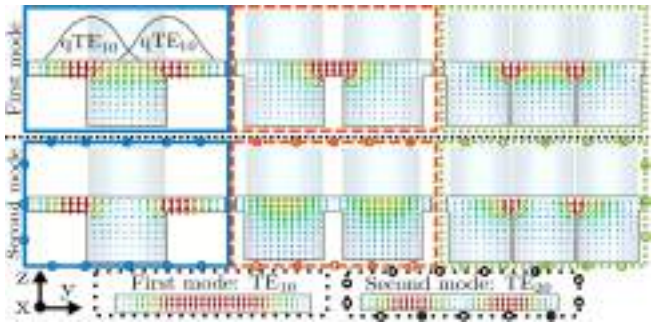

(c)

Fig. 7. Dispersion diagrams when the number of holes is modified for (a) The glide-symmetric and (b) Mirror-symmetric holey unit cells. The geometrical parameters of the unit cells are: p = 2.4 mm, g = 0.3 mm, r = 0.75 mm and h = 1 mm. First and second propagating modes are displayed in the figure. (c) Electric field distributions for the propagating modes in the reference and glide-symmetric unit cells when modifying the number of holes.

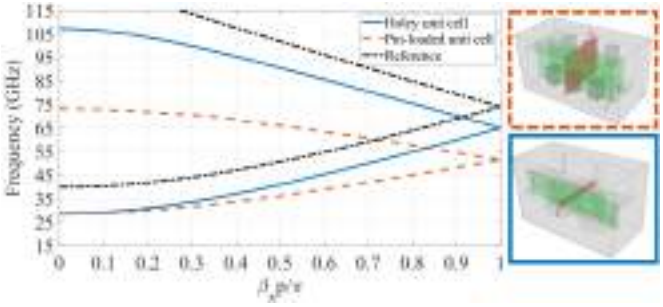

(a)

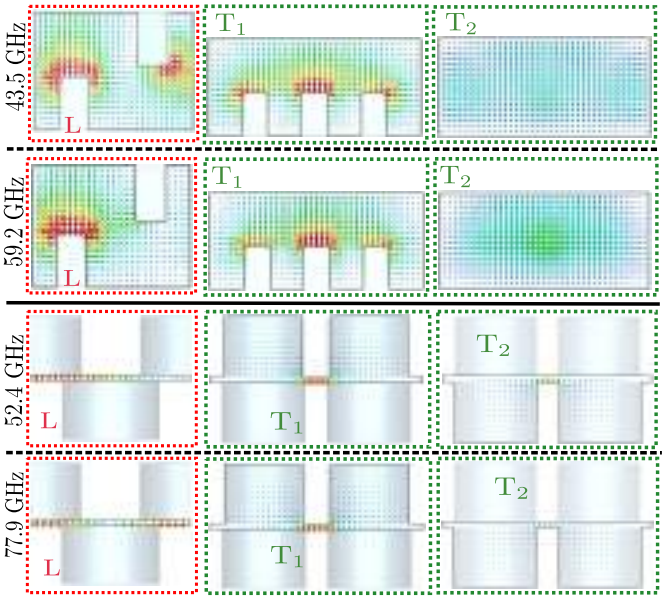

(b)

Fig. 8. Comparison between holey and pin loaded unit cells. (a) Dispersion diagrams of the first propagating mode and (b) Electric field distributions in different cut views at the same phase difference ($\beta_x p/\pi = 0.75$) between limits of the unit cell (p = 2.4 mm). The first propagating mode is displayed in the figure.

the structure with pins in waveguide were analyzed in our previous work [28]. The results show the beneficial effect of the glide-symmetric structure with pins for the design of waveguide phase shifters. Since both holey and pin-loaded waveguides can tune the propagation constant depending on the dimensions of holes and pins, respectively, it is of interest to analyze the advantages and disadvantages of their use. In Fig. 8(a), the dispersion diagram of the fundamental mode in a glide-symmetric configuration is illustrated. In order to make a fair comparison, the geometrical parameters of both unit cells have been adapted so the same cutoff frequency with the same unit cell period p and the same waveguide width (WR15 waveguide size) is obtained. Thus, the height of the pins has been set to 0.85 mm. It is observed that the pin-loaded waveguide is more frequency-dispersive compared to the holey waveguide. That is, the dispersion curve of the holey waveguide maintains approximately parallel to the reference curve in a wider bandwidth.

To get a physical insight on the behavior of both holey and structure with pins configurations, the electric field distribution at different sections of the unit cells is analyzed in Fig. 8(b). For the computation, a fixed phase constant ($\beta_x p/\pi = 0.75$) has been selected. As the mode is propagating in the unit cells, the pin-loaded design has more noticeable differences in the boundary conditions between transversal sections. The electric field in the transversal cut T_1 has different boundary conditions due to the presence of pins compared to the ones in T_2 where there is no structure with pins. This inhomogeneity in the structure along different transversal sections is not observed for the holey unit cell where the transversal sections are very

similar among them approaching to a single-ridged waveguide section. This fact provokes that glide-symmetric holey waveguides are low-dispersive over a wide range of frequency in contrast with the dispersive behavior of the pin-loaded waveguide. This enhanced performance can be exploited for the design of wideband and low-dispersive components with fine tunability of their dispersive properties, as it was depicted in the previous subsection. In addition, the reduced size of pins as the frequency increases implies in general a higher manufacturing complexity compared to the implementation of holes.

C. Stopband Analysis

In this subsection, we study the filtering capabilities of the mirror-symmetric and broken glide-symmetric holey structures. We analyze the effect of the geometrical parameters that define the holey unit cells on the stopband region. The Eigenmode solver of *CST* is not able to compute the attenuation in periodic structures, namely the real part α of the propagation constant $\gamma = \alpha + j\beta$. To solve this problem, we perform a Bloch analysis, similar to [48], [49], based on the multi-modal transfer-matrix method detailed in the Appendix. The multi-modal transfer matrix **T** is extracted from the generalized scattering matrix **S** of a single unit cell [50], [51]. The **S** matrix is computed via full-wave simulations with the frequency solver (tetrahedral mesh) of *CST*.

From the different configurations presented in Fig. 9, the most demanding for the multi-modal method are the glide-symmetric structures, due to the strong coupling of higher-order Floquet harmonics [49], [52]–[54]. Thus, mirror-symmetric and broken glide-symmetric structures will demand, in general, a lower number of modes N. During the computation of the results, it is observed that the choice of modes that possess a maximum of electric field in the center of the waveguide (area between holes) favours the convergence of results. It is found that $N = 3$ modes are needed in the glide-symmetric holey configuration. See that the undesired stopband disappears and the results converge. $N = 2$ modes are used in the computation of broken glide-symmetric structures. Only one mode ($N = 1$) is needed in the mirror-symmetric configuration due to the lower higher-order coupling between modes.

As previously discussed in Section II.A, the glide-symmetric structure suppresses the stopband between first and second modes, so the fundamental mode propagates in the entire WR15 frequency range. This fact can be appreciated in Fig. 9(a). In order to create a stopband in the glide-symmetric structure and exploit its filtering properties, the glide symmetry must be conveniently broken. This can be achieved by using holes of different radii and heights, as previously discussed in [44]. Alternatively, work in [45] presents a holey unit cell with braided glide symmetry that provides a high attenuation value. In this work, different configurations of the holes are depicted in detail to produce stopbands in holey unit cells. As an example, Fig. 9(b) shows the creation of a stopband from 65 GHz to 75 GHz after breaking glide symmetry by modifying the radius r_2 of the intermediate bottom holes.

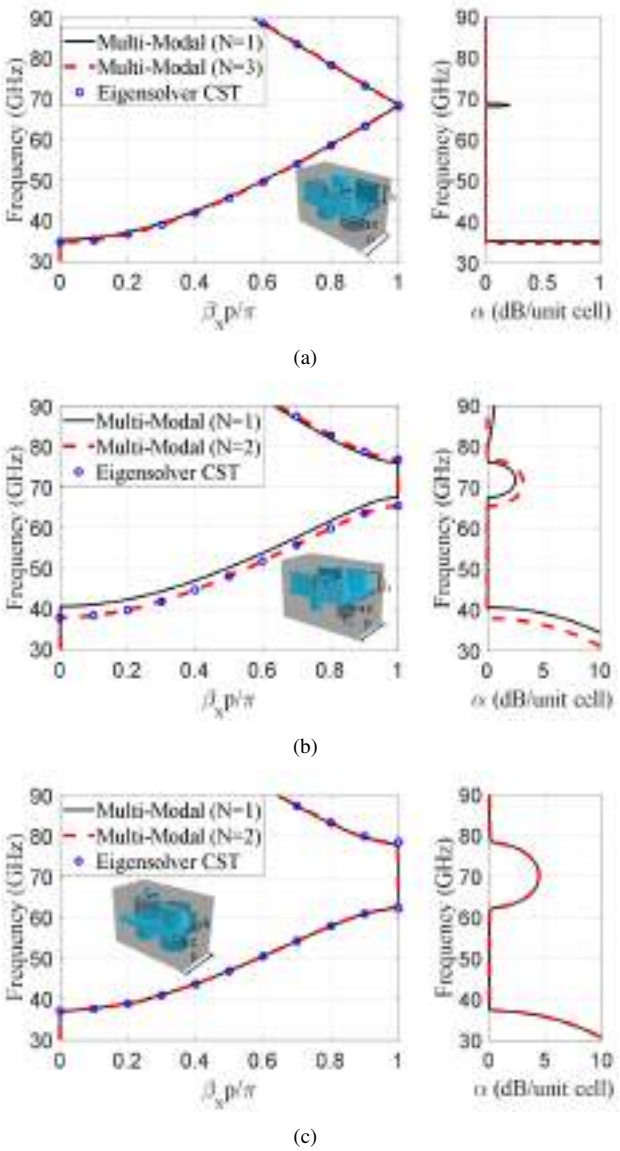

Fig. 9. Dispersion diagrams of the (a) Glide-symmetric, (b) Broken glide-symmetric ($r \neq r_2$) and (c) Mirror-symmetric unit cells with two holes. Attenuation (α) and phase (β_x) constants are shown in the figure. The geometrical parameters of the unit cells are: $r = 0.72$ mm, $r_2 = 0.2$ mm, $g = 0.25$ mm, $h = 1$ mm, and $p = 2.4$ mm.

On the other hand, the mirror-symmetric configuration shows an inherent stopband between the first and second modes, as shown in Fig. 9(c), located approximately at the upper part of the WR15 frequency range. Good agreement is observed in the computation of the phase constant β_x between the multi-modal method and the Eigenmode solver of *CST*. Note that no comparison is shown for the attenuation constant α, since the Eigenmode solver of *CST* cannot compute it.

Finite number of concatenated unit cells can be also studied with the use of the multi-modal method by simply cascading the transfer matrix. This is of interest for the design of filters made of periodic arrangements. Simulation time and computational efforts are saved, since simulating a large number of concatenated cells in a commercial software like *CST* is time consuming. Fig. 10 presents the $|S_{21}|$ parameter of the broken

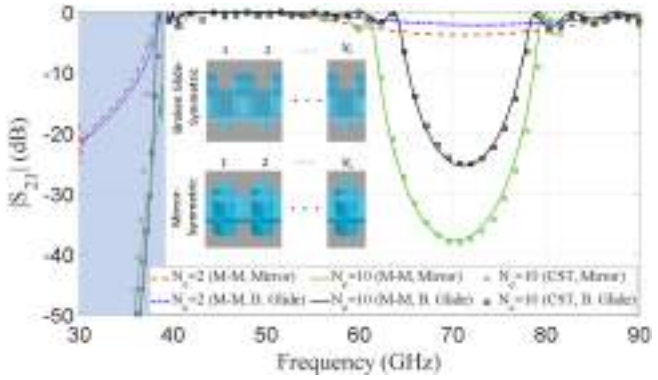

Fig. 10. $|S_{21}|$ parameter of finite mirror-symmetric and broken glide-symmetric structures as a function of the number of concatenated unit cells N_c. The cutoff range of the waveguide is shadowed in blue. In the legend, M-M states for the multi-modal technique. The geometrical parameters of the unit cell are: $r = 0.72$ mm, $g = 0.25$ mm, $h = 1$ mm, and $p = 2.4$ mm.

glide-symmetric (labeled as "B. Glide") and mirror-symmetric (labeled as "Mirror") structures as a function of the number of concatenated unit cells, N_c. The stopband centered at 70 GHz observed in Figs. 9(b) and 9(c) is also appreciated in Fig. 10. As shown in these figures, the mirror-symmetric configuration offers a higher attenuation constant in the rejection band compared to the broken glide-symmetric one. This will be discussed in detail later. Note that the maximum value of the attenuation constant α is slowly converging to the values evidenced in Fig. 9 as the number of concatenated unit cells N_c increases. As an example, the maximum attenuation constant is 4.35 dB/unit cell for the mirror-symmetric structure with periodic holes, while in the finite mirror-symmetric structures: $\alpha = 1.92$ dB/unit cell ($N_c = 2$), and $\alpha = 3.82$ dB/unit cell ($N_c = 10$). For validation purposes, a full-wave simulation in *CST* of the complete structures with 10 unit cells is also presented in Fig. 10 (green circles and black squares). As shown, there is a good agreement between *CST* and the multi-modal approach.

Fig. 11 presents the influence on the dispersion diagram of the number of holes placed in the unit cell. Both broken glide-symmetric and mirror-symmetric configurations follow the same pattern. The attenuation constant is higher for the case of a single hole and lower for the case of two holes. Placing three holes is an intermediate case. This fact can be better understood by looking at the electric field at the stopband region (70 GHz) of several concatenated unit cells. The attenuation constant is greater in the case of a single hole because the maximum amplitude of the fundamental mode coincides with the center of the hole. Thus, in this case, the mode is more strongly perturbed than the other two cases. Conversely, α is lower in the case of placing two holes since the maximum of the electric field occupies precisely the undrilled region between these two holes and, as a consequence, the wave propagation is less perturbed.

Fig. 12 illustrates the influence of the hole depth h on the attenuation and phase constants for the broken glide-symmetric and mirror-symmetric structures. In general, the deeper the hole is, the wider the stopband and the higher

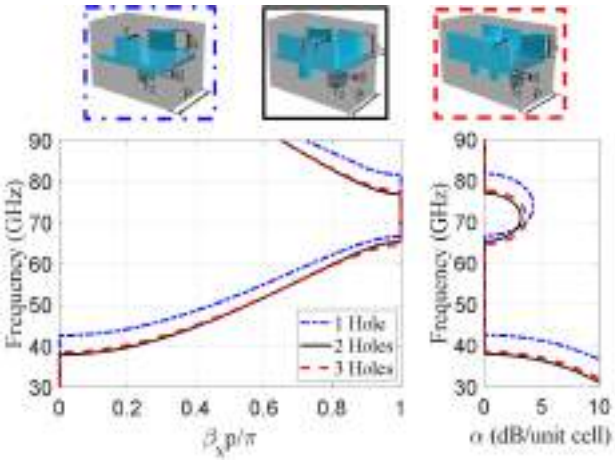

(a)

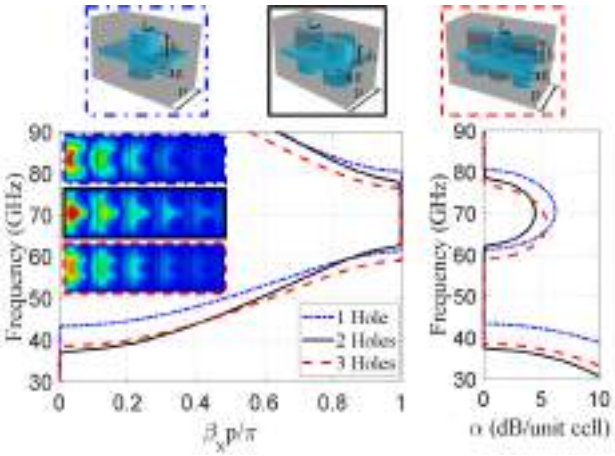

(b)

Fig. 11. Dispersion diagrams of the (a) Broken glide-symmetric and (b) Mirror-symmetric structures as a function of the number of holes. Attenuation (α) and phase (β_x) constants are shown in the figure. The inset shows the electric field at the stopband region (70 GHz) for the three cases under study. The geometrical parameters of the unit cells are: $r_1 = 0.72$ mm (1 and 2 holes), $r = 0.60$ mm (3 holes), $r_2 = 0.20$ mm, $g = 0.25$ mm, $h = 1$ mm, and $p = 2.4$ mm.

the attenuation constant are. However, there is a limit value where increasing the hole depth has no longer influence in the dispersion diagram. Note that for $h = 0$, the holey waveguide turns into a common hollow waveguide and the stopband closes. The parameter h was expressed in terms of wavelength (at 70 GHz) to give a further insight on the physical mechanisms that rule the structures. From that, it can be appreciated that such electrically-small values as $h = \lambda/200$ (21 μm) provoke noticeable attenuations in the stopband region: 0.42 dB/unit cell and 0.88 dB/unit cell for the broken glide-symmetric and mirror-symmetric configurations, respectively. Therefore, in waveguides with closely-spaced metal plates, any small protuberances repeated along the waveguide may cause noticeable losses due to the opening of narrow stopbands in the frequency range of the fundamental mode. These losses also exist for holey waveguides whose small protuberances are repeated in a non-periodic way. If the mirror-symmetric unit cell defines a holey waveguide but the locations and sizes of the holes vary among the unit cells, the produced losses

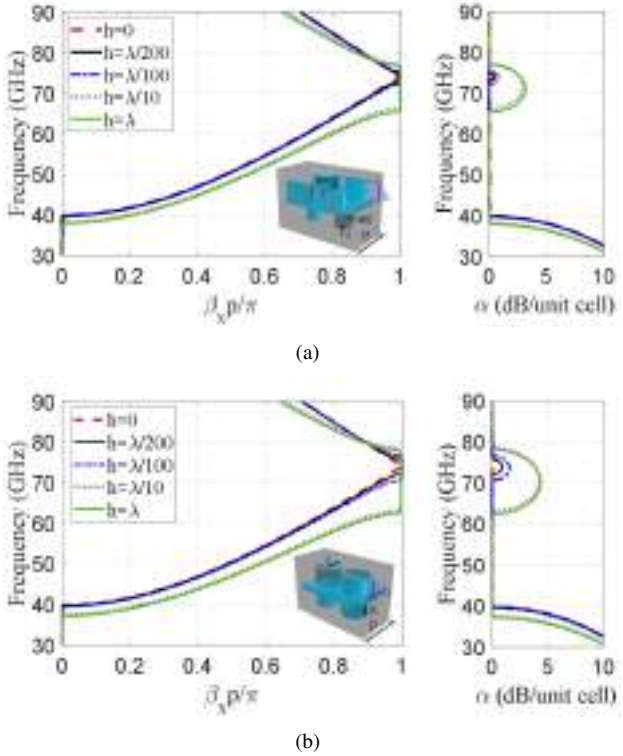

(a)

(b)

Fig. 12. Dispersion diagrams of the (a) Broken glide-symmetric ($r \neq r_2$) and (b) Mirror-symmetric unit cells with two holes as a function of the hole depth. Attenuation (α) and phase (β_x) constants are shown in the figure. The geometrical parameters of the unit cells are: $r_1 = 0.72$ mm, $r_2 = 0.20$ mm, $g = 0.25$ mm, and $p = 2.4$ mm.

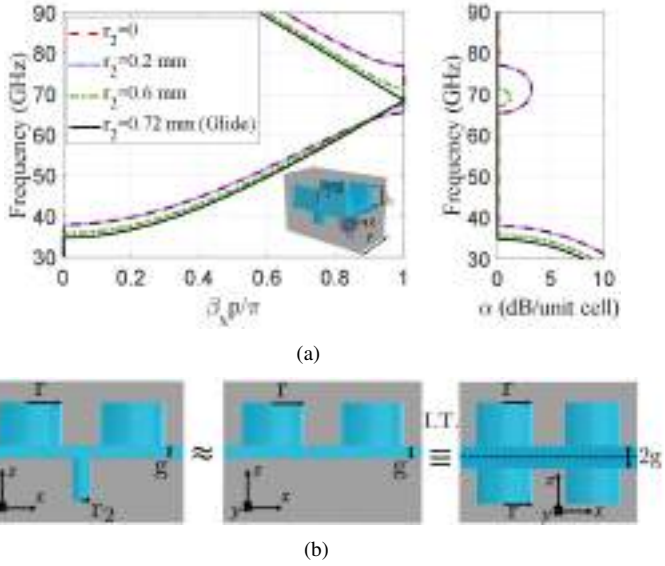

(a)

(b)

Fig. 13. (a) Dispersion diagram of the broken glide-symmetric ($r \neq r_2$) unit cell with two holes as a function of the radius r_2. Attenuation (α) and phase (β_x) constants are shown in the figure. The geometrical parameters of the unit cell are: $r_1 = 0.72$ mm, $g = 0.25$ mm, $h = 1$ mm, and $p = 2.4$ mm. (b) Illustration of the performance of 1D broken glide-symmetric structures for small values of r_2.

will be variable and depend on the non-periodic configuration. However, its drop in transmission will be around the stopband that appears in the mirror-symmetric unit cell.

The radius of the intermediate holes r_2 determines the stopband region and the attenuation factor in the broken glide-symmetric configuration. Fig. 13(a) illustrates the dispersion diagram of the broken glide-symmetric structure with two holes when varying the radius r_2. It can be appreciated that smaller values of r_2 provoke wider stopbands and higher attenuation constants. In addition, note that the dispersion curves are quite similar in the cases $r = 0$ (no intermediate holes) and $r = 0.20$ mm. This fact allows us to explain why in Figs. 11 and 12 the mirror-symmetric structure presents a higher attenuation constant compared to the broken glide-symmetric one. The effect of the intermediate holes in the dispersion curves is negligible for small values of r_2. Therefore, the intermediate holes can be eliminated and the operation of the periodic structure remains the same, as shown in the schematic of Fig. 13(b). By applying image theory, the bottom metallic plate of the waveguide (situated at a distance g) will create an image of the upper holes at a distance $2g$. That is, the broken glide-symmetric configuration for small values of r_2 is equivalent to a mirror-symmetric structure of double gap height $2g$, which offers a smaller attenuation constant compared to a mirror-symmetric structure of gap height g (see Fig. 5(b)). It should be remarked that image theory is applicable because of the mirror symmetry of the unit cell.

III. Applications: Waveguide Phase Shifter and Filter

Based on the results obtained in the previous section for the holey unit cells, two proof-of-concept prototypes have been fabricated. The selected designs are a wideband low-dispersive phase shifter and a filter in order to validate the performance of the glide-symmetric and mirror-symmetric unit cells, respectively. Their dispersion diagrams correspond to Figs. 3(a) and 3(b) (green lines) with a slight modification in the size of the hole radius. The mirror-symmetric unit cell is selected in the design of the filter because it produces greater attenuation in the stopband compared to the broken glide-symmetric unit cell. A reference WR15 waveguide is also included to compare the performance of the phase shifter and the filter. The three designs have been implemented in the same metallic pieces, as it is illustrated in Fig. 14(a). Planar view and key geometries are depicted in Figs. 14(b) and 14(c). The phase shifter and the filter are composed by a concatenation of ten glide-symmetric and mirror-symmetric holey unit cells, respectively. The waveguide has been split in two different parts (blue and grey pieces) in order to ease the manufacturing process. The operation frequency range is between 50 to 75 GHz. In order to prevent field leakage throughout the air gap due to an imperfect assembly, we make use of the gap-waveguide technology [41]. Thus, glide-symmetric EBG (electromagnetic bandgap) holes, marked in yellow in Fig. 14(a), are placed on both sides of the reference waveguide, filter and phase shifter. As the width of the holey waveguide unit cells is w = 3.76 mm, the feeding sections are waveguides with the width and the height corresponding to the WR15 waveguide to have appropriate flange connections in the setup. Nevertheless, waveguide transitions between feeding

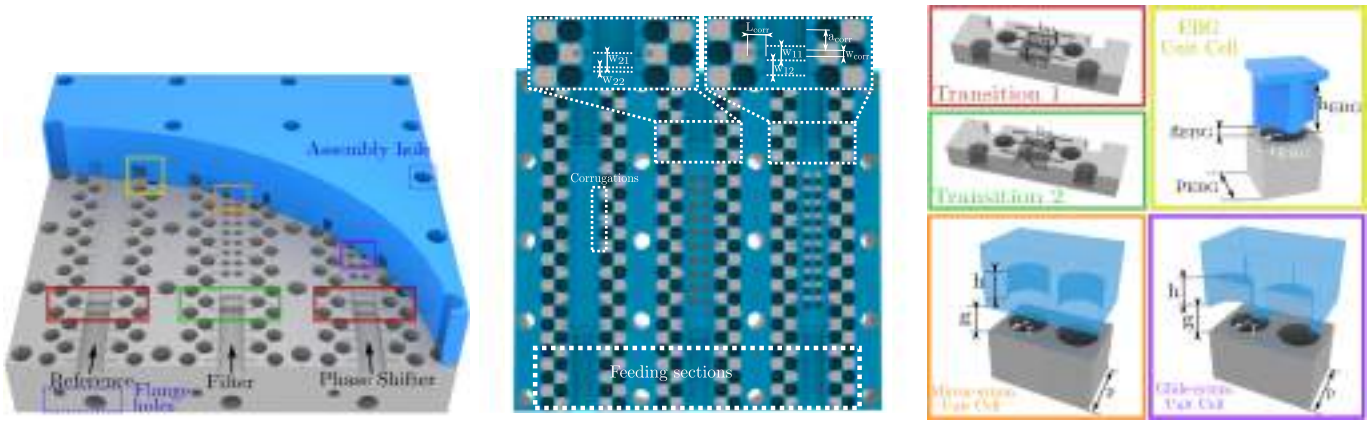

(a) (b) (c)

Fig. 14. Design of the prototype composed by the reference waveguide, filter and phase shifter: (a) 3D view, (b) Planar view of the forming layers and (c) Relevant geometries that composed the design. The dimensions are: $w_{11} = 1.5$ mm, $w_{12} = 1.5$ mm, $w_{21} = 1.5$ mm, $w_{22} = 0.4$ mm, $L_{\text{corr}} = 1.8$ mm, $a_{\text{corr}} = 2$ mm, $w_{\text{corr}} = 0.6$ mm, $h_{11} = 0.28$ mm, $h_{12} = 0.7$ mm, $h_{13} = 0.6$ mm, $h_{21} = 0.18$ mm, $h_{22} = 0.4$ mm, $h_{23} = 1$ mm, $g_{\text{EBG}} = 0.05$ mm, $r_{\text{EBG}} = 1.25$ mm, $p_{\text{EBG}} = 3.22$ mm, $h_{\text{EBG}} = 3$ mm, $g = 0.3$ mm, $r = 0.72$ mm, $p = 2.4$ mm and $h = 1$ mm.

sections and the designs are required since the height of the waveguide in the unit cells are set to g = 0.3 mm. Two different transitions are implemented for the phase shifter and filter, because they have different input impedances. The transition implemented for the reference WR15 waveguide is the same as for the phase shifter, in order to avoid any additional phase shift discrepancy introduced by the feeder.

The dimensions of glide-symmetric EBG holes are $p_{\text{EBG}} = 3.22$ mm, $r_{\text{EBG}} = 1.25$ mm, $h_{\text{EBG}} = 3$ mm, and $g_{\text{EBG}} = 0.05$ mm. In this manner, the applied gap-waveguide technology can operate from 45 GHz to 85 GHz since this is the location of the bandgap in the EBG structure. The parameter g_{EBG} indicates the gap between layers, so the dimension of this parameter is selected to be the value at the worst case. In general, smaller gap heights provide wider stopbands.

Despite of the presence of glide-symmmetric EBG holes to prevent leakage throughout the gap, field resonances may exist at certain frequencies in the space between the EBG holes and the waveguide. In order to avoid the unwanted resonances, wall corrugations in the waveguide are demonstrated to be an effective solution [42], [55]. Fig. 14(b) illustrates the corrugations implemented in the prototype to cancel field resonances.

The phase shifter and filter are formed by cascading ten holey unit cells. Using this number of unit cells, it is expected to obtain in the filter a rejection band from 61 GHz and in the phase shifter, a phase shift value around 180º in the entire frequency range. The electric field distributions in the gap between layers, at different frequencies, for the reference, filter and phase shifter are illustrated in Fig. 15. Note that a higher field intensity along the waveguide width is observed at the middle of the three designs due to the narrowing of the waveguide height in this part. Moreover, it can be appreciated the absence of field leakage in the gap. At the lower frequencies (Figs. 15(a) and 15(b)), the input power reaches the output ports without visible attenuation. However, in both filter and phase shifter structures, the output signals are out-of-phase compared with the reference waveguide. At an intermediate operating frequency (Fig. 15(c)), the filter begins to produce effect since the selected frequency is in the stopband region (see Fig. 9(c)). On the other hand, the phase shifter still provides the same out-of-phase signal. Lastly, in Fig. 15(d), the attenuation provided by the filter increases and the amplitude of the signal propagates in a shorter distance regarding the intermediate frequency. In contrast, at the output port of the phase shifter keeps arriving the 180º phase shift, showing the low-dispersive behavior of the phase shifter.

A. Experimental Validation

Fig. 16 illustrates the manufactured prototype, containing the reference waveguide, phase shifter and filter. The prototype was manufactured in CNC (Computer Numerical Control) technology. In order to measure the prototype, two setups have been employed since the R&S-ZVA67 VNA is limited up to 66.5GHz. Therefore, ZVA-Z110E Converters in WR10 are used to reach up to 75 GHz. The produced insertion losses when the WR10 setup is applied are negligible. Fig. 17 shows the simulated and measured results for the three manufactured designs. In simulations, aluminium is used instead of PEC in order to make a realistic comparison with the measurements. There exists a good agreement between the measurements and the simulation results, insertion loss being in all cases less than 2 dB. In the case of the filter, the rejection band reaches the 20 dB of attenuation from 63 GHz onwards. Note that the attenuation in the rejection band would be greater if a larger number of unit cells were employed to compose the filter. The peak in the attenuation is achieved around 70 GHz where the attenuation α in the mirror-symmetric unit cell has its maximum. This is in good agreement with the results presented in Fig. 9(c), where the attenuation and phase constants of the same mirror-symmetric unit cell are analyzed. Regarding the phase shifter, low insertion losses and good impedance matching band are obtained in a wide frequency range. The additional ripples in the reflection coefficient are produced by the coaxial to waveguide transitions used in the

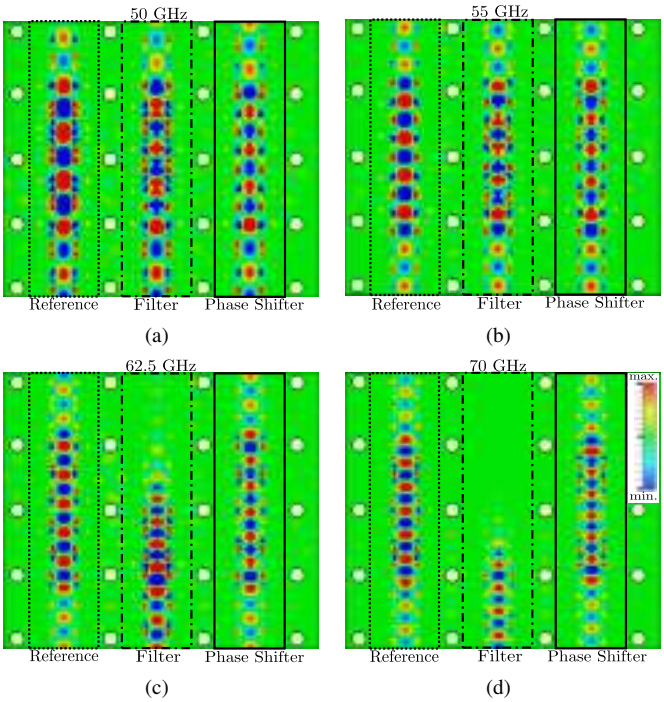

Fig. 15. Amplitude of the electric field distribution in the gap between layers at different frequencies in the operating band for the reference waveguide, filter and phase shifter at: (a) 50 GHz, (b) 55 GHz, (c) 62.5 GHz and (d) 70 GHz.

Fig. 16. Forming layers of the manufactured prototype and details under microscope.

setup. In spite of that, good agreement between simulations and measurements in the $|S_{11}|$ are observed.

Finally, the phase shift measurements for the phase shifter and filter are shown in Fig. 18. For the phase shifter, a $180^{o}\pm5^{o}$ is achieved from 56.5 GHz to 74.5 GHz (27.5% frequency bandwidth). These results illustrate that a low-dispersive phase shifter (with respect to the reference waveguide) can be implemented with the use of holey waveguide whose holes are arranged in a glide-symmetric configuration. In addition, note that the dispersion of the filter (holey waveguide with mirror-symmetric holes) is higher out of the rejection band compared to the phase shifter (holey waveguide with glide-symmetric holes). This behavior is expected due to the approximated parallel fundamental mode of the holey waveguide in glide-symmetric configuration compared to the fundamental mode of the reference waveguide. At the lower part of the frequency

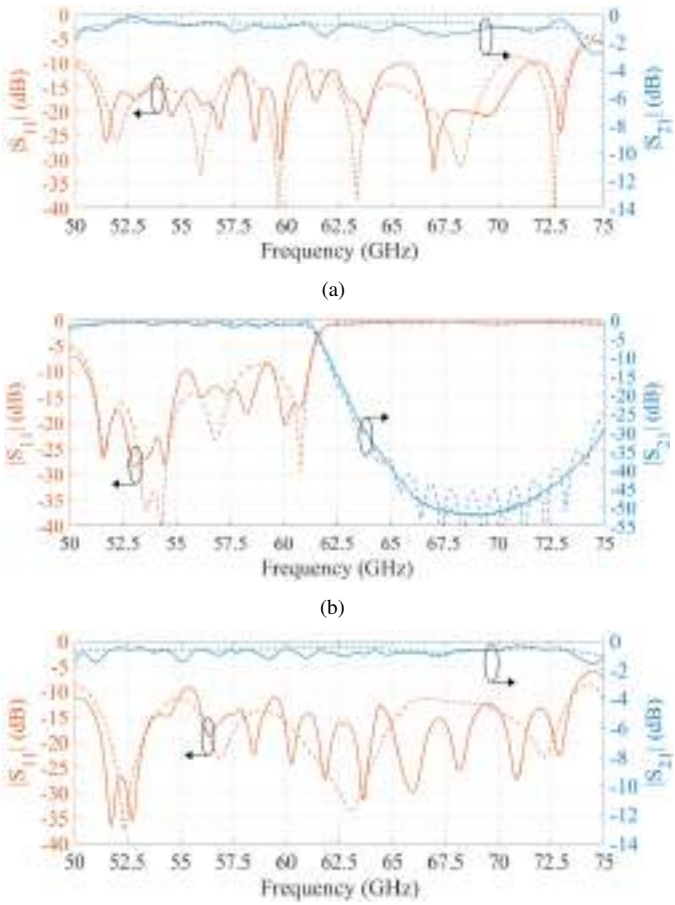

Fig. 17. Simulated (dashed lines) and measured (solid lines) results in magnitude of the S-parameters for the: (a) Reference waveguide, (b) Filter and (c) Phase shifter.

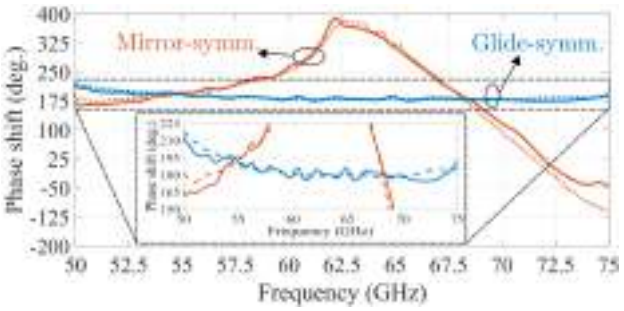

Fig. 18. Simulated (dashed lines) and measured (solid lines) results in phase of the S-parameters for the phase shifter (in blue) and for the filter (in orange).

band, there is an increase in the error of the produced phase shift due to two causes. First, at the lower frequencies of the stopband region of the EBG structure (50 GHz), the attenuation constant is low and thus, the electric field can propagate further in the transversal direction (see Fig. 15(a)). This fact produces an enlargement of the effective waveguide width that provokes a higher phase shift. When the frequency increases, the attenuation constant of the EBG structure is higher and the effective waveguide width becomes stable and similar to the one selected in the dispersion diagrams. Second, the first mode

of the unit cell exhibits a lower dispersive behaviour beyond 54 GHz. Compared to the state-of-art hollow waveguide phase shifter [29], in this work it is obtained a wideband fully-metallic phase shifter with low-dispersive behavior and cost-effective design. Furthermore, it is of interest to compare the phase dispersion observed in the passband region of the filter with the phase shift produced by the phase shifter. As observed in Fig. 18, a lower dispersion is obtained when the holes are arranged in a glide-symmetric configuration (the case of the phase shifter) compared to a mirror-symmetric configuration (the case of the filter). This fact agrees with the results presented in Section II.A. In addition, good agreement is obtained in both the passband and rejection band of the filter, despite the fact that in the latter the amplitude signal received suffers from a great attenuation.

IV. Conclusion

In this paper, the dispersion and filtering properties of the holey waveguides are analyzed in detail. Glide-symmetric holey waveguides are demonstrated to be low dispersive in a large frequency bandwidth. On the other hand, both mirror-symmetric and broken glide-symmetric holey waveguides offer inherent stopbands that are beneficial for filter design. In addition, we show that the mirror-symmetric configuration provides a greater attenuation compared to the broken glide-symmetric one. A comparison between holey and pin-loaded waveguides is also carried out. The results show that periodic holey configurations are less frequency-dispersive compared to periodic structure with pins. The main properties of the holey waveguide with glide-symmetric and mirror-symmetric configurations are exploited to design a wideband phase shifter and a filter, respectively. They are prototyped in the WR15 waveguide by employing gap-waveguide technology. Moreover, the implementations of the phase shifter and filter provides an easy manufacturing since they are composed by holes that can be easily fabricated with drilling techniques in gap waveguides. The experimental results are in good agreement with the simulations. The phase shifter presents a phase shift of $180^{\text{o}}\pm5^{\text{o}}$ from 56.5 GHz to 74.5 GHz (27.5% frequency bandwidth) and the filter offers a rejection band of 20-dB from 63 GHz to 75 GHz. The manufactured devices show cost-effective implementations of filters and low-dispersive phase shifters in millimeter-wave frequencies.

Appendix A
Multi-Modal Transfer-Matrix Method

For the 1D periodic structure under study in this work, the eigenvalue problem that leads to the dispersion relation is presented in [48], [56] as

$$\mathbf{T}\begin{pmatrix}\mathbf{V}\\ \mathbf{I}\end{pmatrix} = e^{\gamma p}\begin{pmatrix}\mathbf{V}\\ \mathbf{I}\end{pmatrix} \tag{1}$$

where

$$\mathbf{T} = \left(\begin{array}{ccc|ccc} \overbrace{A^{11}}^{\mathbf{A}} & \dots & A^{1N} & \overbrace{B^{11}}^{\mathbf{B}} & \dots & B^{1N} \\ \vdots & \ddots & \vdots & \vdots & \ddots & \vdots \\ A^{N1} & \dots & A^{NN} & B^{N1} & \dots & B^{NN} \\ \hline C^{11} & \dots & C^{1N} & D^{11} & \dots & D^{1N} \\ \vdots & \ddots & \vdots & \vdots & \ddots & \vdots \\ \underbrace{C^{N1}}_{\mathbf{C}} & \dots & C^{NN} & \underbrace{D^{N1}}_{\mathbf{D}} & \dots & D^{NN} \end{array}\right) \tag{2}$$

is the multi-modal transfer matrix of dimensions $2N \times 2N$, $\mathbf{V}$ and $\mathbf{I}$ are $N \times 1$ arrays containing the voltages and currents at the output ports, $\gamma = \alpha + j\beta$ is the propagation constant, p is the period of the unit cell and N is the number of considered modes.

If the structure under study is symmetrical and reciprocal, the $2N$-rank eigenvalue problem of (1) can be reduced to the N-rank eigenvalue problem [56]

$$\mathbf{AV} = \cosh(\gamma p)\mathbf{V} \tag{3}$$

which have two degenerate set of eigenvalues.

References

[1] D. M. Pozar. *Microwave Engineering*, 4th edition, Wiley, 2011.

[2] M. Alonso-del Pino, C. Jung-Kubiak, T. Reck, C. Lee and G. Chattopadhyay, "Micromachining for Advanced Terahertz: Interconnects and Packaging Techniques at Terahertz Frequencies," *IEEE Microw. Mag.*, vol. 21, no. 1, pp. 18-34, Jan. 2020.

[3] P. -S. Kildal, E. Alfonso, A. Valero-Nogueira and E. Rajo-Iglesias, "Local Metamaterial-Based Waveguides in Gaps Between Parallel Metal Plates," *IEEE Antennas Wireless Propag. Lett.*, vol. 8, pp. 84-87, 2009.

[4] P. -S. Kildal, A. U. Zaman, E. Rajo-Iglesias, E. Alfonso and A. Valero-Nogueira, "Design and experimental verification of ridge gap waveguide in bed of nails for parallel-plate mode suppression," *IET Microw. Antennas Propag.*, vol. 5, no. 3, pp. 262-270, 2011.

[5] E. Rajo-Iglesias, M. Ferrando-Rocher and A. U. Zaman, "Gap Waveguide Technology for Millimeter-Wave Antenna Systems," *IEEE Commun. Mag.*, vol. 56, no. 7, pp. 14-20, July 2018.

[6] A. Farahbakhsh, D. Zarifi and A. U. Zaman, "60-GHz Groove Gap Waveguide Based Wideband H -Plane Power Dividers and Transitions: For Use in High-Gain Slot Array Antenna," *IEEE Trans. Microw. Theory Techn.*, vol. 65, no. 11, pp. 4111-4121, Nov. 2017.

[7] A. Tamayo-Domínguez, J. Fernández-González and M. Sierra-Castañer, "3-D-Printed Modified Butler Matrix Based on Gap Waveguide at W-Band for Monopulse Radar," *IEEE Trans. Microw. Theory Techn.*, vol. 68, no. 3, pp. 926-938, March 2020.

[8] W. Hong *et al.*, "Multibeam Antenna Technologies for 5G Wireless Communications," *IEEE Trans. Antennas Propag.*, vol. 65, no. 12, pp. 6231-6249, Dec. 2017.

[9] M. Akbari, A. Farahbakhsh and A. Sebak, "Ridge Gap Waveguide Multilevel Sequential Feeding Network for High-Gain Circularly Polarized Array Antenna," *IEEE Trans. Antennas Propag.*, vol. 67, no. 1, pp. 251-259, Jan. 2019.

[10] A. Vosoogh *et al.*, "Compact Integrated Full-Duplex Gap Waveguide-Based Radio Front End For Multi-Gbit/s Point-to-Point Backhaul Links at E-Band," *IEEE Trans. Microw. Theory Techn.*, vol. 67, no. 9, pp. 3783-3797, Sept. 2019.

[11] J. Esteban and J. M. Rebollar, "Characterization of corrugated waveguides by modal analysis," *IEEE Trans. Microw. Theory Techn.*, vol. 39, no. 6, pp. 937-943, June 1991.

[12] S. Marini, Á. Coves, V. E. Boria and B. Gimeno, "Efficient Modal Analysis of Periodic Structures Loaded With Arbitrarily Shaped Waveguides," *IEEE Trans. Microw. Theory Techn.*, vol. 58, no. 3, pp. 529-536, March 2010.

[13] J. E. Varela and J. Esteban, "Characterization of Waveguides With a Combination of Conductor and Periodic Boundary Contours: Application to the Analysis of Bi-Periodic Structures," *IEEE Trans. Microw. Theory Techn.*, vol. 60, no. 3, pp. 419-430, March 2012.

[14] O. Quevedo-Teruel, M. Ng Mou Khen, E. Rajo-Iglesias, "Numerical and experimental studies of split ring resonators loaded on the sidewalls of rectangular waveguides," *IET Microw. Antennas Propag.*, vol. 3, no. 8, pp. 1262-1270, December 2009.

[15] R. S. Kshetrimayum and Lei Zhu, "Guided-wave characteristics of waveguide based periodic structures loaded with various FSS strip layers," *IEEE Trans. Antennas Propag.*, vol. 53, no. 1, pp. 120-124, Jan. 2005.

[16] C. Bachiller, H. Esteban, F. Díaz, J. V. Morro and V. E. Boria, "Radio-frequency performance comparison of several H-plane rectangular waveguide filters loaded with circular dielectric posts," *IET Microw. Antennas Propag.*, vol. 10, no. 5, pp. 536-545, 13 4 2016.

[17] G. Goussetis, A. P. Feresidis and P. Kosmas, "Efficient Analysis, Design, and Filter Applications of EBG Waveguide With Periodic Resonant Loads," *IEEE Trans. Microw. Theory Techn.*, vol. 54, no. 11, pp. 3885-3892, Nov. 2006.

[18] Alejandro Pons-Abenza *et al.*, "Design and implementation of evanescent mode waveguide filters using dielectrics and additive manufacturing techniques," *AEU-Int. J. Electron. Commun.*, vol. 116, no. 153065, March 2020.

[19] M. Baquero-Escudero, A. Valero-Nogueira, M. Ferrando-Rocher, B. Bernardo-Clemente and V. E. Boria-Esbert, "Compact Combline Filter Embedded in a Bed of Nails," *IEEE Trans. Microw. Theory Techn.*, vol. 67, no. 4, pp. 1461-1471, April 2019.

[20] A. Coves et al., "A novel band-pass filter based on a periodically drilled SIW structure," *Radio Science*, vol. 51, no. 4, pp. 328-336, April 2016.

[21] L. Silvestri, E. Massoni, C. Tomassoni, A. Coves, M. Bozzi and L. Perregrini, "Substrate Integrated Waveguide Filters Based on a Dielectric Layer With Periodic Perforations," *IEEE Trans. Microw. Theory Techn.*, vol. 65, no. 8, pp. 2687-2697, Aug. 2017.

[22] T. Yang, M. Ettorre and R. Sauleau, "Novel Phase Shifter Design Based on Substrate-Integrated-Waveguide Technology," *IEEE Microw. Wireless Compon. Lett.*, vol. 22, no. 10, pp. 518-520, Oct. 2012.

[23] M. Ebrahimpouri, S. Nikmehr and A. Pourziad, "Broadband Compact SIW Phase Shifter Using Omega Particles," *IEEE Microw. Wireless Compon. Lett.*, vol. 24, no. 11, pp. 748-750, Nov. 2014.

[24] W. Zhang, Z. Shen, K. Xu and J. Shi, "A Compact Wideband Phase Shifter Using Slotted Substrate Integrated Waveguide," *IEEE Microw. Wireless Compon. Lett.*, vol. 29, no. 12, pp. 767-770, Dec. 2019.

[25] J. L. Cano, A. Mediavilla and A. Tribak, "Parametric Design of a Class of Full-Band Waveguide Differential Phase Shifters," *Electronics*, vol. 8, no. 346, March 2019.

[26] M. Chung, D. Je, S. Han and S. Kim, "Development of a 85-115 GHz 90-deg phase shifter using corrugated square waveguide," in *44th European Microwave Conference*, Rome, 2014, pp. 1146-1149.

[27] S. A. Razavi and A. U. Zaman, "A compact phase shifter in groove gap waveguide for millimeter-wave applications," in *12th European Conference on Antennas and Propagation (EuCAP 2018)*, London, 2018, pp. 1-3.

[28] Á. Palomares-Caballero, A. Alex-Amor, P. Padilla, F. Luna and J. Valenzuela-Valdes, "Compact and Low-Loss V-Band Waveguide Phase Shifter Based on Glide-Symmetric Pin Configuration," *IEEE Access*, vol. 7, pp. 31297-31304, 2019.

[29] M. Farahani, M. Nedil and T. A. Denidni, "A Novel Hedgehog Waveguide and Its Application in Designing a Phase Shifter Compatible With Hollow Waveguide Technology," *IEEE Trans. Microw. Theory Techn.*, vol. 67, no. 10, pp. 4107-4117, Oct. 2019.

[30] R. Mittra and S. Laxpati, "Propagation in a wave guide with glide reflection symmetry," *Canadian Journal of Physics*, vol. 43, no. 2, pp. 353–372, 1965.

[31] A. Hessel, M.H. Chen, R.C.M. Li, and A.A. Oliner, "Propagation in periodically loaded waveguides with higher symmetries," *Proc. IEEE*, vol. 61, no. 2, pp. 183–195, Feb. 1973.

[32] G. Valerio, F. Ghasemifard, Z. Sipus and O. Quevedo-Teruel, "Glide-Symmetric All-Metal Holey Metasurfaces for Low-Dispersive Artificial Materials: Modeling and Properties," *IEEE Trans. Microw. Theory Techn.*, vol. 66, no. 7, pp. 3210-3223, July 2018.

[33] Q. Chen, F. Ghasemifard, G. Valerio, O. Quevedo-Teruel, "Modeling and Dispersion Analysis of Coaxial Lines With Higher Symmetries," *IEEE Trans. Microw. Theory Techn.*, vol. 66, no. 10, pp. 4338-4345, Oct. 2018.

[34] O. Quevedo-Teruel, M. Ebrahimpouri and M. Ng Mou Kehn, "Ultra-wideband Metasurface Lenses Based on Off-Shifted Opposite Layers," *IEEE Antennas Wireless Propag. Lett.*, vol. 15, pp. 484-487, Dec. 2016.

[35] A. Alex-Amor, G. Valerio, F. Ghasemifard, F. Mesa, P. Padilla, J. M. Fernández-González and O. Quevedo-Teruel, "Wave Propagation in Periodic Metallic Structures with Equilateral Triangular Holes," *Applied Sciences*, vol. 10, no. 1600, Feb. 2020.

[36] A. Palomares-Caballero, P. Padilla, A. Alex-Amor, J. Valenzuela-Valdés, and O. Quevedo-Teruel, "Twist and Glide Symmetries for Helix Antenna Design and Miniaturization," *Symmetry*, vol. 11, no. 349, March 2019.

[37] A. Alex-Amor, F. Ghasemifard, G. Valerio, M. Ebrahimpouri, P. Padilla, J. M. Fernández-González and, O. Quevedo-Teruel ,"Glide-Symmetric Metallic Structures with Elliptical Holes for Lens Compression," *IEEE Trans. Microw. Theory Techn.*, 2020.

[38] R. Quesada, D. Martín-Cano, F. J. García-Vidal and J. Bravo-Abad, "Deep-subwavelength negative-index waveguiding enabled by coupled conformal surface plasmons", *Opt. Lett.*, vol. 39, no. 10, May 15, 2014.

[39] M. Ebrahimpouri, O. Quevedo-Teruel and E. Rajo-Iglesias, "Design Guidelines for Gap Waveguide Technology Based on Glide-Symmetric Holey Structures," *IEEE Microw. Wireless Compon. Lett.*, vol. 27, no. 6, pp. 542-544, June 2017.

[40] F. Ghasemifard, M. Norgren, O. Quevedo-Teruel and G. Valerio, "Analyzing Glide-Symmetric Holey Metasurfaces Using a Generalized Floquet Theorem," *IEEE Access*, vol. 6, pp. 71743-71750, 2018.

[41] M. Ebrahimpouri, E. Rajo-Iglesias, Z. Sipus and O. Quevedo-Teruel, "Cost-Effective Gap Waveguide Technology Based on Glide-Symmetric Holey EBG Structures," *IEEE Trans. Microw. Theory Techn.*, vol. 66, no. 2, pp. 927-934, Feb. 2018.

[42] A. Vosoogh, H. Zirath and Z. S. He, "Novel Air-Filled Waveguide Transmission Line Based on Multilayer Thin Metal Plates," *IEEE Trans. Terahertz Sci. Technol.*, vol. 9, no. 3, pp. 282-290, May 2019.

[43] Q. Chen, O. Zetterstrom, E. Pucci, A. Palomares-Caballero, P. Padilla, O. Quevedo-Teruel, "Glide-Symmetric Holey Leaky-Wave Antenna with Low Dispersion for 60-GHz Point-to-Point Communications," *IEEE Trans. Antennas Propag.*, vol. 68, no. 3, pp. 1925-1936, March 2020.

[44] P. Padilla, A. Palomares-Caballero, A. Alex-Amor, J. Valenzuela-Valdés, J. M. Fernández-González, O. Quevedo-Teruel, "Broken glide-symmetric holey structures for bandgap selection in gap-waveguide technology," *IEEE Microw. Wireless Compon. Lett.*, vol. 29, no. 5, pp. 327-329, Apr. 2019.

[45] A. Monje-Real, N. J. G. Fonseca, O. Zetterstrom, E. Pucci, O. Quevedo-Teruel, "Holey Glide-Symmetric Filters for 5G at Millimeter-Wave Frequencies," *IEEE Microw. Wireless Compon. Lett.*, vol. 30, no. 1, pp. 31-34, Jan. 2020.

[46] W. J. R. Hoefer and M. N. Burton, "Closed-Form Expressions for the Parameters of Finned and Ridged Waveguides," *IEEE Trans. Microw. Theory Techn.*, vol. 30, no. 12, pp. 2190-2194, Dec. 1982.

[47] D. Dasgupta and P. K. Saha, "Rectangular Waveguide with Two Double Ridges," *IEEE Trans. Microw. Theory Techn.*, vol. 31, no. 11, pp. 938-941, Nov. 1983.

[48] M. Bagheriasl, O. Quevedo-Teruel, and G. Valerio, "Bloch analysis of artificial lines and surfaces exhibiting glide symmetry," *IEEE Trans. Microw. Theory Techn.*, vol. 67, no. 7, pp. 2618–2628, 2019.

[49] M. Bagheriasl, and G. Valerio,"Bloch Analysis of Electromagnetic Waves in Twist-Symmetric Lines," *Symmetry*, vol. 11, no. 5, pp. 620, 2019.

[50] J. Shekel, "Matrix Analysis of Multi-Terminal Transducers," *Proc. IRE*, vol. 42, no. 5, pp. 840–847, 1954.

[51] T. Reveyrand, "Multiport conversions between S , Z , Y , h , ABCD , and T parameters," *in 2018 Int. Work. Integr. Nonlinear Microw. Millimetre-wave Circuits*, no. 6, 2018, pp. 1–3.

[52] G. Valerio, Z. Sipus, A. Grbic, O. Quevedo-Teruel, "Accurate equivalent-circuit descriptions of thin glide-symmetric corrugated metasurfaces," *IEEE Trans. Antennas Propag.*, vol. 65, no. 5, pp. 2695-2700, May 2017.

[53] F. Mesa, R. Rodríguez-Berral, and F. Medina, "On the computation of the dispersion diagram of symmetric one-dimensionally periodic structures," *Symmetry*, vol. 10, no. 8, p. 307, 2018.

[54] B. A. Mouris, A. Fernández-Prieto, R. Thobaben, J. Martel, F. Mesa and O. Quevedo-Teruel, "On the Increment of the Bandwidth of Mushroom-Type EBG Structures With Glide Symmetry," *IEEE Trans. Microw. Theory Techn.*, vol. 68, no. 4, pp. 1365-1375, April 2020.

[55] A. Palomares-Caballero, A. Alex-Amor, P. Escobedo, J. Valenzuela-Valdes, and P. Padilla, "Low-Loss Reconfigurable Phase Shifter in Gap-Waveguide Technology for mm-Wave Applications," *IEEE Trans. Circuits Syst. II-Express Briefs*, 2020.

[56] F. Mesa, G. Valerio, R. Rodríguez-Berral, and O. Quevedo-Teruel, "Simulation-Assisted Efficient Computation of the Dispersion Diagram of Periodic Structures," *IEEE Antennas Propag. Mag.*, 2020.

Ángel Palomares-Caballero was born in Jaén, Spain, in 1994. He received the B.Sc. and M.Sc.degrees in telecommunication engineering from the University of Granada (UGR), Granada, Spain, in 2016 and 2018, respectively. Since 2017, he has been with the Signal Theory, Telematics and Communications Department, University of Granada, where he is currently a Ph.D.student with a national Predoctoral Fellowship. His current research interests include millimeter-wave antennas and phase shifters, gap-waveguide technology, and structures with higher symmetries.

Antonio Alex-Amor received the B.Sc. degree in telecommunication engineering from Universidad de Granada, in 2016, and the M.Sc. degree in telecommunication engineering from Universidad Politécnica de Madrid (UPM), in 2018, where he is currently pursuing the Ph.D. degree. Since 2016, he has been with the Radiation Group, Signal, Systems and Radiocommunications Department, UPM. From 2018-2019, he joined the Department of Language and Computer Science, Universidad de Málaga. In 2020, he joined the Signal Theory, Telematics and Communications Department, University of Granada. He received the Best Electromagnetics Paper Award at the 14th European Conference on Antennas and Propagation (EuCAP 2020). His current research interests include the use of liquid crystal as tunable dielectric, metamaterials, structures with higher symmetries and radiofrequency energy harvesting systems.

Pablo Padilla was born in Jaén, Spain, in 1982. He received the Telecommunication Engineering degree and the Ph.D. degree from the Radiation Group (Signal, Systems and Radiocommunications Department) of the Technical University of Madrid (UPM), Spain, in 2005 and 2009, respectively. In 2007, he was with the Laboratory of Electromagnetics and Acoustics, École Polytechnique Fédérale de Lausanne, Switzerland, as an invited Ph.D. Student. In 2009, he carried out a Postdoctoral stay at the Helsinki University of Technology (AALTO-TKK). In 2009, he became Assistant Professor at the Signal Theory, Telematics and Communications Department of the University of Granada, where he is currently Associate Professor, since 2012. In 2017, he was an invited Visiting Professor at the Royal Institute of Technology of Stockholm. He has authored more than 65 high-impact journal contributions and more than 60 contributions to international symposia. His research interests include a variety of topics related mainly to electromagnetism and communication issues (radiofrequency devices, antennas and propagation).

Juan Valenzuela-Valdés was born in Marbella, Spain. He received the Telecommunication Engineering degree from the Universidad de Malaga, Spain, in 2003, and the Ph.D. degree from the Universidad Politécnica de Cartagena, Spain, in 2008, where he joined the Department of Information Technologies and Communications, in 2004. In 2007, he joined EMITE Ing., Murcia, Spain, as the Head of research. In 2011, he joined the Universidad de Extremadura, and in 2015, he joined the Universidad de Granada, where he is currently an Associate Professor. He has also received several prizes, including a National Prize to the Best Ph.D. in Mobile Communications by Vodafone. He also holds several national and international patents. His publication record comprised of more than 100 publications, including 50 JCR (Journal Citation Reports) indexed articles and seven book chapters. (Updated March 2019). His current research interests include wireless communications, radiofrequency devices, antennas and propagation. He is the head of SWAT research group (https://swat.ugr.es/) at the University of Granada and cohead of Singular Laboratory of Electromagnetic characterization of microwave and millimeter devices and antennas.

2.1.3 Wideband Gap-Waveguide Phase Shifter Based on a Glide-Symmetric Ridge

The ridge waveguide technology has been used for the design of antenna components at millimeter-wave frequencies [20, 40]. The following publication proposes a phase shifter in this type of waveguide technology. The design is based on the inclusion of holes in glide symmetry with semi-circular base in the ridge. In this way, the phase shift provided by the periodic structure becomes flexible in design and the desired phase behavior can be adjusted. As a proof of concept, a phase shifter has been fabricated that provides a phase shift of 90º from 33 GHz to 43 GHz with low insertion loss. One of the relevant features of the proposed phase shifter design is that the reference waveguide is also a ridge waveguide unlike what is found in the literature.

Wideband Gap-Waveguide Phase Shifter Based on a Glide-Symmetric Ridge

Ángel Palomares-Caballero, Carlos Megías, Carlos Molero, Antonio Alex-Amor, and Pablo Padilla

***Abstract*—This letter presents a gap-waveguide phase shifter based on ridged unit cells with glide-symmetric configuration. The proposed unit cell design provides a higher stable phase shift compared to a conventional ridged unit cell whose ridge height and waveguide width are tuned to achieve a stable phase shift. Through the insertion of glide-symmetric holes with semi-circle base in the ridged waveguide, a stable phase shift in a wide frequency range is achieved. Depending on the radii of the holes, the operating frequency range of the phase shifter can be tuned. A 90^o phase shifter in millimeter-wave range is designed and manufactured to validate the analysis. The experimental results reveal a 85$^o\pm$ 5^o phase shift from 33 GHz to 43 GHz (26.3% bandwidth). In this bandwidth, the reflection coefficient is below -10 dB with a maximum insertion loss of 0.7 dB.**

***Index Terms*—Glide symmetry, millimeter-wave frequencies, phase shifter, ridge gap-waveguide, wideband.**

I. Introduction

PHASE shift in multi-beam antennas is a critical mechanism to achieve the adequate performance of this kind of radiating systems. One of the most attractive network to produce multi-beam radiation is the Butler matrix. For millimeter-wave applications, this beamforming network has been implemented in different waveguide technologies such as substrate integrated waveguide [1], rectangular waveguide [2], groove gap waveguide (GGW) [3] and printed ridge gap waveguide (PRGW) [4]. In all the previous works, a phase shifter in the corresponding technology had to be designed. Ridge waveguide (RW) technology and its evolution in gap waveguide [5] have gained interest to develop millimeter-wave antennas [6] and multi-port components [7], [8]. Nevertheless, there are few reported ridge gap-waveguide (RGW) phase shifters in the literature. A RW phase shifter based on multiple steps is proposed in [9], while [10] proposes an approach based on a optimization of a smooth-ridge waveguide model. However, the phase shift is calculated considering another waveguide technology (rectangular waveguide) as a reference and gap-waveguide technology is not employed. The insertion of materials with different permittivity in the RW is another way to introduce phase shift. In [11], the propagation constant is modified in the RW through the rotation of a dielectric slab placed atop the ridge. Liquid crystal (LC) is used in [12] inside a gap-waveguide to properly bias the material but the phase shift has no ability to be stable in frequency and also has large insertion losses. Materials with different relative permeability are also employed in the design of phase shifter in ridge gap waveguide [13]. Additionally, mechanical approach by taking advantage of the gap-waveguide technology is applied in [14] to vary the waveguide length and produce the phase shift.

Waveguide phase shifters loaded with pins [15] and holes [16] that present glide symmetry have demonstrated the benefits for producing and tuning phase shift in waveguides. This kind of higher symmetry greatly enhances the performance of radio-frequency devices [17]. In this letter, we present a gap-waveguide phase shifter that exploits the use of ridged unit cells with glide symmetry to produce a stable phase shift response over a wide bandwidth in millimeter waves.

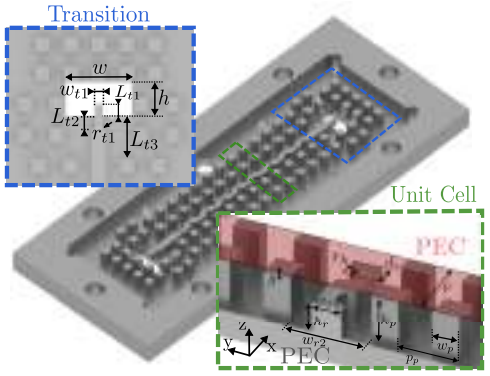

Fig. 1: Proposed gap-waveguide phase shifter with glide-symmetric ridged unit cells. Planar view of the rectangular waveguide to ridge gap waveguide transition. Dimensions (in mm): $w = 5.69$, $h = 2.845$, $w_t = 0.725$, $L_{t1} = 1$, $L_{t2} = 1.1$, $L_{t3} = 3.5$, $r_t = 0.3$, $p = 3.6$, $d_x = 0.9$, $r_h = 0.6$, $w_{r1} = 1.3$, $w_{r2} = 3.6$, $h_r = 1.55$, $h_p = 2.37$, $p_p = 2.7$, $w_p = 1.2$, $g = 0.03$.

II. Glide-symmetric RGW Unit cell

The proposed ridge gap-waveguide phase shifter is illustrated in Fig. 1. It is composed by glide-symmetric ridged (GSR) waveguide unit cells and two rectangular waveguide to ridge gap-waveguide transitions inspired by [18] to design a back-to-back device. The electromagnetic bandgap pin lattice provides a stopband from 12 GHz to 61 GHz that allows the proper operation of the RGW in the WR22 frequency

Manuscript received 30 June 2022; revised 28 July 2022; accepted 22 August 2022. This work was supported in part by the Spanish Government under Project PID2020-112545RB-C54 and, Project RTI2018-102002-A-I00, in part by "Junta de Andalucía" under Project B-TIC-402-UGR18, Project A-TIC-608-UGR20, Project PYC20-RE-012-UGR and Project P18.RT.4830, and in part by the Predoctoral Grant FPU18/01965. *(Corresponding author: Ángel Palomares-Caballero.)*

Ángel Palomares-Caballero, Carlos Molero and Pablo Padilla are with the Department of Signal Theory, Telematics and Communications, University of Granada (UGR), 18071 Granada, Spain (e-mail: angelpc@ugr.es; cmoleroj@ugr.es; pablopadilla@ugr.es).

Carlos Megías is with the Department of Computer Architecture and Technology, CITIC, ETSIIT, University of Granada, 18071 Granada, Spain (email: narg@ugr.es)

Antonio Alex-Amor is with the Information Technologies Department, Universidad CEU San Pablo, 28003 Madrid, Spain (email: antonio.alexamor@ceu.es)

range. Gap-waveguide technology has been selected for its robustness under manufacturing tolerances. Additionally, the proposed phase shifter can also be adopted in conventional ridge waveguide considering perfect electric conductor (PEC) conditions in the design process.

The strategy for the phase shifter design is based on obtaining a unit cell that produces a constant phase shift along the frequency. Once this is achieved, multiple unit cells are concatenated until the desired phase shift is reached. The main difference of the proposed unit cell regarding a conventional RGW line [5] is the insertion of holes with semi-circle base placed along the x-direction. These holes present a glide-symmetric configuration where the symmetry plane is the XZ plane placed in the middle of the ridge and, the separation between hole centers is half of the unit cell period p.

In order to study the phase shift behavior produced by a unit cell, the dispersion diagrams are very useful to assess this characteristic [16]. For the simulated dispersion diagrams, the periodicity value of the pins p_p has been reduced to match the periodicity p of the unit cell. Fig. 2(a) shows the dispersion diagram of a conventional RGW unit cell where its main dimensions are modified. For the computation of the phase shift in Fig. 2(b), we select as the reference the RGW unit cell whose dimensions are: $h_r = 1.4$ mm and, $w_r = 3.6$ mm (black line with circled markers in Fig. 2(a)). As the ridge height h_r increases, the fundamental mode of the RGW unit cell lowers regarding to the reference RGW unit cell. This lowering of the modes in the dispersion diagram is translated into an increase of the phase shift for the RGW unit cells with higher ridge height. This is because the TE mode supported by the RGW unit cell approaches a TEM mode and therefore, decreases its cutoff frequency. However, the phase shifts obtained are not stable along the frequency range as can be observed in Fig. 2(b). On the other hand, another approach to introduce phase shift in a conventional RGW unit cell is by narrowing the width of the waveguide w_{r2} (green line with squared markers). In this case, the mode in the dispersion diagram goes up regarding the mode of the reference RGW unit cell due to an increase of the cutoff frequency of TE mode. A combination of both effects can be applied to achieve a RGW unit cell with stable phase shift along a wide frequency range (yellow line with downward-pointing triangles).

The use of GSR unit cells instead of conventional RGW unit cells with modified parameters provides an advantage in the design of phase shifters. The proposed glide-symmetric configuration is the one that produces the largest bandwidth regarding other hole configuration in the unit cell. This can be observed in the dispersion diagram of Fig. 2(c) since stopbands do not appear for GSR unit cell. The parameter d_x in Fig. 2(c) stands for the distance between the center of the holes and that of the unit cell. This parameter is of special attention to preserve the glide symmetry configuration. If d_x is not equal to a quarter of the period of the unit cell, the distance between hole centers is not equal to half of the unit cell period and a stopband appears. This implies a reduction of the operating frequency range and also a loss of linearity of the propagating mode near the stopband [19]. Note that the glide-symmetric configuration of the holes makes the stopband to vanish while

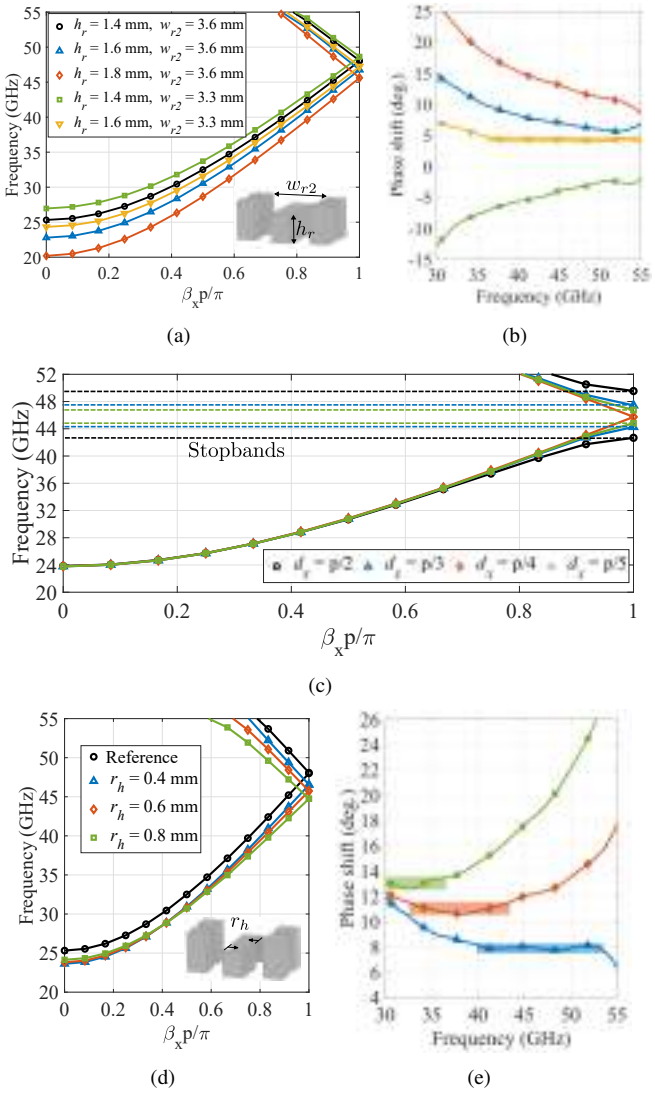

Fig. 2: (a) Dispersion diagram of a conventional RGW unit cell when the height and width of the ridge are varied. (b) Phase shift obtained from Fig. 2(a). (c) Dispersion diagram of the GSR unit cell when hole displacement d_x is varied. (d) Dispersion diagram of the GSR unit cell when hole radius is varied. (e) Phase shift obtained from Fig. 2(d). To compute the phase shift, the reference RGW unit cell corresponds to $h_r = 1.4$ mm and $w_{r2} = 3.6$ mm. The other dimensions can be found in Fig. 1.

the mirror-symmetric configuration ($d_x = p/2$) provides the widest stopband according to the results discussed in [16].

Figs. 2(d) and 2(e) present the dispersion diagram and the produced phase shift of the GSR unit cell. The ridge height of the GSR unit cell must be slightly higher than the reference RGW unit cell to reduce the cutoff frequency and achieve the desired effect of the glide-symmetric holes. The increase in ridge height leads to set a higher offset in the produced phase shift while the glide-symmetric holes enable a wideband fine tuning. The reference RGW unit cell is the same as the one considered for the Fig. 2(b). The modification of the hole radii allows a fine variation of phase constant (β_x) along the frequency in the dispersion diagram. Depending on the value of the hole radii, the slope of the fundamental mode is varied and subsequently, the produced phase shift shown in Fig. 2(e).

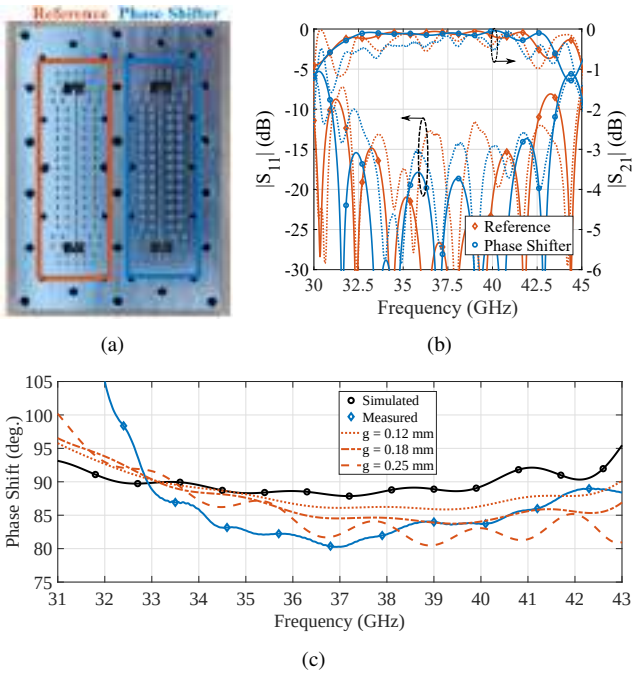

Fig. 3: RGW reference line and phase shifter: (a) Prototypes. (b) Measured and simulated magnitude of transmission and reflection parameters. The solid and dashed lines correspond to simulated and measured results, respectively. (c) Simulated and measured phase shift.

The modification in the slope of the mode is mainly from 30 GHz onwards. As the hole radius increases, a lower slope is obtained in the dispersion diagram regarding of GSR unit cells. This relevant effect enables a stable and higher phase shift depending on the selected hole radius as illustrated in Fig. 2(e). In this figure, three different ranges of frequencies with phase-stable behavior are achieved. The smaller the radius, the smaller the phase shift produced by the unit cell but the produced stable phase shift has a higher value than the one obtained for the best case in Fig. 2(b) (yellow line).

III. Phase Shifter Design and Experimental Validation

Based on the proposed GSR unit cell, a 90º phase shifter has been designed by the concatenation of eight unit cells whose dimensions are in the caption of Fig. 1. A RGW reference line with the same length of the phase shifter has also been designed. The dimensions of the unit cell employed in the RGW reference line correspond to the unit cell with $h_r = 1.4$ mm and $w_{r2} = 3.6$ mm in Fig. 2(a). The manufactured back-to-back designs of the RGW reference line and phase shifter are displayed in Fig. 3(a). Same transitions have been used in both designs to accurately measure the phase shift. The simulation of this design has been performed with CST Studio Suite where the metal considered in the structure is aluminum, the same metal as used in the prototype. In Fig. 3(b), the simulated and measured $|S_{21}|$ and $|S_{11}|$ of the RGW reference line and phase shifter are shown. The experimental results show a common impedance bandwidth where $|S_{11}|$ is below -10 dB from 33 GHz to 43 GHz with a maximum insertion loss of 0.7 dB. Tolerances of $\pm 75\mu$m in the position of the holes due to manufacturing has also been studied in simulation but the effect of possible stopband in the transmission coefficient is negligible. In the impedance bandwidth, the output phase difference between the reference line and phase shifter is calculated and presented in Fig. 3(c). The expected phase shift from the simulated result was approximately 90º$\pm$ 2º in the bandwidth under consideration. Measured results reveal a phase shift of 85º$\pm$ 5º. A further study has been carried out to find out the cause of this slight difference between simulated and measured results. The parameter g (see Fig. 1) has been varied and the simulated results are shown in Fig. 3(c). The larger the air gap g, the greater the variation in the phase shift, besides a reduction in the average phase shift in the considered bandwidth. Nevertheless, the phase shifter design can be considered robust under this gap tolerance.

Finally, Table I presents a comparison with other related waveguide phase shifters found in the literature. The proposed RGW phase shifter provides a wideband performance comparable to other state-of-the-art waveguide phase shifters. Specifically, if we compare with the other wideband ridge waveguide phase shifter [10], it uses a rectangular waveguide as a reference while in the proposed design the reference is a ridge waveguide. This is of interest when the same waveguide technology is required in a more complex circuit. Furthermore, the phase shifter design in [10] relies on an optimization process as opposed to the one presented in this work, which is based on dispersion diagrams. This provides greater physical insight and lower computational cost but with lower compactness in the phase shifter.

TABLE I:
Comparison of phase shifters in mm-wave band with this work

Ref.	Frequency (GHz)	Waveguide Technology	Max. IL (dB/º)	Stable Phase Shift	Compactness (º/λ)†
[4]*	27-33.6 (21.78%)	PRGW	$8.88\cdot10^{-3}$	Yes (45º$\pm$2º)	30
[10]	33-50 (40.1%)	RW	$4.44\cdot10^{-3}$	Yes (92º$\pm$2º)	48.58
[12]	20-27 (29.78%)	RGW & LC	$14.3\cdot10^{-3}$	No	58.92
[14]	75-76.5 (1.98%)	RGW	$8.33\cdot10^{-4}$	No	197.37
[15]	46-60 (26.41%)	GGW	$4.65\cdot10^{-3}$	No	141.5
[16]	56.5-74.5 (27.5%)	GGW	$11.11\cdot10^{-3}$	Yes (180º$\pm$5º)	31.22
This work	33-43 (26.3%)	RGW	$8.24\cdot10^{-3}$	Yes (85º$\pm$5º)	24.67

* Simulated results.
† At center frequency.

IV. Conclusion

This paper presents a RGW phase shifter with a stable phase shift response in a wide frequency range. By tuning the radii of the glide-symmetric holes and the height of the ridge of the unit cell, a stable phase shift can be achieved in a desired frequency range. A 90º phase shifter is designed and manufactured. The measured results reveal a low loss and wideband phase shifter whose produced phase shift is 85º$\pm$ 5º from 33 GHz to 43 GHz. The RGW phase shifter enables the potential development of cost-effective Butler matrix in ridge waveguide. Additionally, the GSR unit cell allows a wideband control of the β which can potentially be used for the design of leaky-wave antennas in ridge waveguide.

REFERENCES

[1] Y. Cao, K. Chin, W. Che, W. Yang and E. S. Li, "A Compact 38 GHz Multibeam Antenna Array With Multifolded Butler Matrix for 5G Applications," *IEEE Antennas Wirel.Propag. Lett.*, vol. 16, pp. 2996-2999, 2017.

[2] K. Tekkouk, J. Hirokawa, R. Sauleau, M. Ettorre, M. Sano and M. Ando, "Dual-Layer Ridged Waveguide Slot Array Fed by a Butler Matrix With Sidelobe Control in the 60-GHz Band," *IEEE Trans. Antennas Propag.*, vol. 63, no. 9, pp. 3857-3867, Sept. 2015.

[3] A. Tamayo-Domínguez, J. Fernández-González and M. Sierra-Castañer, "3-D-Printed Modified Butler Matrix Based on Gap Waveguide at W-Band for Monopulse Radar," *IEEE Trans. Microw. Theory Techn.*, vol. 68, no. 3, pp. 926-938, March 2020.

[4] I. Afifi and A. -R. Sebak, "Wideband 4 × 4 Butler Matrix in the Printed Ridge Gap Waveguide Technology for Millimeter-Wave Applications," *IEEE Trans. Antennas Propag.*, vol. 68, no. 11, pp. 7670-7675, Nov. 2020,

[5] E. Rajo-Iglesias, M. Ferrando-Rocher and A. U. Zaman, "Gap Waveguide Technology for Millimeter-Wave Antenna Systems," *IEEE Commun. Mag.*, vol. 56, no. 7, pp. 14-20, July 2018.

[6] J. Liu, A. Vosoogh, A. U. Zaman and J. Yang, "A Slot Array Antenna With Single-Layered Corporate-Feed Based on Ridge Gap Waveguide in the 60 GHz Band," *IEEE Trans. Antennas Propag.*, vol. 67, no. 3, pp. 1650-1658, March 2019.

[7] A. Beltayib and A. Sebak, "Analytical Design Procedure for Forward Wave Couplers in RGW Technology Based on Hybrid PEC/PMC Waveguide Model," *IEEE Access*, vol. 7, pp. 119319-119331, 2019.

[8] A. Farahbakhsh, "Ka-Band Coplanar Magic-T Based on Gap Waveguide Technology," *IEEE Microw. Wireless Compon. Lett.*, vol. 30, no. 9, pp. 853-856, Sept. 2020.

[9] J. L. Cano, A. Mediavilla, and A. Tribak, "Parametric design of a class of full-band waveguide differential phase shifters," *Electronics* ,vol.8,no. 3, p. 346, Mar. 2019.

[10] E. Villa, B. Aja, J. Cagigas, E. Artal and L. de la Fuente, "Four-State Full Q-Band Phase Shifter Using Smooth-Ridged Waveguides," *IEEE Microw. Wireless Compon. Lett.*, vol. 27, no. 11, pp. 995-997, Nov. 2017.

[11] A. Ghasemi and J. Laurin, "Beam Steering in Narrow-Wall Slotted Ridge Waveguide Antenna Using a Rotating Dielectric Slab," *IEEE Antennas Wirel. Propag. Lett.*, vol. 17, no. 10, pp. 1773-1777, Oct. 2018.

[12] M. Nickel *et al.*, "Ridge Gap Waveguide Based Liquid Crystal Phase Shifter," *IEEE Access*, vol. 8, pp. 77833-77842, 2020.

[13] M. A. Abdelaal, S. I. Shams and A. A. Kishk, "Compact RGW Differential Phase Shifter for Millimeter-Wave Applications," in *2018 18th International Symposium on Antenna Technology and Applied Electromagnetics (ANTEM)*, Waterloo, ON, 2018.

[14] H. Kirino and K. Ogawa, "A 76GHz phased array antenna using a waffle-iron ridge waveguide," in *Proceedings of the Fourth European Conference on Antennas and Propagation*, Barcelona, 2010.

[15] Á. Palomares-Caballero, A. Alex-Amor, P. Padilla, F. Luna and J. Valenzuela-Valdes, "Compact and Low-Loss V-Band Waveguide Phase Shifter Based on Glide-Symmetric Pin Configuration," *IEEE Access*, vol. 7, pp. 31297-31304, 2019.

[16] Á. Palomares-Caballero, A. Alex-Amor, P. Padilla and J. F. Valenzuela-Valdés, "Dispersion and Filtering Properties of Rectangular Waveguides Loaded With Holey Structures," *IEEE Trans. Microw. Theory Techn.*, vol. 68, no. 12, pp. 5132-5144, Dec. 2020.

[17] O. Quevedo-Teruel, Q. Chen, F. Mesa, N. J. G. Fonseca, G. Valerio, "On the benefits of glide symmetries for microwave devices," *IEEE Journal of Microwaves*, vol. 1, no. 1, pp. 457-469, winter 2021.

[18] A. U. Zaman and P. Kildal, "Wide-Band Slot Antenna Arrays With Single-Layer Corporate-Feed Network in Ridge Gap Waveguide Technology," *IEEE Trans. Antennas Propag.*, vol. 62, no. 6, pp. 2992-3001, June 2014.

[19] O. Quevedo-Teruel, M. Ebrahimpouri and M. Ng Mou Kehn, "Ultrawideband Metasurface Lenses Based on Off-Shifted Opposite Layers," *IEEE Antennas Wirel. Propag. Lett.*, vol. 15, pp. 484-487, Dec. 2016.

2.1.4 Low-Loss Reconfigurable Phase Shifter in Gap-Waveguide Technology for mm-Wave Applications

In the literature, it is a challenge to obtain reconfigurable phase shifters in waveguides for millimeter-wave frequencies. In the below publication, a mechanically reconfigurable phase shifter design is proposed through the use of gap-waveguide technology based on glide-symmetric holes. Taking advantage of the fact that the gap-waveguide technology allows the design to be divided into two layers, a metallic strip capable of deforming under pressure is placed on one side of the waveguide before assembling. Using a pressing screw placed externally and in the middle of the metallic strip, the metallic strip deforms in a controlled manner and shapes the lateral side of the gap waveguide. Through this deformation, the phase constant of the waveguide is modified while preserving good transmission and low reflection. The experimental validation of this design is performed for a prototype that has an operating band from 64 GHz to 75 GHz reaching a maximum reconfigurable phase shift of 250^{o}.

THIS IS A POSTPRINT VERSION OF THE PAPER:

Á. Palomares-Caballero, A. Alex-Amor, P. Escobedo, J. Valenzuela-Valdés and P. Padilla, "Low-Loss Reconfigurable Phase Shifter in Gap-Waveguide Technology for mm-Wave Applications," in *IEEE Transactions on Circuits and Systems II: Express Briefs*, vol. 67, no. 12, pp. 3058-3062, Dec. 2020.

- Journal Impact Factor (JIF) in JCR 2020: 3.292
- Category: ENGINEERING, ELECTRICAL & ELECTRONIC. JIF Rank: 97/273 (Q2).

Disclaimer:
This work has been published on IEEE Transactions on Circuits and Systems II: Express Briefs. DOI: 10.1109/TCSII.2020.3000058

Low-Loss Reconfigurable Phase Shifter in Gap-Waveguide Technology for mm-Wave Applications

Ángel Palomares-Caballero, Antonio Alex-Amor, Pablo Escobedo, Juan Valenzuela-Valdés, Pablo Padilla

***Abstract*—In this brief, we present a low-loss mechanically reconfigurable phase shifter implemented in gap-waveguide technology for mm-wave frequencies. The proposed design gives a practical implementation of tuning elements inside the waveguide providing alternatives to the use of the E-plane split waveguide at high frequencies in order to avoid leakage losses. The depicted phase shifter design is based on a H-plane split waveguide. The phase shift is controlled by means of a tuning screw, which exerts pressure on a flexible metallic strip inserted inside the waveguide. The flexible strip bends with different curvature radii and determines the phase shift at the output port. Cost-effective manufacturing and simple implementation of the flexible metallic strip are achieved by means of the gap-waveguide design. A prototype has been manufactured for validation purposes. Good impedance matching is achieved from 64 GHz to 75 GHz providing a 15.8% impedance bandwidth. The results show a maximum phase shift of 250º with a maximum and mean insertion loss (IL) of 3 dB and 1.7 dB, respectively.**

***Index Terms*—Phase shifter, gap-waveguide technology, low-loss, reconfigurable waveguide, mm-waves.**

I. Introduction

RECONFIGURABILITY is playing a fundamental role in present and future mm-wave communication systems. Thus, reconfigurable phase shifters are necessary to provide beamforming capabilities to the antennas [1]. However, this kind of phase shifters has to be implemented in a proper technology to present low losses and fulfill demanding requirements. Waveguide technology is a good candidate since it provides reduced losses in the mm-wave frequency range. Some examples of mechanically reconfigurable phase shifters in waveguide technology at K-band can be found in [2], [3]. In both designs, short waveguide couplers with mechanical reconfigurable elements at the output ports have been used to achieve the desired phase shift in reflection. Another solution in waveguide technology is presented in [4], where the wide side of the waveguide is adjustable to achieve the desired phase shift at the output port of the waveguide. Similarly, [5] shows a reconfigurable phase shifter based on a piezoelectric actuator, where the side wall of the waveguide is in this case a perfect magnetic conductor (PMC). Other approaches to obtain phase shift employ PIN diodes [6]–[12]. Nevertheless, PIN diodes suffer from high losses in mm-wave regime. Some reconfigurable material such as liquid crystals [13]–[17] or ferroelectrics [18]–[20] are also used to vary the phase shift. These approaches are currently attractive but present some drawbacks such as complex implementation in waveguide and high insertion losses incurred when the frequency increases.

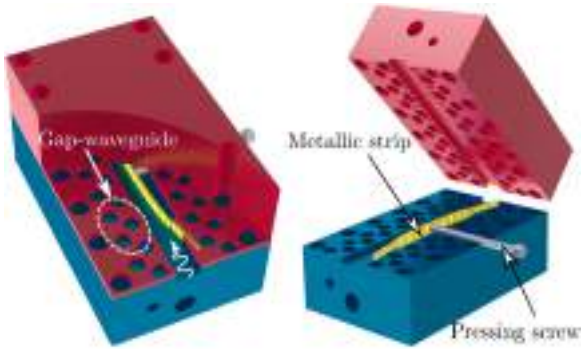

Fig. 1: Tunable phase shifter design model.

Waveguide technology has evolved in order to provide a less demanding manufacturing process. Gap-waveguide technology [21] enables the waveguide fabrication in two separate parts with no mandatory perfect electrical contact in the assembly, avoiding possible leakage throughout the gap. This fact permits to relax the requirements of manufacturing providing a low-cost fabrication. Besides, taking advantage of the waveguide fabrication in splitted parts, tuning elements can be easily implemented inside the waveguide in order to modify the phase of the propagating signal. For example, in [22] and [23], gap-waveguide based on glide-symmetric holes [24] has been used to design a mm-wave phase shifter inserting a dielectric slab and pinned structures, respectively. This work presents a tunable phase shifter based on gap-waveguide technology. The reconfigurable behavior of the phase shifter is achieved by means of a flexible metallic strip inserted in the side wall of the waveguide. The variation of the curvature radius of the flexible metallic strip is produced by a tuning screw that exerts a pressure on the center of the strip. It allows to narrow the wide side of the waveguide and modify the propagation

Manuscript submitted February X, 2020. This work was supported in part by the Spanish Research and Development National Program under Projects TIN2016-75097-P, B-TIC-402-UGR18, RTI2018-102002-A-I00 and the pre-doctoral grant FPU18/01965. *(Corresponding author: Ángel Palomares-Caballero.)*

Á. Palomares-Caballero, A. Alex-Amor, Juan Valenzuela-Valdés and P. Padilla are with the Departamento de Teoría de la Señal, Telemática y Comunicaciones, Universidad de Granada, 18071 Granada, Spain (e-mail: angelpc@ugr.es; aalex@ugr.es; juanvalenzuela@ugr.es; pablopadilla@ugr.es).

A. Alex-Amor is with the Information Processing and Telecommunications Center, Universidad Politécnica de Madrid, 28040 Madrid, Spain (e-mail: aalex@gr.ssr.upm.es).

P. Escobedo is with Bendable Electronics and Sensing Technologies (BEST) Group, School of Engineering, University of Glasgow, Glasgow G12 8QQ, UK (e-mail: pablo.escobedo@glasgow.ac.uk).

constant (β_g), producing an adjustable phase shift. Figure 1 depicts the design of the proposed tunable phase shifter.

Some patents about mechanically tunable phase shifter in conventional waveguide technology are in [25], [26]. The latter inserts a pair of dielectric rods inside the waveguide in order to change the phase shift. However, low phase shift is achieved and increase in the insertion losses are expected due to the wave propagation in the dielectric material at high frequencies. Additionally, no in-depth details are provided about the manufacturing issues and performance of a real prototype. There exist examples of commercially available phase shifters in waveguide technology [27], [28]. Nevertheless, their way of implementing the phase shift in waveguide is not reported. In addition, they are bulky and high-cost designs due to the complexity of implementing the phase shift mechanism. The proposed phase shifter design exploits the advantages of the gap-waveguide technology to allow a cost-effective device with low losses. To the best of the authors' knowledge, this is the first reported mechanically reconfigurable gap-waveguide phase shifter in mm-waves frequencies.

The paper is organized as follows. Section II presents the phase shifter design and its reconfigurable behavior. Section III shows the experimental results obtained with the prototype as well as the comparison with the simulation results. Finally, conclusions are provided in Section IV.

II. Phase Shifter Design

A top view of the proposed phase shifter is illustrated in Fig. 2. The contour of the metallic strip can be modeled with an elliptical profile, whose semi-major axis a_e is fixed and whose semi-minor axis b_e depends on the position of the tuning screw. The more pressure the screw exerts, the larger b_e is. Since the waveguide works in its fundamental mode, the propagation constant β_g for the TE_{10} [29] is presented in Eq. (1). The right-hand side of this expression shows the dependence with the narrowing of the waveguide ($\omega - h_e(x, b_e)$). Therefore, when the signal propagates along the waveguide, the propagation constant $\beta_g(x, b_e)$ varies according to selected position x of the waveguide and b_e. Note that fundamental mode is considered in the entire length of the phase shifter, $2a_e$. The expressions for $\beta_g(x, b_e)$ and the approximated phase shift ϕ obtained along the waveguide are represented as:

$$\beta_g(x, b_e) = \frac{2\pi}{\lambda_g(x, b_e)} = 2\pi \frac{\sqrt{1 - \left(\dfrac{\lambda_o}{2(\omega - h_e(x, b_e))}\right)^2}}{\lambda_o} \quad (1)$$

$$\phi(b_e) = \int_{-a_e}^{a_e} \beta_g(x, b_e)\, dx \quad (2)$$

where λ_o is the free-space wavelength and w is the size of the broadside in waveguide rectangular size 15 (WR15). From Eqs. (1)-(2), it is clear that a variation in the profile of the ellipse produces a modification in the total phase shift. The selection of the dimensions a_e and b_e are based on the proposed model and represent a tradeoff between three main aspects of the phase shifter: operational frequency range, maximum phase shift and compactness. The phase shift results provided by this model are shown at the end of this section compared with the simulations in *CST Microwave Studio*.

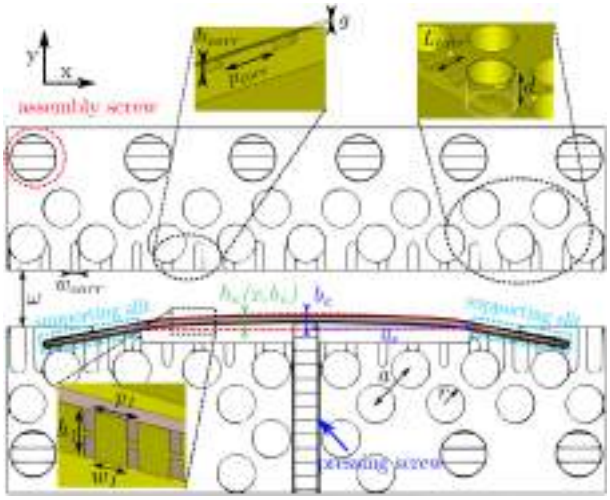

Fig. 2: Description of the upper layer of the phase shifter. Dimensions: a_e = 11 mm, b_e = 0.55 mm, ω = 3.76 mm, a = 3.22 mm, r = 1.25 mm, w_{corr} = 0.6 mm, h_{corr} = 0.25 mm, p_{corr} = 2 mm, L_{corr} = 1.8 mm, h_1 = 1.8 mm, p_1 = 1.1 mm, w_1 = 0.8 mm.

In order to allow an easy implementation of the metallic strip inside the waveguide, gap-waveguide technology based on glide-symmetric holes is chosen [24]. The dimensions for the glide-symmetric holes are depicted in Fig. 2, where the gap height g and the depth of the holes d are set at 0.05 mm and 3 mm, respectively. This electromagnetic bandgap (EBG) structure provides a stopband for the gap leakage from 45 GHz to 85 GHz, covering the frequency range of the waveguide standard WR15. Figures 3(a) and 3(b) show the effect of the gap-waveguide technology in the proposed phase shifter. It is observed how the phase shift can be controlled by changing the curvature radius of the metallic strip.

In order to prevent undesired resonances between glide-symmetric EBG holes and the waveguide, corrugations are implemented to avoid resonant fields [30], [31]. In addition, a vertical thin gap g_s (shown in Fig. 3(c)) should exist between the long side of the metallic strip and the upper and lower surface of the waveguide to permit the flexible movement of the metallic strip. These thin gaps may cause resonant fields in the same manner as previous situation. For that reason, the flexible metallic strip has also a corrugated shape in order to prevent resonances. A transversal cut of the phase shifter is illustrated in Fig. 3(c), where 50 μm gaps are included in both sides of the metallic strip to observe the E-field distribution in presence of an imperfect electrical contact between the metallic strip and the waveguide walls. No resonances are observed, since the electric field is confined in the waveguide despite the existence of thin air gaps. Figure 4(a) illustrates the simulated $|S_{21}|$ of the phase shifter for a design with and without corrugations. These corrugations, on both the metallic strip and the waveguide wall, enhance the transmission in the entire operating frequency range. When the strip corrugations are not included (blue lines), peaks in the upper part of the frequency range begin to appear due to

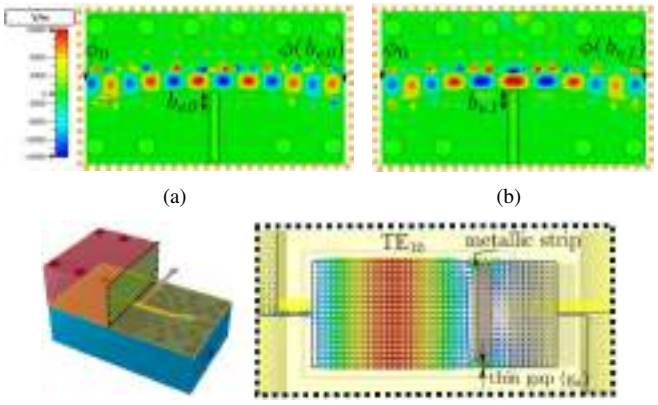

(c)

Fig. 3: Amplitude of the E-field distribution: (a) top view of the gap between layers at 65 GHz when the tuning screw does not exert any pressure, (b) when the tuning screw exerts a pressure. The phase changes as a consequence of the tuning screw. (c) 3D views of the selected cutting planes and transversal cut of the phase shifter showing the fundamental propagative mode.

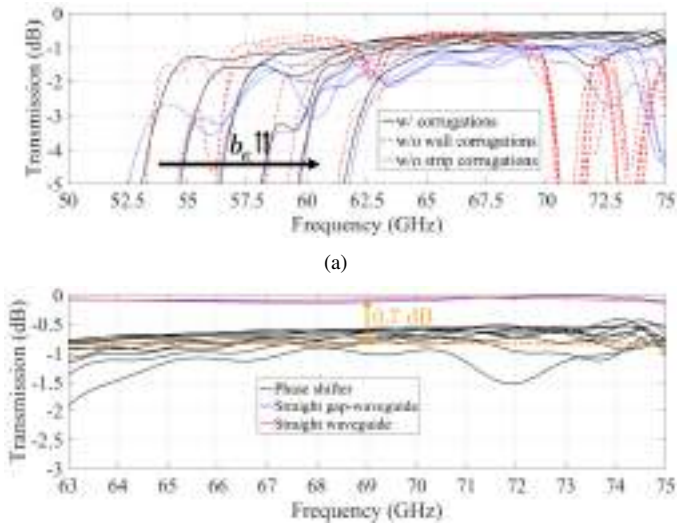

(a)

(b)

Fig. 4: Simulated transmission coefficient: (a) with (w/) and without (w/o) strip and wall corrugations for different curvature radii (different b_e values). (b) Comparison with a straight gap-waveguide and conventional waveguide that have the same length as the phase shifter (for different curvature radii).

resonances. Other deeper peaks in transmission show up in the case of not implementing the wall corrugations. Moreover, as the metallic strip employs dielectric material for its structure, additional insertion losses exist. To take into account these losses, a comparison between the phase shifter, a straight gap-waveguide and a conventional hollow waveguide is shown in Fig. 4(b). The increase of insertion losses because of the addition of the metallic strip is about 0.7 dB compared to the straight WR15 gap-waveguide section.

The simulated phase shift results are presented in Fig. 5 along with the results provided by the model. Good agreement is observed between the simulation and the model results, providing more phase shift dispersion when the radius of curvature increases. For lower curvature radii, which entail larger broadside waveguide, the deviation of the phase shift

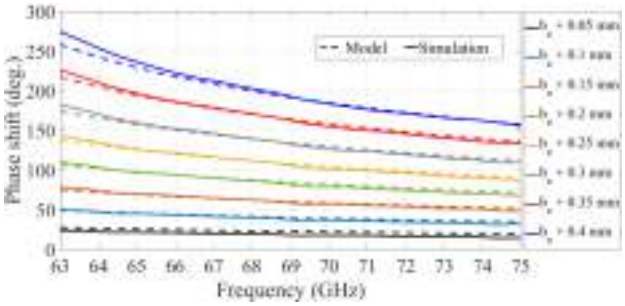

Fig. 5: Simulated phase shift for different curvature radii and comparison with the proposed model for b_e = 0.55 mm.

tends to decrease. This is because of the resulting propagation constant, which is less dispersive when the screw does not increase the curvature radius (reference position). According to this effect, a less dispersive phase shifter can be designed by extending the phase shift area (i.e. enlarging the range of the semi-major axis a_e) and employing smaller curvature radii.

III. Experimental Validation

In order to validate the simulation results, a prototype of the proposed phase shifter was manufactured in CNC (Computer Numerical Control) technology. Figure 6(a) shows the forming layers of the reconfigurable phase shifter, as well as the final assembly. Figure 6(b) shows the effect of the pressing screw over the metallic strip. The flexible metallic strip has been manufactured in FR4 (substrate thickness of 0.4 mm and $\epsilon_r = 4.5$) to obtain the desired flexible behavior to implement the reconfigurability in the phase shifter. The gaps between the metallic strip and the lower and upper surface of the waveguide were measured to assess the correct assumption of gap sizes. The measured gaps have a size of 25μm $\pm$ 10μm. Figures 7(a) and 7(b) show the effect of the gap sizes in the produced phase shift and insertion losses, respectively. For gap sizes bigger than 100 μm, the gaps have a significant effect in the performance of the phase shifter because of the existence of electric field that is not guided properly by the metallic strip. Since the measured gaps are less than this value, the electric field remains confined by the metallic strip, similarly to that shown in Fig. 3(c).

The measured and simulated scattering parameters, for the complete range of curvature radius, are shown in Fig. 8(a). They have been measured using the ZVA-Z110E Converters that are connected to the vector network analyzer (VNA) R&S-ZVA67. The frequency multipliers ZVA-Z110E are capable of raising the measurement range to 110 GHz because the VNA is limited approximately up to 66.5 GHz. A frequency range from 63 to 75 GHz is established. The measured results show a shift in the lowest limit frequency, achieving a $|S_{11}|$ lower than -10 dB from 64 to 75 GHz (15.8% impedance bandwidth). This large impedance bandwidth is due to the taper in the waveguide width provided by the elliptical profile of the metallic strip. There is a smooth decrease in waveguide width up to the middle of the phase shifter and then, the waveguide width experiments a smooth increase to the width of the output port. The values obtained for the measured reflection

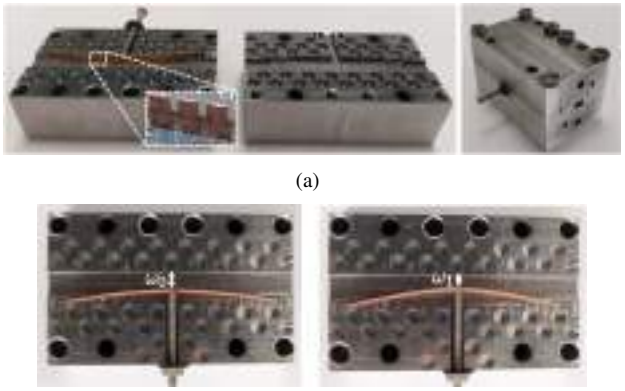

(a)

(b)

Fig. 6: Manufactured prototype: (a) forming layers and assembled prototype, (b) detail of the modification of the curvature radius by the pressing screw.

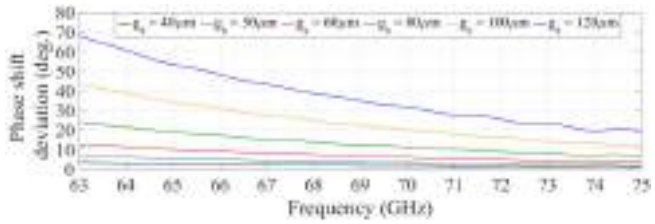

(a)

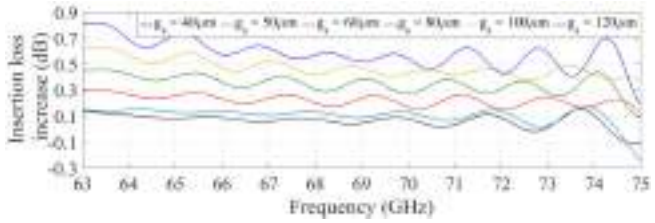

(b)

Fig. 7: Effect of the vertical gap g_s (illustrated in Fig. 3(c)) between the metallic strip and the upper and lower surfaces of the waveguide: (a) on the phase shift, and (b) on the insertion losses. The reference simulation of the phase shifter has a g_s = 30 μm and a curvature radius b_e = 0.8 mm.

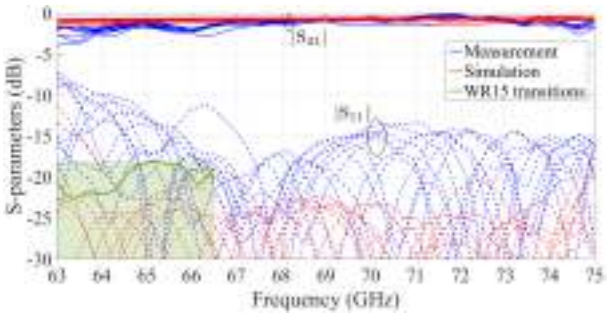

(a)

(b)

Fig. 8: Measured S-parameters: (a) magnitude of the phase shifter for the complete range of radius of curvature and comparison with the simulated results and, (b) measurement setup in WR10.

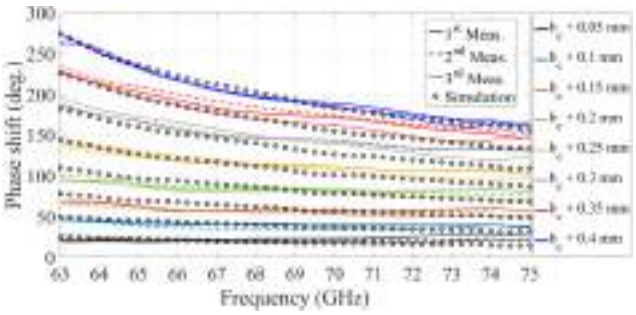

Fig. 9: Measured phase shift for three consecutive measurements in comparison with the simulation results for b_e = 0.55 mm.

coefficient are greater than the simulation results. This fact is due to the standard waveguide size 10 (WR10) used by the ZVA-Z110E Converters employed in the measurement setup. The transitions between WR10 and WR15 (waveguide size of the phase shifter) increase the $|S_{11}|$. The measurement setup in WR15 has not been used since it is limited up to 66.5 GHz due to the 1.85 mm coaxial to WR15 waveguide transitions. For the sake of validation, a measurement with the setup in WR15 has also been done, in the range of 63 to 66.5 GHz, and it is observed the decrease in the reflection value approaching to simulation levels (green line in Fig. 8(a)). Furthermore, low insertion losses are obtained with a mean value of 1.7 dB and lower than 3 dB in the impedance bandwidth.

The measured phase shift is shown in Fig. 9. In order to assess the repeatability of the prototype, three consecutive measurements have been carried out. This test ensures that the metallic strip returns to its original position after being deformed by the tuning screw. The screw has a standard metric 1.6 (M1.6), whose pitch thread is 0.35 mm. Therefore, an increment in $b_{ellipse}$ of 0.05 mm implies approximately 0.14 screw turns. The phase shift resolution will depend on the precision with which the pressing screw is turned. For instance, in the presented prototype, one turn on the pressing screw is approximately translated into a mean phase shift of 180^o. The measurement results present a good agreement with the simulation results providing the same dynamic range for the phase shift. The small discrepancies evidenced could be associated to approximating the real deformation of the metallic strip with an elliptical profile. Moreover, the repeatability of the measurements show the good performance of the flexible metallic strip to set the desired phase shift. Finally, a comparison between the proposed phase shifter and other reconfigurable phase shifters in mm-wave frequencies is illustrated in Table I. The proposed reconfigurable phase shifter achieves a better performance in insertion losses and FoM (figure-of-merit) along the operating frequency [13]. The return losses (RL) achieved by our phase shifter has good

performance compared with the referenced works except for [26]. However, that work provides low phase shift. Some of the reported tunable phase shifters require a complex setup [5] or a more complicated implementation of the tuning elements in the waveguide [15]. By applying the gap waveguide to the phase shifter design, more options in the location of the gap for the split waveguide is achieved in contrast with the traditional implementation using E-plane split waveguide [13]. In addition, compared with the commercial devices [27], [28], the gap-waveguide phase shifter presents a reduced volume and low cost that allow a cost-effective and easy integration in a full system.

TABLE I:
Comparison of reconfigurable phase shifters in mm-wave band with this work

Ref.	Frequency (GHz)	Technology	Max. IL (dB)	RL (dB)	ϕ_{max} (^{o})	FoM (^{o}/dB)	Complexity/ Cost
[5]	230-250	Piezoelectric	3	10	380	127	High
[6]	26-30	PIN Diode	7.8	10	348.75	44.7	Low/Medium
[8]	33-50	PIN Diode	10	10	270	30	Low/Medium
[13]	85-110	Liquid Crystal	8	n. a.	900	125-145	High
[15]	99-105	Liquid Crystal	2.7	6	318	118-148	High
[18]	30-40	Ferroelectric	9	5	360	36-50	Low
[19]	50-54	Ferroelectric	6	n. a.	30	5	Low
[26]	>75	Waveguide	n. a.	25	30	n. a.	Medium
[27], [28]	50-75	Waveguide	1	18	180	180	High
This work	64-75	Gap-waveguide	3	12	250	95-152	Low

IV. Conclusion

This paper presents the first mechanically reconfigurable phase shifter design in gap-waveguide technology for mm-wave frequencies. The gap-waveguide technology enables a low-complex prototype that allows the inclusion of a flexible metallic strip inside the waveguide. This element provides the reconfigurability behavior of the phase shifter. A prototype has been manufactured to validate the simulation design. The experimental results show an operational frequency bandwidth from 64 to 75 GHz with averaged insertion loss of 1.7 dB and a maximum dynamic phase shift of 250^o.

References

[1] W. Hong *et al.*, "Multibeam Antenna Technologies for 5G Wireless Communications," *IEEE Trans. Antennas Propag.*, vol. 65, no. 12, pp. 6231-6249, Dec. 2017.

[2] Q. Zhang, C. Yuan and L. Liu, "Studies on mechanical tunable waveguide phase shifters for phased-array antenna applications," in *IEEE International Symposium on Phased Array Systems and Technology (PAST)*, Waltham, MA, 2016.

[3] L. Polo-López, J. L. Masa-Campos, J. A. Ruiz-Cruz, "Reconfigurable H-plane waveguide phase shifters prototyping with additive manufacturing at K-band" *Int. J. RF Microw. Comput. Aided Eng.*, vol. 29, e21980, 2019;

[4] Y. Yang, C. Yuan, G. Cheng and B. Qian, "Ku-Band Rectangular Waveguide Wide Side Dimension Adjustable Phase Shifter," *IEEE Trans. Plasma Sci.*, vol. 43, no. 5, pp. 1666-1669, May 2015.

[5] A. A. Ibrahim, H. N. Shaman and K. Sarabandi, "A Sub-THz Rectangular Waveguide Phase Shifter Using Piezoelectric-Based Tunable Artificial Magnetic Conductor," *IEEE Trans. THz Sci. Technol.*, vol. 8, no. 6, pp. 666-680, Nov. 2018

[6] J. G. Yang and K. Yang, "Ka-Band 5-Bit MMIC Phase Shifter Using InGaAs PIN Switching Diodes," in *IEEE Microw. Wireless Compon. Lett.*, vol. 21, no. 3, pp. 151-153, March 2011.

[7] B. Muneer, Z. Qi and X. Shanjia, "A Broadband Tunable Multilayer Substrate Integrated Waveguide Phase Shifter," *IEEE Microw. Wireless Compon. Lett.*, vol. 25, no. 4, pp. 220-222, April 2015.

[8] E. Villa, B. Aja, J. Cagigas, E. Artal and L. de la Fuente, "Four-State Full Q-Band Phase Shifter Using Smooth-Ridged Waveguides," *IEEE Microw. Wireless Compon. Lett.*, vol. 27, no. 11, pp. 995-997, Nov. 2017.

[9] W. J. Liu, S. Y. Zheng, Y. M. Pan, Y. X. Li and Y. L. Long, "A Wideband Tunable Reflection-Type Phase Shifter With Wide Relative Phase Shift," *IEEE Trans. Circuits Syst. II, Exp. Briefs*, vol. 64, no. 12, pp. 1442-1446, Dec. 2017.

[10] M. T. ElKhorassani *et al.*, "Electronically Controllable Phase Shifter with Progressive Impedance Transformation at K Band," *Appl. Sci.*, vol. 9, no. 23, 2019.

[11] A. Singh and M. K. Mandal, "Electronically Tunable Reflection Type Phase Shifters," *IEEE Trans. Circuits Syst. II, Exp. Briefs*, vol. 67, no. 3, pp. 425-429, March 2020.

[12] Y. Xiong, X. Zeng and J. Li, "A Tunable Concurrent Dual-Band Phase Shifter MMIC for Beam Steering Applications," *IEEE Trans. Circuits Syst. II, Exp. Briefs*, 2020.

[13] R. Reese *et al.*, "Liquid Crystal Based Dielectric Waveguide Phase Shifters for Phased Arrays at W-Band," *IEEE Access*, vol. 7, pp. 127032-127041, 2019.

[14] A. Franc, O. H. Karabey, G. Rehder, E. Pistono, R. Jakoby and P. Ferrari, "Compact and Broadband Millimeter-Wave Electrically Tunable Phase Shifter Combining Slow-Wave Effect With Liquid Crystal Technology," *IEEE Trans. Microw. Theory Techn.*, vol. 61, no. 11, pp. 3905-3915, Nov. 2013.

[15] M. Jost *et al.*, "Liquid crystal based low-loss phase shifter for W-band frequencies," *Electron. Lett.*, vol. 49, no. 23, pp. 1460-1462, 7 Nov. 2013.

[16] M. Jost *et al.*, "Miniaturized Liquid Crystal Slow Wave Phase Shifter Based on Nanowire Filled Membranes," *IEEE Microw. Wireless Compon. Lett.*, vol. 28, no. 8, pp. 681-683, Aug. 2018.

[17] A. Alex-Amor, *et al.*, "Generalized Director Approach for Liquid-Crystal-Based Reconfigurable RF Devices," *IEEE Microw. Wireless Compon. Lett.*, vol. 29, no. 10, pp. 634-637, Oct. 2019.

[18] Z. Zhao, X. Wang, K. Choi, C. Lugo and A. T. Hunt, "Ferroelectric Phase Shifters at 20 and 30 GHz," *IEEE Trans. Microw. Theory Techn.*, vol. 55, no. 2, pp. 430-437, Feb. 2007.

[19] Z. Wang *et al.*, "Millimeter wave phase shifter based on ferromagnetic resonance in a hexagonal barium ferrite thin film", *Appl. Phys. Lett.*, vol. 97, no. 7, Aug. 2010.

[20] V. Sharmaa, Y. Khivintsev, I.Harward, B.J. Kuanr and Z. Celinski, "Fabrication and characterization of microwave phase shifter in microstripgeometry with Fefilm as the frequency tuning element" *J. Magn. Magn. Mater.*, vol. 489, no. 165412, June 2019.

[21] P. Kildal, E. Alfonso, A. Valero-Nogueira and E. Rajo-Iglesias, "Local Metamaterial-Based Waveguides in Gaps Between Parallel Metal Plates," *IEEE Antennas Wirel.Propag. Lett.*, vol. 8, pp. 84-87, 2009.

[22] E. Rajo-Iglesias, M. Ebrahimpouri and O. Quevedo-Teruel, "Wideband Phase Shifter in Groove Gap Waveguide Technology Implemented With Glide-Symmetric Holey EBG," *IEEE Microw. Wireless Compon. Lett.*, vol. 28, no. 6, pp. 476-478, June 2018.

[23] Á. Palomares-Caballero, A. Alex-Amor, P. Padilla, F. Luna and J. Valenzuela-Valdes, "Compact and Low-Loss V-Band Waveguide Phase Shifter Based on Glide-Symmetric Pin Configuration," *IEEE Access*, vol. 7, pp. 31297-31304, 2019.

[24] M. Ebrahimpouri, E. Rajo-Iglesias, Z. Sipus and O. Quevedo-Teruel, "Cost-Effective Gap Waveguide Technology Based on Glide-Symmetric Holey EBG Structures," *IEEE Trans. Microw. Theory Techn.*, vol. 66, no. 2, pp. 927-934, Feb. 2018.

[25] J. Reindel, "Variable Printed Circuit Waveguide Filter," U.S. Patent 4 990 871, Feb. 5, 1991.

[26] K. W. Brown, D. M. Gritters and A. W. Chang, "Waveguide Mechanical Phase Adjuster," U.S. Patent 9 196 940, Nov. 24, 2015.

[27] Pasternack, "0 to 180 Degree WR-15 Waveguide Phase Shifter", 2018. Available: https://www.pasternack.com/images/ProductPDF/PE-W15PS1001.pdf

[28] SAGE Millimeter, Inc., "V-band Micrometer Driven Phase Shifter", 2015. Available: https://sftp.eravant.com/content/datasheets/STP-18-15-M2.pdf

[29] D. M. Pozar. *Microwave Engineering*, 4th edition, Wiley, 2011.

[30] A. Vosoogh, H. Zirath and Z. S. He, "Novel Air-Filled Waveguide Transmission Line Based on Multilayer Thin Metal Plates," *IEEE Trans. THz Sci. Technol.*, vol. 9, no. 3, pp. 282-290, May 2019.

[31] A. Tamayo-Domínguez, H. Azkiou, J. M. Fernández-González and O. Quevedo-Teruel, "Space Reduction Between Parallel Gap Waveguides Using Stacked Glide-Symmetric Metal Sheets," in *13th European Conference on Antennas and Propagation (EuCAP)*, Krakow, Poland, 2019.

2.2 Radiating systems

2.2.1 Millimeter-Wave 3-D-Printed Antenna Array Based on Gap-Waveguide Technology and Split E-Plane Waveguide

This publication presents the design of a 4x4 waveguide antenna array whose central frequency is 70 GHz. The contribution of this work is the ability to use in a combined way the gap-waveguide technology based on glide-symmetric holes and split E-plane waveguides in an antenna arrays for millimeter-waves frequencies. Due to the geometries applied in the design, the prototype was fabricated with 3D printing based on SLA with subsequent copper plating. This results in a low cost fabrication for the considered frequency range. Experimental results showed an operating band from 68 GHz to 74 GHz, with a gain above 19 dBi with a maximum of 20 dBi and an average efficiency of 74%.

Millimeter-Wave 3D-Printed Antenna Array based on Gap-Waveguide Technology and Split E-plane Waveguide

Ángel Palomares-Caballero, Antonio Alex-Amor, Juan Valenzuela-Valdés, and Pablo Padilla

***Abstract*—A multilayer aperture antenna array in millimeter-wave band is presented in this communication. The antenna array is based on glide-symmetric holey gap-waveguide technology combined with E-plane insertion gaps for a low-cost and low-loss design. The radiating part of the antenna array is formed by an array of sixteen aperture antennas, grouped in four sets of 2x2 antenna subarrays in E-plane configuration. The 2x2 subarrays are fed by a one-to-four corporate feeding network in E-plane with holey gap-waveguide technology. The antenna array has been manufactured with high precision stereolithography (SLA) and subsequent metal plating. This design procedure yields a low-cost and low-weight manufacturing process for functional prototypes. The complete array has been manufactured and measured, comparing its performance with the simulation results. Measurements show an input reflection coefficient below -10 dB which ranges from 68 GHz to 74 GHz. The measured radiation patterns suit adequately the defined ones in the design stage. Moreover, gain above 19 dBi in the entire operating frequency band is achieved with a 74.1% mean antenna efficiency.**

***Index Terms*—Aperture antenna array, gap-waveguide technology, millimeter-wave, stereolithography (SLA).**

I. Introduction

Millimeter-wave bands are promising frequency ranges for future communication systems [1]. Antennas at these frequencies provide high directivity to compensate free space propagation losses. However, the manufacturing of millimeter-wave antennas is challenging since high accuracy and perfect assembly are needed. Recently, gap-waveguide technology has arisen as a solution for accomplishing the latter conditions with low-loss performance and low manufacturing cost [2]. Several slotted arrays based on gap-waveguide technology have been reported [3]- [6]. In them, the use of pin lattice-based metasurface structures is introduced to define the guiding structures of the array [10], [11]. However, the increase of frequency at the millimeter-wave bands forces the pin structures to become smaller and hard to be manufactured.

Manuscript received XXXXXX XX, 2019; accepted XXXXX XX, 2020. This work was supported in part by the Spanish Program of Research, Developmentand Innovation under Project TIN2016-75097-P, Project RTI2018-102002-A-I00 and, Project EQC2018-004988-P, in part by "Junta de Andalucía" under Project B-TIC-402-UGR18 and Project P18.RT.4830 and in part by the predoctoral grant FPU18/01965. *(Corresponding author: Ángel Palomares-Caballero.)*

Á. Palomares-Caballero, A. Alex-Amor, J. Valenzuela-Valdés and P. Padilla are with the Department of Signal Theory, Telematics and Communications, Universidad de Granada, 18071 Granada, Spain (e-mail: angelpc@ugr.es; aalex@ugr.es; juanvalenzuela@ugr.es; pablopadilla@ugr.es).

A. Alex-Amor is with the Information Processing and Telecommunications Center, Universidad Politécnica de Madrid, 28040 Madrid, Spain (e-mail: aalex@gr.ssr.upm.es).

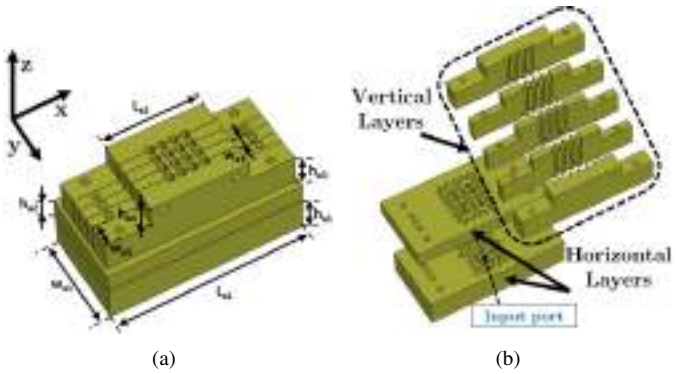

(a) (b)

Fig. 1. Multilayer aperture antenna array in millimeter-wave band: (a) Assembled array view, and (b) The different layers that conform it. Dimensions: L_{a1} = 60 mm, L_{a2} = 30 mm, w_{a1} = 30 mm, w_{a2} = 6.9 mm, w_{a3} = 3.49 mm, h_{a1} = 11.25 mm, h_{a2} = 6.35 mm, h_{a3} = 10 mm, h_{a4} = 6.37 mm.

Gap-waveguide technology based on glide-symmetric holes presents an advantage in regard to pin structure manufacturing at such frequencies [12]. A variety of guiding, filtering and phase shifting structures have been designed using this type of gap waveguide technology [13]- [16] with high performance in terms of propagation losses and cost-effective fabrication. However, only [17] presents an antenna design based on this novel gap-waveguide technology.

All the previous works have been manufactured with metallic milling, which leads to a higher cost compared to incoming 3D printing techniques. Specifically, the 3D printing technique based on stereolithography (SLA) is an adequate candidate for manufacturing high-precision and low-weight prototypes at millimeter-wave bands [18], [19]. Some works make use of this manufacturing technique to design high-frequency arrays [20]- [22]. A subsequent metallic plating stage is needed after SLA manufacturing. Another attractive 3D printing technique is direct metal laser sintering (DMLS). Antenna arrays in [23]- [25] apply this manufacturing technique. The principal disadvantage of DMLS is the surface roughness that is not negligible and produces high losses at upper bands of the millimeter-wave frequency range.

In this document, we present an aperture antenna array based on glide-symmetric gap-waveguide technology centered at 70 GHz. The operating frequency band ranges from 66 to 74 GHz. This range covers both access and backhaul millimeter-wave applications for 5G [26]. It is included in a band of interest for 5G above the WiGig (Wireless Gigabit Alliance) frequency band targets to high speed indoor applications. This

wide 5G frequency band for millimeter-wave is composed by two bands. The first frequency band, ranging from 66 to 71 GHz, is addressed to the radio access network for 5G connections since the propagation losses at this frequency band is lower than its adjacent band (57-66 GHz). The second band, ranging from 71-76 GHz, is intended to support fixed high-speed connection for different applications such as macro or micro cell backhaul links, and front haul connection between a base station and theirs remote radio heads to extend the coverage area.

The design consists on a multilayer design composed by means of stacking horizontal and vertical layers, as shown in Fig. 1. The vertical and horizontal layer gaps are located in the E-plane and the H-plane of the gap-waveguide elements, respectively. Layers with the gap in the H-plane need the gap-waveguide technology to avoid field leakage throughout the gap in millimeter-wave frequencies. Four 2x2 aperture antenna subarrays conform the radiating part that is fed by a corporate feeding network. A fully-functional prototype has been manufactured in SLA with subsequent copper plating, and conveniently measured for its validation. The relevance and novelty of our work is based on two main aspects. First, we propose a novel design antenna array that uses holey glide-symmetric gap-waveguide and E-plane waveguide structure to reduce the propagation losses in a multilayer array design. In our work, we propose a feasible multilayer design array with a combination between the traditionally used split H-plane waveguide structures with glide symmetric holes, and split E-plane waveguide structures that does not require such elements. Secondly, we demostrate the potential use of SLA to fabricate multilayer array design at millimeter-wave frequencies. Although multilayer array prototoypes based on gap-waveguide technology are commonly manufactured in CNC because of higher accuracy compared to traditional 3-D printing techniques, with the appearance of SLA technique, a high-precision and cost-efective fabrication is possible [19]. The document is organized as follows. Section II depicts the principal elements that constitutes the antenna array design. In this section gap-waveguide technology selected, the corporate feeding network and the subarrays are conveniently described and simulated. Section III provides the measurements of the manufactured prototype and the discussion of the results. Finally, the conclusions are detailed in Section IV.

II. Antenna Array Design

The antenna array design is formed by two horizontal layers and five vertical layers. All of them are stacked and not welded but assembled with mechanical pressure by screws. Thus, in the array assembling, there are inevitably gaps between layers of at least some tens of microns. Therefore, the gap-waveguide technology and E-plane configurations are adopted to avoid any field leakage due to the layer gaps. Note that gaps are considered between all stacked layers in the design process.

A. Glide-symmetric Holey Gap-waveguide Technology

Gap-waveguide technology based on glide-symmetric holes provides a wide stopband in a cost-effective way [13]. The

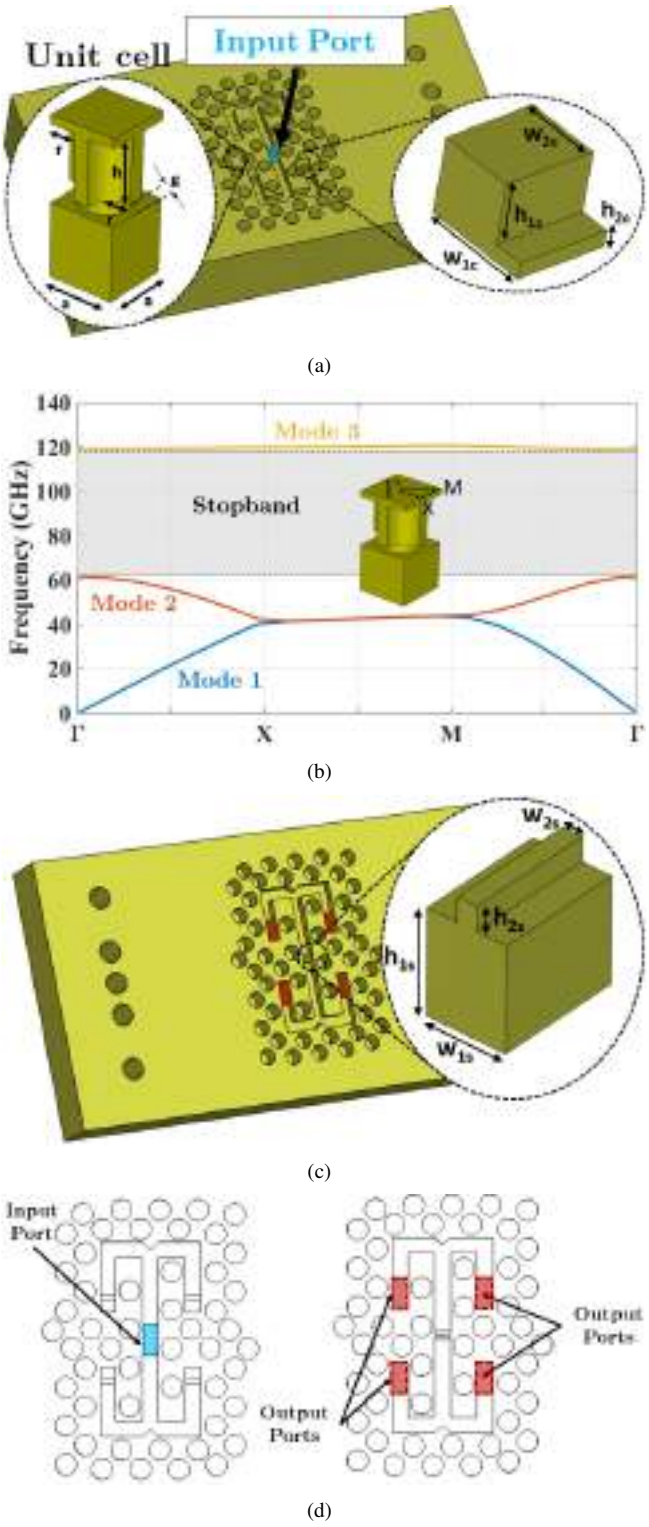

Fig. 2. Design of the corporate feeding network: (a) Bottom part (1st horizontal layer), w_{1c} = 1.4mm, h_{1c} = 0.75 mm, w_{2c} = 1mm, h_{2c} = 0.2 mm; (b) Dispersion diagram of the employed EBG unit cell; (c) Upper part (2nd horizontal layer), w_{1s} = 0.85 mm, h_{1s} = 1 mm, w_{2s} = 0.25 mm, h_{2s} = 0.2 mm; and, (d) Planar views of bottom and upper parts.

electromagnetic bandgap (EBG) unit cell is shown in Fig. 2(a). The dimensions used for our simulated EBG structure are: a = 2.26 mm, r = 0.88 mm, h = 2.2 mm and g = 0.03 mm. The considered gap size is in the range of reported multi-

layer antennas at millimeter-wave frequencies. The provided stopband of the EBG unit cell ranges from 62 GHz to 118 GHz as it is shown in Fig. 2(b). The unit cell dimensions are chosen in such a way that they fit inside the corporate feeding network and at the same time the stopband is included in the target operating frequency band (66-74 GHz). This is why the lowest frequency limit of the stopband is close to the start operating frequency.

B. 1-to-4 Corporate Feeding Network

Figs. 2(a), 2(c) and 2(d) show the two halves that form the corporate feeding network both in 3D and planar views. The waveguides that compose this design and the feeding port (input port) have WR-10 waveguide dimensions. The input port is located at the bottom of the first horizontal layer, as shown in Fig. 2(a) and Fig. 2(d). Each horizontal layer of the feeding network occupies half of the width of the waveguides. When the layers are stacked, they form a feeding network with split E-plane waveguides. The gap between layers is preserved in the middle of the wider side of the waveguide (E-plane) except in the H-plane divider located next the input port and in the 90º bends before the output ports. Because there are locations in the feeding network where the gap is not kept in the E-plane, glide-symmetric holey gap-waveguide is implemented between layers. The feeding network distributes in-phase and equally the input power among the output ports (highlighted in red). These ports connect the feeding network with the four subarrays. The matching elements in the power dividers and the 90º bends are shown in detail in Figs. 2(a), 2(c) and 2(d).

The simulated performance of the feeding network design is illustrated in Fig. 3. The reflection coefficient is maintained below -10 dB from 66 GHz to 74 GHz, with an approximately balanced and in-phase transmission coefficients. The maximum amplitude and phase variations are 1 dB and 1.8º, respectively. Although the feeding network has E-plane power dividers, the in-phase output fields are obtained due to the presence of E-plane bends before the output ports.

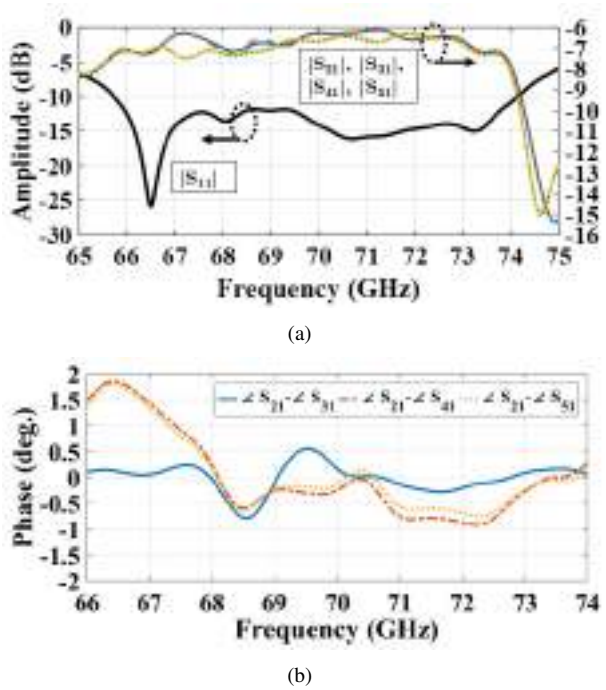

(a)

(b)

Fig. 3. Performance of the corporate feeding network: (a) Amplitude of the S-parameter simulated results, (b) Phase imbalance between the output ports.

C. 2x2 Aperture Antenna Subarray

The configuration of the 2x2 aperture antenna subarrays is shown in Figs. 4(a) and 4(b). The power division from the output ports of the corporate feeding network to the aperture antennas is carried out by H-plane and E-plane power dividers as they are illustrated in Fig. 4(c). The H-plane power divider is located at the joint between the second horizontal layer and the vertical layers and just above the output ports of the feeding network. This fact is observed on the left part of Fig. 4(c). E-plane power dividers are implemented before the antenna apertures as it is illustrated on the right part of Fig. 4(c). These power dividers design are formed by stacking the vertical layers in the horizontal direction as it is shown in Figs. 4(a) and 4(b). This stack of layers does not need any gap-waveguide technology since the gap is preserved in the E-plane location of the waveguide belonging to subarray antenna design. Absence of leakage is only produced by split E-plane waveguides because it does not exist disruption of the surface currents. The array antennas are E-plane aperture antennas with a separation between them of $0.87\lambda_0$ in x and y directions, where λ_0 is the free-space wavelength at 74 GHz.

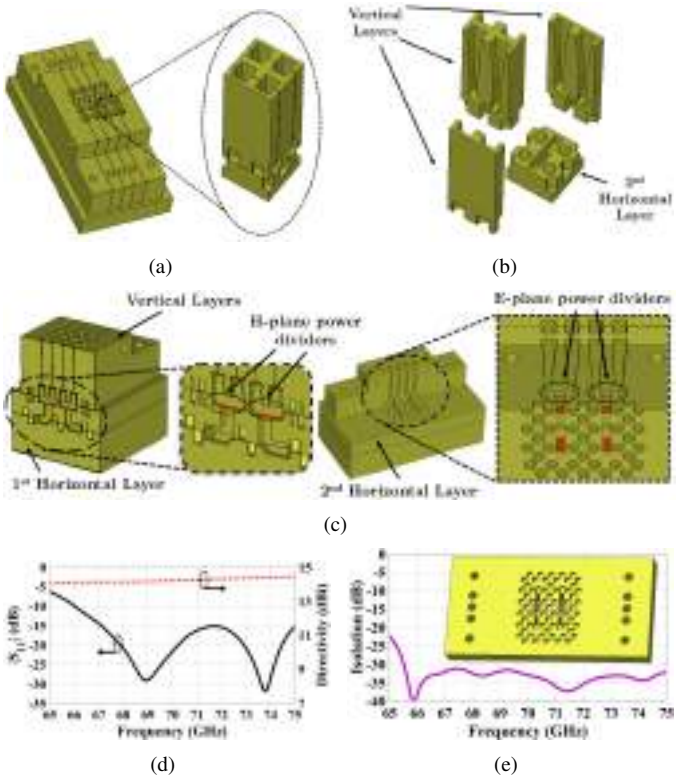

(a) (b) (c) (d) (e)

Fig. 4. Subarray: (a) Assembled view, (b) Exploded view, (c) E-plane and H-plane power dividers locations, (d) Simulated reflection coefficient and directivity, and (e) Simulated isolation level between subarrays.

The simulation results in periodic conditions for the subarray design are illustrated in Fig. 4(d). An impedance matching under -10 dB is obtained in the complete operating frequency range with a stable directivity in frequency of 14 dBi.

Glide-symmetric EBG holes are also necessary between the upper part of the second horizontal layer and the bottom part of each vertical layer. This need is due to the existing gap that surrounds the H-plane power dividers. However, there are areas where holes cannot be placed, as Fig. 4(e) shows highlighted. Despite that, more than 30 dB of isolation level between subarrays is achieved in the entire frequency range. Fig. 5 illustrates an E-field comparison between the antenna array design with and without the implementation of the gap-waveguide technology. The electric field at different frequencies inside the gap between the first and the second horizontal layers for both designs, with gap-waveguide and without gap-waveguide technology, are shown in Figs. 5(c) and 5(d), respectively. Gap size corresponding to the EBG unit cell has been introduced between layers in both antenna designs for a fair comparison. It is clearly seen the importance of the glide-symmetric holes to not produce leakage and thus, loss in antenna efficiency as illustrated in Fig. 5(e).

D. Details of the gap-waveguide performance and field confinement

For the sake of completeness, two cases of study have been carried out for the selected EBG unit cell and waveguide dimensions. They demonstrate the beneficial use of this gap-waveguide technology when a split waveguide is designed. It is important to note that the structures with and without gap-waveguide have the same gap of 30 μm. The first comparison is shown in Fig. 6 between a E-plane split waveguide with the use of gap-waveguide technology (marked in red) and without gap-waveguide technology (marked in blue). In this case the gap is in the ZY plane and it is displaced from the center of the wide side of the waveguide since if the gap is located at the center, no leakage occurs. The S-parameters are illustrated in Fig. 6(b). A drop of the transmission coefficient is observed in the design without gap-waveguide. In Fig. 6(c) the electric fields reveal the absence of leakage when holey EBG structures are employed. Conversely, field resonances appear in the gap region due to the leakage provoked by the absence of EBG holes (case without gap waveguide). Note that the electric field in this figure is represented in absolute value in order to observe the electric field in the waveguide (oriented along z direction) and in the gap (oriented along x direction since it is a parallel-plate mode). The second comparison corresponds to the H-plane bend implemented in the proposed array before the outputs of the feeding network (Fig. 4(c)). The gap is in the ZY plane as it is observed in Fig. 7(a). The transmission coefficient for the case in which the gap-waveguide technology is not used (Fig. 7(b)) suffers a drop in the transmission coefficient which does not occur for the case with gap-waveguide technology. In addition, Fig. 7(c) confirms these losses and the existence of leakage when the gap-waveguide technology is not employed. Since the proposed array has zones where the gap is not located in the center of the wide side of the waveguide,

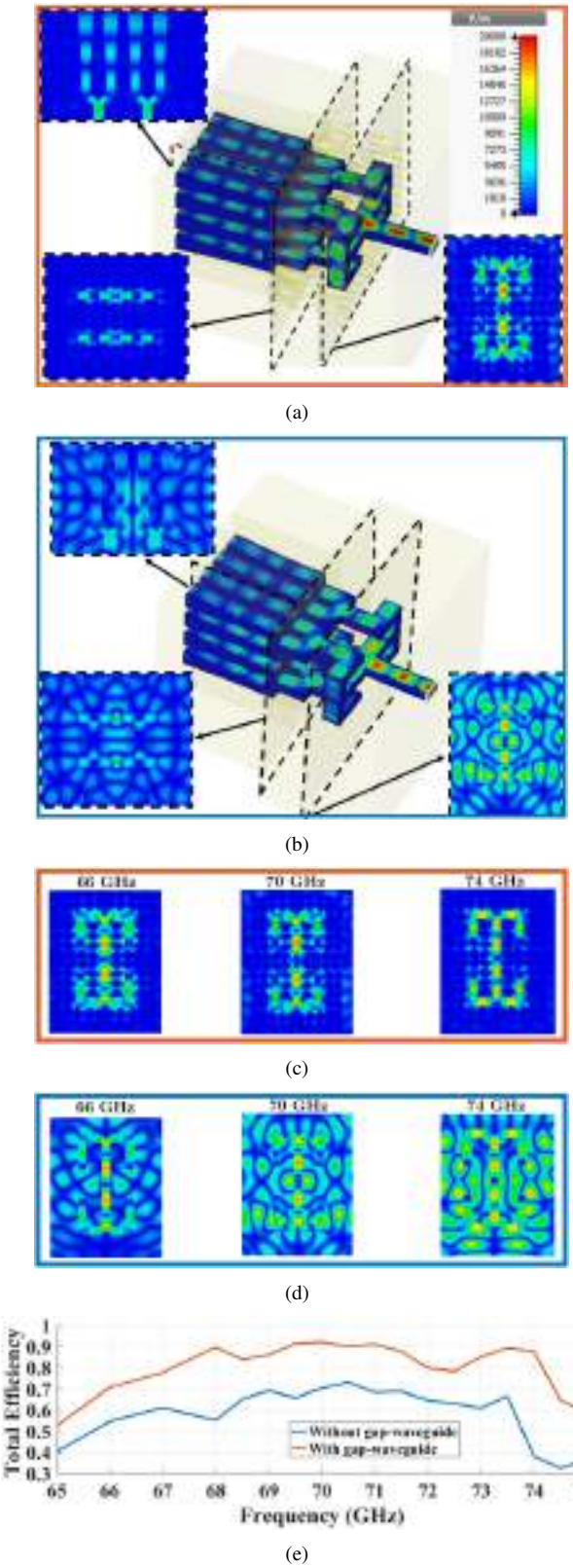

(a) (b) (c) (d) (e)

Fig. 5. Simulated E-field distribution inside the antenna array and between layers at 70 GHz: (a) With gap-waveguide and, (b) Without gap-waveguide. Electric field at different frequencies in the gap between horizontal layers of the antenna array for: (c) The design with gap-waveguide technology and, (d) The design without gap-waveguide technology. (e) Total antenna efficiency comparison.

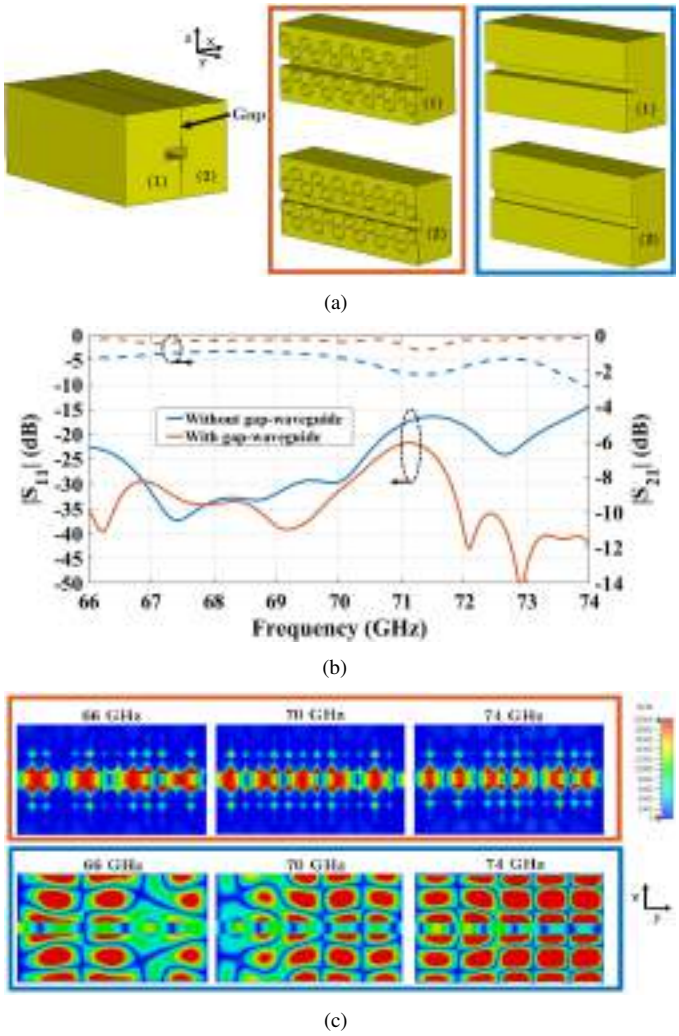

(a)

(b)

(c)

Fig. 6. Performance comparison between a E-plane split waveguide with gap-waveguide and without gap-waveguide: (a) Design and forming layers, (b) Simulated S-parameters and, (c) Electric field at different frequencies in the gap.

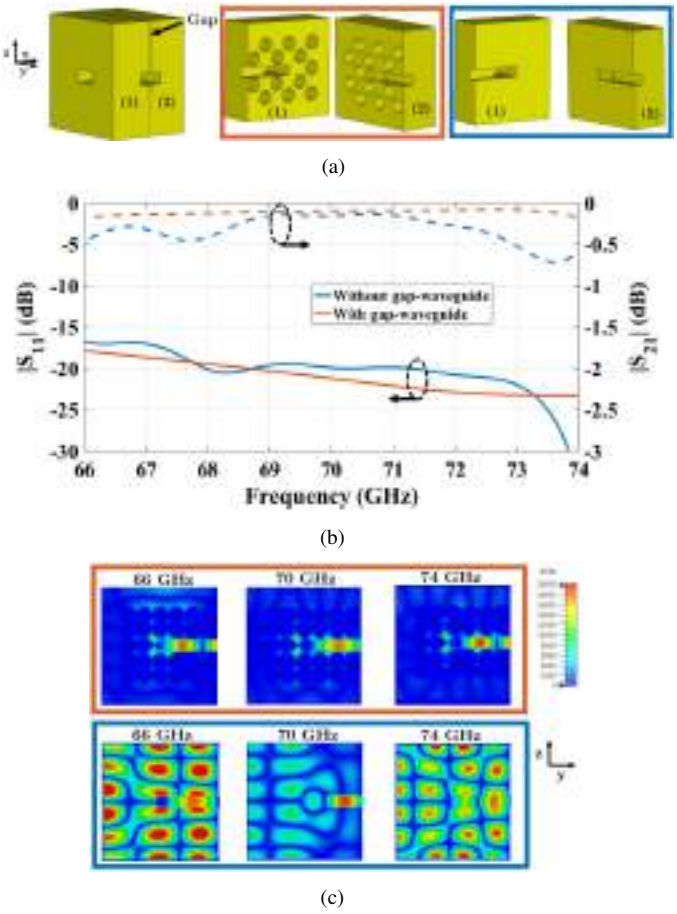

(a)

(b)

(c)

Fig. 7. Performance comparison between a H-plane bend waveguide with gap-waveguide and without gap-waveguide: (a) Design and forming layers, (b) Simulated S-parameters and, (c) Electric field at different frequencies in the gap.

the application of gap-waveguide technology is mandatory to avoid leakage throughout the gap.

III. Manufacturing, Measurements and Discussion

High-precision SLA with a posterior copper plating stage was the selected manufacturing technique due to its low cost compared to milling fabrication. The used plastic material and type of plating for the fabrication are Accura Xtreme White [27] and electroplating, respectively. Fig. 8 shows different views of the fabricated antenna array. The antenna is composed by 7 different forming layers to guarantee a proper metal plating. Detail view on the manufactured parts of the antenna array is shown in Fig. 8(c). Good geometry definitions are observed under the microscope. An extension of the size of the antenna array was needed to place the holes of the assembling screws which in spite of their size do not affect the radiation pattern measurements. Moreover, the first horizontal layer was thicken in order to allow the screwed connection with the waveguide flange. The dimensions of the antenna array design without the assembling parts are 15.8 x 23.35 x 22.8 mm. The reflection coefficient was measured with R&S ZVA-Z110E Converters from 65 GHz to 75 GHz. Fine sampling has been applied to reveal any possible glitch caused by poor contact between forming layers. The measurement is compared to the simulation results in Fig. 9. The measured reflection coefficient presents a shift in the lowest frequency of the operating band, from 66 GHz to 68 GHz, preserving the rest of the operating band below -10 dB. To determine the cause of the $|S_{11}|$ modification with respect to the simulated one, a variation analysis based on the manufacturing tolerances is carried out. An assembly tolerance that taking into account the misalignment between forming layers of the feeding network is also introduced in the variation analysis. This tolerance has been selected since it is the antenna array part where there are more zones with the gap not placed in the E-plane of the waveguide. The variation analysis shows that the measurement result is included in the variability range. The antenna simulation with tolerances which best fits the measurement result is highlighted in Fig. 9. The tolerances for this case are: tol_{XY} = +30 μm, tol_{Z} = +55 μm and Δ_{xy} = 50 μm, which correspond to tolerance in XY plane, tolerance in z direction and misalignment between layers, respectively.

Once the $|S_{11}|$ of the array is measured and discussed, the radiation patterns of the antenna array are measured,

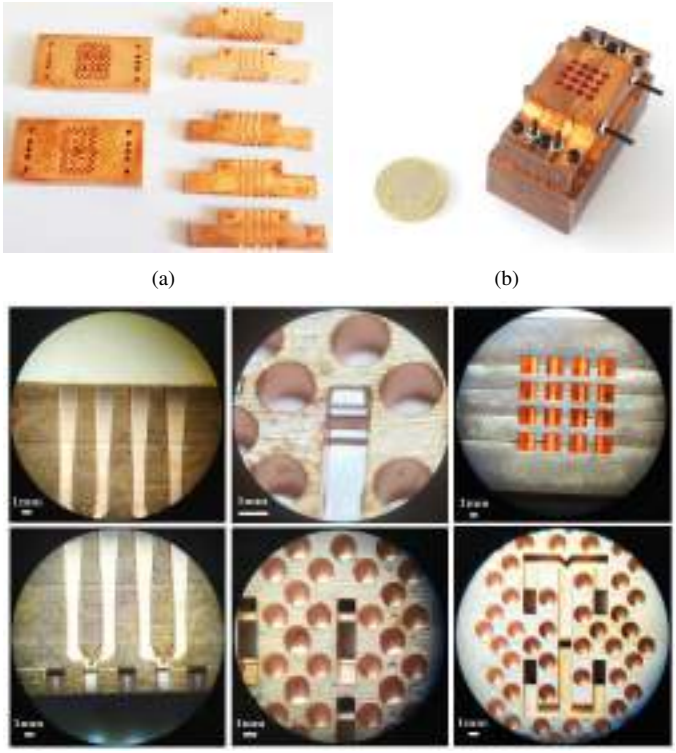

(a) (b)

(c)

Fig. 8. Manufactured prototype: (a) Forming layers, (b) Stacked antenna array, and (c) Details under microscope.

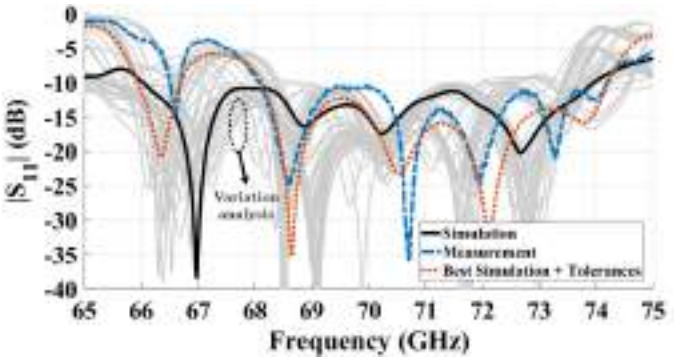

Fig. 9. Comparison of the simulated, simulated with manufacturing tolerances and measured reflection coefficient of the fabricated antenna array. Black line represents the nominal simulation and grey lines show the effect of manufacturing tolerances over the nominal simulation.

for the lowest, center and highest frequency values of the operating band. Those measurements have been carried out at the millimeter-wave antenna measuring facilities of the University of Granada. Fig. 10 depicts the radiation measurement setup. Laser alignment has been used in order to improve the accuracy of the alignment between the probe antenna and the antenna array. The E-plane and H-plane copolar and crosspolar measurements are provided in Fig. 11. The measured radiation patterns and their corresponding simulated values are in good agreement, keeping the beamwidth of the principal lobe and levels for the side lobes below -12 dB for all radiation cuts. Crosspolar levels remain under -22 dB. Fig.

Fig. 10. Detail of the measurement setup at the millimeter-wave antenna measuring facilities of the University of Granada.

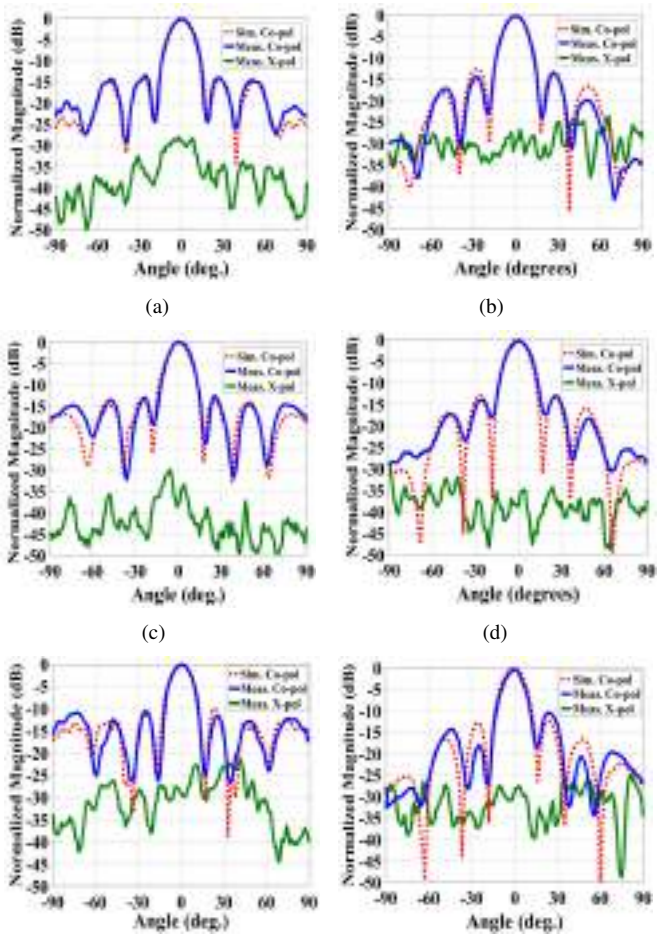

(a) (b)

(c) (d)

(e) (f)

Fig. 11. Simulated and measured E-plane radiation patterns of the proposed antenna array at different frequencies: (a) 68 GHz, (c) 71 GHz, and (e) 74 GHz. Simulated and measured H-plane radiation patterns of the proposed antenna array at different frequencies: (b) 68 GHz, (d) 71 GHz, and (f) 74 GHz. The simulations include the fastening screws.

12 shows the directivity, gain and antenna efficiency values of the antenna array for its entire operating frequency range. For a fair comparison, simulation results correspond to the antenna array with tolerances that best fits the measurements. The measured gain is approximately 20 dBi in the entire frequency range, except above 73 GHz, where it drops. Also, the antenna efficiency mean value is 74.1% that confirms the

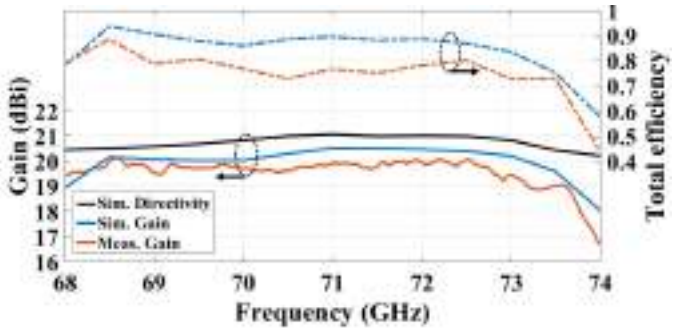

Fig. 12. Radiation performance of proposed antenna array over the operating frequency bandwidth.

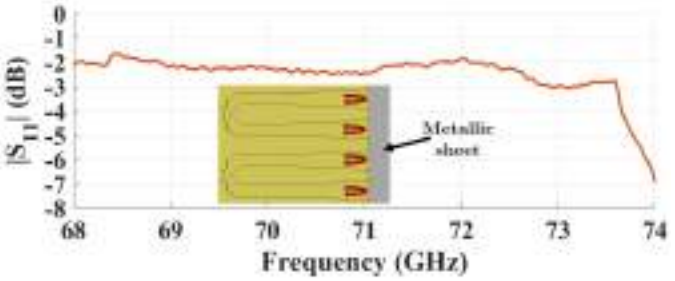

Fig. 13. Measured reflection coefficient when the aperture is short-circuited. This value is twice (round trip) the sum of the ohmic and leakage losses.

correct consideration of the gap value for the EBG unit cell.

In order to verify the existence of leakage in the upper frequency range of the antenna array two kind of measurements are carried out. First one consists of measuring the reflection coefficient of the antenna array when the antennas are short-circuited [28]. This measurement contains twice the insertion losses provided by the fabricated antenna array. Fig. 13 provides the measurement result when the antenna array is short-circuited by a metallic sheet. It is observed that in the high frequency zone part of the operating band, the reflection coefficient value decreases. The estimated losses of the frequency zone where the gain drops are caused by leakage, since the antenna losses in the rest of the band are mainly due to ohmic losses. A maximum of 1 dB of simulated ohmic losses is obtained for non-ideal copper conductivities. The second measurement to check the presence of leakage is based on 2D far-field radiation patterns. The measurements are illustrated in Fig. 14. They reveal the existence of unwanted radiation from 73 GHz which coincides with the drop in the measured gains. This decrease in gain may be provoked by the imperfect alignment between horizontal layers (Δ_{xy}) in the assembly procedure. This parameter is of great importance in the performance of the glide-symmetric holey structures because it affects the stopband of gap waveguide [15]. Since there is a misalignment for the simulation which best fits the measurement, the observed leakage can be explained.

The proposed antenna array is compared with other millimeter-wave antenna arrays in Table I. Same level of antenna gain and efficiency is achieved in this work compared to the state-of-the-art works. The main advantages of our antenna array design are its lower cost, weight and complexity

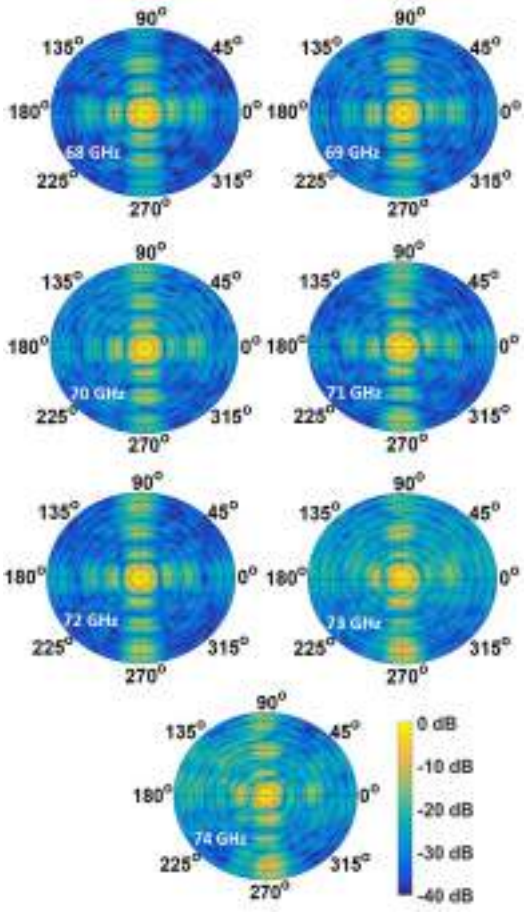

Fig. 14. 2-D far-field radiation pattern of the proposed antenna array at different frequencies.

provided by SLA manufacturing with the combined used of glide-symmetric holey gap-waveguide and split E-plane waveguide structures in a multilayer array antenna. In comparison, CNC milling designs suffer from higher manufacturing complexity than the 3D-printing ones leading to increase the prototype cost. Therefore, this prototype provides an insight of a low-cost and robust solution for multilayer millimeter-wave antenna array designs with gap-waveguide technology.

IV. CONCLUSIONS

In this work, we have proposed an aperture antenna array design based on gap-waveguide technology and manufactured with high-precision stereolithography process with latter metallic plating. The novel gap-waveguide technology based on glide-symmetric holey structures in combination with split E-plane waveguide enables a multilayer antenna array design for 3-D printed manufacturing. A prototype of the complete 4x4 aperture antenna array has been manufactured and measured. To best of the authors' knowledge, the antenna array proposed in this paper is the first multilayer gap-waveguide array manufactured by SLA and metal plating with good radiation performance at 70 GHz.

TABLE I
COMPARISON BETWEEN PROPOSED AND REFERRED MILLIMETER-WAVE ANTENNA ARRAYS

Ref.	Frequency Band (GHz)	Bandwidth	Fabrication Technique	Max. Gain (dBi)	Antenna Efficiency	Scale	Cost
[3]	57-65	13.1%	CNC	26	60%-80%	8x8	Medium
[7]	50-67.8	30.2%	CNC	27.5	80%-90%	8x8	Medium
[8]	56.5-67	17%	CNC	27	70%-85%	8x8	Medium
[9]	55.5-67	18.8%	CNC	32.5	80%-90%	16x16	Medium
[21]	78.5-79	0.6%	SLA	22.5	n.a	10x10	Low
[24]	28-36	25%	DMLS	27.5	90%	8x8	Low
[29]	72-85	16.5%	CNC	19.91	n.a	4x4	Medium
This work	68-74	8.5%	SLA	20.02	71%-89%	4x4	Low

REFERENCES

[1] Y. Li, E. Pateromichelakis, N. Vucic, J. Luo, W. Xu and G. Caire, "Radio Resource Management Considerations for 5G Millimeter Wave Backhaul and Access Networks," *IEEE Commun. Mag.*, vol. 55, no. 6, pp. 86-92, June 2017.

[2] E. Rajo-Iglesias, M. Ferrando-Rocher and A. U. Zaman, "Gap Waveguide Technology for Millimeter-Wave Antenna Systems," *IEEE Commun. Mag.*, vol. 56, no. 7, pp. 14-20, July 2018.

[3] A. Vosoogh and P. Kildal, "Corporate-Fed Planar 60-GHz Slot Array Made of Three Unconnected Metal Layers Using AMC Pin Surface for the Gap Waveguide," *IEEE Antennas Wirel. Propag. Lett.*, vol. 15, pp. 1935-1938, 2016.

[4] D. Zarifi, A. Farahbakhsh, A. U. Zaman and P. Kildal, "Design and Fabrication of a High-Gain 60-GHz Corrugated Slot Antenna Array With Ridge Gap Waveguide Distribution Layer," *IEEE Trans. Antennas Propag.*, vol. 64, no. 7, pp. 2905-2913, July 2016.

[5] A. Vosoogh, P. Kildal and V. Vassilev, "Wideband and High-Gain Corporate-Fed Gap Waveguide Slot Array Antenna With ETSI Class II Radiation Pattern in V-Band," *IEEE Trans. Antennas Propag.*, vol. 65, no. 4, pp. 1823-1831, April 2017.

[6] A. Jiménez Sáez, A. Valero-Nogueira, J. I. Herranz and B. Bernardo, "Single-Layer Cavity-Backed Slot Array Fed by Groove Gap Waveguide," *IEEE Antennas Wirel. Propag. Lett.*, vol. 15, pp. 1402-1405, 2016.

[7] A. Farahbakhsh, D. Zarifi and A. U. Zaman, "A mmWave Wideband Slot Array Antenna Based on Ridge Gap Waveguide With 30% Bandwidth," *IEEE Trans. Antennas Propag.*, vol. 66, no. 2, pp. 1008-1013, Feb. 2018.

[8] J. Liu, A. Vosoogh, A. U. Zaman and J. Yang, "A Slot Array Antenna With Single-Layered Corporate-Feed Based on Ridge Gap Waveguide in the 60 GHz Band," *IEEE Trans. Antennas Propag.*, vol. 67, no. 3, pp. 1650-1658, March 2019.

[9] A. Farahbakhsh, D. Zarifi and A. U. Zaman, "60-GHz Groove Gap Waveguide Based Wideband H-Plane Power Dividers and Transitions: For Use in High-Gain Slot Array Antenna," *IEEE Trans. Microw. Theory Tech.*, vol. 65, no. 11, pp. 4111-4121, Nov. 2017.

[10] P. Kildal, E. Alfonso, A. Valero-Nogueira and E. Rajo-Iglesias, "Local Metamaterial-Based Waveguides in Gaps Between Parallel Metal Plates," *IEEE Antennas Wirel. Propag. Lett.*, vol. 8, pp. 84-87, 2009.

[11] A. Berenguer, V. Fusco, D. E. Zelenchuk, D. Sánchez-Escuderos, M. Baquero-Escudero and V. E. Boria-Esbert, "Propagation Characteristics of Groove Gap Waveguide Below and Above Cutoff," *IEEE Trans. Microw. Theory Tech.*, vol. 64, no. 1, pp. 27-36, Jan. 2016.

[12] M. Ebrahimpouri, O. Quevedo-Teruel and E. Rajo-Iglesias, "Design Guidelines for Gap Waveguide Technology Based on Glide-Symmetric Holey Structures," *IEEE Microw. Wirel. Compon. Lett.*, vol. 27, no. 6, pp. 542-544, June 2017.

[13] M. Ebrahimpouri, E. Rajo-Iglesias, Z. Sipus and O. Quevedo-Teruel, "Cost-Effective Gap Waveguide Technology Based on Glide-Symmetric Holey EBG Structures," *IEEE Trans. Microw. Theory Tech.*, vol. 66, no. 2, pp. 927-934, Feb. 2018.

[14] Á. Palomares-Caballero, A. Alex-Amor, P. Padilla, F. Luna and J. Valenzuela-Valdés, "Compact and Low-Loss V-Band Waveguide Phase Shifter Based on Glide-Symmetric Pin Configuration," in *IEEE Access*, vol. 7, pp. 31297-31304, 2019.

[15] P. Padilla, Á. Palomares-Caballero, A. Alex-Amor, J. Valenzuela-Valdés, J. M. Fernandez-González and O. Quevedo-Teruel, "Broken Glide-Symmetric Holey Structures for Bandgap Selection in Gap-Waveguide Technology," *IEEE Microw. Wirel. Compon. Lett.*, vol. 29, no. 5, pp. 327-329, May 2019.

[16] E. Rajo-Iglesias, M. Ebrahimpouri and O. Quevedo-Teruel, "Wideband Phase Shifter in Groove Gap Waveguide Technology Implemented With Glide-Symmetric Holey EBG," *IEEE Microw. Wirel. Compon. Lett.*, vol. 28, no. 6, pp. 476-478, June 2018.

[17] Q. Liao, E. Rajo-Iglesias and O. Quevedo-Teruel, "Ka -Band Fully Metallic TE40 Slot Array Antenna With Glide-Symmetric Gap Waveguide Technology," *IEEE Trans. Antennas Propag.*, vol. 67, no. 10, pp. 6410-6418, Oct. 2019.

[18] A. Tamayo-Domínguez, J. Fernández-González and M. Sierra-Pérez, "Groove Gap Waveguide in 3-D Printed Technology for Low Loss, Weight, and Cost Distribution Networks," *IEEE Trans. Microw. Theory Tech.*, vol. 65, no. 11, pp. 4138-4147, Nov. 2017.

[19] A. I. Dimitriadis *et al.*, "Polymer-Based Additive Manufacturing of High-Performance Waveguide and Antenna Components," *Proc. IEEE*, vol. 105, no. 4, pp. 668-676, April 2017.

[20] G. P. Le Sage, "3D Printed Waveguide Slot Array Antennas," *IEEE Access*, vol. 4, pp. 1258-1265, 2016.

[21] J. Tak, A. Kantemur, Y. Sharma and H. Xin, "A 3-D-Printed W-Band Slotted Waveguide Array Antenna Optimized Using Machine Learning," *IEEE Antennas Wirel. Propag. Lett.*, vol. 17, no. 11, pp. 2008-2012, Nov. 2018.

[22] M. García-Vigueras, E. Menargues, T. Debogovic, E. de Rijk and J. R. Mosig, "Cost-effective dual-polarised leaky-wave antennas enabled by three-dimensional printing," *IET Microw. Antennas Propag.*, vol. 11, no. 14, pp. 1985-1991, 19 11 2017.

[23] E. García-Marín, J. L. Masa-Campos, P. Sánchez-Olivares and J. A. Ruiz-Cruz, "Evaluation of Additive Manufacturing Techniques Applied to Ku-Band Multilayer Corporate Waveguide Antennas," *IEEE Antennas Wirel. Propag. Lett.*, vol. 17, no. 11, pp. 2114-2118, Nov. 2018.

[24] Y. Li *et al*., "3-D Printed High-Gain Wideband Waveguide Fed Horn Antenna Arrays for Millimeter-Wave Applications," *IEEE Trans. Antennas Propag.*, vol. 67, no. 5, pp. 2868-2877, May 2019.

[25] G. Huang, S. Zhou, T. Chio and T. Yeo, "Fabrication of a High-Efficiency Waveguide Antenna Array via Direct Metal Laser Sintering," *IEEE Antennas Wirel. Propag. Lett.*, vol. 15, pp. 622-625, 2016.

[26] G. Varrall, *5G Spectrum and Standards*. Artech House, 2nd Edition, 2016.

[27] 3DSYSTEMS, "Accura Xtreme White 200", 2015. Available: https://www.3dsystems.com/sites/default/files/accura-xtreme-white-200-usen.pdf

[28] A. Gomez-Torrent, U. Shah and J. Oberhammer, "Wideband 220 – 330 GHz Turnstile OMT Enabled by Silicon Micromachining," in *2018 IEEE/MTT-S International Microwave Symposium - IMS*, Philadelphia, PA, 2018, pp. 1511-1514.

[29] B. Gao, Y. Ren, H. Wu, X. Liao, K. Li and F. Wang, "A Novel Corporate-Feed Horn Sub-Array Antenna for the 77 GHz-Band," *IEEE Access*, vol. 6, pp. 37166-37172, 2018.

Ángel Palomares-Caballero was born in Jaén, Spain, in 1994. He received the B.Sc. and M.Sc.degrees in telecommunication engineering from the University of Granada (UGR), Granada, Spain, in 2016 and 2018, respectively. Since 2017, he has been with the Signal Theory, Telematics and Communications Department, University of Granada, where he is currently a Ph.D.student with a national Predoctoral Fellowship. His current research interests include millimeter-wave antennas and phase shifters, gap-waveguide technology, and structures with higher symmetries.

Antonio Alex-Amor received the B.Sc. degree in telecommunication engineering from Universidad de Granada, in 2016, and the M.Sc. degree in telecommunication engineering from Universidad Politécnica de Madrid (UPM), in 2018, where he is currently pursuing the Ph.D. degree. Since 2016, he has been with the Radiation Group, Signal, Systems and Radiocommunications Department, UPM. From 2018-2019, he joined the Department of Language and Computer Science, Universidad de Málaga. In 2020, he joined the Signal Theory, Telematics and Communications Department, University of Granada. He received the Best Electromagnetics Paper Award at the 14th European Conference on Antennas and Propagation (EuCAP 2020). His current research interests include the use of liquid crystal as tunable dielectric, metamaterials, structures with higher symmetries and radiofrequency energy harvesting systems.

Juan Valenzuela-Valdés was born in Marbella, Spain. He received the degree in telecommunications engineering from the Universidad de Malaga, Spain, in 2003, and the Ph.D. degree from the Universidad Politécnica de Cartagena, Spain, in 2008, where he joined the Department of Information Technologies and Communications, in 2004. In 2007, he joined EMITE Ing. as the Head of research. In 2011, he joined the Universidad de Extremadura, and in 2015, he joined the Universidad de Granada, where he is currently an Associate Professor. He has also received several prizes, including a National Prize to the Best Ph.D. in Mobile Communications by Vodafone. He also holds several national and international patents. His publication record comprised of more than 100 publications, including 50 JCR indexed articles and seven book chapters. (Updated March 2019). His current research interests include wireless communications, radiofrequency devices, antennas and propagation. He is the head of SWAT research group (https://swat.ugr.es/) at the University of Granada and cohead of Singular Laboratory of Electromagnetic characterization of microwave and millimeter devices and antennas.

Pablo Padilla was born in Jaén, Spain, in 1982. He received the Telecommunication Engineering degree and the Ph.D. degree from the Radiation Group (Signal, Systems and Radiocommunications Department) of the Technical University of Madrid (UPM), Spain, in 2005 and 2009, respectively. In 2007, he was with the Laboratory of Electromagnetics and Acoustics, École Polytechnique Fédérale de Lausanne, Switzerland, as an invited Ph.D. Student. In 2009, he carried out a Postdoctoral stay at the Helsinki University of Technology (AALTO-TKK). In 2009, he became Assistant Professor at the Signal Theory, Telematics and Communications Department of the University of Granada, where he is currently Associate Professor, since 2012. In 2017, he was an invited Visiting Professor at the Royal Institute of Technology of Stockholm. He has authored more than 65 high-impact journal contributions and more than 60 contributions to international symposia. His research interests include a variety of topics related mainly to electromagnetism and communication issues (radiofrequency devices, antennas and propagation).

2.2.2 Metal-Only Reflectarray Unit Cell for Dual-Polarization Control

In this contribution to an international congress, a new design of a metal-only unit cell for reflectarray design is presented. In addition to the feature of using only metal in its structure, another feature of special attention is the phase independent control of the reflected orthogonal polarizations. The central operating frequency for the presented unit cell is set at 60 GHz but it can operate in other frequency range by a simple geometrical scaling. Also this unit cell preserves a linear performance in the reflected phase response for different situations of oblique incidence.

THIS IS A POSTPRINT VERSION OF THE PAPER:

Á. Palomares-Caballero, C. Molero, P. Padilla, M. García-Vigueras and R. Gillard, "Metal-Only Reflectarray Unit Cell for Dual-Polarization Control," in *2022 16th European Conference on Antennas and Propagation (EuCAP)*, 2022.

Disclaimer:
This work has been published on 16th European Conference on Antennas and Propagation. DOI: 10.23919/EuCAP53622.2022.9769306

Metal-Only Reflectarray Unit Cell for Dual-Polarization Control

Ángel Palomares-Caballero*†, Carlos Molero*, Pablo Padilla*, María García-Vigueras†, Raphaël Gillard†
*Departamento de Teoría de la Señal, Telemática y Comunicaciones, Universidad de Granada, 18071 Granada, Spain
†UMR CNRS 6164, INSA Rennes, IETR, 35708 Rennes, France
email: angelpc@ugr.es

***Abstract*—A metal-only reflectarray unit cell to independently control two polarizations is proposed in this paper. The unit cell is based on a nonresonant cross-shaped geometry backed by a metallic plate. Unlike previous metal-only nonresonant unit cell, the metallic arms of the proposed one are not connected to its neighboring unit cells. This fact enables the propagation of the incident wave along the longitudinal direction of the unit cell more specifically, along parallel-plate waveguides formed between unit cells. Depending on the polarization of the impinging wave, the propagation occurs in the waveguides located at vertical or horizontal directions. The simulated results for a designed unit cell at 60GHz show the independent modification of the phase response for one polarization being unaffected the phase response of orthogonal one. Moreover, phase linearity and a phase shift range over 360º are achieved along a operating frequency range with good phase stability under oblique incidence.**

***Index Terms*—Dual polarization, metal-only, millimeter-waves, polarization control, reflectarray antenna.**

I. Introduction

Reflectarray antennas have gained a lot of interest during the last years since they provide a more versatile and cost-effective design than the traditional parabolic reflectors [1]. When the frequency increases, for example, up to millimeter-wave frequencies, dielectric material in reflectarray can be a source of losses in the antenna because dielectrics with low loss tangent are hard to find at millimeter-waves. Besides, the greater the volume of dielectric used in the unit cell implementation, the greater are the dielectric losses [2], [3]. Thus, metal-only antenna designs are desired to increase the total efficiency of the reflectarrays and avoid outgassing problem for space applications.

In the literature, there exist some reflectarray designs implemented without the use of any dielectric material. The works in [4], [5] present a reflectarray design formed by metal-only unit cells. These unit cells share the same configuration: the reflectarray unit cells are patterned on a metallic plate which is at a certain distance from a metallic ground plane. Other alternatives to design metal-only reflectarrays have been shown in [6]–[8]. In these works, the beam collimation produced by the reflectarray is achieved by means of the depths of 1-D or 2-D perforated grooves. The phase introduced by each unit cell of the reflectarray is determined by the round trip propagation of the wave inside the groove. Alternatively to unit cells based on grooves, nonresonant elements such as squared metallic blocks have been proposed as a reflectarray unit cell [9]. Since the unit cell is a nonresonant element, the gain bandwidth of the reflectarray can be broadened. In this direction, other nonresonant unit cells have been analyzed for metal-only reflectarray design [10]–[12]. Metallic cylinders or crosses orthogonally connected to surrounding unit cells have been explored in the previous works. Finally, some other complex geometries for the unit cells have been employed for designing reflectarrays. In [13], dual-branch helixes are implemented as reflectarray unit cells to obtain a wideband performance keeping unaltered the incident circular polarization. In [14], the considered unit cell is a metallic cylinder etched with a rectangular groove. By the 90º rotation of the unit cell, an out-of-phase response is obtained which is used to implement a mechanically-reconfigurable 1-bit reflectarray.

In addition to the increase of the total efficiency by the use of metal-only reflectarray, another desired characteristic for a reflectarray antenna is the control of the polarization. However, there is a lack in the literature of metal-only unit cells that provide two independent orthogonal polarization control. In this work, a metal-only reflectarray unit cell that controls separately the vertical (V-pol) and horizontal (H-pol) polarizations is proposed. Unlike other works whose unit cells relied on resonant elements in the horizontal and vertical directions to gain the polarization control [15], [16], in this work, the proposed unit cell is a nonresonant element. More precisely, the fundamental element that achieves the phase tuning for each polarization can be seen as a parallel-plate back-shorted waveguide with finite width. The document is organized as follows. Section II presents and analyzes the proposed reflectarray unit cell for V-pol and H-pol. In Section III, the height of parallel plates in the unit cells is studied and its effect in the phase response of each polarization. In addition, the oblique incidence performance is assessed in Section IV. Finally, the conclusions are drawn in Section IV.

II. Proposed Reflectarray Unit Cell

The reflectarray unit cell proposed in this work is illustrated in Fig. 1(a). The figure shows a central metallic block of height L surrounded by four metal steps whose heights are L_V in the vertical direction (highlighted in red) and L_H in the horizontal one (highlighted in green). This unit cell allows the propagation along its longitudinal direction (z-direction) for both from V-pol and H-pol. Fig. 1(b) illustrates a planar view of the proposed unit cell indicating the propagating zones

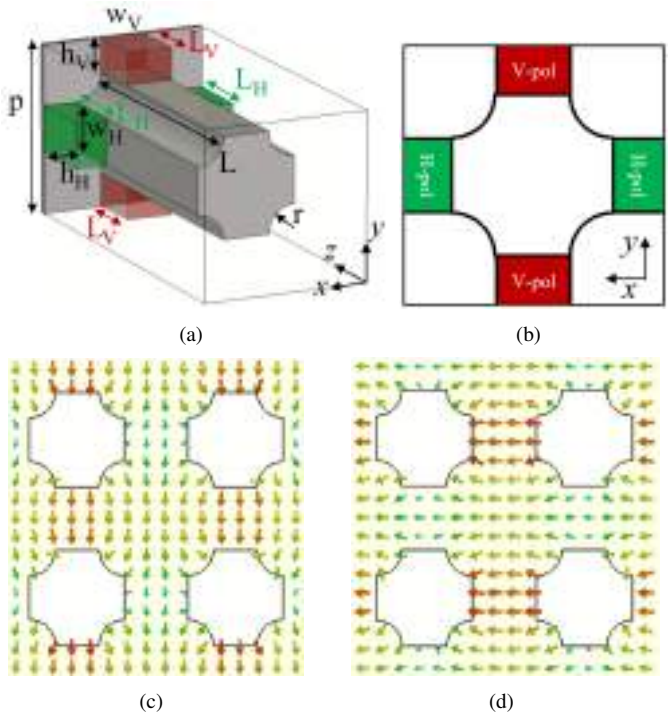

Fig. 1. (a) 3-D view of the proposed reflectarray unit cell. (b) Planar view of the unit cell indicating the propagating zones for V-pol and H-pol. Electric-fied distribution for a 4-cell unit environment when the excitation is a (c) vertical-polarized plane wave and, (d) a horizontal-polarized plane wave. The dimensions are: p = 2.5 mm, $h_V = h_H$ = 0.5 mm, $w_V = w_H$ = 0.7 mm, L = 4 mm and, r = 0.4 mm.

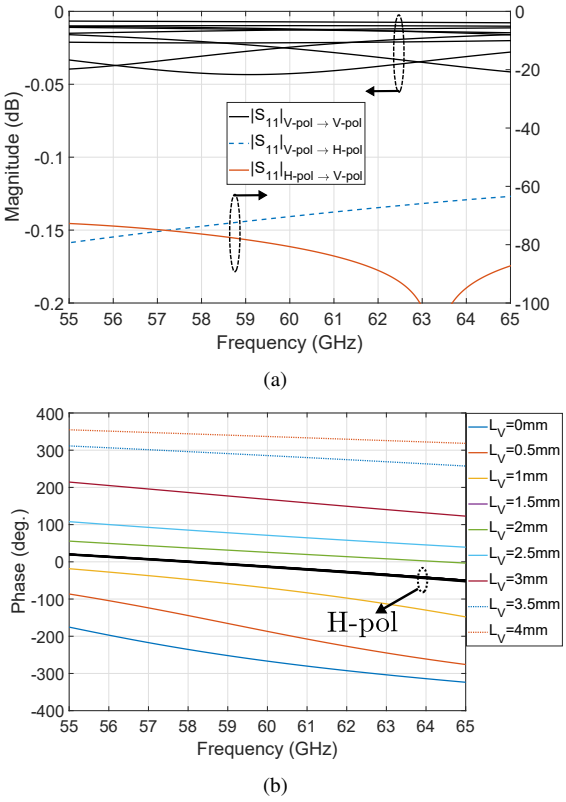

Fig. 2. (a) S-parameters in magnitude of the proposed unit cell. (b) S-parameters in phase of the proposed unit cell when $L_H = 1.5$ mm and L_V is varied.

and which polarization propagates along these zones. The propagating zones are seen as parallel-plate waveguides with finite width (w_V for V-pol and, w_H for H-pol) and with a short-circuited wall located at their bottom. The short-circuited wall produces the reflection of the wave, which propagates in the parallel-plate waveguide. The reason why each zone only allows a polarization is because parallel-plate waveguides are formed between unit cells in y- and the x-directions as it is illustrated in Figs. 1(c) and 1(d), respectively. For a considered polarization, the wave can propagate in the zones where the metal surfaces are orthogonal to the incident electric field (E-field) since the wave is propagating in a parallel-plate waveguide whose height is $2h_{V,H}$ and its width is $w_{V,H}$. For the orthogonal polarization, these zones cannot support wave propagation because the incident E-field is parallel to the metallic surfaces producing a waveguide condition with a high cutoff frequency as the waveguide width is now $2h_{V,H}$. Figs. 1(c) and 1(d) show the E-field distribution when a vertical-polarized or a horizontal-polarized wave impinges to the unit cells, respectively. For instance, in the V-pol case of Fig. 1(c), the greater E-field amplitude distribution is concentrated between the vertical arms (y-direction) of nonresonant cross-shaped element. The E-field in this case is minimum between the horizontal arms (x-direction) of nonresonant cross-shaped element because the waveguide condition commented above. Additionally, the complementary case occurs in the Fig. 1(d) where the minimum of the E-field is at the vertical arms and the maximum E-field at horizontal arms. In this way, both polarizations can be independently controlled by the position of the short-circuit at the end of the parallel-plate waveguide. The position of the short-circuit for the V-pol and H-pol is determined by the parameter L_V and L_H, respectively.

The electromagnetic (EM) characterization of the proposed unit cell is performed with CST Microwave Studio. Unit cell boundary conditions in the x- and y-directions are imposed for the simulation of the unit cell illustrated in Fig. 1(a) and, the frequency solver of the CST is employed. The magnitude and phase responses of the unit cell for V-pol and H-pol incident waves at normal incidence are shown in Fig. 2. The frequency range is centered at 60 GHz but the unit cell can be designed to work in a different frequency range by size scaling due to its fully-metallic structure. Fig. 2(a) shows the reflection coefficients $|S_{11}|$ of the unit cell when the incident plane wave is V-pol. Black solid lines represent the co-polarized magnitude response for different values of L_V. It can be observed that for all assessed cases, the reflection coefficient is very close to 0 dB being the maximum of losses 0.05 dB. This is because of the ohmic losses of the metal employed in the unit cell, in this case aluminium ($\sigma = 3.56 \cdot 10^7$ S/m). On the other hand, the cross-polarized magnitude response, which accounts the power transmission between the V-pol and H-pol

in the unit cell, is under -60 dB for the worst case in the considered frequency range. Therefore, almost all power is conserved in the same polarization when reflected in the unit cell. The observed performances are preserved on a quite large frequency range.

Fig. 2(b) presents the phase response of each incident polarization, V-pol and H-pol, when the position of the short-circuit L_V for the V-pol is modified keeping L_H fixed. The variation of L_V allows to set different levels of phase shift produced by the unit cell with good phase linearity along the frequency. The variation of the phase shift reaches beyond 360º for all the frequencies under consideration which allows this unit cell to be used for the design of a reflectarray. In addition, due to the independent behavior between the two polarizations explained above, the phase response for the H-pol is practically unchanged when L_V is varied. This demonstrates the expected and desired behavior for polarization-independent control in the unit cell.

III. Effect of the Height of Parallel-Plate Waveguides

One of the most interesting parameter to be analyzed in the proposed unit cell is the height of the parallel-plate waveguides, say, h_V and h_H for V-pol and H-pol, respectively. Fig. 3 shows the phase responses for V-pol and H-pol for different values of height of the parallel-plates waveguides. Also, in each case, the phase response is assessed for different L_V values. The phase difference shown in Figs. 3(b), 3(d) and 3(f) is defined as the absolute value of the difference in the phase response fixing a reference case. The reference case is the reflected phase produced by the unit cell for H-pol when L_V is 0 mm. The other cases that are compared with the reference case correspond to the phase shift response for the H-pol produced by other L_V value.

Analyzing the results of Fig. 3, a general conclusion can be obtained. As the height of the parallel-plate waveguides increases, the phase linearity improves but the phase difference in the orthogonal polarization (H-pol) worsens. The first effect, the enhancement of the phase linearity as h_V and h_H increase, is because the waveguide impedance is more similar to impedance of free space. This fact improves the phase linearity of the reflectarray unit cell as it has been previously reported for dielectric reflectarray unit cells [17]. The second observed effect is the increase of the phase difference for the H-pol as height of the parallel-plate waveguides increases. With the increase of h_V and h_H, the distance between orthogonal waveguides decreases and also, the cutoff frequency of the waveguides is reduced for the orthogonal polarization. Both factors contribute slightly to amplify the effect of the modification of the short-circuit position governed by the parameter L_V. Besides, it can be appreciated that the greater phase differences are achieved for higher values of L_V. These situations entail a shorter length for the cut-off waveguides and therefore a greater effect of the short-circuit position since the wave has not been fully attenuated. Nevertheless, the phase difference for the worst case is under 9º in the whole operating frequency

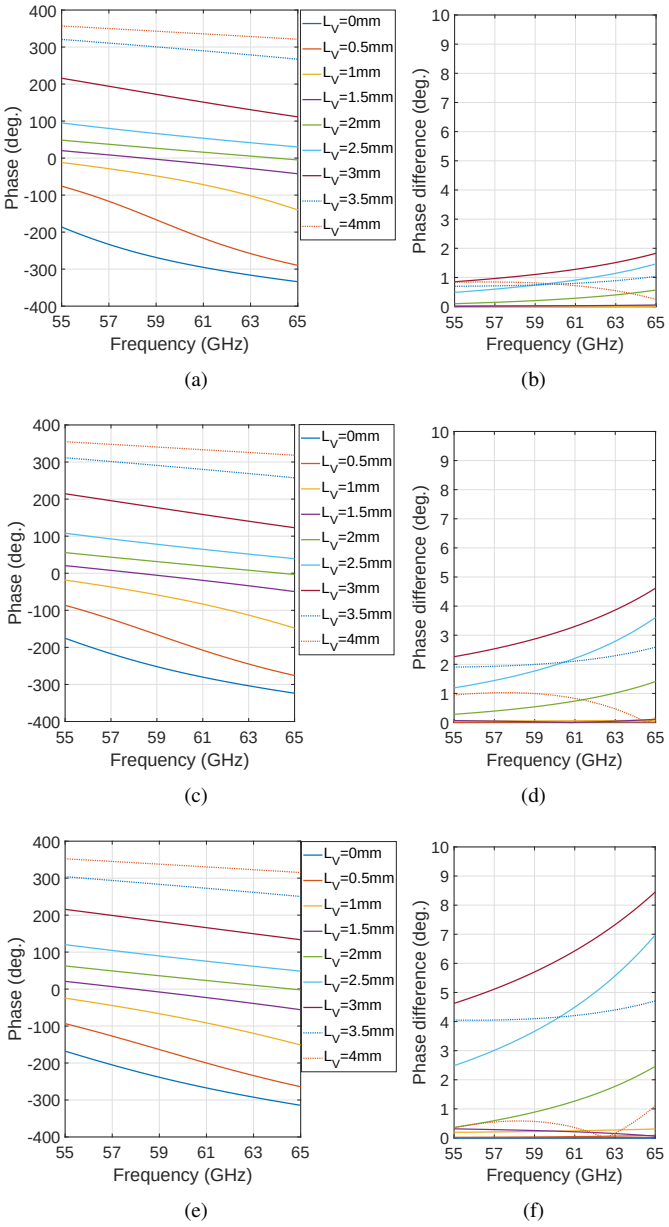

Fig. 3. Phase response for the V-pol when $L_H = 1.5$ mm, L_V is varied and (a) $h_V = h_H = 0.375$ mm, (c) $h_V = h_H = 0.5$ mm, and (e) $h_V = h_H = 0.625$ mm. Difference phase shift response for the H-pol when L_V is varied and (b) $h_V = h_H = 0.375$ mm, (d) $h_V = h_H = 0.5$ mm, and (f) $h_V = h_H = 0.625$ mm.

range. Finally, another consequence of decreasing the height of the waveguides is the increase of phase shift range at the expense of deteriorating the phase linearity specially for lower values of L_V.

IV. Performance for Oblique Incidence

The oblique incidence performance of the unit cell is also analyzed in this work because it is of great importance in the design of reflectarrays with a realistic feed such horn antenna [1]. Fig. 4 presents the simulated results of the proposed unit cell under the oblique incidence of a plane wave. It is sufficient

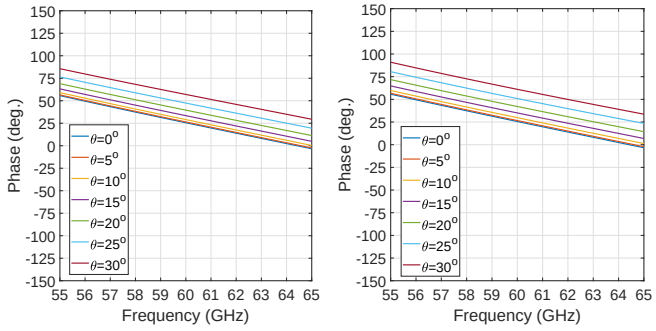

(a) (b)

Fig. 4. Phase response for the V-pol under different oblique angles (θ) when $h_V = h_H = 0.5$ mm. L_V and L_H are fixed and equal to 2 mm and 1.5 mm, respectively. (a) Performance in the E-plane (YZ plane). (b) Performance in the H-plane (XZ plane).

to only consider the V-pol due to the symmetry of the unit cell. For the oblique incidence, the E- and H-planes are defined regarding axis of Fig. 1(a) where E- and H-planes correspond to YZ and XZ planes, respectively. The results presented in Figs. 4(a) and 4(b) reveal a modification of the phase response with the variation of the oblique angle. As the value of θ increases, the difference regarding the normal incidence ($\theta = 0^o$) also increases. The maximum phase difference at 60 GHz is 31.4º and 35.5º for the E-plane and H-plane, respectively. It is also observed that the phase linearity are preserved along the frequency for both planes even with the increase of the oblique angle. This unit cell behavior provides robustness since the phase curve does not suffer great changes when the angle of incidence is modified and thus, the phase error committed in the reflectarray design is minimized.

V. Conclusion

In this paper, a metal-only reflectarray unit cell for independent polarization control is presented. The unit cell is based on a metallic nonresonant cross-shaped that is not physically connected by its arms to the neighboring unit cells. The reflected phase response of each polarization is tuned by the position of a short-circuited wall located at the end of the parallel-plate waveguides formed between unit cells. The proposed unit cell is designed to operate in millimeter-waves centered at 60 GHz but other frequency range can be tuned by an easy size scaling of the unit cell. The electromagnetic performance of the unit cell demonstrates the independent tuning of the phase response for each incident polarization. Additionally, the range of the phase shift produced by the unit cell is beyond 360º in the operating frequency range which is suitable for the design of reflectarray antennas. Besides, the values of the waveguide heights have been swept in order to observe the effects produced in the phase response for each polarization. As the heights increase, the linearity of the phase response along the frequency is enhanced at the cost of increasing the phase variation for the orthogonal mode. Finally, the oblique incidence performance has been assessed revealing acceptable variation of the phase response up to 30º with a linearity in phase that is preserved over the frequency.

Acknowledgment

This work was supported in part by the Spanish Government under Project PID2020-112545RB-C54, in part by "Junta de Andalucía" under Project B-TIC-402-UGR18, Project A-TIC-608-UGR20, Project P18.RT.4830 and Project PYC20-RE-012-UGR, and in part by the Predoctoral Grant FPU18/01965.

References

[1] P. Nayeri, F. Yang, and A. Z. Elsherbeni, *Reflectarray Antennas: Theory, Designs, and Applications. USA: Wiley, 2018.*

[2] Y. Cui, S. A. Nauroze, R. Bahr and E. M. Tentzeris, "3D Printed One-shot Deployable Flexible "Kirigami" Dielectric Reflectarray Antenna for mm-Wave Applications," in *2020 IEEE/MTT-S International Microwave Symposium (IMS)*, 2020, pp. 1164-1167.

[3] H. Yi, S. Qu, K. Ng, C. H. Chan and X. Bai, "3-D Printed Millimeter-Wave and Terahertz Lenses with Fixed and Frequency Scanned Beam," *IEEE Trans. Antennas Propag.*, vol. 64, no. 2, pp. 442-449, Feb. 2016.

[4] R. Deng, F. Yang, S. Xu and M. Li, "A Low-Cost Metal-Only Reflectarray Using Modified Slot-Type Phoenix Element With 360° Phase Coverage," *IEEE Trans. Antennas Propag.*, vol. 64, no. 4, pp. 1556-1560, April 2016.

[5] K. Q. Henderson and N. Ghalichechian, "Circular-Polarized Metal-Only Reflectarray With Multi-Slot Elements," *IEEE Trans. Antennas Propag.*, vol. 68, no. 9, pp. 6695-6703, Sept. 2020.

[6] D. Wang, R. Gillard, and R. Loison, "A 60 GHz passive repeater array with quasi-endfire radiation based on metal groove unit-cells," *Int. J. Microw. Wirel. Technol.*, vol. 8, no. 3, pp. 431–436, 2016.

[7] Y. H. Cho, W. J. Byun and M. S. Song, "Metallic-Rectangular-Grooves Based 2D Reflectarray Antenna Excited by an Open-Ended Parallel-Plate Waveguide," *IEEE Trans. Antennas Propag.*, vol. 58, no. 5, pp. 1788-1792, May 2010.

[8] Y. H. Cho, W. J. Byun and M. S. Song, "High Gain Metal-Only Reflectarray Antenna Composed of Multiple Rectangular Grooves," *IEEE Trans. Antennas Propag.*, vol. 59, no. 12, pp. 4559-4568, Dec. 2011.

[9] W. Lee and Y. J. Yoon, "A Broadband Dual-Metallic-Reflectarray Antenna for Millimeter-Wave Applications," *IEEE Antennas Wirel. Propag. Lett.*, vol. 16, pp. 856-859, 2017.

[10] H. Chou, C. Lin and M. Wu, "A High Efficient Reflectarray Antenna Consisted of Periodic All-Metallic Elements forthe Ku-band DTV Applications," *IEEE Antennas Wirel. Propag. Lett.*, vol. 14, pp. 1542-1545, 2015.

[11] H. Chou and J. W. Liu, "Synthesis and Characteristic Evaluation of Convex Metallic Reflectarray Antennas to Radiate Relatively Orthogonal Multibeams," *IEEE Trans. Antennas Propag.*, vol. 66, no. 8, pp. 4008-4016, Aug. 2018.

[12] B. Zhang, C. Jin, Q. Lv, J. Chen and Y. Tang, "Low-RCS and Wideband Reflectarray Antenna With High Radiation Efficiency," *IEEE Trans. Antennas Propag.*, vol. 69, no. 7, pp. 4212-4216, July 2021.

[13] G. Kong, X. Li, Q. Wang and J. Zhang, "A Wideband Reconfigurable Dual-Branch Helical Reflectarray Antenna for High-Power Microwave Applications," *IEEE Trans. Antennas Propag.*, vol. 69, no. 2, pp. 825-833, Feb. 2021.

[14] P. Mei, S. Zhang and G. F. Pedersen, "A Low-Cost, High-Efficiency and Full-Metal Reflectarray Antenna With Mechanically 2-D Beam-Steerable Capabilities for 5G Applications," *IEEE Trans. Antennas Propag.*, vol. 68, no. 10, pp. 6997-7006, Oct. 2020.

[15] C. Molero Jimenez, E. Menargues and M. García-Vigueras, "All-Metal 3-D Frequency-Selective Surface With Versatile Dual-Band Polarization Conversion," *IEEE Trans. Antennas Propag.*, vol. 68, no. 7, pp. 5431-5441, July 2020.

[16] C. Molero *et al.*, "Metamaterial-Based Reconfigurable Intelligent Surface: 3D Meta-Atoms Controlled by Graphene Structures," *IEEE Commun. Mag.*, vol. 59, no. 6, pp. 42-48, June 2021.

[17] Y. He, Z. Gao, D. Jia, W. Zhang, B. Du and Z. N. Chen, "Dielectric Metamaterial-Based Impedance-Matched Elements for Broadband Reflectarray," *IEEE Trans. Antennas Propag.*, vol. 65, no. 12, pp. 7019-7028, Dec. 2017.

2.2.3 Wideband 3-D-Printed Metal-only Reflectarray for Controlling Orthogonal Linear Polarizations

Based on the preliminary unit cell design presented in the previous publication, this paper presents a more comprehensive analysis of a metal-only unit cell with wideband behavior offering independent control in reflection for orthogonal linear polarizations. This fact allows the design of a reflectarray that produces a circularly-polarized radiated beam from a linearly-polarized primary antenna in millimeter waves. The proof-of-concept is manufactured with 3D printing and the reflectarray prototype presents a measured 3-dB gain bandwidth of nearly 41% and a 3-dB axial ratio bandwidth of approximately 44%. The central frequency of the reflectarray is 41 GHz. These experimental results show that the proposed design outperforms metal-only reflectarray designs that compose the state-of-the-art.

Wideband 3-D-Printed Metal-only Reflectarray for Controlling Orthogonal Linear Polarizations

Ángel Palomares-Caballero, Carlos Molero, Pablo Padilla, María García-Vigueras, and Raphaël Gillard

***Abstract*—This paper presents a metal-only reflectarray that enables the control of incident orthogonal polarizations in a large bandwidth. The proposed reflectarray is based on a unit cell whose tuning elements allow the independent control of the reflection phase value for the vertical and horizontal impinging polarizations. Due to the symmetry of the unit cell, the same performance is produced by each polarization when its reflection phase response is modified. The proposed unit cell provides a fairly linear phase response along the frequency with a phase variation in the orthogonal polarization of $\pm 1^{o}$. The performance under oblique incidence and the frequency limitation of the unit cell are also investigated. From this unit cell, a metal-only reflectarray that produces circular polarization from a linear polarization is designed. The reflectarray presents a simulated directivity greater than 27 dBi with an axial ratio below 1.5 dB from 32 GHz to 50 GHz (43.9% of bandwidth). A prototype is fabricated and the measured results agree well with the simulated ones. The obtained aperture efficiency is between 56% and 41% in the considered frequency band. The measured realized gain ranges from 27 dBi to 30.3 dBi where the achieved radiation efficiency is greater than 97%.**

***Index Terms*—3D unit cell, dual polarization, metal-only, millimeter-waves, polarization control, reflectarray antenna.**

I. Introduction

REFLECTOR antenna is one of the key radiating element for the future communications paradigms. Both passive [1], [2] and active [3], [4] reflector antennas have been proposed to enhance the link budget in forthcoming wireless communications. Another application in which reflectors or reflectarrays are widely used is in space applications due to the high directivity and versatility provided by this type of antennas [5]. All of the above applications are intended to work in millimeter-wave frequencies to achieve either a higher bandwidth or because the desired frequency is in that range. The direct consequence is the use of metal-only structures in the antennas to obtain greater efficiency [6] and avoid outgassing problems in space applications.

Metal-only reflectarrays have been reported in the literature with different designs and implementations. Following the conventional reflectarray (RA) designs formed by stacked layers of PCBs, [7]–[9] present reflectarrays formed by stacking perforated metallic sheets. Their structures only use metal avoiding dielectric substrates. In [10] and [11], advantage is taken of parallel-plate metallic waveguides to efficiently reflect the incoming wave to broadside and endfire directions, respectively. Metallic square waveguides are also been considered as RA unit cells in [12] and its 3-D printed version in [13], [14] at V-band. An alternative approach to design metal-only RA unit cells is the one proposed in [6] where convex or nonresonant elements are defined. RA designs that employ this geometry for their reflective elements are presented in [15]–[19]. These works demonstrate that large gain bandwidths can be achieved with the adequate choice of the nonresonant element geometry, resulting in a great advantage regarding previous resonant RA unit cells. More complex geometries for metal-only RA unit cells have also been reported. For instance, in [20], a dual-branch helix has been used to obtain a linear phase response along the frequency and preserve the incident circular polarization. Another example is found in [21] where metallic cylinders etched with a rectangular groove provide a stable phase difference and thus, are good candidates to design a two-states RA.

In all the above metal-only reflectarrays, only the phase response of a single polarization can be tuned in the RA design. However, the independent control for orthogonal polarizations of an incident wave in a RA is a desired requirement to extend its functionalities. There are RA unit cells that offer a control of orthogonal polarizations as the one proposed in [22] but, most of them are based on the stacking of PCB layers that have dielectric material in their structure. Nonetheless, in the literature, it is very hard to find this independent polarization control for metal-only RA. The recent development of 3D unit cells offers new possibilities to independently control two orthogonal polarizations and thus, RA unit cells based on this geometry can be developed. The three-dimensional geometry allows a high level for controling orthogonal polarizations as can been observed in dual-band metal-only polarizer in [23]. Based on this design procedure, some metal-only reflectarrays have been conceptually proposed [4] and implemented for a single polarization [24]. However, the design of some of the last RA unit cells are based on resonant elements which provide narrowband performance.

In this paper, a metal-only RA with wideband performance and independent control of incident polarizations is presented. In order to achieve this wideband control of the orthogonal polarizations, the RA unit cells have a 3D geometry which enables the excitation of two orthogonal transverse electro-

This work was supported in part by the Spanish Government under Project PID2020-112545RB-C54 and, Project RTI2018-102002-A-I00, in part by "Junta de Andalucía" under Project B-TIC-402-UGR18, Project A-TIC-608-UGR20, Project PYC20-RE-012-UGR and Project P18.RT.4830, and in part by the Predoctoral Grant FPU18/01965. *(Corresponding author: Ángel Palomares-Caballero.)*

Á. Palomares-Caballero, C. Molero, and P. Padilla are with the Department of Signal Theory, Telematics and Communications, Universidad de Granada, 18071 Granada, Spain (e-mail: angelpc@ugr.es; cmoleroj@ugr.es; pablopadilla@ugr.es).

M. García-Vigueras, and R. Gillard are with UMR CNRS 6164, INSA Rennes, IETR, 35708 Rennes, France (e-mail: Maria.Garcia-Vigueras@insa-rennes.fr; Raphael.Gillard@insa-rennes.fr).

magnetic (TEM) modes. The work in [25] is also based in the excitation of TEM modes in a 3D unit cell in order to achieve broadband polarization conversion. However, such unit cell operated in transmission and its topology was not conceived to operate in reflection. In addition, the purely metallic nature of the proposed RA structure enables an easy and feasible redesign by geometric scaling for tuning in the desired frequency band. To the best of the authors' knowledge, it is the first design of a metal-only RA with wideband performance and independent control of incident orthogonal linear polarizations. The outline of this paper is the following one. Section II presents and discusses the electromagnetic (EM) performance of the proposed RA unit cell. In Section III, the design of a circular-polarized RA is done by means of the proposed RA unit cells. Section IV shows the prototype and its measurements as well as a discussion of the results. Finally, Section IV presents the conclusions from this work.

II. Reflectarray Unit Cell: Design and Analysis

Fig. 1 illustrates the geometric evolution of the proposed RA unit cell from its original design (labelled as (0)) to its optimized design (labelled as (3)). RA unit cell (0) can be seen as a combination of horizontal and vertical parallel plates whose groove depths are varied independently for each polarization. It is similar to the RA unit cells introduced in [10], [11] but here for both x- and y-directions. All the unit cells designs illustrated in Fig. 1 only use metal in their structure. The tuning elements, highlighted in red and green, are metallic blocks whose heights h_{V} and h_{H} are modified to change the phase reflection response of the vertical (V-pol) and horizontal (H-pol) polarizations, respectively. Impinging wave is vertically polarized when the electric field (E-field) is in y-direction while it is horizontally polarized when the E-field is in the x-direction. The propagation of the incident wave is considered in the z-direction and the reflected one is in the minus z-direction. In the performed EM simulations, periodic environment is applied along the x- and y-directions since the local periodicity approach is widely used in the literature for analysing quasi-periodic structures such as reflectarrays. The EM software used in all the simulations of the paper is CST Studio Suite whose Frequency Solver is employed for the RA unit cell simulations while the Time Solver, for the complete RA design. The design procedure for both RA unit cell and complete RA is aimed for the frequency band from 32 GHz to 50 GHz. This frequency range corresponds to the full operating frequency band of the WR22 waveguide standard.

Coming back to the RA unit cell evolution shown in Fig.1, geometric modifications have been introduced from (0) to (3) unit cell designs. These modifications have an impact in the EM performance of the original RA unit cell. Fig. 2 shows the reflection phase response of each RA unit cell design when the parameter h_{V} varies, keeping the value of parameter h_{H} fixed in the sweep. Due to the desired independent phase response of each polarization, the phase response for the H-pol should not be changed. In order to clearly observe this fact, the phase difference for the H-pol is also included in Fig. 2 in which the phase response reference is the case when h_{H} is

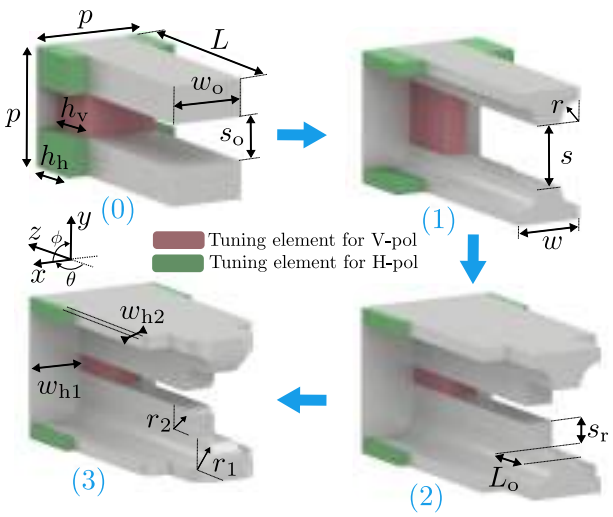

Fig. 1. Design evolution of the proposed RA unit cell. The dimensions are: p = 4, w_{o} = 2.54, L = 7.6, s_{o} = 1.46, w = 2.1, s = 1.92, r = 0.64, s_{r} = 0.72, L_{o} = 1.52, r_1 = 0.64, r_2 = 0.4, w_{h1} = 1.6 and, w_{h2} = 0.24. All dimensions are in mm.

minimum. Notice that all the RA unit cell designs presented in Fig. 1 are symmetric both for x- and y-directions and thus, it is enough to analyze the variation of one of the tuning parameters, h_{V} in our case. Figs. 2(a) and 2(b) show the EM performance for both orthogonal polarizations. It can be observed that the phase range is approximately 720° because the length of the RA unit cell L is almost one wavelength at the center frequency. Nevertheless, the phase response along the frequency illustrated in Fig. 2(a) is quite nonlinear with an inadequate phase difference to achieve the independent control of both polarizations (see Fig. 2(b)). For RA unit cell (1), the reflection phase response and the phase variation of the orthogonal polarization are displayed in Figs. 2(c) and 2(d), respectively. With the inclusion of roundness with a radius r on the edges of the parallel plate, a higher linearity in the phase response can be achieved and also, a decrease in the variation of the phase response for the H-pol. The separation between parallel plates for this RA unit cell is also greater ($s > s_{\mathrm{o}}$) providing a better impedance matching with free space and thus, enhancing the phase linearity along the frequency [26]. Figs. 2(e) and 2(f) display the phase behaviour of both polarizations for the RA unit cell (2). The only geometrical modifications regarding the RA unit cell (1) is the narrowing of the separation between parallel plates (labelled as s_{r} in Fig. 1) starting from a particular distance L_{o} from the beginning of the unit cell design. This inclusion produces an improvement of the phase linearity along the frequency as can be observed in Fig. 2(e) and a reduction of the phase difference in the phase response of the H-pol shown in Fig. 2(f). This enhancement in the phase response is at expense of limiting the length range of the tuning parameter h_{V}. However, it is not a problem because the tuning phase response is still beyond 360°, required value for a suitable RA design. An additional design improvement can be done by rounding the edges of the ends of the parallel-plate waveguides by r_1 and r_2 as it is illustrated in the RA unit cell (3) of Fig. 1. In this way, the linear phase response

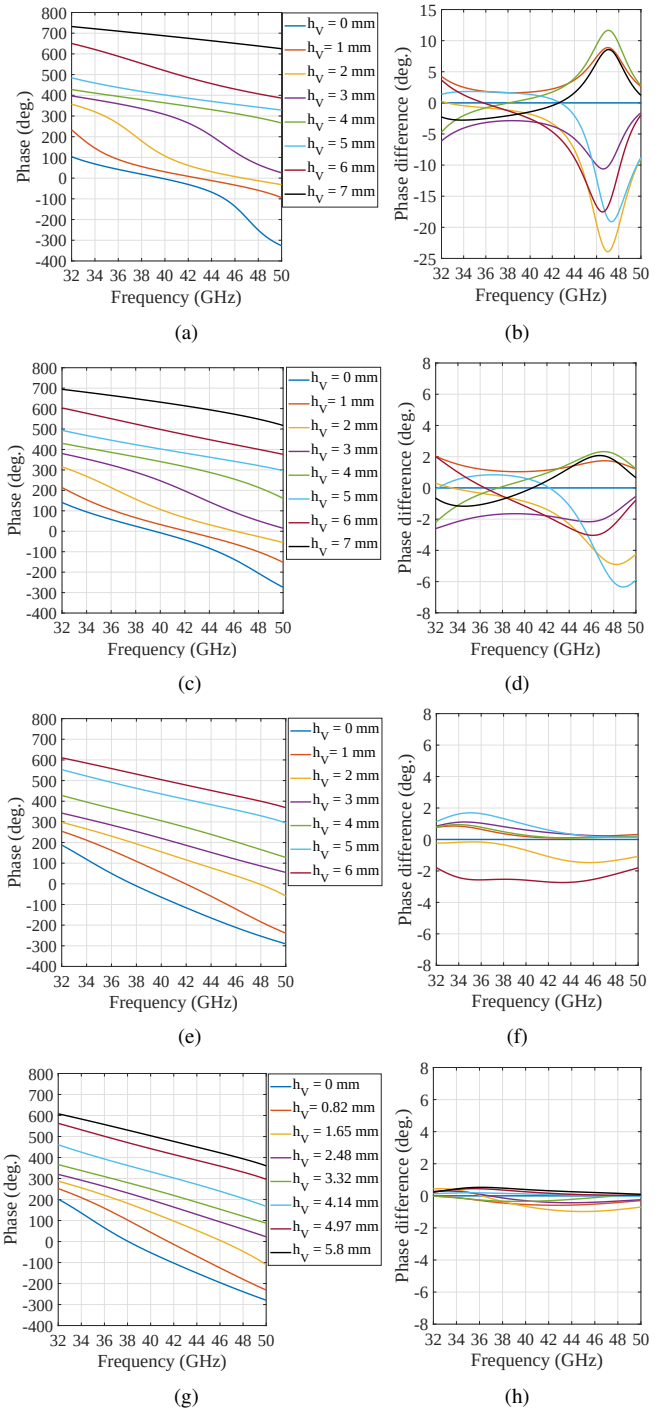

Fig. 2. Reflection phase response with a V-pol plane wave excitation under a normal incidence when tuning length h_V is modified: (a) RA unit cell (0), (c) RA unit cell (1), (e) RA unit cell (2) and, (g) RA unit cell (3). Phase difference in the orthogonal polarization (H-pol) when tuning length h_V is modified: (b) RA unit cell (0), (d) RA unit cell (1), (f) RA unit cell (2) and, (h) RA unit cell (3).

is preserved as it is shown in Fig. 2(g) and the phase response difference in the H-pol is further enhanced by reducing the range of variation between +0.5º and -1º. Therefore, this RA unit cell design meets the desired requirements and it is the one selected for the RA antenna design.

The magnitude performance of the selected RA unit cell is

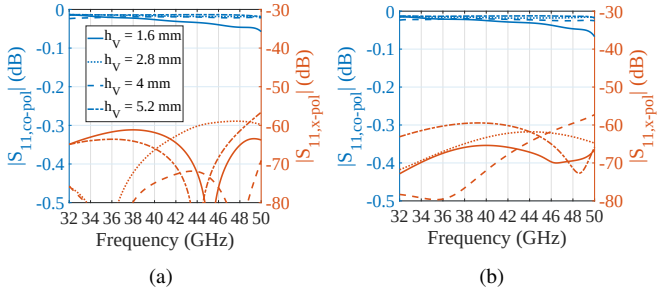

Fig. 3. Co-polarized and cross-polarized reflection in magnitude of the RA unit cell (3) in: (a) normal incidence and, (b) oblique incidence ($\phi = 90^{\text{o}}$ and $\theta = 20^{\text{o}}$).

shown in Fig. 3. It can be seen that the cross-polar component has a negligible excitation since it is below -60 dB over the considered bandwidth. The performance is similar to the unit cell presented in [27] because of the employed 3D geometry. This fact is preserved for different values of h_V and for oblique incidence situations as displayed in Fig. 3(b).

Fig. 4 shows the E-field distribution of the selected RA unit cell when it is illuminated by a V-pol plane wave. The E-field distributions have been plotted at different planes of interest (H, V_0 and V_1) indicated in Fig. 4(a). The vector and the magnitude distributions of the y component of the E-field are illustrated in Fig. 4(b). From this figure, it can be realized that the electric field is propagating mainly along the parallel-plate waveguide (subfigure framed in orange and blue). In contrast, in the V_1 plane, which contains the propagating path for the H-pol, the V-pol can hardly propagate with the magnitude of the E-field being close to zero as shown in the subfigures framed in green included in Fig. 4(b). This fact is due to the mode field distribution when the V-pol plane wave is impinged on the RA unit cell. Almost all the power propagates along the conductors that form the parallel plate waveguide where the tuning element is placed. On both sides of this waveguide, the E-field decays strongly in the x-direction as can be seen in the plane H of Fig. 4(b). Beyond the tuning element, the E-field distribution between RA unit cells is rapidly attenuated because the mode becomes evanescent since it becomes a TE_{10} waveguide mode whose waveguide width is $2w_{\text{h1}}$. This can be observed in the waveguide zone indicated in the planes V1 and H of Fig. 4(b). The same rationale is valid for an illumination of the RA unit cell with a H-pol plane wave. All above observations give an explanation about the remarkable isolation in the phase response tuning of the incident orthogonal polarizations.

The electric field distribution analyzed in the unit cell shows that the highest electric field intensity is located in the gap of the parallel-plate waveguide. The size of this gap determines the maximum power-handling capacity before multipactor phenomenon appears, which is of particular concern in satellite applications. Using the commercial software SPARK3D, the calculation of the multipactor power threshold is performed. At 41 GHz, the maximum power-handling capacity is 8699 W.

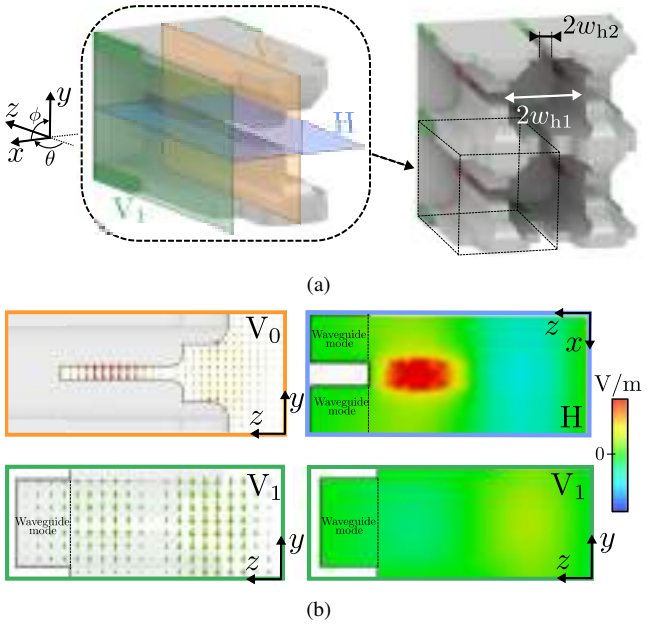

Fig. 4. (a) 3-D view of the proposed reflectarray unit cells and some of the planes of interest. (b) E-field distribution in the planes of interest when a V-pol plane wave impinges the unit cell under normal incidence. The subfigures on the left are vector plots while the subfigures on the right are magnitude plots

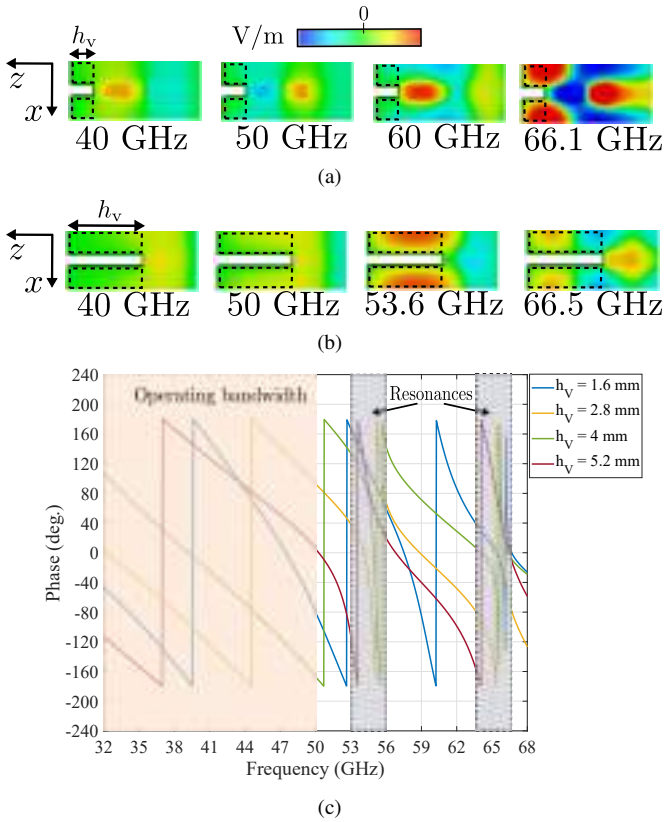

Fig. 5. E-field distribution of unit-cell environment of two cells in the plane of interest H at different frequencies: (a) when $h_V = 1.6$ mm and, (b) when $h_V = 5.2$ mm. (c) Phase response of the proposed RA unit cell in an extended frequency range. The excitation of the unit cell is a V-pol plane wave under normal incidence.

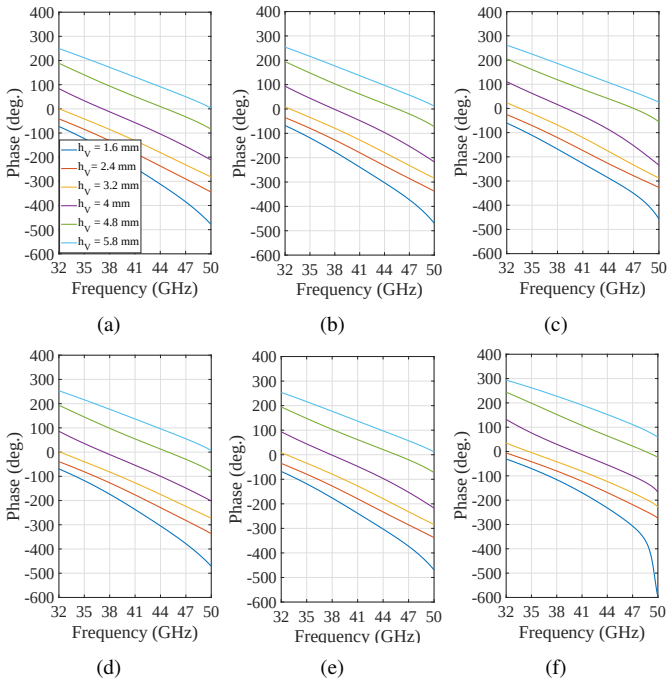

Fig. 6. Reflection phase response of the proposed reflectarray unit cell under oblique incidence when h_V varies. Oblique incidence in the E-plane ($\phi = 90^o$) where: (a) $\theta = 10^o$, (b) $\theta = 20^o$ and, (c) $\theta = 30^o$. Oblique incidence in the H-plane ($\phi = 0^o$) where: (d) $\theta = 10^o$, (f) $\theta = 20^o$ and, (g) $\theta = 30^o$. The excitation is a V-pol plane wave.

A. *Resonances in the unit cell*

As described above, the selected RA unit cell mostly allows the wave propagation along its structure to the polarization whose E-field is perpendicular to the parallel-plate waveguide (see Fig. 4(b), subfigure framed in orange). Nevertheless, although in the regions where the E-field amplitude is very weak or even evanescent, some cavity resonances can be generated if the resonance conditions are fulfilled for a certain frequency. In Figs. 5(a) and 5(b), the plane of interest H is displayed for a unit-cell environment of two cells with different length for the tuning element and at different frequencies. It can be seen how the large part of the incident E-field tends to propagate along the area of the parallel plate waveguides. However, when the frequency increases or the tuning length h_V is longer, some resonances appear in the evanescent regions, i.e., the regions enclosed with dashed line in Figs. 5(a) and 5(b). These resonances completely alter the linear phase response of the unit cell as displayed in Fig. 5(c). The reflection coefficient in phase for different tuning length values has been investigated and all the possible resonances between unit cells occur outside of the operating bandwidth. This physical insight reveals the performance limitation in frequency of the proposed RA unit cell. Nonetheless, the operating frequency band where the reflection phase produces an acceptable phase linearity is from 32 GHz to 50 GHz, this is, a 43.9% bandwidth.

B. *Oblique incidence performance*

Fig. 6 presents the reflection phase behavior of the selected RA unit cell under oblique incidence. Figs. 6(a), 6(b) and

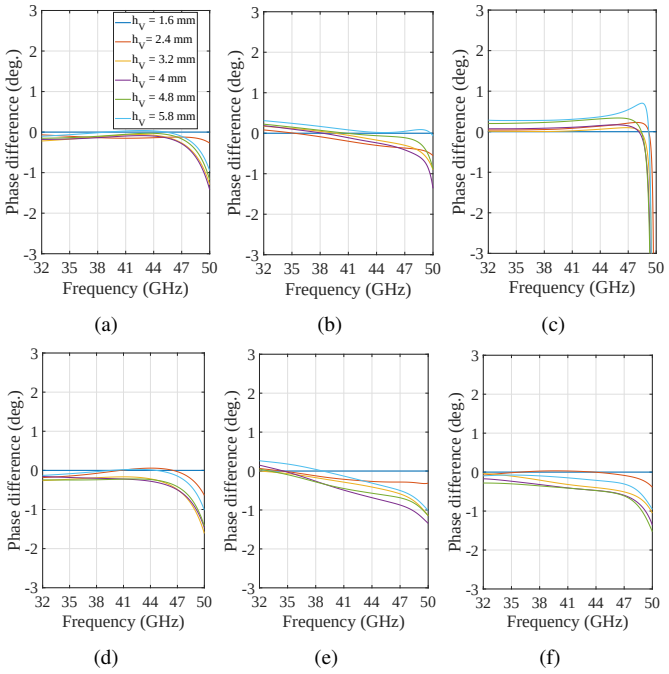

Fig. 7. Phase difference in the orthogonal polarization of the proposed reflectarray unit cell under oblique incidence when h_V varies. Oblique incidence in the E-plane ($\phi = 90^o$) where: (a) $\theta = 10^o$, (b) $\theta = 20^o$ and, (c) $\theta = 30^o$. Oblique incidence in the H-plane ($\phi = 0^o$) where: (d) $\theta = 10^o$, (f) $\theta = 20^o$ and, (g) $\theta = 30^o$. The excitation is a V-pol plane wave.

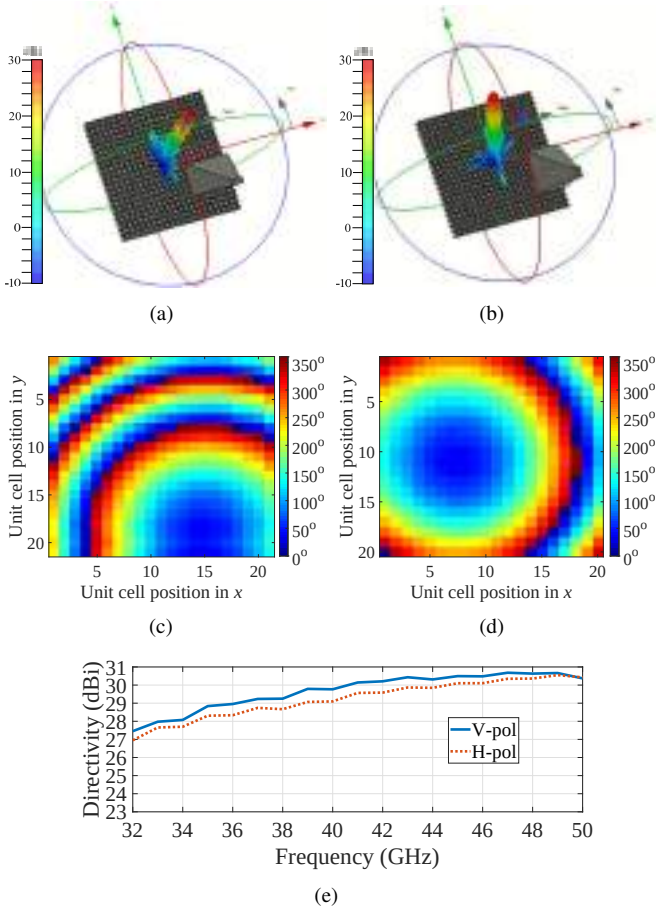

Fig. 8. Simulated 3-D radiation pattern at 41 GHz of a reflectarray based on the proposed RA unit cell: directivity (a) for V-pol and, (b) for H-pol. Their reflected beam directions are ($\phi = 45^o$, $\theta = 10^o$) and ($\phi = 105^o$, $\theta = 20^o$), respectively. The phase maps required for (c) V-pol and, (d) for H-pol. (e) Simulated directivity along the frequency for both incident linear polarizations.

6(c) correspond to oblique incidence in the E-plane while, Figs. 6(d), 6(e) and 6(f) correspond to oblique incidence in the H-plane. E-plane stands for the YZ plane ($\phi = 90^o$ and θ varies) and H-plane stands for the XZ plane ($\phi = 0^o$ and θ varies) of the axis illustrated in Fig. 1. Observing the simulated results for both planes and different oblique incidence angles, the linear phase response is maintained along the frequency range for the different tuning lengths and approximately preserving the phase difference between curves. As expected, as the value of the angle of incidence increases, the performance deteriorates especially for the high end of the frequency range where the slope of the phase curves starts to increase. This is a consequence of the frequency approach of the out-of-band resonances towards the operating bandwidth. For the sake of completeness, the phase difference for the orthogonal polarization is presented in Fig. 7 under the same oblique incidence conditions shown in Fig. 6. Notice that the independent control of the orthogonal polarization is kept and the absolute phase difference is not more than 2º for almost all the oblique incidence cases under study. The only case that exceeds this error at the end of the frequency range is the one presented in the Fig. 7(c). A huge increase in the phase difference appears near 50 GHz. This fact is also a consequence, in this particular case of oblique incidence, of a displacement of the out-of-band resonances closer to the operating bandwidth. The behavior presented above is for a V-pol plane wave impinging on the RA unit cell. The same performance is obtained in the case of an H-pol plane wave excitation due to the symmetry exhibited by the RA unit cell design.

C. Independent beam control by incident polarization

Thanks to the wideband linear phase-response of the selected unit cell and its independent control of orthogonal polarizations, an example of RA design where the reflected beam for each linear polarization has different outgoing direction is shown in Fig. 8. A more detailed view of the RA system can be seen in Fig. 9(a) except that the directions for the V-pol and H-pol linear polarizations are ($\phi = 45^o$, $\theta = 10^o$) and ($\phi = 105^o$, $\theta = 20^o$), respectively. The phase maps required in each polarization to achieve the above-mentioned directions are shown in Figs. 8(c) and 8(d). Lastly, Fig. 8(e) presents the directivity achieved by the RA over the considered frequency range. We observe a similar directivity for both polarizations with the same behavior along the frequency.

III. Circularly-Polarized Reflectarray Design

Complementary to the previous subsection II.C, this section is devoted to the design and analysis of a RA that provides a circular polarization from a linear polarization. In order to generate the circularly-polarized reflected wave, the RA is rotated by 45º regarding the feed antenna which has a linear polarization. In this manner, both orthogonal polarizations are

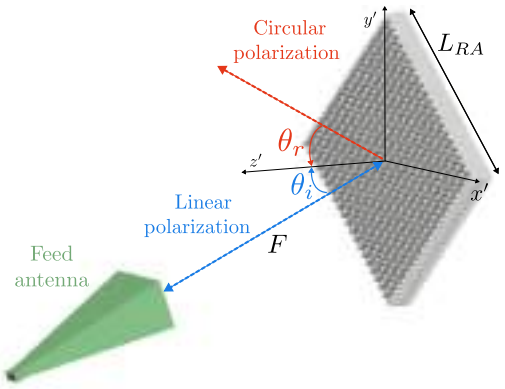

(a)

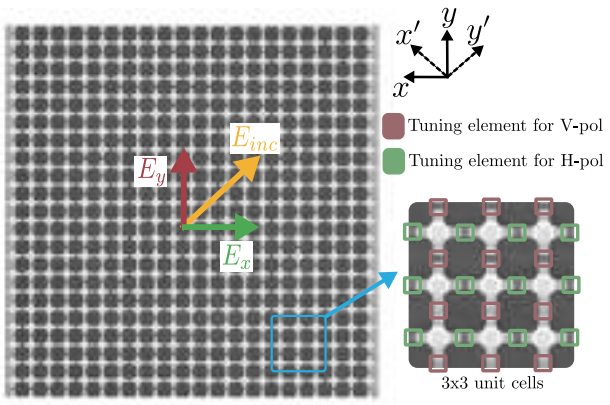

(b)

Fig. 9. (a) 3D view of the reflectarray system. (b) Front view of the proposed reflectarray design. The dimensions are: F = 123.2 mm, L_{RA} = 84 mm, and $\theta_i = \theta_r = 20^o$.

excited in the RA structure [22]. Additionally, to improve the blockage efficiency, the feed antenna illuminates the RA with an offset angle $\theta_i = 20^o$. Fig. 9(a) illustrates the depicted RA system whose selected feed antenna is a commercial 20 dBi horn antenna (Flann WR22 Standard Gain Horn). The distance between the RA and the center of the horn antenna aperture is F [see caption of Fig. 9] and F/L_{RA} =1.47, which ensures an amplitude taper from the center of the RA to the edges approximately equal to -10 dB at the center frequency. The reflected angle of the beam θ_r radiated by the RA has been chosen to be equal to the incident angle ($\theta_r = \theta_i$) and in the same radiation plane, that is, the Z`Y` plane in Fig. 9(a). If a direction other than the specular direction is chosen for the reflected beam, a beam squint with frequency will appear [28], which will be more noticeable the more different is the direction selected regarding to the specular one. The total number of RA unit cells employed in the RA design has been set to 21x21 and thus, at 32 GHz and 50 GHz, the electric size of the RA is 9λ x 9λ and 14λ x 14λ, respectively.

In order to achieve an increase in the directivity of the feed antenna and transform the linear polarization received in the RA to a circular polarization, the phase maps for the V-pol and H-pol have to be carefully calculated. Firstly, the phase map calculation of a single polarization, for instance V-pol, has been considered. The phase of the incident wave

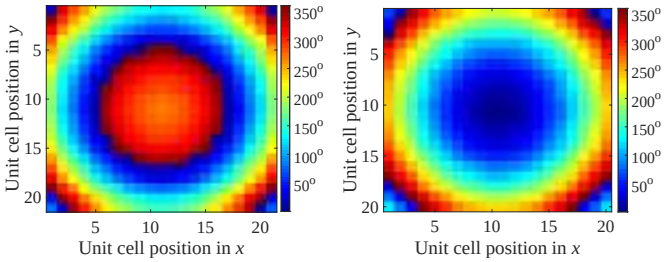

(a) (b)

Fig. 10. Phase maps in reflectarray at 41 GHz: (a) for V-pol and, (b) for H-pol.

at the center of each V-pol tuning element is obtained by simulation. In Fig. 9(b), these tuning elements are highlighted for a RA zone of 3x3 unit cells. In the same figure, the decomposition of the incident E-field (E_{inc}) into the E-field for the V-pol (E_y) and H-pol (E_x) is also displayed. The simulated phases are obtained at 41 GHz, the center frequency of the operating bandwidth. In this manner, a more accurate design in terms of phase correction in the RA is possible when compared to the phases calculated through ray tracing method [29]. Once the incident phases are obtained, the phase map of the RA is computed since the positions of RA unit cells and the direction of the reflected beam is known [5]. For the orthogonal polarization (H-pol), a similar procedure is done. The phases obtained from the simulation are the ones corresponding to the central zones of the tuning elements for H-pol. To produce the circular polarization, both orthogonal polarizations must have a difference phase of $\pm 90^o$. In our RA design, it is selected a phase difference equals to $+90^o$ and in consequence, the circular polarization is LHCP. The opposite circular polarization, RCHP, can be produced if the linear polarization of the horn antenna is aligned to the x'-direction instead of the y'-direction (see axis in Fig. 9). The phase maps for both polarizations are displayed in Fig. 10. It is important to say that a constant phase reference can be added to the presented phase maps without introducing any error on the theoretical design of the reflectarray [5]. Nevertheless, this constant phase reference should be chosen carefully because it modifies the physical structure of the RA since the lengths of the tuning elements change accordingly. This implies that the unit cells located in the central zone of the RA, which has the greatest influence due to the amplitude taper, must respect a good linearity of the phase response with frequency. For the unit cell used, the performance of the RA is specially affected at the ends of the operating bandwidth. The phase maps presented in Fig. 10 produce satisfactory performances for the directivity and axial ratio (AR) in the considered frequency range.

Based on the computed phase maps, the physical implementation of these phase responses in the RA has been carried out by a lookup table that relates the lengths of the tuning element with their reflection phase values. This lookup table has been created with the simulated reflection phase shift values at 41 GHz and their corresponding tuning lengths. Due to the similarity of the phase response of the RA unit cell in normal

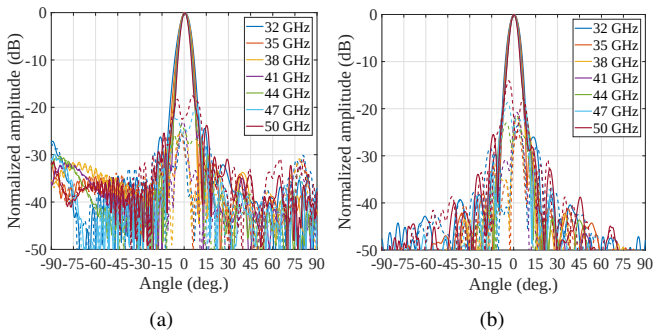

Fig. 11. Simulated results of the normalized radiation patterns of the reflectarray along the operating bandwidth: (a) for the E-plane and, (b) for the H-plane. The solid and dashed lines correspond to LHCP and RHCP, respectively.

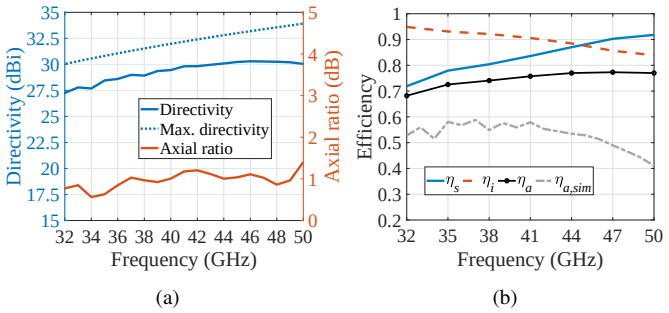

Fig. 12. (a) Simulated directivity, maximum achievable directivity and AR at the main beam direction. (b) Efficiency of the RA along the frequency.

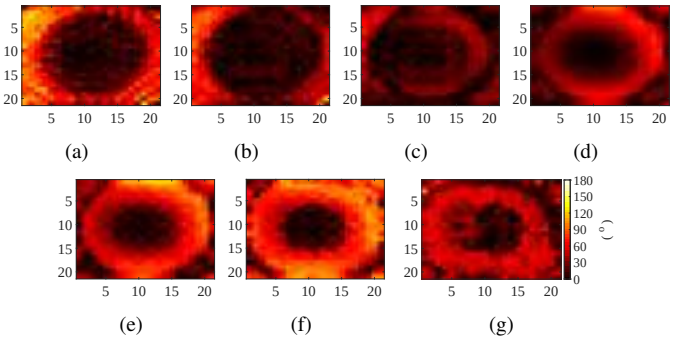

Fig. 13. Error phase maps for V-pol at different frequencies: (a) 32 GHz, (b) 35 GHz, (c) 38 GHz, (d) 41 GHz, (e) 44 GHz, (f) 47 GHz and, (g) 50 GHz.

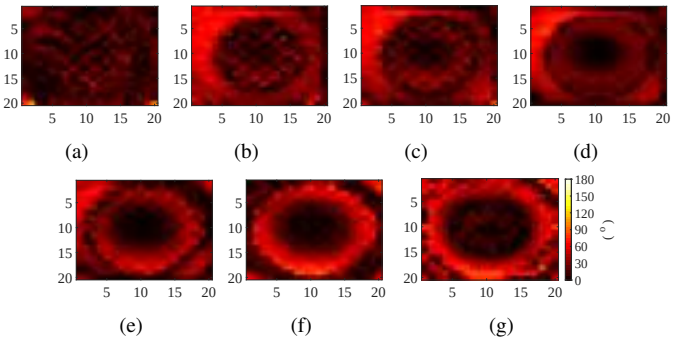

Fig. 14. Error phase maps for H-pol at different frequencies: (a) 32 GHz, (b) 35 GHz, (c) 38 GHz, (d) 41 GHz, (e) 44 GHz, (f) 47 GHz and, (g) 50 GHz.

and oblique incidence, each "phase - tuning length" entry of the lookup table is extracted from the simulated results of the unit cell at normal incidence. In this manner, the robustness of the unit cell phase response is examined in a RA where the unit cells receive different oblique incidence angles Fig. 11 presents the simulated results of the considered RA. The metal considered in the simulations is silver ($\sigma = 6.3 \cdot 10^7$ S/m). Normalized radiation patterns for LHCP and RHCP in their principal cuts, E-plane and H-plane, are shown in Fig. 11(a) and 11(b), respectively. The E-plane corresponds to the Z'Y' plane (see Fig. 9(a)) while, the H-plane is referred to the plane Z'X' when the z' axis is aligned with the main beam direction; this is $\phi = 90^o$ and $\theta = 20^o$. From the simulated normalized patterns displayed in Figs. 11(a) and 11(b), it can be observed the stability of the main beam direction for LHCP as well as a secondary lobe level below -20 dB along the entire frequency range. The cross polarization, which is RHCP, is around 20 dB lower than the LHCP in almost the entire considered band with the exception of the high end of frequencies.

In Fig. 12(a), the provided directivity and AR by the RA are presented. Additionally, the maximum directivity that the reflectarray can produce is also included. The achieved directivity ranges from 27.25 dBi to 30.3 dBi with an AR below 1.5 dB for the entire frequency range. To calculate the different efficiencies that impact the aperture efficiency of the RA, the analysis presented in [30] has been used. The coefficients q and q_e of the cosine models of the feed antenna and RA unit cell radiation patterns have been obtained by simulation. Since a large frequency range is considered, these coefficients vary with frequency and consequently, the amplitude taper in the plane of the reflectarray also changes with frequency. The range of values for q is from 9.5 to 20 while q_e goes from 0.5 to 0.85. The illumination efficiency (η_i) and spillover efficiency (η_s) over the frequency are presented in Fig. 12(b). In addition to these two efficiencies, the aperture efficiency (η_a) resulting from the product of η_i and η_s and, the aperture efficiency obtained in simulation ($\eta_{s,sim}$), which is calculated by the difference between the maximum achievable directivity and the produced directivity, are shown [see Fig. 12(a)]. We can observe that η_a is between 68% and 77% while $\eta_{a,sim}$ is not greater than 58%. This difference is due to additional efficiency factors considered in the full-wave simulation, which decrease η_a. Thanks to the metal-only structure of the RA, the material losses, in this case metal, are very low and a simulated radiation efficiency is above 97% in the frequency range.

Other efficiency factors such as blockage efficiency or return loss efficiency are negligible in our RA design. This is because the feed antenna illuminates the RA at oblique incidence and the reflection coefficient of the horn antenna is around -25 dB in the considered frequency range. Another relevant efficiency factor is the phase efficiency that takes into account the deviation from the desired phase distribution at RA aperture. Error phase maps have been calculated to observe the phase deviation produced at different frequencies. The calculation of these errors has been carried out by the difference between the desired phase distribution in the RA aperture and the one extracted, in the plane of the aperture,

TABLE I
SOURCE OF LOSSES (IN DECIBELS) IN THE REFLECTARRAY ANTENNA SYSTEM

RA unit cell	Feed antenna	Spillover	Illumination	Phase error
0.01 - 0.07	0.04 - 0.15	0.36 - 1.42	0.22 - 0.75	0.94 - 2.73

with CST Studio Suite. It is important to point out that for a correct calculation of the phase distribution in this aperture, the effect of the incident wave in simulation must be removed and only the wave reflected by the RA must be considered. The error phase maps for V-pol and H-pol at different frequencies are shown in Fig. 13 and Fig. 14, respectively. Phase errors located in the central area of RA are the ones that degrade performance the most, since this is the area that receives most of the illumination from the feed antenna. The cause of these phase errors is due to the perturbation of the unit cell phase response by the non-periodic environment, the modification of the oblique incidence angle across the RA and the non-perfect phase behavior of the unit cell in frequency. Nevertheless, in general, we do not find very large phase errors along the frequency for the two polarizations in the proposed RA design. In addition, it can be observed how the phase errors are greater at the higher frequencies of the operating band. This results in a reduction of the phase efficiency. Additionally, it is relevant to note that there is some loss in the polarization efficiency due to the excitation of the cross-polar component in certain areas of the RA. This produces an undesired radiation around the specular direction. These efficiency factors decrease the η_a. By taking into account the phase responses at different frequencies in the RA design process combined with an optimization algorithm, an improved aperture efficiency could be achieved. Nevertheless, this would lead to a higher computational cost in the design process. Table I summarizes the sources of losses that are present in the proposed RA design over the considered frequency band.

IV. FABRICATION, MEASUREMENTS AND DISCUSSION

In order to experimentally verify the design process presented in the previous sections, the RA has been fabricated and characterized in the anechoic chamber of University of Granada. A photo of the prototype is shown in Fig. 15(a). Thanks to the geometry of the proposed unit cell, it can be easily manufactured in 3D printing allowing a low cost and low weight prototype. Indeed, the manufacturing process followed for the prototype is based on stereolithography (SLA) 3D printing and a subsequent silver metallization. The printer used was the Form 3 from Formlabs with the high temp resin that allows a high precision printing with a thickness layer of 25 μm. The 3D printer achieves a XY resolution of 25 μm and the laser spot size is 85 μm. In relation to the tolerances, for feature size lower than 4 mm, the standard deviation is 30 μm. These properties in the 3D printing process produce a reliable manufacturing of the proposed reflectarray design. Regarding the metallization process, it was carried out by JetMetal [31], a company that offers a silver coating in plastic pieces by means of spray metallization. The silver coating has a thickness of 2.5 μm which is approximately 7 times the skin depth for the minimum operating frequency. According to [32], the average roughness produced in this metallization process is 2 μm which reduces the conductivity achieved by the silver. This decrease in the conductivity is almost negligible since it maintains the conductivity around $3{\cdot}10^7$ S/m.

(a) (b)

Fig. 15. (a) Prototype of the RA design. (b) Setup to measure the RA.

In Fig. 15(b), the implementation of the RA system is displayed. Some supports have been printed with the same 3-D printer to align the feeding horn with the center of the RA and the main beam direction of the RA with the receiving horn antenna of the measurement setup. The comparison between simulated and measured radiation patterns in the E- and H-planes for the LHCP and RHCP are presented in Fig. 16. We can observe a remarkable agreement for both the co- and cross-polarization at different frequencies. The half power beam width (HPBW) at 35 GHz, 41 GHz and 47 GHz are approximately 7º, 6º, 5º, respectively. In the HPBW, the maximum levels of cross-polar component, both simulated and measured, are -24.8 $\text{dB}^{sim.}_{35GHz}$, -27.5 $\text{dB}^{meas.}_{35GHz}$, -20.8 $\text{dB}^{sim.}_{41GHz}$, -24.1 $\text{dB}^{meas.}_{41GHz}$, -18.7 $\text{dB}^{sim.}_{47GHz}$ and -16.3 $\text{dB}^{meas.}_{47GHz}$. It can be noted that the cross-polar component increases with frequency. In order to complete the assessment of the proposed RA and to report more information about its radiation pattern performance, Figs. 17 and 18 show the measured 3-D LHCP and RHCP at different frequencies. In Fig. 17, we can observe the narrowing of the main beam as the frequency increases and, the appearance of side lobe levels at $\phi = 45$º or 135º. Nevertheless, the maximum side lobe level is not greater than -20 dB. On the other hand, in Fig. 18, it is more clearly seen how the RHCP level increases with frequency and around the main beam zone. At 50 GHz, the highest level of cross-polar is achieved and it is -12.3 dB.

Fig. 19 illustrates the measured AR for different frequencies in the considered bandwidth. A 3-D acquisition has been carried out to observe how the AR behaves for different azimuth and elevation angles up to $\theta = 20$º. From this figure, we can observe the low value for AR around the main direction of the RA and how it is maintained along the frequency. It is noted a decrease in the angular region where the AR is below 3 dB as the frequency increases. The reason for this is because of the increase of the RHCP around the main direction with frequency. This leads to the cross-pol discrimination being below 15 dB and hence to the AR being greater than 3 dB [33].

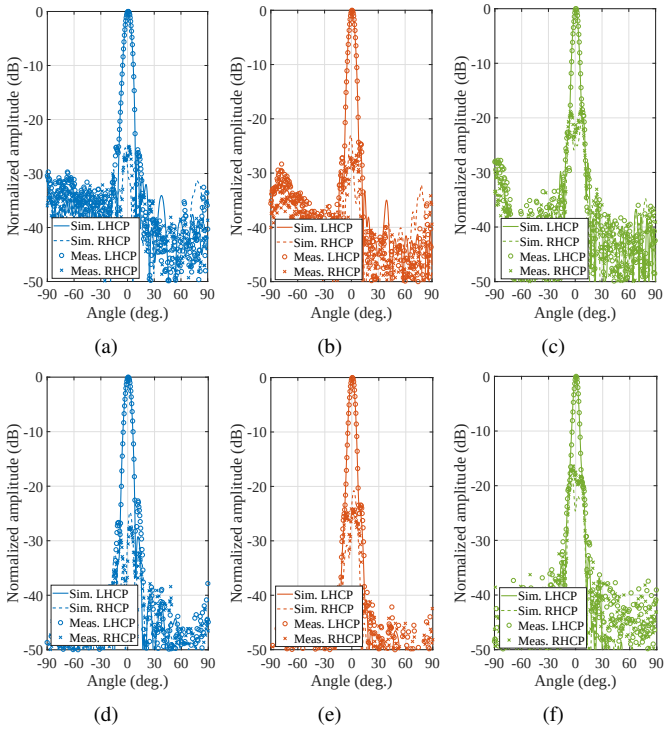

Fig. 16. Simulated and measured results of the normalized radiation patterns of the reflectarray along the operating bandwidth. For the E-plane: (a) at 35 GHz, (b) at 41 GHz and, (c) at 47 GHz. For the H-plane: (d) at 35 GHz, (e) at 41 GHz and, (f) at 47 GHz.

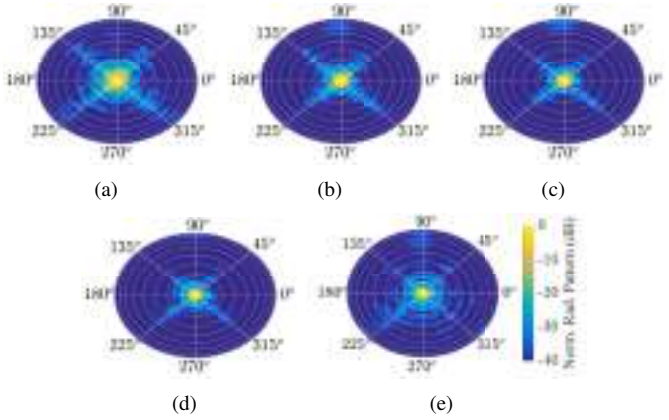

Fig. 17. Measured 3-D LHCP at different frequencies: (a) 32 GHz, (b) 36.5 GHz, (c) 41 GHz, (d) 45.5 GHz and, (e) 50 GHz. The radial lines mark the azimuth angles ϕ while their intersection with the concentric circles mark the elevation angles θ. The angular distance between each concentric circle is 10^{o}.

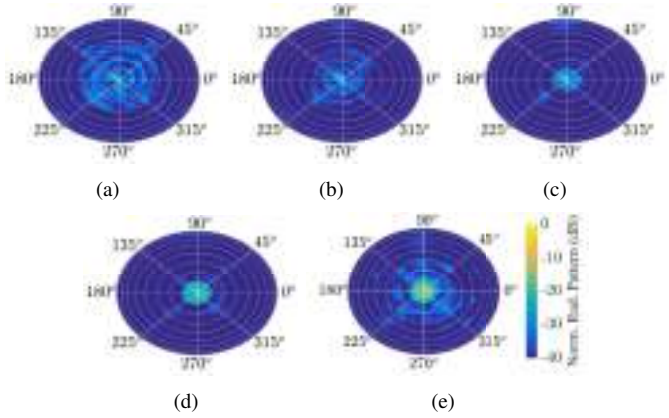

Fig. 18. Measured 3-D RHCP at different frequencies: (a) 32 GHz, (b) 36.5 GHz, (c) 41 GHz, (d) 45.5 GHz and, (e) 50 GHz. The angle of the radial lines mark the azimuth angles ϕ while their intersection with the concentric circles mark the elevation angles θ. The angular distance between each concentric circle is 10^{o}.

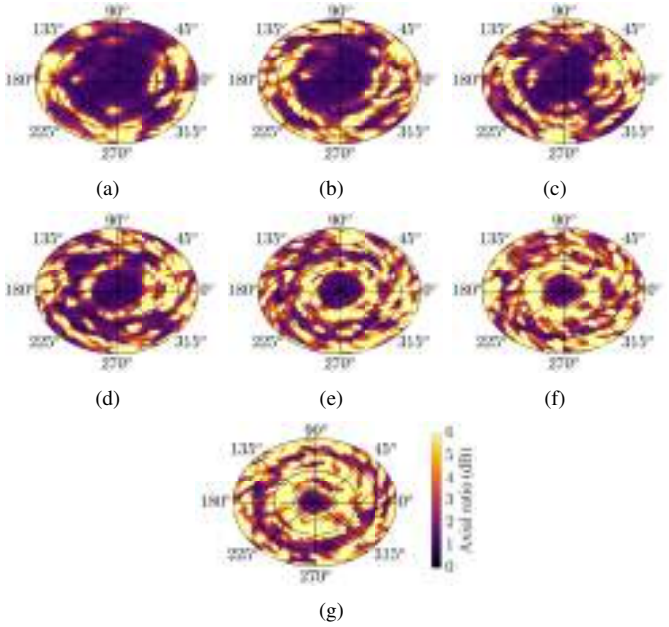

Fig. 19. Measured 3-D axial ratio at different frequencies: (a) 32 GHz, (b) 35 GHz, (c) 38 GHz, (d) 41 GHz, (e) 44 GHz, (f) 47 GHz and, (g) 50 GHz. The angle of the radial lines mark the azimuth angles ϕ while their intersection with the concentric circles mark the elevation angles θ. The angular distance between each concentric circle is 5^{o}.

To conclude with the RA characterization, Fig. 20 presents a comparison of the simulated and measured results for the realized gain and AR in the main beam direction. Both the realized gain and the measured AR are very close to the results obtained in simulation. This good agreement in the measured realized gain indicates that the high radiation efficiency is also obtained in the fabricated RA. Besides, the measured 3-dB AR bandwidth is also covered over the considered frequency range.

A performance comparison with the state-of-the-art metal-only RAs is done. Table II presents the main features of comparison between the proposed RA design and those reported in the literature. In this work, a wider 3-dB gain bandwidth with similar peak aperture efficiency is obtained compared to the other works. However, we can highlight that it is the first metallic RA that allows the control of both incident linear polarizations in addition to produce a large 3-dB AR bandwidth (43.9%). Recent work in [34] also achieves the independent control but for orthogonal circular polarizations. Its operating bandwidth is below millimeter frequencies with a lower peak aperture efficiency and 3-dB gain bandwidth regarding the proposed RA.

For the sake of completeness, Table III shows a comparison with the state-of-the-art works about fully-dielectric RAs in millimeter-wave frequencies. To make a fair comparison, the

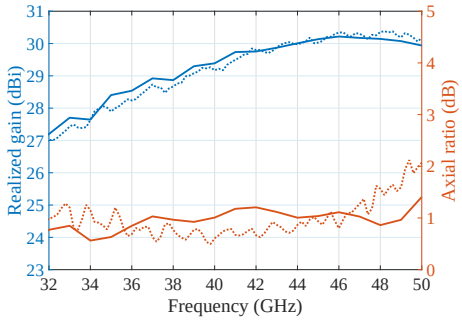

Fig. 20. Simulated and measured realized gain and AR at the main beam direction. The solid and dashed lines correspond to simulated and measured results, respectively.

included works either produce circular polarization or independently control the incident linear polarizations. It can be seen that although the other works can achieve similar 3-dB gain and AR bandwidths, the aperture efficiency is lower than the one obtained with the proposed RA. This is because it is difficult to find dielectrics with lower losses than metal in this frequency range and thus, metal-only RAs achieve higher radiation efficiency. Particular attention should be paid to the work in [35]. In that work, a unit cell design that controls the phase of both orthogonal incident polarizations by modifying the length of dielectric cuboids has been proposed. Nevertheless, the unit cell design relies on dielectrics, unlike the RA unit cell proposed in this work, which only uses metal in its structure. One of the consequences of using only metallic structures is the strong boundary conditions they impose, which in our design allow a negligible phase variation of the orthogonal polarization (lower than 1°). In contrast, the dielectric RA unit cell presented in [35] shows high phase variation for the polarization that is not intended to be modified. Additionally, our RA design mitigates the shadowing effect that appears in [35] and [36] since all the RA unit cells have the same length (L in Fig. 1). A high aperture efficiency is also obtained in this work with wider 3-dB gain bandwidth. Finally, it is noteworthy to say that thanks to the performance offered by the proposed RA unit cell, the 3-dB AR bandwidth is extended but in the presented results we have only considered the standard frequency band supported by WR22 waveguide.

V. Conclusions

A metal-only RA design that allows the phase control of impinging orthogonal polarizations is presented in this paper. Based on a unit cell with 3-D geometry, an independent phase tuning in a wide frequency range is achieved. In each unit cell, the modification of the reflected phase is implemented by the variation of the lengths of some metallic blocks in the propagating path of the wave inside the RA unit cell. The simulated results reveal a fairly linear reflected phase response along the frequency with high level of independent phase tuning in both orthogonal polarizations. In addition, this performance is maintained up to an angle of approximately 30° in oblique incidence. Thanks to this performance provided by the RA unit cell, a circularly-polarized RA antenna is designed. The RA is rotated by 45° regarding the linearly-polarized feed antenna to excite both polarizations in the unit cells that compose the RA. A prototype is fabricated and the measured results agree with the ones obtained in simulation. The presented RA antenna, which operates from 32 GHz to 50 GHz, produces a 3-dB gain bandwidth of 40.96% with a 2-dB AR bandwidth of 43.9%. Besides, the measured AR performs well in azimuth and elevation angles keeping the minimum values for AR around main beam direction. Finally, the measured realized gain has good agreement with the simulated one providing a radiation efficiency greater than 97% with a peak aperture efficiency of 55.4%.

TABLE II
Comparison between the proposed RA and reported metal-only RAs

Ref.	Center freq. (GHz)	3-dB Gain bandwidth	Peak aperture efficiency	Dual-pol control	3-dB AR bandwidth
[8]	60	10%	35%	No	26.5%
[10]	60	16.67%	60.3%	No	n. a.
[12]	75	9.2%	30.2%	No	n. a.
[15]	100	22.2%	50.1%	No	n. a.
[16]	94	19.8%	44.8%	No	n. a.
[17]	12.3	9.75%*	50%	No	n. a.
[18]	38	10.5%	n. a.	No	n. a.
[20]	9.3	24.2%*	50.6%	No	25%
[21]	27	22.2%	n. a.	No	n. a.
[34]†	27	18.2%	38%	Yes	18.2%
This work	41	40.96%	55.4%	Yes	43.9%

* 1-dB gain bandwidth.
† Independent control of circular polarizations.

TABLE III
Comparison between the proposed RAs and reported fully-dielectric RA at millimeter-waves

Ref.	Center freq. (GHz)	3-dB Gain bandwidth	Peak aperture efficiency	Radiation efficiency*	3-dB AR bandwidth
[35]	33	30%	34%	88.5%	42.7%
[37]	31	37.5%	32.5%	63% - 89%	43.2%
[38]	35	28.57%	16.4%	88.5%	n. a.
[39]	30	17.24%	16.5%	20% - 50%	19.3%
This work	41	40.96%	55.4%	97% - 99%	43.9%

* If the value is not given explicitly, it is calculated from the reflection losses of the RA unit cell.

Acknowledgment

The authors would like to thank Carmelo García-García for his help in the measurements and the spanish company Carlos Valero S.L. for its help and expertise in the metallization process.

References

[1] C. K. Anjinappa, F. Erden and I. Güvenç, "Base station and passive reflectors placement for urban mmWave networks," *IEEE Trans. Veh. Technol.*, vol. 70, no. 4, pp. 3525-3539, April 2021.

[2] W. Khawaja, O. Ozdemir, Y. Yapici, F. Erden and I. Guvenc, "Coverage enhancement for NLOS mmWave links using passive reflectors," *IEEE Open Journal of the Communications Society*, vol. 1, pp. 263-281, 2020.

[3] M. Di Renzo *et al.*, "Smart radio environments empowered by reconfigurable intelligent surfaces: how it works, state of research, and the road ahead," *IEEE J. Sel. Areas Commun.*, vol. 38, no. 11, pp. 2450-2525, Nov. 2020.

[4] C. Molero *et al.*, "Metamaterial-based reconfigurable intelligent surface: 3D meta-atoms controlled by graphene structures," *IEEE Commun. Mag.*, vol. 59, no. 6, pp. 42-48, June 2021.

[5] P. Nayeri, F. Yang, and A. Z. Elsherbeni, *Reflectarray antennas: theory, designs, and applications*. USA: Wiley, 2018.

[6] H. Chou, Y. Chen and H. Ho, "An all-metallic reflectarray and its element design: exploring the radiation characteristics of antennas for directional beam applications," *IEEE Antennas Propag. Mag.*, vol. 60, no. 5, pp. 41-51, Oct. 2018.

[7] R. Deng, F. Yang, S. Xu and M. Li, "A low-cost metal-only reflectarray using modified slot-type phoenix element with 360° phase coverage," *IEEE Trans. Antennas Propag.*, vol. 64, no. 4, pp. 1556-1560, April 2016.

[8] K. Q. Henderson and N. Ghalichechian, "Circular-polarized metal-only reflectarray with multi-slot elements," *IEEE Trans. Antennas Propag.*, vol. 68, no. 9, pp. 6695-6703, Sept. 2020.

[9] Y. G. Antonov, M. I. Sugak, S. V. Ballandovich, G. A. Kostikov and L. M. Liubina, "Design of wideband reflectarray antennas," in *2020 14th European Conference on Antennas and Propagation (EuCAP)*, 2020, pp. 1-5.

[10] Y. H. Cho, W. J. Byun and M. S. Song, "Metallic-rectangular-grooves based 2D reflectarray antenna excited by an open-ended parallel-plate waveguide," *IEEE Trans. Antennas Propag.*, vol. 58, no. 5, pp. 1788-1792, May 2010.

[11] D. Wang, R. Gillard, and R. Loison, "A 60 GHz passive repeater array with quasi-endfire radiation based on metal groove unit-cells," *Int. J. Microw. Wirel. Technol.*, vol. 8, no. 3, pp. 431–436, 2016.

[12] Y. H. Cho, W. J. Byun and M. S. Song, "High gain metal-only reflectarray antenna composed of multiple rectangular grooves," *IEEE Trans. Antennas Propag.*, vol. 59, no. 12, pp. 4559-4568, Dec. 2011.

[13] G. -B. Wu, Y. -S. Zeng, K. F. Chan, B. -J. Chen, S. -W. Qu and C. H. Chan, "High-gain filtering reflectarray antenna for millimeter-wave applications," *IEEE Trans. Antennas Propag.*, vol. 68, no. 2, pp. 805-812, Feb. 2020.

[14] B. Chen, H. Yi, K. B. Ng, S. Qu and C. H. Chan, "3D printed reflectarray antenna at 60 GHz," in *2016 International Symposium on Antennas and Propagation (ISAP)*, 2016, pp. 92-93.

[15] R. Deng, F. Yang, S. Xu and M. Li, "A 100-GHz metal-only reflectarray for high-gain antenna applications," *IEEE Antennas Wirel. Propag. Lett.*, vol. 15, pp. 178-181, 2016.

[16] W. Lee and Y. J. Yoon, "A broadband dual-metallic-reflectarray antenna for millimeter-wave applications," *IEEE Antennas Wirel. Propag. Lett.*, vol. 16, pp. 856-859, 2017.

[17] H. Chou, C. Lin and M. Wu, "A high efficient reflectarray antenna consisted of periodic all-metallic elements for the Ku-band DTV applications," *IEEE Antennas Wirel. Propag. Lett.*, vol. 14, pp. 1542-1545, 2015.

[18] H. Chou and J. W. Liu, "Synthesis and characteristic evaluation of convex metallic reflectarray antennas to radiate relatively orthogonal multi-beams," *IEEE Trans. Antennas Propag.*, vol. 66, no. 8, pp. 4008-4016, Aug. 2018.

[19] B. Zhang, C. Jin, Q. Lv, J. Chen and Y. Tang, "Low-RCS and wideband reflectarray antenna with high radiation efficiency," *IEEE Trans. Antennas Propag.*, vol. 69, no. 7, pp. 4212-4216, July 2021.

[20] G. Kong, X. Li, Q. Wang and J. Zhang, "A wideband reconfigurable dual-branch helical reflectarray antenna for high-power microwave applications," *IEEE Trans. Antennas Propag.*, vol. 69, no. 2, pp. 825-833, Feb. 2021.

[21] P. Mei, S. Zhang and G. F. Pedersen, "A low-cost, high-efficiency and full-metal reflectarray antenna with mechanically 2-D beam-steerable capabilities for 5G applications," *IEEE Trans. Antennas Propag.*, vol. 68, no. 10, pp. 6997-7006, Oct. 2020.

[22] S. M. A. Momeni Hasan Abadi and N. Behdad, "Broadband true-time-delay circularly polarized reflectarray with linearly polarized feed," *IEEE Trans. Antennas Propag.*, vol. 64, no. 11, pp. 4891-4896, Nov. 2016.

[23] C. Molero Jimenez, E. Menargues and M. García-Vigueras, "All-metal 3-D frequency-selective surface with versatile dual-band polarization conversion," *IEEE Trans. Antennas Propag.*, vol. 68, no. 7, pp. 5431-5441, July 2020.

[24] J. Velasco, I. Parellada-Serrano, and C. Molero, "Fully metallic reflectarray for the Ku-band based on a 3D architecture," *Electronics*, vol. 10, no. 21, p. 2648, Oct. 2021.

[25] C. Molero, H. Legay, T. Pierré and, M. García-Vigueras, "Broadband 3D-printed polarizer based on metallic transverse electro-magnetic unit-cells" *IEEE Trans. Antennas Propag.*, vol. 70, no. 6, pp. 4632-4644, June 2022.

[26] Y. He, Z. Gao, D. Jia, W. Zhang, B. Du and Z. N. Chen, "Dielectric metamaterial-based impedance-matched elements for broadband reflectarray," *IEEE Trans. Antennas Propag.*, vol. 65, no. 12, pp. 7019-7028, Dec. 2017.

[27] Á. Palomares-Caballero, C. Molero, P. Padilla, María García-Vigueras, and Raphaël Gillard, "Metal-only reflectarray unit cell for dual-polarization control," in *2022 16th European Conference on Antennas and Propagation (EuCAP)*, 2022.

[28] S. D. Targonski and D. M. Pozar, "Minimization of beam squint inmicrostrip reflectarrays using an offset feed," in *Proc. IEEE Antennas Propag. Soc. Int. Symp.*, Baltimore, MD, USA, Jul. 1996.

[29] E. Plaza, G. Leon, S. Loredo and F. Las-Heras, "A simple model for analyzing transmitarray Lenses," *IEEE Antennas Propag. Mag.*, vol. 57, no. 2, pp. 131-144, April 2015.

[30] A. Yu, F. Yang, A. Z. Elsherbeni, J. Huang, and Y. R. Samii, "Aperture efficiency analysis of reflectarray antennas," *Microw. Opt. Technol. Lett.*, vol. 52, no. 2, pp. 364–372, Feb. 2010.

[31] Jet Metal Tecnnologies. *Metallization principle*. Accessed: Jun. 2022. [Online]. Available: http://jetmetal-tech.com

[32] W. Feuray *et al.*, "Evaluation of metal coating techniques up to 66 GHz and their application to additively manufactured bandpass filters," in *2017 47th European Microwave Conference (EuMC)*, 2017, pp. 512-515.

[33] C. Pfeiffer and B. Tomasic, "Multi-octave linear-to-circular polarizers," in *2017 IEEE International Symposium on Antennas and Propagation & USNC/URSI National Radio Science Meeting*, 2017, pp. 673-674

[34] J. Zhu, S. Liao, S. Li and Q. Xue, "Additively manufactured metal-only millimeter-wave dual circularly polarized reflectarray antenna with independent control of polarizations," *IEEE Trans. Antennas Propag.*, 2022, doi: 10.1109/TAP.2022.3184474.

[35] Q. Cheng *et al.*, "Dual circularly polarized 3D printed broadband dielectric reflectarray with a linearly polarized feed," *IEEE Trans. Antennas Propag.*, vol. 70, no. 7, pp. 5393-5403, July 2022.

[36] P. Nayeri, M. Liang, R. A. Sabory-García, M. Tuo, F. Yang, M. Gehm, H. Xin, and A. Z. Elsherbeni, "3D printed dielectric reflectarrays: low-cost high-gain antennas at sub-millimeter waves," *IEEE Trans. Antennas Propag.*, vol. 62, no. 4, pp. 2000–2008, 2014.

[37] P. Mei, S. Zhang and G. F. Pedersen, "A wideband 3-D printed reflectarray antenna with mechanically reconfigurable polarization," *IEEE Antennas Wirel. Propag. Lett.*, vol. 19, no. 10, pp. 1798-1802, Oct. 2020.

[38] Y. -X. Sun, D. Wu and J. Ren, "Millimeter-wave dual-polarized dielectric resonator reflectarray fabricated by 3D printing with high relative permittivity material," *IEEE Access*, vol. 9, pp. 103795-103803, 2021.

[39] B. Li, C. Y. Mei, Y. Zhou and X. Lv, "A 3-D-printed wideband circularly polarized dielectric reflectarray of cross-shaped element," *IEEE Antennas Wirel. Propag. Lett.*, vol. 19, no. 10, pp. 1734-1738, Oct. 2020.

2.2.4 Metal-Only Reflect-Transmit-Array Unit Cell with Polarization-Dependent Performance

In order to exploit the benefits provided by the unit cell presented in the previous publications, a unit cell design for metal-only reflect-transmit-arrays is proposed in the following contribution. This extends the radiation capability to the full-space. Thanks to the polarization selectivity of the unit cell with 3D geometry used, the transmission and reflection phases can be tuned independently over a large bandwidth. This allows the realization of a reflect-transmit-array design where the angle of the main beams in reflection and transmission are set independently. In this paper, to demonstrate this electromagnetic capability, the design of a reflect-transmit-array has been carried out by having independent steering beams at a center frequency of 40 GHz.

THIS IS A POSTPRINT VERSION OF THE PAPER:

Á. Palomares-Caballero, C. Molero, Juan F. Valenzuela-Valdés, P. Padilla, M. García-Vigueras and R. Gillard, "Metal-Only Reflect-Transmit-Array Unit Cell with Polarization-Dependent Performance," in *2023 17th European Conference on Antennas and Propagation (EuCAP)*, 2023.

Disclaimer:
This work has been accepted in 17th European Conference on Antennas and Propagation.

Metal-Only Reflect-Transmit-Array Unit Cell with Polarization-Dependent Performance

Ángel Palomares-Caballero*, Carlos Molero*, Juan F. Valenzuela-Valdés*, Pablo Padilla*,
María García-Vigueras†, Raphaël Gillard†
*Departament of Signal Theory, Telematics and Communications, Universidad de Granada (CITIC-UGR),
18071 Granada, Spain
†UMR CNRS 6164, INSA Rennes, IETR, 35708 Rennes, France
email: angelpc@ugr.es

***Abstract*—A metal-only reflect-transmit-array unit cell whose operation is dependent on the incident polarization is presented. The proposed unit cell is based on 3D geometry which allows a high level of independent phase tuning for orthogonal and linear incident polarizations. In our unit cell, the horizontal polarization is reflected while the vertical polarization is transmitted. The modification of the reflected phase is done by the length of a metal block located at the end of the slits where the horizontal polarization propagates. The modification of the transmitted phase is changed by the depth of the corrugations implemented in the slit that supports the propagation of the vertical polarization. The results obtained in transmission mode show an impedance matching below -15 dB with a linear phase response from 30 GHz to 50 GHz. For the reflected polarization, there is almost total reflection with phase performance that is also linear along the frequency.**

***Index Terms*—Metal-only, millimeter-waves, polarization control, reflect-transmit-array.**

I. Introduction

Reflectarrays and transmitarrays emerged as versatile antenna solutions to increase the directivity of a primary radiating source. Reflectarrays [1] provide the collimation of the incident wave towards the desired direction by reflection while the transmitarray [2] performs it in transmission. Recently, a new type of antenna array has been proposed that combines the performance of both a reflectarray and a transmitarray in the same physical structure. This new antenna design concept has been referred to as reflect-transmit-array (RTA) antenna [3]. Due to the behavior that allows this type of antenna array, the elements that form it must provide both transmission and reflection, both with a similar magnitude. Regarding the introduced phase by the RTA antenna, this also has a similar value in both reflection and transmission making equal the angles of reflection and transmission of the main beams [3]–[5]. This situation does not allow to select independently the main direction of radiation in both reflection and transmission. In view of this issue, some works have proposed some solutions such as using the array-sparse method [6] or using a unit cell with a different phase response in dual band [7]. Nevertheless, some disadvantages appear when employing the previous solutions which is that the aperture efficiency decreases or that the desired performance is not in the same frequency band.

One manner to address these problems is that the reflection or transmission operation is each associated with a different polarization. That is, the RTA antenna should be polarization selective. In this way, the phase introduced in each orthogonal polarization can be independently tuned. Several RTA antennas based on this design strategy have been proposed for orthogonal linear polarizations [8]–[13]. In some of the previous works, this polarization-dependent behavior is achieved by stacking PCB layers where there is a pair of layers that are gratings in horizontal and vertical arrangement. There are also other works in the literature showing RTA antenna designs selective to orthogonal circular polarizations [14], [15].

Up to now, the RTA designs with polarization-dependent performance presented in the literature need the use of dielectrics which leads to reduce the antenna efficiency, specially when the frequency increases. In this paper, a new approach to design a RTA antenna with only metal structures is presented. The proposed metal-only unit cell design has a 3D geometry to take advantage of the benefits offered by this kind of structures [16]. More specifically, the one that allows for an independent control of different impinging linear polarizations [17]. Up to now, using 3D unit cells, only radiofrequency devices in transmission as polarizers [17], [18] and transmitarrays [19], or in reflection as reflectarrays [20]–[22], have been reported. Here, the proposed metal-only unit cell allows an independent selection of the phase value introduced for transmission and reflection depending on the incoming linear polarization.

II. Proposed RTA Unit Cell

In Fig. 1(a), the metal-only RTA unit cell is illustrated. All the parts seen in this figure are metal, more specifically aluminum has been considered as the material for all the simulations in this work. For the electromagnetic (EM) analysis of the unit cell, a plane wave excitation in positive z-direction has been considered. When this incident wave has the electric field (E-field) in y-direction, it will be regarded as vertically polarized (V-

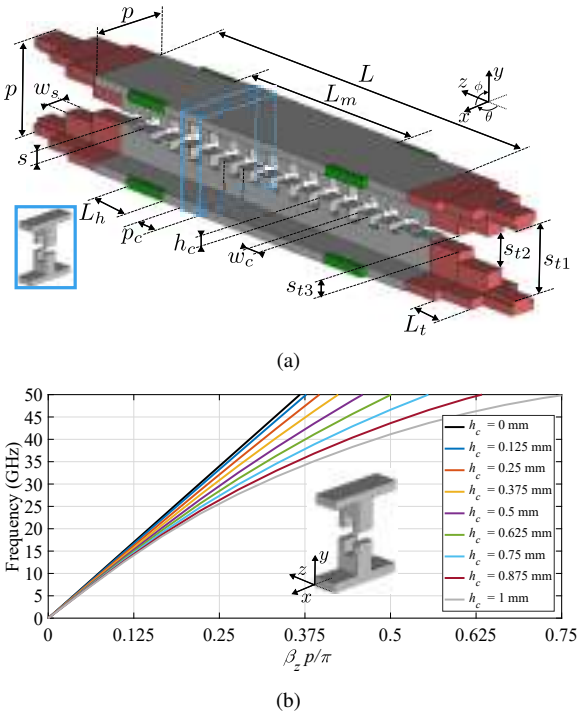

(a)

(b)

Fig. 1. (a) 3-D view of the proposed metal-only RTA unit cell. (b) Dispersion diagram of the corrugated unit cell. The dimensions (in mm) are: $p = 4$, $w_s = 0.8$, $L = 17.2$, $L_m = 9$, $L_t = 1.55$, $s_{t1} = 2.84$, $s_{t2} = 1.49$, $s_{t3} = 0.67$, $s = 0.5$, $p_c = 1.1$ and $w_c = 0.5$.

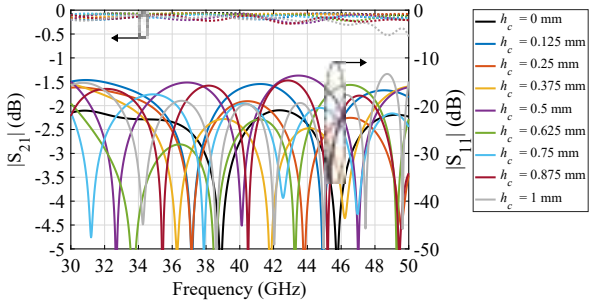

(a)

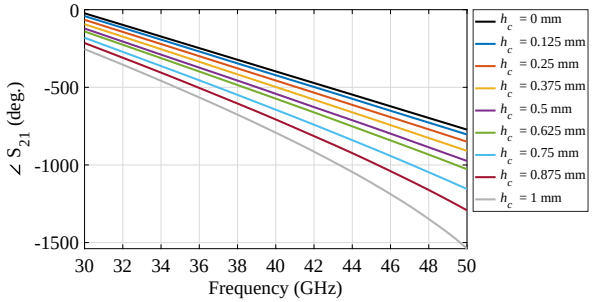

(b)

Fig. 2. S-parameters when a V-pol wave impinges on the unit cell and the h_c is swept: (a) in magnitude and, (b) in phase.

pol) while if it has the E-field in x-direction, it will be regarded as horizontally polarized (H-pol). In the EM analysis, the Frequency Solver of CST Studio Suite is employed where the periodic boundary conditions are set in the x- and y-directions of the unit cell. In a periodic environment, the unit cells are connected in the x-axis and they can be viewed as an array of parallel plate waveguides that are separated of a distance p in the x- and y-directions. The input port in the simulation is located in negative z-direction while the output port is placed in positive z-direction.

In order to better describe the unit cell, its most important parts have been highlighted in different colors in Fig. 1(a). The beginning and end of the structure (colored in red) are formed by three sections where each one of them corresponds to a slit with thickness w_s and width s_t. The length of these sections is L_t and the slits are aligned along both the x- and y- directions, they are symmetrical. These sections have been included to provide a good impedance matching between the free space and that of the slits located in the gray part. Following the characteristic impedance characterization procedure shown in [18], the impedance of these three sections has been designed to implement a binomial impedance transformer [23]. The block highlighted in green in Fig. 1(a) represents the phase tuning element for horizontal polarization. Depending on the L_h value, the reflected phase is modified. This part of the unit cell design is based on [22]. The last part of the unit cell is highlighted in gray. This corresponds to a slit of thickness w_s and width s, which has implemented corrugations along its length L. Metal corrugations are a way to realize slow wave structures and therefore modify the phase of the wave propagating along them. Fig. 1(b) shows the dispersion diagram of the unit cell with corrugations. As it can be seen in this figure, by increasing the depth of the corrugation h_c, the phase constant β_z is modified producing a higher phase shift. In addition, the modification of the β_z preserves the linearity along the frequency which is beneficial for the design of broadband transmitarray. It is important to point out that at the beginning and at the end of the slit with corrugations, a taper in h_c of the corrugated unit cells is needed to keep the reflection level low. The value of L has been selected to cover the 360º phase shift at the center frequency.

A. *Transmission and reflection performance*

After detailing the structure of the proposed unit cell, this subsection presents the phase and magnitude performances in both reflection and transmission.

Fig. 2 shows the results in phase and magnitude when the incident wave is V-pol in case of normal incidence ($\phi = 0^o$, $\theta = 0^o$). It can be seen that the reflection coefficient $|S_{11}|$ remains below -15 dB from 30 GHz to 50 GHz for all values of the range set for h_c. Consequently, the transmission coefficient $|S_{21}|$ stays quite high, above -0.5 dB over the entire frequency band. In relation to the phase introduced in transmission [see

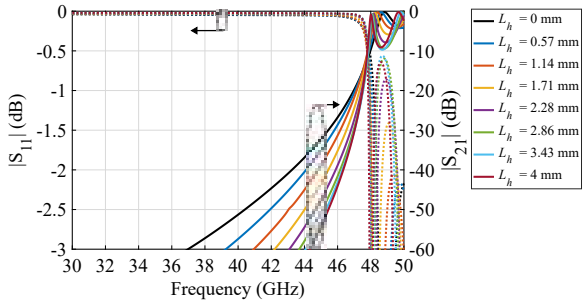

(a)

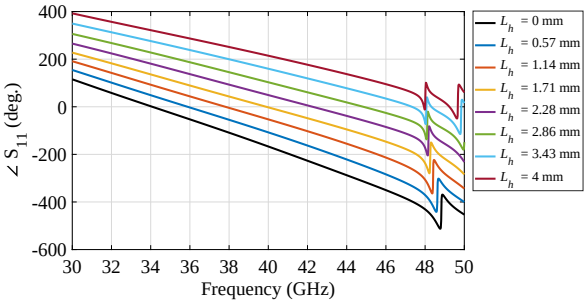

(b)

Fig. 3. S-parameters when a H-pol wave impinges on the unit cell and the h_c is swept: (a) in magnitude and, (b) in phase.

Fig. 2(b)], by modifying the value of h_c, the produced phase shift $\angle S_{21}$ is tuned reaching a range of 360º. Moreover, as predicted from the dispersion diagram, the phase shift keeps a linear behavior over the frequency band. Cross polarization values have been omitted for the sake of conciseness but these are below -50 dB across the whole band.

Regarding the reflection performance when an H-pol wave is impinging, the results are shown in Fig. 3. In this case, the tuning of the reflected phase is modified by the L_h value. The behavior of the $|S_{11}|$ and $|S_{21}|$ can be found in Fig. 3(a). It can be observed that there is almost total reflection up to about 47 GHz. From this frequency the $|S_{21}|$ increases greatly. This is due to the separation between metal plates in the y-direction. This separation value allows the propagation of TE_{10} along the unit cell since its cutoff frequency for the $p - w_s$ separation is 46.8 GHz. This problem has a straightforward solution by redesigning the unit cell to reduce the separation value and thus, increase the cutoff frequency of the undesired TE_{10} mode. In Fig. 3(b), it is shown the reflected phase value $\angle S_{11}$ when L_h is swept. The reflected phase behavior over the frequency is also linear and covers the 360º of variation necessary for reflectarray design. At the end of the frequency band, this desired phase behavior deteriorates due to the undesired propagation of the TE_{10} mode.

In order to show that there is independence in the phase tuning of both incident linear polarizations, Fig. 4 is displayed. This shows the transmission phase along the

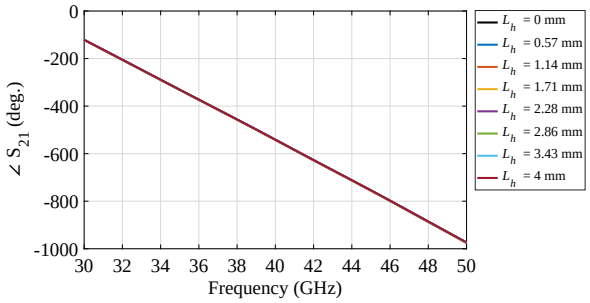

Fig. 4. Transmission phase in the vertical polarization when the length of the tuning elements L_h of the horizontal polarization is varied. The value for the depth of corrugation is fixed ($h_c = 0.5$ mm) for all curves where L_h is swept.

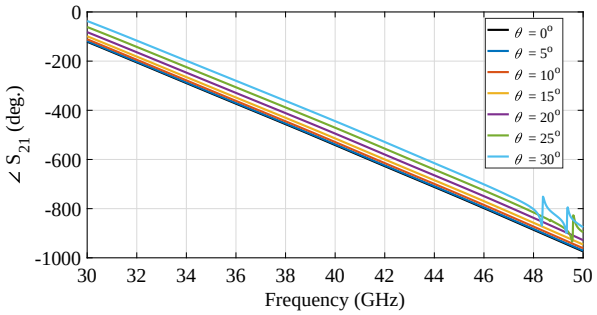

(a)

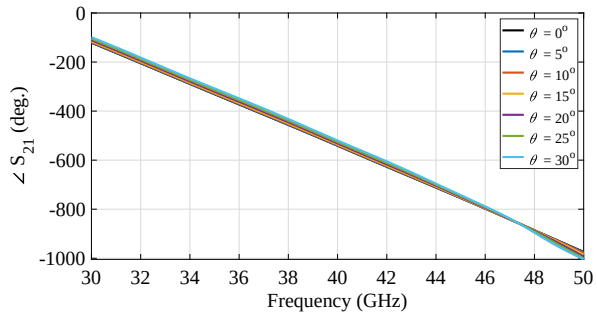

(b)

Fig. 5. Phase response for the V-pol under different oblique angles (θ) when $h_c = 0.5$ mm. (a) In the H-plane. (b) In the E-plane.

frequency when the tuning parameter L_h for horizontal polarization is modified. It can be seen how there is no disturbance of the $|S_{21}|$ curve, this is thanks to the 3D geometry used in the unit cell that allows a large decoupling between both orthogonal linear polarizations.

B. Oblique Incidence Performance

This subsection presents the performance of the proposed unit cell in oblique incidence situations. For this purpose, it has been studied how the phase in transmission and reflection is modified when the angle of incidence θ varies. The planes under study are the H-plane (XZ plane) and the E-plane (YZ plane). Fig. 5 displays the phase response along the frequency when a V-pol wave impinges and the θ is modified. The

depth value h_c is fixed for all values of θ and planes analyzed. When the value of θ is varied, the phase value in transmission is also modified but in an acceptable manner and maintaining the desired linear behavior in the whole frequency band. Also, it can be noted how the oblique incidence on the E-plane is the one that produces the least modification in the transmitted phase. On the other hand, Fig. 6 shows the reflected phase response when the value of θ changes. As in the previous case, the reflected phase is altered in an allowable manner while preserving linearity with frequency. Complementary to the previous polarization, for horizontal polarization, the H-plane is the most robust to changes in θ.

III. RTA Farfield Results

Once the unit cell has been thoroughly analyzed, this section shows its application in a complete RTA antenna. For this purpose, the simulated farfields have been calculated for a RTA composed of 21 x 21 unit cells illuminated by a standard WR22 horn with 20 dBi gain in oblique incidence ($\phi = -90^o$, $\theta = 20^o$). Fig. 7 shows the 3D radiation diagrams obtained when the array is illuminated with vertical and horizontal polarization. In the case of V-pol illumination, the phase map of the array has been computed to collimate the transmitted wave on the positive z-axis ($\phi = 0^o$, $\theta = 180^o$) as shown in Fig. 7(a). In contrast, for illumination with a H-pol wave, the collimation of the wave is done in reflection towards the direction: ($\phi = 90^o$, $\theta = 20^o$). This can be seen in Fig. 7(b). The resulting directivities produced by the RTA for both polarization situations are approximately 29.5 dBi.

IV. Conclusion

In this paper, a metal-only unit cell design has been presented that enables transmission or reflection depending on the impinging linear polarization. Thanks to the 3D geometry of the proposed unit cell, the modification of the reflected and transmitted phases is performed independently. For phase tuning in reflection, the length of the metal block located in the slit that supports the propagation of the horizontal polarization is modified. For phase tuning in transmission, corrugations have been included along the slit that allow the propagation of vertical polarization. Depending on the depth of the corrugations, the value of the transmitted phase is tuned. For both reflection and transmission, the performance achieved is as desired with linear phase response from 30 GHz to 50 GHz covering a phase tuning range of 360º. The unit cell has also been analyzed for different angles at oblique incidence. The simulated results have shown a good performance in oblique incidence, maintaining the linear phase response up to approximately 30º. The proposed unit cell has been used in a complete RTA antenna design. The radiation pattern results obtained demonstrate the collimation of the incident wave into two different directions depending on the polarization used in the feeder. Furthermore, a substantial increase of the incident wave directivity is observed in both polarization cases. The proposed design shows the capability of being metal-only and having a polarization-dependent behavior, which has not been presented before for RTAs.

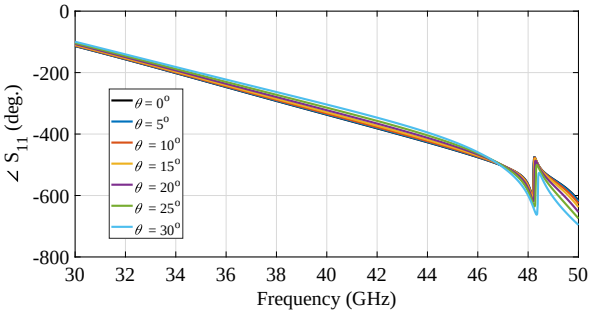

(a)

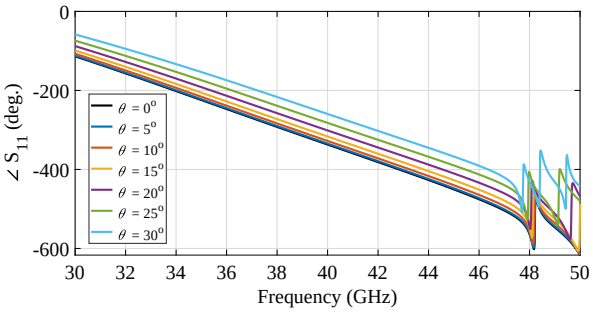

(b)

Fig. 6. Phase response for the H-pol under different oblique angles (θ) when $L_h = 2$ mm. (a) In the H-plane. (b) In the E-plane.

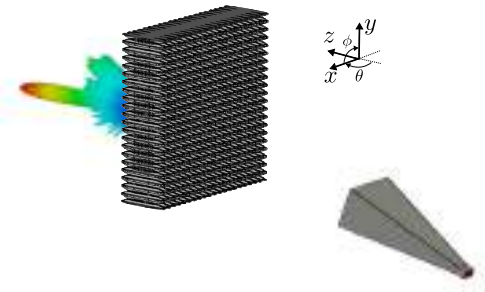

(a)

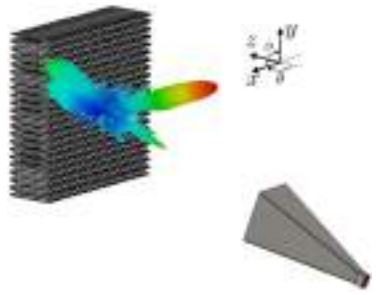

(b)

Fig. 7. Farfield results of the proposed RTA antenna at 40 GHz when it is illuminated by a: (a) V-pol wave and, (b) H-pol wave. The feeder is a standard WR22 horn antenna.

ACKNOWLEDGMENT

This work was supported in part by the Spanish Government under Project PID2020-112545RB-C54, Project RTI2018-102002-A-I00, Project TED2021-129938B-I00 and Project TED2021-131699B-I00; in part by the "Junta de Andalucía" under Project A-TIC-608-UGR20, Project PYC20-RE-012-UGR, and Project P18.RT.4830; and in part by the Predoctoral Grant FPU18/01965.

REFERENCES

[1] P. I. Theoharis, R. Raad, F. Tubbal, M. U. A. Khan and A. Jamalipour, "Wideband Reflectarrays for 5G/6G: A Survey," *IEEE Open J. Antennas Propag.*, vol. 3, pp. 871-901, 2022.

[2] J. R. Reis, M. Vala and R. F. S. Caldeirinha, "Review Paper on Transmitarray Antennas," *IEEE Access*, vol. 7, pp. 94171-94188, 2019.

[3] F. Yang, R. Deng, S. Xu, and M. Li, "Design and experiment of a near-zero-thickness high-gain transmit-reflect-array antenna using anisotropic metasurface," *IEEE Trans. Antennas Propag.*, vol. 66, no. 6, pp. 2853–2861, Jun. 2018.

[4] M. R. Akram, G. Ding, K. Chen, Y. Feng, and W. Zhu, "Ultrathin single layer metasurfaces with ultra-wideband operation for both transmisión and reflection," *Adv. Mat.*, vol. 32, no. 12, Mar. 2020, Art. no. 197308.

[5] M. Wang, S. Xu, F. Yang and M. Li, "A 1-Bit Bidirectional Reconfigurable Transmit-Reflect-Array Using a Single-Layer Slot Element With PIN Diodes," *IEEE Trans. Antennas Propag.*, vol. 67, no. 9, pp. 6205-6210, Sept. 2019.

[6] S. L. Liu, X. Q. Lin, Y. H. Yan and Y. L. Fan, "Generation of a High-Gain Bidirectional Transmit–Reflect-Array Antenna With Asymmetric Beams Using Sparse-Array Method," *IEEE Trans. Antennas Propag.*, vol. 69, no. 9, pp. 6087-6092, Sept. 2021.

[7] X. Wang, J. Ding, B. Zheng, S. An, G. Zhai, and H. Zhang, "Simultaneous realization of anomalous reflection and transmission at two frequencies using bi-functional metasurfaces," *Sci. Rep.*, vol. 8, p. 1876, Jan. 2018.

[8] T. Cai, G. -M. Wang, X. -L. Fu, J. -G. Liang and Y. -Q. Zhuang, "High-Efficiency Metasurface With Polarization-Dependent Transmission and Reflection Properties for Both Reflectarray and Transmitarray," *IEEE Trans. Antennas Propag.*, vol. 66, no. 6, pp. 3219-3224, June 2018.

[9] W. Song *et al.*, "A Single-Layer Reflect-Transmit-Array Antenna With Polarization-Dependent Operation," *IEEE Access*, vol. 9, pp. 167928-167935, 2021.

[10] S. Liu and Q. Chen, "A Wideband, Multifunctional Reflect-Transmit-Array Antenna With Polarization-Dependent Operation," *IEEE Trans. Antennas Propag.* vol. 69, no. 3, pp. 1383-1392, March 2021.

[11] G. Shang *et al.*, "Transmission–Reflection-Integrated Multiplexed Janus Metasurface," *ACS Appl. Electron. Mater.* vol. 3, no. 6, pp. 2638-2645, 2021.

[12] H. Yi, S. -W. Qu, K. -B. Ng, C. K. Wong and C. H. Chan, "Terahertz Wavefront Control on Both Sides of the Cascaded Metasurfaces," *IEEE Trans. Antennas Propag.*, vol. 66, no. 1, pp. 209-216, Jan. 2018.

[13] Y. Wang *et al.*, "Broadband High-Efficiency Ultrathin Metasurfaces With Simultaneous Independent Control of Transmission and Reflection Amplitudes and Phases," *IEEE Trans. Microw. Theory Tech.*, vol. 70, no. 1, pp. 254-263, Jan. 2022.

[14] W. Yang, K. Chen and Y. Feng, "Multifunctional Metasurface for Broadband Reflect-Transmit-Array Antenna at 5G Millimeter-Wave Band," in *2022 16th European Conference on Antennas and Propagation (EuCAP)*, 2022, pp. 1-5.

[15] J. Feng *et al.*, "Reflect-Transmit-Array Antenna With Independent Dual- Circularly Polarized Beam Control," *IEEE Antennas Wirel. Propag. Lett.*, 2022, doi: 10.1109/LAWP.2022.3202955.

[16] A. Alex-Amor, Á. Palomares-Caballero and C. Molero, "3-D Metamaterials: Trends on Applied Designs, Computational Methods and Fabrication Techniques," *Electronics*, vol. 11, no. 3, p. 410, Jan. 2022.

[17] C. Molero Jimenez, E. Menargues and M. García-Vigueras, "All-Metal 3-D Frequency-Selective Surface With Versatile Dual-Band Polarization Conversion," *IEEE Trans. Antennas Propag.*, vol. 68, no. 7, pp. 5431-5441, July 2020.

[18] C. Molero, H. Legay, T. Pierré and M. García-Vigueras, "Broadband 3D-Printed Polarizer Based on Metallic Transverse Electro-Magnetic Unit-Cells," *IEEE Trans. Antennas Propag.*, vol. 70, no. 6, pp. 4632-4644, June 2022.

[19] X. Wang, Y. Cheng and Y. Dong, "Millimeter-Wave Dual-Polarized Metal Transmitarray Antenna With Wide Gain Bandwidth," *IEEE Antennas Wirel. Propag. Lett.*, vol. 21, no. 2, pp. 381-385, Feb. 2022.

[20] C. Molero *et al.*, "Metamaterial-Based Reconfigurable Intelligent Surface: 3D Meta-Atoms Controlled by Graphene Structures," *IEEE Commun. Mag.*, vol. 59, no. 6, pp. 42-48, June 2021.

[21] Á. Palomares-Caballero, C. Molero, P. Padilla, M. García-Vigueras and R. Gillard, "Metal-Only Reflectarray Unit Cell for Dual-Polarization Control," in *2022 16th European Conference on Antennas and Propagation (EuCAP)*, 2022, pp. 1-4.

[22] Á. Palomares-Caballero, C. Molero Jiménez, P. Padilla, M. García-Vigueras and R. Gillard, "Wideband 3-D-Printed Metal-only Reflectarray for Controlling Orthogonal Linear Polarizations," to be appear in *IEEE Trans. Antennas Propag.*

[23] D. Pozar, *Microwave Engineering*, 4th ed. Hoboken, NJ, USA: Wiley, 2004.

2.2.5 Metamaterial-Based Reconfigurable Intelligent Surface: 3D Meta-Atoms Controlled by Graphene Structures

RIS is a topic of great interest in the paradigm of future wireless communications, however, the design of RIS reported in the literature is subject to the use of 2D layers. In the following publication, a design of RIS based on unit cells (or meta-atoms) with 3D geometry is proposed. The use of 3D geometry allows independent control of the incident polarizations offering greater opportunities in the control of the wireless environment. The use of graphene as a reconfigurable material is also proposed where its sheet resistance value is modified to obtain 1-bit reconfiguration in the meta-atom. In addition, the use of graphene extends the functionalities of RIS by allowing an absorption state with the selection of an intermediate sheet resistance value. All these functionalities have been numerically verified through the design of a 3D RIS whose central operating frequency is 28 GHz.

THIS IS A POSTPRINT VERSION OF THE PAPER:

C. Molero, Á. Palomares-Caballero, A. Alex-Amor, I. Parellada-Serrano, F. Gamiz, P. Padilla, J. Valenzuela-Valdés, "Metamaterial-Based Reconfigurable Intelligent Surface: 3D Meta-Atoms Controlled by Graphene Structures," in *IEEE Communications Magazine*, vol. 59, no. 6, pp. 42-48, June 2021.

- Journal Impact Factor (JIF) in JCR 2021: 9.030
- Category: ENGINEERING, ELECTRICAL & ELECTRONIC. JIF Rank: 22/276 (Q1).
- Category: TELECOMMUNICATIONS. JIF Rank: 7/93 (Q1).

Disclaimer:
This work has been published on IEEE Communications Magazine. DOI: 10.1109/MCOM.001.2001161

Metamaterial-Based Reconfigurable Intelligent Surface: 3-D Meta-Atoms Controlled by Graphene Structures

Carlos Molero, Ángel Palomares-Caballero, Antonio Alex-Amor, Ignacio Parellada-Serrano, Francisco Gamiz, Pablo Padilla, and Juan F. Valenzuela-Valdés

ABSTRACT

The upcoming high-speed wireless communication systems will be hosted by millimeter and sub-millimeter-wave frequency bands. At these frequencies, electromagnetic waves suffer from severe propagation losses and non-line-of-sight (NLOS) scenarios. A new wireless communication paradigm has arrived to resolve this situation through the use of reconfigurable intelligent surfaces (RIS). These metadevices are designed to reconfigure the wireless environment in a smart way. Traditional RIS designs based on the implementation of 2-D configurations have been considered up to now. However, 3-D structures enable an extra degree of freedom in the design that can be taken as an advantage for the development of improved RIS structures with advanced functionalities. This article proposes the implementation of a novel electronically-reconfigurable RIS based on the use of 3-D graphene meta-atoms. The reconfigurability lies on the graphene conductivity, easily tunable with a biasing voltage. Different conductivity values vary the meta-atom electromagnetic response, modifying the RIS functionality. A multi-objective optimization framework determines the optimal phase state of each meta-atom to accomplish the desired RIS performance. The operation of the RIS as an efficient beam steerer/splitter, absorber and polarization selector is validated with full-wave results.

INTRODUCTION

Wireless communications in the present 5G and future 6G systems will dramatically provide an enhancement of several key performance indicators such as the user data rate, the spectral efficiency and latency [1]. These improvements in the requirements of the communication system entail breakthroughs in the employed technologies. The use of millimeter-waves (mm-waves) and terahertz communications, beamforming capability of the antennas or ultra-dense networks are some of the proposed technologies to achieve the latter communications requirements. A recent paradigm for wireless communication is based on reconfigurable intelligent surface (RIS) [2]. It allows smart modifications of the communication environment in order to fulfill the needs of the wireless links among users. Some of the desirable functionalities for a RIS are: beam steering, beam splitting, wave absorption, polarization and phase control of the reflected wave [3], [4]. The applications of these RIS functionalities in the wireless communication are the avoidance of the non-line-of-sight (NLOS) scenarios, interference mitigation, block of eavesdropping and jamming or multi-user coverage. Normally, the design and implementation of the RIS is based on coding metasurfaces composed by unit cells called meta-atoms [2]. The meta-atoms must incorporate reconfigurable elements, e. g. PIN diodes, to set the functionality of the RIS [5] according to the requirements of the users.

Diversity of designs and implementations of RIS are beginning to emerge [4], [6]. Most of them employ PIN diodes in the unit cell to achieve different phase shift responses to define the phase states of the meta-atom. Besides, printed circuit boards (PCB) technology is the preferable manufacturing technique for the implementation of the RIS unit cells. Recently, huge advances in 3-D manufacturing technology as well as numerous options to fabricate tridimensional designs are commercially available. Specially, this kind of manufacturing technique enables the cost-effective realization of 3-D complex prototypes, sometimes infeasible with traditional techniques, e.g. computer numerical control (CNC). This new reality of multiple 3D-printing manufacturing processes has been leveraged by the antenna engineering community to realize radiofrequency (RF) designs covering from microwave band to millimeter-waves.

3-D metastructures offer advanced functionalities compared to classical 1-D and 2-D metasurfaces (see Table I). First, fully metallic configurations can be conceived in 3-D configurations, avoiding the presence of dielectrics (and the associated dielectric losses) and enhancing the efficiency of the device. Additionally, in 1-D and 2-D metasurfaces, the degrees of freedom controlling the structure behavior are mainly included in the elements extended along the transverse x and y components. This is the case, for example, given in PCB manufacturing. However, 3-D printing techniques allow for the inclusion of elements not only along the plane containing the transverse directions (as in 2-D designs), but also along the propagation direction z. This additional degree of freedom associated to 3-D structures can be exploited in the design of novel RIS with advanced functionalities: beam steering, beam splitting, absorption and polarization selectivity. In particular, polarization control of the incident electromagnetic waves is a challenging task in conventional 2-D metasurfaces, since independent current control of the different polarization states is hardly achievable. This is different in 3-D structures, where an independent control of the polarization states is possible, as it will be discussed in detail later.

2-D reconfigurable metagratings [7], [8] have recently

emerged as an alternative of gradient metasurfaces such as RIS. They present an enhanced beam steering with greater simplicity from the geometrical and analytical point of view, since they are based on classical gratings and patch arrays. However, their beam directions in beam steering- and beam splitting-operations are restricted to a few pointing angles.

An interesting alternative to conventional PIN diodes for reconfigurability is the inclusion of biasing-controlled graphene layers in the meta-atom. This kind of reconfigurable structures are being increasingly employed to design RF devices such as attenuators, tunable antennas, absorbers, etc [9]. The graphene sheet is biased by a given voltage. The variation of this voltage modifies the conductivity of graphene and therefore, the surface resistance of the layer. For example, a graphene pad placed in the middle of a microstrip line allows good propagation for a certain value of the sheet resistance, and otherwise increases the insertion losses if a different value is induced. The result is a reconfigurable microstrip attenuator. Graphene structures have been implemented for layered structures only for RIS working in the terahertz band [10]. In this article, we present a novel RIS design based on 3-D meta-atoms with reconfigurability performance provided by graphene structures. A convenient tuning of the surface resistance drastically changes the behavior of the meta-atom. The proposed design conceives a step further from the conventional RIS by profiting the third dimension in the meta-atom. Additionally, the negligible polarization time of graphene is potential for real-time reconfiguration of the radiation performance of the RIS, which is a key feature in future communication systems.

The article is organized as follows. The following section depicts the proposed RIS based on 3-D meta-atoms and the reconfigurable mechanism based on graphene structures. Then, we detail the design procedure followed to obtain the required functionality in a RIS. Later, we discuss the multiple functions provided by the RIS that are analyzed by full-wave electromagnetic simulations. Finally, the conclusions are drawn in the last section.

3-D META-ATOMS STRUCTURE

Metallic meta-atoms with 3-D architecture are actually unit-cell configurations exploiting the three spatial dimensions for the control of electromagnetic waves. Unlike 2-D devices, 3-D meta-atoms use the propagation direction to add new degrees of freedom [11]. This issue is key, resulting in the increase of the number of functionalities of the RIS. 3-D metallic meta-atoms are based on multi-purpose waveguide architectures, as for instance, waveguides with square, triangular or hexagonal sections. The scattering control of the electromagnetic waves demands small dimensions of the waveguide, in order to avoid diffractive and dispersive phenomena that would introduce additional handicaps. This is a design constraint assumed, leading us to impose waveguide dimensions no longer than $\lambda/2$ at the desired operation frequency.

The structure of the RIS under consideration is shown in Fig. 1, consisting of a fully-metallic configuration comprising modified square waveguide sections backed by a metallic plane. Fully-metallic designs are desired in RF since they avoid dielectric losses. Moreover the operation frequency in fully-metallic designs can readily be translated to other frequency ranges just by applying a simple scaling in the dimensions of the structure.

2-D structures	Feature	3-D structures
PCB technology and layer stacking	**Manufacturing**	3-D printing (Single piece)
Dielectric losses (Substrates)	**Losses**	Ohmic losses (Printed/coated metal)
Standard	**Functionalities**	Advanced (More degrees of freedom)
Not proportional to increasing frequency (Complex to scale)	**Profile at mm-waves**	Proportional to increasing frequency (Easy to scale)
Low cost (PCB manufacturing)	**Price**	Medium cost (3-D printing + coating)
Challenging (Complex current control)	**Polarization Control**	Easy (Independent pol. states)

TABLE I: Feature comparison between 2-D and 3-D structures for RIS design.

The 3-D meta-atoms of the proposed RIS are placed periodically along horizontal x- and vertical y- directions. The square geometry of the waveguide section supports the existence of degenerate modes; namely, modes that are orthogonal to each other and have the same cutoff frequency. This fact encourages us to address a control of different field polarizations by using both degenerate modes, as shown in Fig. 1 for horizontal (H-pol) and vertical (V-pol) polarizations. This could potentially lead to enhanced information transmission, as data can be multiplexed in both degenerate (orthogonal) states.

The ground plane at the bottom of the structure ensures full-reflection response. This means that the square waveguides that define each meta-atom are short-circuited at the end. This scenario imposes the incident radiation to be reflected back. The intelligent behavior of the structure comes from an efficient manipulation of these reflected waves. This is achieved by adding electromagnetic resonators at each lateral walls of the waveguide in the form of apertures, as illustrated in Fig. 1. The presence of these resonators does not alter the amplitude response of the reflected wave, but does change its phase response. In other words, each meta-atom acts as an individual phase shifter. The outgoing phase associated with every single meta-atom then depends on the geometry of their resonators. Certain resonator geometries facilitate the phase control. A suitable aperture geometry is the split-ring resonator, that has been object of study in the field of metamaterial design [12].

The reconfigurability of RIS by using the structure presented in this work is easily achievable by modifying artificially the geometry of the split rings per meta-atom. For this, graphene sections printed on silicon-slabs are a good alternative. Graphene sheets are in physical contact with the split rings as it is shown in Fig. 1. An ON/OFF-switching behavior is easily induced in graphene just by biasing it with a given voltage V_b. Higher-voltages biasing induce an effective high conductivity in the graphene layer, thus graphene becomes a

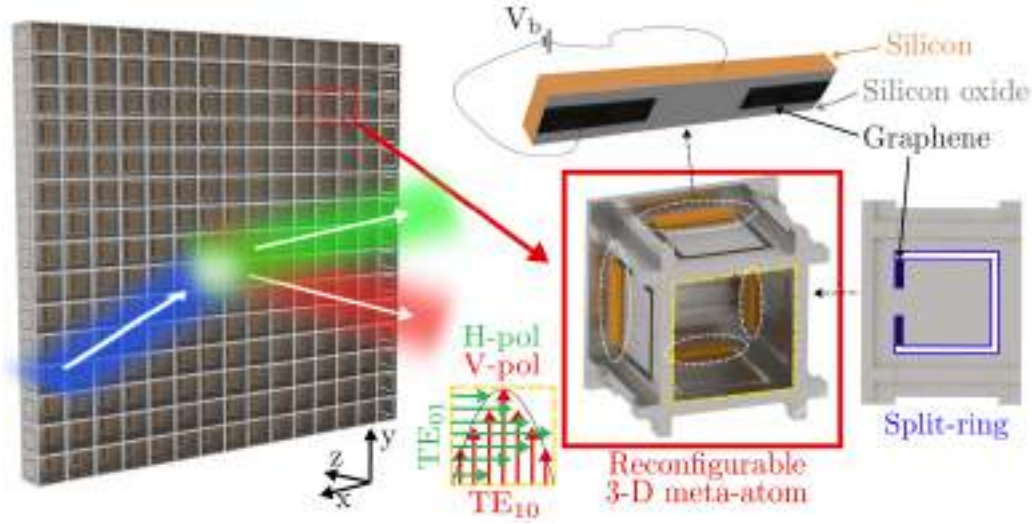

Fig. 1: Proposed RIS design formed by reconfigurable 3-D meta-atoms based on graphene structures, and key geometries and structures of the meta-atom.

good conductor. Lower voltages reduce considerably the conductivity in graphene, so graphene becomes worse conductor. The surface resistance R_s of the graphene sheet moves from lower values (ON) to higher values (OFF) [9]. The dichotomy between better/worse conductor is conceived as an ON/OFF switching, respectively. When ON is activated, the graphene layers act as additional metallic sections of the split ring, modifying its original shape. This provokes a global reduction of the length of the resonator. When OFF is activated, this additional layer does not act, and the split-ring recovers its original shape. The double shape of the split rings induced by the graphene sheets is translated to the outgoing phase in the form of two different phase states. A first phase state is defined at 0 degrees, related to graphene in ON. A second state is defined at 180 degrees, induced by graphene in OFF. It is worth remarking that an operation frequency is previously selected in order to decide the split ring dimensions.

Concerning the manufacturing process of the structure under consideration, several 3-D printing options are available to achieve a successful fabrication. Stereolitography (SLA) followed by a metal plating is one of the most interesting option to realize 3-D components since it provides high-precision at printing millimeter-wave devices [11]. Higher precision in the 3-D manufacturing is also feasible employing micromachining techniques with a later metallization, such as the SU-8 or deep reactive ion etching (DRIE) processes, which are now emerging as suitable manufacturing techniques for sub-millimeter wave structures. Another option to manufacture fully-metallic structures is the direct metal laser sintering (DMLS). This last, unlike the above manufacturing options, directly prints the structure on a metallic piece. Nonetheless, it is important to consider that this 3-D printing technique suffers from moderate roughness surface and consequently, the performance of the structure can be affected by efficiency losses.

RECONFIGURABLE MATERIALS

Different materials can be employed in order to reconfigure the meta-atoms. Although the proposed one in Fig. 1 is graphene, other materials could be employed with this goal. For example, binary or ternary chalcogenide alloys like GeTe or GeSbTe present high resistance in the amorphous off-state and low resistance in the crystalline on-state [13]. The phase transition between the two states is reversible and can be achieved by short heating pulses either by electrical current or by light. Moreover, other 2-D materials can be used: transition metal dichalcogenides, TMDs (MoS_2, WS_2, $MoSe_2$, WSe_2, HfS_2, and others) and 2-D dielectrics such as hexagonal boron nitride (hBN) could be deposited by chemical vapor deposition on sacrificial substrates. Once the 2-D material layers are grown, they are transferred to the target substrate for its structural and electrical characterization. An open issue is the comparison of conductivity tunability of these structures with the one obtained with graphene.

Graphene is a zero-bandgap material (i.e., a semimetal) showing an ambipolar behavior. The conductivity of the graphene layer can be electrostatically modulated by a perpendicular electric field. Such an electric field can be obtained, for example, by capacitively coupling a graphene layer on top of a silicon oxide (SiO_2) and silicon (Si) structure, and applying a DC voltage between the graphene and the SiO_2/Si substrate, as illustrated in Fig. 1. The SiO_2 acts as an insulator in order to prevent the short-circuit between the graphene and the silicon when the voltage is applied. This principle is extensively exploded in graphene field-effect transistors GFETs [9], and GFET chemical sensors.

High-quality graphene layers can be obtained through mechanical exfoliation of highly oriented pyrolytic graphite (HOPG), by epitaxially growth on silicon carbide (SiC) substrates, and by CVD on sacrificial metal foils and later transfer to the final substrates [9]. In opposite to mechanical exfoliation and epitaxially growth techniques, CVD and plasma chemical vapor deposition (PCVD) can provide graphene samples with a few centimeters of size at the time that they keep the high

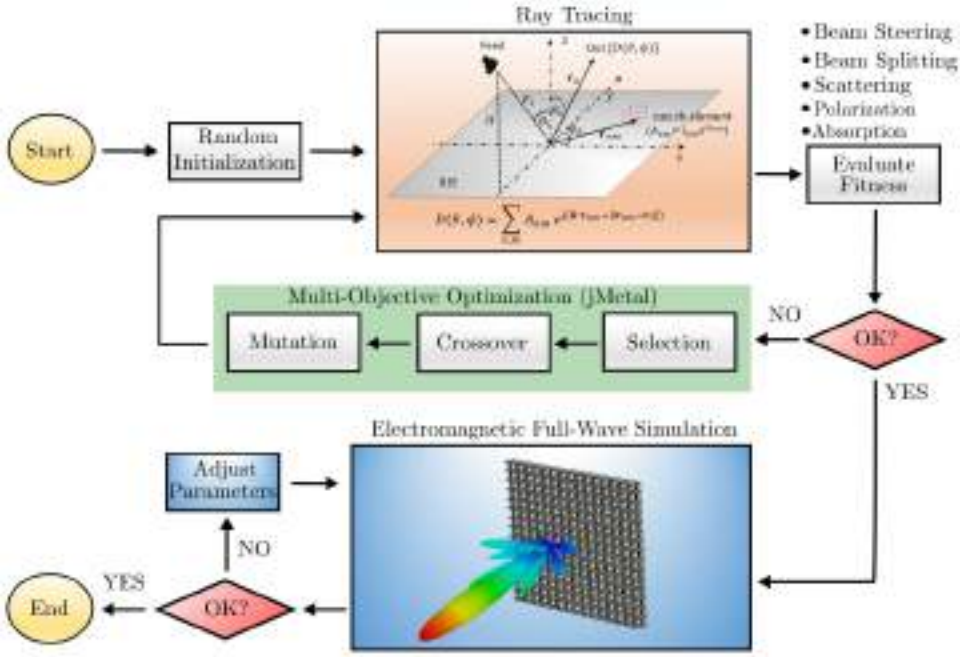

Fig. 2: Flowchart that describes the design procedure of the metamaterial-based RIS.

quality of the graphene sheet. This technique would be the suitable one for the fabrication of the employed graphene structures inserted in the 3-D meta-atom. The graphene layers are in physical contact with metallic walls of each 3-D meta-atom while the silicon substrates do not touch any point of that structure. In this way, an adequate voltage polarization can be carried out by grounding the metallic-structure of the RIS and wiring each silicon slab in order to apply certain voltage to generate the ON/OFF states.

As it is pointed above, graphene structures are placed at the split-rings of the 3-D meta-atom to tune its geometry. When the graphene has low surface resistance (high conductivity) the slit that defines the split-ring is shortened and therefore, modifying the phase shift response from the original split-ring. Nevertheless, the range of values for the surface resistance of the graphene is not discrete and depends on the polarization voltage. In this range, there may be values that allow the 3-D meta-atom to absorb the power of the incident wave. As it is shown in [14], the maximum losses produced by the graphene are in a determined range of surface resistance values (Ω/sq). The absorption should occur when there is good impedance matching between the incident wave and reconfigurable meta-atom. In this case, the energy that carries the incident wave is not reflected but dissipated in the graphene structures due to the favorable impedance matching between the RIS and the free space.

DESIGN PROCEDURE

From a formal point of view, the total radiation of the RIS can be decomposed into the sum of the individual contributions of the meta-atoms that form it. Thus, the radiation of each meta-atom contributes to create constructive or destructive patterns at certain spatial regions. By properly adjusting the states (ON/OFF) of the meta-atoms, the energy can, for example, be concentrated at a particular direction of space. As previously discussed, these states correspond to a variation of the outgoing phase when the incident wave impinges the structure. For the present configuration, the geometrical parameters of the meta-atoms are engineered so that the ON/OFF states show a phase difference of 180 degrees while maintaining the same amplitude level. In other words, the information of the ON/OFF states can be codified with the phase states 0 and 180 degrees, respectively. This fact simplifies the design of the structure, since the RIS can be equivalently seen as a 1-bit reconfigurable reflectarray whose elements are assumed to have identical amplitudes but can take two different phase states.

Fig. 2 presents the flowchart that summarizes the design procedure. We rely on the use of a self-implemented ray-tracing tool to find the optimal coding arrangement of the meta-atoms that ensure the correct performance of the RIS considering the selected operation mode and the distance that can exist between the RIS and the emitting source. The phase distribution of the meta-atoms is then optimized with a multi-objective genetic algorithm based on a Java framework, jMetal [15]. Genetic algorithms are suitable in this kind of scenarios, where multiple objectives, input variables and variable restrictions must be jointly considered. These algorithms typically start with a random initial population (in our case, the phase arrangements in the RIS) and use the information provided by the evaluation of the current population of individuals to create the next population. The validity of the solutions is tested with a fitness value/s produced by a single or several cost functions depending of the optimization goals. The selection of the fitness criteria will depend on the operation mode of the RIS. As an example, the beam-steering mode seeks to redirect the main beam in a single region of space. Thus, the fitness function relates the amount of energy concentrated in that

particular region of space, which must be maximized by the multi-objective optimization. Specifically, the multi-objective algorithm employed is the Non-dominated Sorting Genetic Algorithm (NSGA-II) with binary type variables. The selection is based on a binary tournament selection while the crossover is based on a self-implemented code that exchanges random parts of the selected individuals, i.e., exchanges subzones of the phase arrangements representing each selected individual. All these optimization options and the type of employed multi-objective algorithm are configurable and modifiable because jMetal is an open-source optimization framework.

The ray-tracing tool is a computationally-efficient technique that allows to significantly reduce computational efforts when estimating the optimal coding arrangement of the graphene meta-atoms. However, ray theory does not consider complex phenomena such as interference and diffraction, as well as it assumes zero coupling between adjacent meta-atoms. These simplifications imply that the optimal solution extracted from the ray-tracing method has to be validated with more precise full-wave techniques. Full-wave simulators are general-purpose electromagnetic software that solve the complete set of Maxwell's equations without any simplifying assumptions. In our particular case, we make use of commercial simulator *CST Microwave Studio* to test the validity of the optimal solution. Slight modifications in the simulated model of the RIS could be applied to adjust the performance to the solution given by the ray-tracing tool. If the design requirements are finally met, then the RIS would be fully operational.

FUNCTIONALITIES

The reconfigurability of the intelligent structure by means of the graphene layers provokes that the proposed RIS is suitable for a wide variety of communications scenarios. As an example, the meta-atoms of the RIS can be configured in order to add diversity to the communication channel, so that the channel efficiency is increased [4]. Interferences and unwanted incoming signals that could degrade the performance of the system can be also blocked by taking advantage of the lossy nature of graphene. However, the focusing capabilities of the RIS make the intelligent structure particularly useful in real-time mobile communication systems for multi-user coverage and radio localization enhancement.

BEAM STEERING

One of the most representative functionalities of the RIS consists in the electronic reconfiguration of the beam angle direction to provide LOS user connection in NLOS scenarios. This is achieved by properly modifying the ON/OFF states of the meta-atoms that constitute the RIS. In the design under consideration, the operating frequency is 28 GHz, one of the potential bands for future 5G communications links. For a given angular direction of the incident wave, the coding arrangement of the RIS is determined with the multi-objective optimization algorithm. In this particular scenario, a single objective suffices to find the optimal coding arrangement. Thus, the gain of the RIS should be maximized at the desired pointing direction. The level of the secondary lobes is automatically reduced as the gain is maximized, since the energy is concentrated at a single direction.

Fig. 3 illustrates the beam steering capabilities of our intelligent structure as well as the coding arrangement of the different configurations. The states of the graphene are modeled with an effective surface resistance of $2\,\Omega/\mathrm{sq}$ in the ON state and $2500\,\Omega/\mathrm{sq}$ for the OFF state. No significant ohmic losses are achieved in both states. Graphene becomes a good conductor for a low surface-resistance value, and it turns a non-conducting material when this value switches to a big number [14]. The main beam can be redirected in an efficient manner by simply changing the bias-voltage values of graphene. A focused beam with reduced secondary lobes is formed when all the meta-atoms contributes constructively to radiate an equal-phase wavefront at the desired spatial direction. Thus, each meta-atom should compensate the phase delay provoked by the incident spherical wave, leading to the ring-like coding arrangements observed in Fig. 3. Note that the arrangement of the rings changes proportionally as the main beam is steered, for instance in the Configuration 2, the arrangement of rings move downwards along the x and y axis to tilt the beam in elevation and azimuth directions.

BEAM SPLITTING

Another remarkable feature of the RIS is the ability to split the incident wave in N main lobes. This is of great interest in present wireless communication systems in order to provide multi-user coverage. For this operation mode of the RIS, the multi-objective genetic algorithm includes three objectives to optimize in this particular scenario. First, the gain of the RIS must be maximized at the desired pointing directions. Second, the difference between the amplitudes of the main lobes should be minimized, so all the users receive the same amount of power. The first two objectives do not guarantee by themselves that non-desired secondary lobes that carry an important energy contribution could appear. This is solved by introducing a third objective, which seeks to minimize the radiated energy outside the main lobe direction. A set of trade-off solutions (Pareto front) arise from the multiple objectives included in the optimization process. A decision marker is used to determine which of these trade-off solutions is finally implemented in the full-wave simulator. This decision marker is calculated as the ratio of the sum of gains at the main lobe directions and the difference between their values times the radiated energy outside the desired directions. As a design criteria, we choose the solution of the Pareto front whose value of the decision marker is the highest.

Fig. 3 also shows the beam splitting capabilities of the RIS (Configurations 3 and 4). As a proof of concept, the energy that carries the incident spherical wave that illuminates the structure is divided into two main beams. Similar to the beam-steering operation mode, the ON/OFF states of graphene are modeled with two surface resistance values of $2\ \Omega/\mathrm{sq}$ and $2500\ \Omega/\mathrm{sq}$, respectively. As shown in the figure, both beams have similar gain values and the secondary lobes have been minimized. With the use of the multi-objective optimization algorithm, this scenario can be straightforwardly generalized to

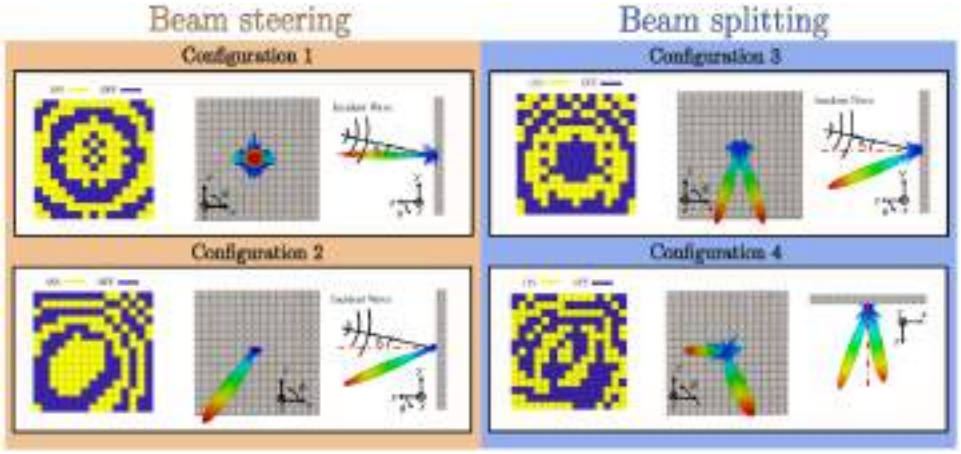

Fig. 3: Beam steering and beam splitting capabilities of the RIS. The reflected beams have the following pointing angles. Configuration 1: $(\phi, \theta) = (90^{\text{o}}, 0^{\text{o}})$; Configuration 2: $(\phi, \theta) = (240^{\text{o}}, 20^{\text{o}})$; Configuration 3: $(\phi, \theta) = (250^{\text{o}}, 20^{\text{o}})$, and $(\phi, \theta) = (300^{\text{o}}, 20^{\text{o}})$; Configuration 4: $(\phi, \theta) = (180^{\text{o}}, 20^{\text{o}})$, and $(\phi, \theta) = (300^{\text{o}}, 30^{\text{o}})$. The azimuth and elevation angles of the incident wave are $\phi_i = 90^{\text{o}}$ and $\theta_i = -10^{\text{o}}$, respectively.

the creation of N main beams, demonstrating the applicability of the proposed RIS.

ADVANCED FUNCTIONALITIES

Apart from previous functionalities, the combination of 3-D structures and graphene in a meta-atom can enable advanced functionalities. Thanks to the square waveguide, which contains a split-ring resonator on each lateral wall, the RIS function for each incident polarization is achieved if the graphene state is selected in pairs, i.e., surface resistance of the graphene in opposite waveguide walls should be the same. Fig. 4 illustrates the performance of the proposed RIS when a vertically polarized wave (V-pol) is steered and a horizontally polarized wave (H-pol) is split (Fig. 4(a)) or it is absorbed (Fig. 4(b)). For both cases, the graphene state placed at each lateral wall of the meta-atom is the same and forms the phase arrangement shown in Configuration 2 for vertically polarized waves. Alternatively, the beam splitting in horizontally polarized waves is controlled by the graphene located at top and bottom walls of the meta-atom. The phase arrangement for this RIS function is the one illustrated in Configuration 3. An additional functionality can be invoked by considering a third state, profiting the capability of graphene for absorption. There exist a series of bias-voltage values that make the conductivity of graphene favorable for this scenario as it was explained before. Since the cell is under cut-off, no propagating field can be found inside. However, this field is practically confined in the split-rings regions at resonance. Graphene, in direct contact with the split rings, exploits its lossy character and absorbs it. The performance of the absorption function is shown in Fig. 4(b) for horizontally polarized waves. For this case, the graphene sheet has an effective surface resistance of 75 Ω/sq. The reflected wave is below -13 dB regarding the maximum of the beam-steering case (absorption higher than 90%).

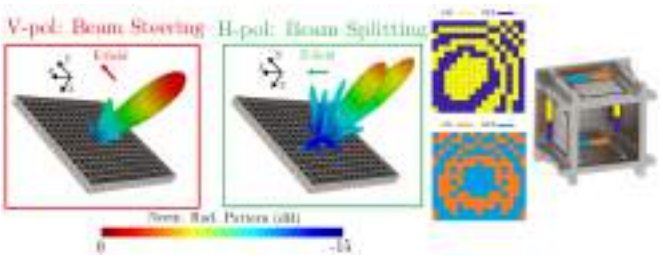

(a)

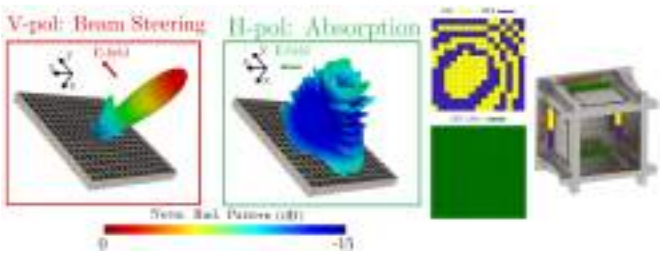

(b)

Fig. 4: Selection of the RIS function depending on the incident polarization: (a) beam steering (V-pol) and beam splitting (H-pol), and (b) beam steering (V-pol) and absorption (H-pol).

CONCLUSIONS

In this article, we have explored the novel concept of 3-D RIS. The inclusion of an additional dimension compared to conventional 2-D configurations brings an extra degree of freedom to the design, leading to an improved RIS with enhanced functionalities. Among the existing and emerging reconfigurable materials, the graphene has been selected to carry out the adjustable behavior of the proposed 3-D RIS. By properly setting the discrete states (ON/OFF) of the graphene meta-atoms, the radiation properties of the RIS can be electronically reconfigured. In order to set the states of the 3-D meta-atoms to fulfill the desired RIS function, a design procedure has been proposed. The main tools that form this design procedure are a self-implemented ray-tracing tool and a multi-objective optimization framework. In this way, an optimal coding arrangement for the RIS is found, ensuring the correct performance of selected operation mode. To validate the proposal, we design a 3-D RIS formed by a mesh of

15×15 graphene meta-atoms operating at 28 GHz. The full-wave results show the beam-steering/splitting and absorption capabilities of the intelligent structure, as well as its operation as a polarization selector. This demonstrates the potential of the proposed RIS for application in real-time multi-user scenarios of future-generation wireless communication systems.

ACKNOWLEDGEMENTS

This work was supported in part by the Spanish Program of Research, Development and Innovation under Project TIN2016-75097-P, Project RTI2018-102002-A-I00 and, Project EQC2018-004988-P, in part by "Junta de Andalucía" under Project B-TIC-402-UGR18 and Project P18.RT.4830 and in part by the predoctoral grant FPU18/01965. The authors would like to thank Alejandro Ramírez-Arroyo for his valuable comments.

REFERENCES

[1] I. F. Akyildiz, A. Kak and S. Nie, "6G and Beyond: The Future of Wireless Communications Systems," *IEEE Access*, vol. 8, pp. 133995-134030, 2020.

[2] C. Liaskos, S. Nie, A. Tsioliaridou, A. Pitsillides, S. Ioannidis and I. Akyildiz, "A New Wireless Communication Paradigm through Software-Controlled Metasurfaces," *IEEE Commun. Mag.*, vol. 56, no. 9, pp. 162-169, Sept. 2018.

[3] Q. Wu and R. Zhang, "Towards smart and reconfigurable environment: Intelligent reflecting surface aided wireless network," *IEEE Commun. Mag.*, vol. 58, no. 1, pp. 106–112, 2020.

[4] M. Di Renzo *et al.*, "Smart Radio Environments Empowered by Reconfigurable Intelligent Surfaces: How It Works, State of Research, and The Road Ahead," *IEEE J. Sel. Areas Commun.*, vol. 38, no. 11, pp. 2450-2525, Nov. 2020.

[5] H. H. Yang *et al.*, "A programmable metasurface with dynamic polarization scattering and focusing control," *Sci. Rep.*, vol. 6, Oct. 2016.

[6] L. Dai *et al.*, "Reconfigurable Intelligent Surface-Based Wireless Communications: Antenna Design, Prototyping, and Experimental Results," *IEEE Access*, vol. 8, pp. 45913-45923, 2020.

[7] Y. Ra'di and A. Alù, "Reconfigurable metagratings," *ACS Photon.*, vol. 5, no. 5, pp. 1779–1785, Mar. 2018.

[8] F. Liu *et al.*, "Intelligent metasurface with continuously tunable local surface impedance for multiple reconfigurable functions," *Phys. Rev. App.*, vol. 11, 2019.

[9] G. C. Ghivela and J. Sengupta, "The Promise of Graphene: A Survey of Microwave Devices Based on Graphene," *IEEE Microw. Mag.*, vol. 21, no. 2, pp. 48-65, Feb. 2020.

[10] S. E. Hosseininejad *et al.*, "Reprogrammable graphene-based metasurface mirror with adaptive focal point for THz imaging," *Sci. Rep.*, vol. 9, no. 1, Feb. 2019.

[11] A. Sadeqi, H.R. Nejad, R.E. Owyeung, and S. Sonkusale, "Three dimensional printing of metamaterial embedded geometrical optics (MEGO)," *Microsyst. Nanoeng.*, vol. 5, Art. No. 16, 2019.

[12] C. Molero Jimenez, E. Menargues and M. García-Vigueras, "All-Metal 3-D Frequency-Selective Surface With Versatile Dual-Band Polarization Conversion," *IEEE Trans. Antennas Propag.*, vol. 68, no. 7, pp. 5431-5441, July 2020.

[13] P. Guo, *et al.*, "A Review of Germanium-Antimony-Telluride Phase Change Materials for Non-Volatile Memories and Optical Modulators," *Appl. Sci.*, 9(3), 530, 2009.

[14] A. Zhang, Z. Liu, W. Lu, and H. Chen, "Graphene-based dinamically tunable attenuator on a coplanar waveguide or a slotline," *IEEE Trans. Microw. Theory Tech.*, vol. 67, no. 1, pp. 70-77, Jan 2019.

[15] J. Durillo, A. Nebro, F. Luna, B. Dorronsoro, and E. Alba, "jMetal: A Java Framework for Developing Multi-Objective Optimization Metaheuristics," Dpto. de Lenguajes y Ciencias de la Computación, University of Málaga, E.T.S.I. Informática, Tech.Rep. ITI-2006-10, Dec. 2006.

BIOGRAPHIES

CARLOS MOLERO [M'17] (cmoleroj@ugr.es) holds a Ph.D. from the Universidad de Sevilla, (2017). Since 2020, he has a posdoct position in the University of Granada, Spain.

ÁNGEL PALOMARES-CABALLERO (angelpc@ugr.es) is currently pursuing the Ph.D. degree at the University of Granada.

ANTONIO ALEX-AMOR (aalex@ugr.es) holds a Ph.D. from the Universidad Politécnica de Madrid, (2021). He has a posdoct position in the University of Granada, Spain.

IGNACIO PARELLADA-SERRANO (parellada@ugr.es) is currently working toward a Ph.D at the University of Granada.

FRANCISCO GAMIZ [SM'02] (fgamiz@ugr.es) is a Full Professor of the University of Granada and the Head of the Nanoelectronics and Graphene Research Laboratories.

PABLO PADILLA (pablopadilla@ugr.es) is currently an Associate Professor of the University of Granada. His research interests include topics related to electromagnetism and communications.

JUAN F. VALENZUELA-VÁLDES (juanvalenzuela@ugr.es) is currently an Associate Professor of the University of Granada. He is also the Head of the SWAT Research Group. His current research interests include wireless communications, RF devices, antennas, and propagation.

Chapter 3

Conclusions and Future Work

The research carried out in this thesis has been focused on the design and fabrication of waveguide phase shifters and radiating devices for millimeter-wave frequencies. In the development of the different presented RF devices, different design strategies and fabrication technologies have been used to achieve the proposed objectives. This last chapter outlines the main conclusions obtained and the possible future work that can be derived from the results and conclusions drawn in this thesis.

3.1 Main Conclusions

The main conclusions drawn from the contributions comprising this thesis are listed below:

- From [P1], it is demonstrated the design of waveguide phase shifter formed by unit cell with pins that preserved glide symmetry. Using this type of unit cell, a higher phase shift per unit cell is achieved compared to the unit cell that does not have this symmetry configuration. This allows for the more compact design of waveguide phase shifters in millimeter-waves. In addition, because the pins are further apart in the unit cell with glide-symmetric pins, fabrication becomes less complex. In the proposed unit cell, no dielectric material is used so that losses are minimized in this aspect.

- Regarding [P2], the effects of loading a rectangular waveguide with periodic holes is analyzed in detail for the millimeter-wave frequency range. The spatial arrangement of these holes is important and has consequences on the propagation constant of the waveguide. If the holes maintain a configuration in glide symmetry, the resulting unit cell provides a phase shift over a large bandwidth. In another case, a

stopband is produced where this is maximum for the mirror symmetry configuration. Taking advantage of these two configurations of glide and mirror symmetry, it is possible to realize phase shifters and filters in waveguide for millimeter-waves without manufacturing complexity since it consists of a simple drilling of the pieces.

- The periodic structures which produce a phase shift in ridge gap waveguide are presented in [P3]. It is proved that to achieve a controlled phase shift in a unit cell in ridge waveguide technology it is necessary to include half holes on both sides of the ridge. In this way, a higher phase shift per unit cell is achieved compared to introducing the phase shift by modulating both the height and width of the ridge waveguide. In addition, the configuration of these holes in the unit cell must preserve glide symmetry to achieve the highest bandwidth for the fundamental mode. Based on this type of unit cell and as a proof of concept, a phase shifter with a flat phase response for millimeter-wave frequencies is presented whose reference is another ridge waveguide of the same length. Another type of frequency response for the phase shifter can be designed through modification of the value of the holes included in the ridge.

- In [P4], it is detailed the proposed design of a reconfigurable phase shifter in gap-waveguide technology. Taking advantage of the benefits of gap-waveguide technology, we demonstrate the opportunities it offers for relatively simple inclusion of reconfigurable elements within waveguides. In this case, use is made of a flexible metal strip that allows the progressive width change of the waveguide by mechanical action. In this manner, the phase constant along the waveguide and consequently the phase difference value provided by the phase shifter is modified in a simple way.

- In the topic of the radiating devices, [P5] proposes the combined use of gap-waveguide technology based on glide-symmetric and E-plane split waveguide design. Both design strategies provide the possibility of splitting the complete antenna array design into several pieces to achieve a suitable fabrication. By designing on E-plane split waveguides and where this cannot be achieved by implementing gap-waveguide technology, leakage losses in the assembly of the parts that form the fabricated prototype can be minimized. With this multilayer division and robust behavior against assembly tolerances, a low-cost manufacturing of multilayer arrays for millimeter-wave frequencies based on 3D printing can be performed.

- Regarding [P6], it is proposed a metal-only reflectarray unit cell with 3D geometry to achieve low-loss reflection and independent reflected

phase tuning for the impinging orthogonal linear polarizations. In this paper is studied the effect of the height between parallel-plate waveguides, which form the unit cell. Moreover, the phase response of the unit cell under oblique incidence is also analyzed. The results show a promising unit cell for metal-only reflectarray design since the level of independent phase control of each polarization is high with linear phase response over frequency that is maintained for oblique angles.

- In [P7], the unit cell design of [P6] is improved and a new metal-only reflectarray unit cell is proposed. This unit cell has a linear behavior in a wide bandwidth for the phase response as well as a high independence in the control of the reflected orthogonal linear polarization. The proposed unit cell is extensively studied to determine the limits of its wideband performance. As this unit cell has 3D geometry, the fabrication by 3D printing is straightforward and it is demonstrated in the paper with the design and prototype of a reflectarray with large gain bandwidth and high radiation efficiency in millimeter-wave frequencies. In addition, due to the independent control of the reflected phase of the incident orthogonal polarizations, the prototype also provides circular polarization in a large bandwidth. This achieved polarization is of special interest for communications as it mitigates losses in the propagation channel.

- A new reflect-transmit-array unit cell with wideband performance and polarization independence is proposed in [P8]. Exploiting the benefits observed in [P7], one of the polarization is dedicated to being transmitted rather than being reflected as well. This is achieved by the inclusion of slow-wave structures in the slit by means of corrugations. Both the structures that control the phase shift in transmission and reflection do so over a large bandwidth so in consequence, the increase in directivity in both modes of operation occurs also over a large bandwidth. In addition, being a polarization selective structure, it is possible to perform complete reflection, complete transmission or transmission/reflection depending on the angle of the incident polarization in ϕ.

- Finally, in [P9], a RIS design with unit cells having a three-dimensional structure is demonstrated. This provides an additional degree of freedom in the control of the received polarizations since they can be controlled independently. As a reconfigurable element, a structure with graphene in contact with the split-ring resonators, which are included in each of the side walls of the cutoff waveguide, is proposed. Due to the tunability of the surface resistance of graphene at frequencies below 100 GHz, different values are set. These cause a change of the resonant frequency of the split-ring resonator and consequently, a

change of the reflected phase response. Depending on the polarization incident on the RIS, a different polarization reflection behavior can occur resulting in beam steering or splitting or multi-beam situations. Furthermore, due to the range of surface resistances offered by graphene, the proposed RIS can produce a state of absorption of the incident wave which provides advanced functionality.

3.2 Future Work

Based on the research findings obtained in this thesis, the following opportunities for future lines of research are identified:

- Implementation of reconfigurability of the proposed fixed phase shifters. The most direct way is a mechanical reconfiguration where the periodic structures vary some of their geometrical parameters, for example, the height of the pins or the layers forming the gap-waveguide as this technology allow the contact to not be perfect.

- Integration of the proposed phase shifter designs in both fixed and variable beamforming networks. As an example, the proposed tunable phase shifter could be integrated with the presented gap-waveguide antenna array to form a phased array with mechanical reconfiguration at millimeter-wave frequencies.

- Redesign and fabrication by means of micromachining techniques such as SU-8 or Deep reactive-ion etching (DRIE) of a metal-only reflectarray at frequencies above 100 GHz. This frequency range is envisioned for the Sixth Generation (6G) of communications [124]. In this generation of communications, reflectarray will also play an important role in improving the propagation channel. The aforementioned techniques provide the fabrication of metal-only devices with high precision and resolution as can be found in [125].

- Extend the design of the reflect-transmit-array or the RIS with three-dimensional structure to another type of implementation such as the one found in [122]. In this way, a more direct integration of active elements can be achieved by using substrate layers to realize the three-dimensional structure.

- Use the benefits provided by 3D structures for the realization of Simultaneously Transmitting And Reflecting (STAR) RIS designs. This RF device recently proposed on the topic of wireless communications [126] aims to extend the operation of the RIS to the control of the communications channel in both reflection and transmission.

Bibliography

[1] ITU-R Rec. M.2083-0(09/2015), "IMT Vision — Framework and Overall Objectives of the Future Development of IMT for 2020 and Beyond," 2015.

[2] J. Lee, E. Tejedor, K. Ranta-aho, H. Wang, K.-T. Lee, E. Semaan, E. Mohyeldin, J. Song, C. Bergljung, and S. Jung, "Spectrum for 5G: Global Status, Challenges, and Enabling Technologies," *IEEE Communications Magazine*, vol. 56, no. 3, pp. 12–18, 2018.

[3] T. S. Rappaport, S. Sun, R. Mayzus, H. Zhao, Y. Azar, K. Wang, G. N. Wong, J. K. Schulz, M. Samimi, and F. Gutierrez, "Millimeter Wave Mobile Communications for 5G Cellular: It Will Work!" *IEEE Access*, vol. 1, pp. 335–349, 2013.

[4] S. Rangan, T. S. Rappaport, and E. Erkip, "Millimeter-Wave Cellular Wireless Networks: Potentials and Challenges," *Proc. IEEE*, vol. 102, no. 3, pp. 366–385, 2014.

[5] Y. Li, E. Pateromichelakis, N. Vucic, J. Luo, W. Xu, and G. Caire, "Radio Resource Management Considerations for 5G Millimeter Wave Backhaul and Access Networks," *IEEE Communications Magazine*, vol. 55, no. 6, pp. 86–92, 2017.

[6] B. Tezergil and E. Onur, "Wireless Backhaul in 5G and Beyond: Issues, Challenges and Opportunities," *IEEE Communications Surveys & Tutorials*, vol. 24, no. 4, pp. 2579–2632, 2022.

[7] 3GPP TS 38.104 version 17.6.0 Release 17. 5G ; NR; Base Station (BS) radio transmission and reception. [Online]. Available: https://www.etsi.org/deliver/etsi_ts/138100_138199/138104/17.06.00_60/ts_138104v170600p.pdf

[8] T. S. Rappaport, G. R. MacCartney, M. K. Samimi, and S. Sun, "Wideband Millimeter-Wave Propagation Measurements and Channel Models for Future Wireless Communication System Design," *IEEE Trans. Commun.*, vol. 63, no. 9, pp. 3029–3056, 2015.

[9] V. Petrov, T. Kurner, and I. Hosako, "IEEE 802.15.3d: First Standardization Efforts for Sub-Terahertz Band Communications toward 6G," *IEEE Communications Magazine*, vol. 58, no. 11, pp. 28–33, 2020.

[10] X. Ge, S. Tu, G. Mao, C.-X. Wang, and T. Han, "5G Ultra-Dense Cellular Networks," *IEEE Wireless Communications*, vol. 23, no. 1, pp. 72–79, 2016.

[11] T. Nguyen. Small Cell Networks and the Evolution of 5G. [Online]. Available: https://www.qorvo.com/design-hub/blog/small-cell-networks-and-the-evolution-of-5g

[12] C. Balanis, *Antenna Theory: Analysis and Design.* Wiley, 2015.

[13] W. Saad, M. Bennis, and M. Chen, "A Vision of 6G Wireless Systems: Applications, Trends, Technologies, and Open Research Problems," *IEEE Network*, vol. 34, no. 3, pp. 134–142, 2020.

[14] W. Hong, Z. H. Jiang, C. Yu, J. Zhou, P. Chen, Z. Yu, H. Zhang, B. Yang, X. Pang, M. Jiang, Y. Cheng, M. K. T. Al-Nuaimi, Y. Zhang, J. Chen, and S. He, "Multibeam Antenna Technologies for 5G Wireless Communications," *IEEE Trans. Antennas Propag.*, vol. 65, no. 12, pp. 6231–6249, 2017.

[15] D. Pozar, *Microwave Engineering, 4th Edition.* Wiley, 2011.

[16] "IEEE Standard for Definitions of Terms for Antennas," *IEEE Std 145-2013 (Revision of IEEE Std 145-1993)*, pp. 1–50, 2014.

[17] K. Wu, M. Bozzi, and N. J. G. Fonseca, "Substrate Integrated Transmission Lines: Review and Applications," *IEEE Journal of Microwaves*, vol. 1, no. 1, pp. 345–363, 2021.

[18] P.-S. Kildal, E. Alfonso, A. Valero-Nogueira, and E. Rajo-Iglesias, "Local Metamaterial-Based Waveguides in Gaps Between Parallel Metal Plates," *IEEE Antennas Wirel. Propag. Lett.*, vol. 8, pp. 84–87, 2009.

[19] E. Rajo-Iglesias, M. Ferrando-Rocher, and A. U. Zaman, "Gap Waveguide Technology for Millimeter-Wave Antenna Systems," *IEEE Communications Magazine*, vol. 56, no. 7, pp. 14–20, 2018.

[20] K. Tekkouk, J. Hirokawa, R. Sauleau, M. Ettorre, M. Sano, and M. Ando, "Dual-Layer Ridged Waveguide Slot Array Fed by a Butler Matrix With Sidelobe Control in the 60-GHz Band," *IEEE Transactions on Antennas and Propagation*, vol. 63, no. 9, pp. 3857–3867, 2015.

[21] A. Tamayo-Domínguez, J.-M. Fernández-González, and M. Sierra-Castañer, "3-D-Printed Modified Butler Matrix Based on Gap Waveguide at W-Band for Monopulse Radar," *IEEE Transactions on Microwave Theory and Techniques*, vol. 68, no. 3, pp. 926–938, 2020.

[22] Z. Xu, Y. Shen, S. Xue, and S. Hu, "Fully Planar 2-D Multibeam Millimeter-Wave Antenna With Via-Based Phase Shifters," *IEEE Antennas and Wireless Propagation Letters*, vol. 21, no. 11, pp. 2234–2238, 2022.

[23] M. Akbari, M. Farahani, M. D. Ardakani, A. Lalbakhsh, S. Zarbakhsh, S. O. Tatu, A.-R. Sebak, O. M. Ramahi, and T. A. Denidni, "Highly Efficient Front End Direct Conversion Receiver for 28-GHz Wireless Access Point," *IEEE Access*, vol. 9, pp. 88 879–88 893, 2021.

[24] M. Farahani, M. Akbari, M. Nedil, A.-R. Sebak, and T. A. Denidni, "Millimeter-Wave Dual Left/Right-Hand Circularly Polarized Beamforming Network," *IEEE Transactions on Antennas and Propagation*, vol. 68, no. 8, pp. 6118–6127, 2020.

[25] F. Alessandri, M. Mongiardo, and R. Ravanelli, "A compact, wideband, variable phase shifter for reconfigurable satellite beam forming networks," in *1993 23rd European Microwave Conference*, 1993, pp. 556–557.

[26] H. Kirino and K. Ogawa, "A 76 GHz Multi-Layered Phased Array Antenna Using a Non-Metal Contact Metamaterial Waveguide," *IEEE Transactions on Antennas and Propagation*, vol. 60, no. 2, pp. 840–853, 2012.

[27] Y. Ji, L. Ge, J. Wang, Q. Chen, W. Wu, and Y. Li, "Reconfigurable Phased-Array Antenna Using Continuously Tunable Substrate Integrated Waveguide Phase Shifter," *IEEE Transactions on Antennas and Propagation*, vol. 67, no. 11, pp. 6894–6908, 2019.

[28] L. Polo-López, J. l. Masa-Campos, A. T. Muriel-Barrado, P. Sanchez-Olivares, E. Garcia-Marin, J. Córcoles, and J. A. Ruiz-Cruz, "Mechanically Reconfigurable Linear Phased Array Antenna Based on Single-Block Waveguide Reflective Phase Shifters With Tuning Screws," *IEEE Access*, vol. 8, pp. 113 487–113 497, 2020.

[29] D. Sánchez-Escuderos, J. I. Herranz-Herruzo, M. Ferrando-Rocher, and A. Valero-Nogueira, "True-Time-Delay Mechanical Phase Shifter in Gap Waveguide Technology for Slotted Waveguide Arrays in Ka-Band," *IEEE Transactions on Antennas and Propagation*, vol. 69, no. 5, pp. 2727–2740, 2021.

[30] W. Stutzman, "Estimating directivity and gain of antennas," *IEEE Antennas and Propagation Magazine*, vol. 40, no. 4, pp. 7–11, 1998.

[31] A. Farahbakhsh, D. Zarifi, and A. U. Zaman, "60-GHz Groove Gap Waveguide Based Wideband H-Plane Power Dividers and Transitions: For Use in High-Gain Slot Array Antenna," *IEEE Transactions on Microwave Theory and Techniques*, vol. 65, no. 11, pp. 4111–4121, 2017.

[32] C. A. Fernandes, E. B. Lima, and J. R. Costa, "Dielectric Lens Antennas," in *Handbook of Antenna Technologies*. Springer, 2016, pp. 1001–1064.

[33] J. R. Reis, M. Vala, and R. F. S. Caldeirinha, "Review Paper on Transmitarray Antennas," *IEEE Access*, vol. 7, pp. 94 171–94 188, 2019.

[34] M. H. Dahri, M. H. Jamaluddin, M. I. Abbasi, and M. R. Kamarudin, "A Review of Wideband Reflectarray Antennas for 5G Communication Systems," *IEEE Access*, vol. 5, pp. 17 803–17 815, 2017.

[35] C. Liaskos, S. Nie, A. Tsioliaridou, A. Pitsillides, S. Ioannidis, and I. Akyildiz, "A New Wireless Communication Paradigm through Software-Controlled Metasurfaces," *IEEE Communications Magazine*, vol. 56, no. 9, pp. 162–169, 2018.

[36] M. Di Renzo, A. Zappone, M. Debbah, M.-S. Alouini, C. Yuen, J. de Rosny, and S. Tretyakov, "Smart Radio Environments Empowered by Reconfigurable Intelligent Surfaces: How It Works, State of Research, and The Road Ahead," *IEEE Journal on Selected Areas in Communications*, vol. 38, no. 11, pp. 2450–2525, 2020.

[37] T. J. Cui, M. Q. Qi, X. Wan, J. Zhao, and Q. Cheng, "Coding metamaterials, digital metamaterials and programmable metamaterials," *Light: science & applications*, vol. 3, no. 10, pp. e218–e218, 2014.

[38] A. Vosoogh, M. Sharifi Sorkherizi, V. Vassilev, A. U. Zaman, Z. S. He, J. Yang, A. A. Kishk, and H. Zirath, "Compact Integrated Full-Duplex Gap Waveguide-Based Radio Front End For Multi-Gbit/s Point-to-Point Backhaul Links at E-Band," *IEEE Trans. Microw. Theory Tech.*, vol. 67, no. 9, pp. 3783–3797, 2019.

[39] A. Vosoogh, A. Haddadi, A. U. Zaman, J. Yang, H. Zirath, and A. A. Kishk, "W-Band Low-Profile Monopulse Slot Array Antenna Based on Gap Waveguide Corporate-Feed Network," *IEEE Transactions on Antennas and Propagation*, vol. 66, no. 12, pp. 6997–7009, 2018.

[40] J. Liu, A. Vosoogh, A. U. Zaman, and J. Yang, "A Slot Array Antenna With Single-Layered Corporate-Feed Based on Ridge Gap Waveguide in the 60 GHz Band," *IEEE Transactions on Antennas and Propagation*, vol. 67, no. 3, pp. 1650–1658, 2019.

[41] J. Liu, F. Yang, K. Fan, and C. Jin, "Unequal Power Divider Based on Inverted Microstrip Gap Waveguide and Its Application for Low Sidelobe Slot Array Antenna at 39 GHz," *IEEE Transactions on Antennas and Propagation*, vol. 69, no. 12, pp. 8415–8425, 2021.

[42] S. A. Razavi, P.-S. Kildal, L. Xiang, E. Alfonso Alós, and H. Chen, "2x2-Slot Element for 60-GHz Planar Array Antenna Realized on Two Doubled-Sided PCBs Using SIW Cavity and EBG-Type Soft Surface fed by Microstrip-Ridge Gap Waveguide," *IEEE Transactions on Antennas and Propagation*, vol. 62, no. 9, pp. 4564–4573, 2014.

[43] Y. Shi, W. Feng, H. Wang, W. Che, Q. Xue, J. Wang, J. Zhang, X. Qian, M. Zhou, and B. Cao, "Novel w-band ltcc transition from microstrip line to ridge gap waveguide and its application in 77/79 ghz antenna array," *IEEE Transactions on Antennas and Propagation*, vol. 67, no. 2, pp. 915–924, 2019.

[44] M. Ebrahimpouri, O. Quevedo-Teruel, and E. Rajo-Iglesias, "Design Guidelines for Gap Waveguide Technology Based on Glide-Symmetric Holey Structures," *IEEE Microwave and Wireless Components Letters*, vol. 27, no. 6, pp. 542–544, 2017.

[45] M. Ebrahimpouri, E. Rajo-Iglesias, Z. Sipus, and O. Quevedo-Teruel, "Cost-Effective Gap Waveguide Technology Based on Glide-Symmetric Holey EBG Structures," *IEEE Transactions on Microwave Theory and Techniques*, vol. 66, no. 2, pp. 927–934, 2018.

[46] E. Rajo-Iglesias, M. Ebrahimpouri, and O. Quevedo-Teruel, "Wideband Phase Shifter in Groove Gap Waveguide Technology Implemented With Glide-Symmetric Holey EBG," *IEEE Microwave and Wireless Components Letters*, vol. 28, no. 6, pp. 476–478, 2018.

[47] Q. Liao, E. Rajo-Iglesias, and O. Quevedo-Teruel, "*Ka*-Band Fully Metallic TE_{40} Slot Array Antenna With Glide-Symmetric Gap Waveguide Technology," *IEEE Transactions on Antennas and Propagation*, vol. 67, no. 10, pp. 6410–6418, 2019.

[48] A. Vosoogh, H. Zirath, and Z. S. He, "Novel Air-Filled Waveguide Transmission Line Based on Multilayer Thin Metal Plates," *IEEE Transactions on Terahertz Science and Technology*, vol. 9, no. 3, pp. 282–290, 2019.

[49] A. Vosoogh, A. A. Brazález, Y. Li, and Z. S. He, "A compact mass-producible e-band bandpass filter based on multi-layer waveguide technology," in *2020 14th European Conference on Antennas and Propagation (EuCAP)*, 2020, pp. 1–5.

[50] C. Jin, J. Chen, B. Zhang, L. Kong, S. An, Z. S. He, and J. Liu, "Low-Cost mmWave Metallic Waveguide Based on Multilayer Integrated Vertical-EBG Structure and its Application to Slot Array Antenna Design," *IEEE Transactions on Antennas and Propagation*, vol. 70, no. 3, pp. 2205–2213, 2022.

[51] A. Hessel, M. H. Chen, R. Li, and A. Oliner, "Propagation in periodically loaded waveguides with higher symmetries," *Proceedings of the IEEE*, vol. 61, no. 2, pp. 183–195, 1973.

[52] O. Dahlberg, R. Mitchell-Thomas, and O. Quevedo-Teruel, "Reducing the dispersion of periodic structures with twist and polar glide symmetries," *Scientific reports*, vol. 7, no. 1, pp. 1–6, 2017.

[53] F. Ghasemifard, M. Norgren, and O. Quevedo-Teruel, "Twist and polar glide symmetries: an additional degree of freedom to control the propagation characteristics of periodic structures," *Scientific reports*, vol. 8, no. 1, pp. 1–7, 2018.

[54] O. Quevedo-Teruel, M. Ebrahimpouri, and M. Ng Mou Kehn, "Ultrawideband Metasurface Lenses Based on Off-Shifted Opposite Layers," *IEEE Antennas and Wireless Propagation Letters*, vol. 15, pp. 484–487, 2016.

[55] Q. Chen, F. Ghasemifard, G. Valerio, and O. Quevedo-Teruel, "Modeling and dispersion analysis of coaxial lines with higher symmetries," *IEEE Transactions on Microwave Theory and Techniques*, vol. 66, no. 10, pp. 4338–4345, 2018.

[56] O. Quevedo-Teruel, O. Dahlberg, and G. Valerio, "Propagation in waveguides with transversal twist-symmetric holey metallic plates," *IEEE Microwave and Wireless Components Letters*, vol. 28, no. 10, pp. 858–860, 2018.

[57] O. Dahlberg, G. Valerio, and O. Quevedo-Teruel, "Fully metallic flat lens based on locally twist-symmetric array of complementary split-ring resonators," *Symmetry*, vol. 11, no. 4, p. 581, 2019.

[58] Á. Palomares-Caballero, P. Padilla, A. Alex-Amor, J. Valenzuela-Valdés, and O. Quevedo-Teruel, "Twist and glide symmetries for helix antenna design and miniaturization," *Symmetry*, vol. 11, no. 3, p. 349, 2019.

[59] P. Castillo-Tapia, K. Van Gassen, Q. Chen, F. Mesa, Z. Sipus, and O. Quevedo-Teruel, "Dispersion analysis of twist-symmetric dielectric waveguides," *Photonics*, vol. 8, no. 6, p. 206, 2021.

[60] O. Quevedo-Teruel, J. Miao, M. Mattsson, A. Algaba-Brazalez, M. Johansson, and L. Manholm, "Glide-Symmetric Fully Metallic Luneburg Lens for 5G Communications at Ka-Band," *IEEE Antennas and Wireless Propagation Letters*, vol. 17, no. 9, pp. 1588–1592, 2018.

[61] P. Padilla, L. F. Herrán, A. Tamayo-Domínguez, J. F. Valenzuela-Valdés, and O. Quevedo-Teruel, "Glide Symmetry to Prevent the Lowest Stopband of Printed Corrugated Transmission Lines," *IEEE Microwave and Wireless Components Letters*, vol. 28, no. 9, pp. 750–752, 2018.

[62] P. Bantavis, C. G. Gonzalez, R. Sauleau, G. Goussetis, S. Tubau, and H. Legay, "Broadband graded index Gutman lens with a wide field of view utilizing artificial dielectrics: a design methodology," *Opt. Express*, vol. 28, no. 10, pp. 14 648–14 661, May 2020.

[63] F. Fan, M. Cai, J. Zhang, Z. Yan, and J. Wu, "Wideband Low-Profile Luneburg Lens Based on a Glide-Symmetric Metasurface," *IEEE Access*, vol. 8, pp. 85 698–85 705, 2020.

[64] M. Ebrahimpouri and O. Quevedo-Teruel, "Ultrawideband Anisotropic Glide-Symmetric Metasurfaces," *IEEE Antennas and Wireless Propagation Letters*, vol. 18, no. 8, pp. 1547–1551, 2019.

[65] M. Ebrahimpouri, L. F. Herran, and O. Quevedo-Teruel, "Wide-Angle Impedance Matching Using Glide-Symmetric Metasurfaces," *IEEE Microwave and Wireless Components Letters*, vol. 30, no. 1, pp. 8–11, 2020.

[66] A. Alex-Amor, F. Ghasemifard, G. Valerio, M. Ebrahimpouri, P. Padilla, J. M. F. González, and O. Quevedo-Teruel, "Glide-Symmetric Metallic Structures With Elliptical Holes for Lens Compression," *IEEE Transactions on Microwave Theory and Techniques*, vol. 68, no. 10, pp. 4236–4248, 2020.

[67] A. Fox, "An Adjustable Wave-Guide Phase Changer," *Proceedings of the IRE*, vol. 35, no. 12, pp. 1489–1498, 1947.

[68] F. Arndt, J. Bornemann, and R. Vahldieck, "Design of Multisection Impedance-Matched Dielectric-Slab Filled Waveguide Phase Shifters," *IEEE Transactions on Microwave Theory and Techniques*, vol. 32, no. 1, pp. 34–39, 1984.

[69] J. Dittloff, F. Arndt, and D. Grauerholz, "Optimum design of waveguide E-plane stub-loaded phase shifters," *IEEE Transactions on Microwave Theory and Techniques*, vol. 36, no. 3, pp. 582–587, 1988.

[70] F. Alessandri, M. Mongiardo, and R. Sorrentino, "A technique for the fullwave automatic synthesis of waveguide components: application to fixed phase shifters," *IEEE Transactions on Microwave Theory and Techniques*, vol. 40, no. 7, pp. 1484–1495, 1992.

[71] S. Srikanth, "A wide-band corrugated rectangular waveguide phase shifter for cryogenically cooled receivers," *IEEE Microwave and Guided Wave Letters*, vol. 7, no. 6, pp. 150–152, 1997.

[72] M. Farahani, M. Nedil, and T. A. Denidni, "A Novel Hedgehog Waveguide and its Application in Designing a Phase Shifter Compatible With Hollow Waveguide Technology," *IEEE Transactions on Microwave Theory and Techniques*, vol. 67, no. 10, pp. 4107–4117, 2019.

[73] E. Villa, B. Aja, J. Cagigas, E. Artal, and L. de la Fuente, "Four-State Full Q-Band Phase Shifter Using Smooth-Ridged Waveguides," *IEEE Microwave and Wireless Components Letters*, vol. 27, no. 11, pp. 995–997, 2017.

[74] J. L. Cano, A. Mediavilla, and A. Tribak, "Parametric Design of a Class of Full-Band Waveguide Differential Phase Shifters," *Electronics*, vol. 8, no. 3, 2019.

[75] Z. S. He, S. An, J. Liu, and C. Jin, "Variable High Precision Wide D-Band Phase Shifter," *IEEE Access*, vol. 8, pp. 140 438–140 444, 2020.

[76] F. Reggia and E. G. Spencer, "A New Technique in Ferrite Phase Shifting for Beam Scanning of Microwave Antennas," *Proceedings of the IRE*, vol. 45, no. 11, pp. 1510–1517, 1957.

[77] M. Jost, C. Weickhmann, S. Strunck, A. Gäbler, C. Fritzsch, O. Karabey, and R. Jakoby, "Liquid crystal based low-loss phase shifter for W-band frequencies," *Electronics Letters*, vol. 49, no. 23, pp. 1460–1462, 2013.

[78] R. Reese, E. Polat, H. Tesmer, J. Strobl, C. Schuster, M. Nickel, A. B. Granja, R. Jakoby, and H. Maune, "Liquid Crystal Based Dielectric Waveguide Phase Shifters for Phased Arrays at W-Band," *IEEE Access*, vol. 7, pp. 127 032–127 041, 2019.

[79] M. Nickel, A. Jiménez-Sáez, P. Agrawal, A. Gadallah, A. Malignaggi, C. Schuster, R. Reese, H. Tesmer, E. Polat, D. Wang, P. Schumacher, R. Jakoby, D. Kissinger, and H. Maune, "Ridge Gap Waveguide Based

Liquid Crystal Phase Shifter," *IEEE Access*, vol. 8, pp. 77 833–77 842, 2020.

[80] R. Meng, Y. Xia, Y. Li, and Q. Zhu, "The design of optically controlled phase shifter based on silicon photosensitivity," *Microwave and Optical Technology Letters*, vol. 61, no. 3, pp. 838–842, 2019.

[81] Z. Rahimian Omam, W. M. Abdel-Wahab, A. Pourziad, S. Nikmehr, A. Palizban, S. Gigoyan, and S. Safavi-Naeini, "Tunable Substrate Integrated Waveguide Phase Shifter Using High Dielectric Constant Slab," *IEEE Microwave and Wireless Components Letters*, vol. 30, no. 5, pp. 485–488, 2020.

[82] S. Alkaraki, A. L. Borja, J. R. Kelly, R. Mittra, and Y. Gao, "Reconfigurable Liquid Metal-Based SIW Phase Shifter," *IEEE Transactions on Microwave Theory and Techniques*, vol. 70, no. 1, pp. 323–333, 2022.

[83] L. Polo-López, J. L. Masa-Campos, and J. A. Ruiz-Cruz, "Reconfigurable H-plane waveguide phase shifters prototyping with additive manufacturing at K-band," *International Journal of RF and Microwave Computer-Aided Engineering*, vol. 29, no. 12, p. e21980, 2019.

[84] Y.-M. Yang, C.-W. Yuan, G.-X. Cheng, and B.-L. Qian, "Ku-Band Rectangular Waveguide Wide Side Dimension Adjustable Phase Shifter," *IEEE Transactions on Plasma Science*, vol. 43, no. 5, pp. 1666–1669, 2015.

[85] B. T. W. Gillatt, M. D'Auria, W. J. Otter, N. M. Ridler, and S. Lucyszyn, "3-D Printed Variable Phase Shifter," *IEEE Microwave and Wireless Components Letters*, vol. 26, no. 10, pp. 822–824, 2016.

[86] S. Xu and F. Yang, "Reflectarray Antennas," in *Handbook of Antenna Technologies*. Springer, 2016, pp. 1279–1320.

[87] D. Berry, R. Malech, and W. Kennedy, "The reflectarray antenna," *IEEE Transactions on Antennas and Propagation*, vol. 11, no. 6, pp. 645–651, 1963.

[88] D.-C. Chang and M.-C. Huang, "Microstrip reflectarray antenna with offset feed," *Electronics Letters*, vol. 28, no. 16, pp. 1489–1491, 1992.

[89] P. I. Theoharis, R. Raad, F. Tubbal, M. U. A. Khan, and A. Jamalipour, "Wideband Reflectarrays for 5G/6G: A Survey," *IEEE Open Journal of Antennas and Propagation*, vol. 3, pp. 871–901, 2022.

[90] I. F. Akyildiz, C. Han, and S. Nie, "Combating the Distance Problem in the Millimeter Wave and Terahertz Frequency Bands," *IEEE Communications Magazine*, vol. 56, no. 6, pp. 102–108, 2018.

[91] B. Imaz-Lueje, A. F. Vaquero, D. R. Prado, M. R. Pino, and M. Arrebola, "Shaped-Pattern Reflectarray Antennas for mm-Wave Networks Using a Simple Cell Topology," *IEEE Access*, vol. 10, pp. 12 580–12 591, 2022.

[92] R. Deng, F. Yang, S. Xu, and M. Li, "A 100-ghz metal-only reflectarray for high-gain antenna applications," *IEEE Antennas and Wireless Propagation Letters*, vol. 15, pp. 178–181, 2016.

[93] K. Q. Henderson and N. Ghalichechian, "Circular-polarized metal-only reflectarray with multi-slot elements," *IEEE Transactions on Antennas and Propagation*, vol. 68, no. 9, pp. 6695–6703, 2020.

[94] P. Mei, S. Zhang, and G. F. Pedersen, "A Low-Cost, High-Efficiency and Full-Metal Reflectarray Antenna With Mechanically 2-D Beam-Steerable Capabilities for 5G Applications," *IEEE Transactions on Antennas and Propagation*, vol. 68, no. 10, pp. 6997–7006, 2020.

[95] G.-B. Wu, Y.-S. Zeng, K. F. Chan, B.-J. Chen, S.-W. Qu, and C. H. Chan, "High-gain filtering reflectarray antenna for millimeter-wave applications," *IEEE Transactions on Antennas and Propagation*, vol. 68, no. 2, pp. 805–812, 2020.

[96] F. Yang, R. Deng, S. Xu, and M. Li, "Design and Experiment of a Near-Zero-Thickness High-Gain Transmit-Reflect-Array Antenna Using Anisotropic Metasurface," *IEEE Transactions on Antennas and Propagation*, vol. 66, no. 6, pp. 2853–2861, 2018.

[97] S. L. Liu, X. Q. Lin, Y. H. Yan, and Y. L. Fan, "Generation of a High-Gain Bidirectional Transmit–Reflect-Array Antenna With Asymmetric Beams Using Sparse-Array Method," *IEEE Transactions on Antennas and Propagation*, vol. 69, no. 9, pp. 6087–6092, 2021.

[98] T. Cai, G.-M. Wang, X.-L. Fu, J.-G. Liang, and Y.-Q. Zhuang, "High-efficiency metasurface with polarization-dependent transmission and reflection properties for both reflectarray and transmitarray," *IEEE Transactions on Antennas and Propagation*, vol. 66, no. 6, pp. 3219–3224, 2018.

[99] W. Song, Q. Xue, Y. Cai, N. Guo, K. Liu, S. Li, and H. Ding, "A Single-Layer Reflect-Transmit-Array Antenna With Polarization-Dependent Operation," *IEEE Access*, vol. 9, pp. 167 928–167 935, 2021.

[100] S. V. Hum and J. Perruisseau-Carrier, "Reconfigurable reflectarrays and array lenses for dynamic antenna beam control: A review," *IEEE Transactions on Antennas and Propagation*, vol. 62, no. 1, pp. 183–198, 2014.

[101] G. C. Trichopoulos, P. Theofanopoulos, B. Kashyap, A. Shekhawat, A. Modi, T. Osman, S. Kumar, A. Sengar, A. Chang, and A. Alkhateeb, "Design and Evaluation of Reconfigurable Intelligent Surfaces in Real-World Environment," *IEEE Open Journal of the Communications Society*, vol. 3, pp. 462–474, 2022.

[102] X. Pei, H. Yin, L. Tan, L. Cao, Z. Li, K. Wang, K. Zhang, and E. Björnson, "RIS-Aided Wireless Communications: Prototyping, Adaptive Beamforming, and Indoor/Outdoor Field Trials," *IEEE Transactions on Communications*, vol. 69, no. 12, pp. 8627–8640, 2021.

[103] L. Dai, B. Wang, M. Wang, X. Yang, J. Tan, S. Bi, S. Xu, F. Yang, Z. Chen, M. D. Renzo, C.-B. Chae, and L. Hanzo, "Reconfigurable Intelligent Surface-Based Wireless Communications: Antenna Design, Prototyping, and Experimental Results," *IEEE Access*, vol. 8, pp. 45 913–45 923, 2020.

[104] A. Araghi, M. Khalily, M. Safaei, A. Bagheri, V. Singh, F. Wang, and R. Tafazolli, "Reconfigurable Intelligent Surface (RIS) in the Sub-6 GHz Band: Design, Implementation, and Real-World Demonstration," *IEEE Access*, vol. 10, pp. 2646–2655, 2022.

[105] W. Tang, X. Chen, M. Z. Chen, J. Y. Dai, Y. Han, M. D. Renzo, S. Jin, Q. Cheng, and T. J. Cui, "Path Loss Modeling and Measurements for Reconfigurable Intelligent Surfaces in the Millimeter-Wave Frequency Band," *IEEE Transactions on Communications*, vol. 70, no. 9, pp. 6259–6276, 2022.

[106] J.-B. Gros, V. Popov, M. A. Odit, V. Lenets, and G. Lerosey, "A Reconfigurable Intelligent Surface at mmWave Based on a Binary Phase Tunable Metasurface," *IEEE Open Journal of the Communications Society*, vol. 2, pp. 1055–1064, 2021.

[107] M. H. Dahri, M. H. Jamaluddin, M. Khalily, M. I. Abbasi, R. Selvaraju, and M. R. Kamarudin, "Polarization Diversity and Adaptive Beamsteering for 5G Reflectarrays: A Review," *IEEE Access*, vol. 6, pp. 19 451–19 464, 2018.

[108] M. Bozzi, L. Pierantoni, and S. Bellucci, "Applications of Graphene at Microwave Frequencies," *Radioengineering*, vol. 24, pp. 661–669, 09 2015.

[109] C. Fan, B. Wu, Y. Hu, Y. Zhao, and T. Su, "Millimeter-Wave Pattern Reconfigurable Vivaldi Antenna Using Tunable Resistor Based on Graphene," *IEEE Transactions on Antennas and Propagation*, vol. 68, no. 6, pp. 4939–4943, 2020.

[110] J. Zhang and W. Zhu, "Graphene-Based Microwave Metasurfaces and Radio-Frequency Devices," *Advanced Photonics Research*, vol. 2, no. 11, p. 2100142, 2021.

[111] All3DP. The 7 main types of 3d printing technology of 2022. [Online]. Available: https://all3dp.com/1/types-of-3d-printers-3d-printing-technology

[112] R. Sorrentino and O. A. Peverini, "Additive manufacturing: a key enabling technology for next-generation microwave and millimeter-wave systems [point of view]," *Proceedings of the IEEE*, vol. 104, no. 7, pp. 1362–1366, 2016.

[113] J. S. Silva, M. García-Vigueras, T. Debogović, J. R. Costa, C. A. Fernandes, and J. R. Mosig, "Stereolithography-Based Antennas for Satellite Communications in Ka-Band," *Proceedings of the IEEE*, vol. 105, no. 4, pp. 655–667, 2017.

[114] B. Zhang, Y.-X. Guo, H. Zirath, and Y. P. Zhang, "Investigation on 3-D-Printing Technologies for Millimeter- Wave and Terahertz Applications," *Proceedings of the IEEE*, vol. 105, no. 4, pp. 723–736, 2017.

[115] C. Tomassoni, O. A. Peverini, G. Venanzoni, G. Addamo, F. Paonessa, and G. Virone, "3D Printing of Microwave and Millimeter-Wave Filters: Additive Manufacturing Technologies Applied in the Development of High-Performance Filters with Novel Topologies," *IEEE Microwave Magazine*, vol. 21, no. 6, pp. 24–45, 2020.

[116] A. Tamayo-Dominguez, J.-M. Fernandez-Gonzalez, and M. Sierra-Perez, "Metal-Coated 3D-Printed Waveguide Devices for mm-Wave Applications [Application Notes]," *IEEE Microwave Magazine*, vol. 20, no. 9, pp. 18–31, 2019.

[117] B. Zhang, Z. Zhan, Y. Cao, H. Gulan, P. Linnér, J. Sun, T. Zwick, and H. Zirath, "Metallic 3-D Printed Antennas for Millimeter- and Submillimeter Wave Applications," *IEEE Transactions on Terahertz Science and Technology*, vol. 6, no. 4, pp. 592–600, 2016.

[118] P. Sanchez-Olivares, M. Ferreras, E. Garcia Marin, L. Polo-Lopez, A. Tamayo-Dominguez, J. Corcoles, J. M. Fernandez-Gonzalez, J. L. Masa-Campos, J. R. Montejo-Garai, J. M. Rebollar-Machain, J. A. Ruiz-Cruz, M. Sierra Castaner, M. Sierra Perez, M. Barba-Gea, J. L. Besada, and J. Grajal, "Manufacturing Guidelines for W-Band Full-Metal Waveguide Devices: Selecting the Most Appropriate Technology," *IEEE Antennas and Propagation Magazine*, pp. 2–16, 2022.

[119] A. K. Rashid, B. Li, and Z. Shen, "An overview of three-dimensional frequency-selective structures," *IEEE Antennas and Propagation Magazine*, vol. 56, no. 3, pp. 43–67, 2014.

[120] A. Alex-Amor, A. Palomares-Caballero, and C. Molero, "3-D Metamaterials: Trends on Applied Designs, Computational Methods and Fabrication Techniques," *Electronics*, vol. 11, no. 3, 2022.

[121] C. Molero, H. Legay, T. Pierré, and M. García-Vigueras, "Broadband 3D-Printed Polarizer Based on Metallic Transverse Electro-Magnetic Unit-Cells," *IEEE Transactions on Antennas and Propagation*, vol. 70, no. 6, pp. 4632–4644, 2022.

[122] T. Wei, B. Li, H. Li, L. Zhu, and C.-H. Cheng, "Synthesis of 3-D Polarization-Rotating Surface Based on Orthogonally Inserted Parallel-Coupled Slotlines," *IEEE Transactions on Antennas and Propagation*, vol. 70, no. 12, pp. 11 957–11 967, 2022.

[123] Smart and Wireless Applications and Technologies Group (SWAT-UGR). [Online]. Available: https://swat.ugr.es/es/

[124] T. S. Rappaport, Y. Xing, O. Kanhere, S. Ju, A. Madanayake, S. Mandal, A. Alkhateeb, and G. C. Trichopoulos, "Wireless Communications and Applications Above 100 GHz: Opportunities and Challenges for 6G and Beyond," *IEEE Access*, vol. 7, pp. 78 729–78 757, 2019.

[125] A. Gomez-Torrent, T. Tomura, W. Kuramoto, J. Hirokawa, I. Watanabe, A. Kasamatsu, and J. Oberhammer, "A 38 dB Gain, Low-Loss, Flat Array Antenna for 320–400 GHz Enabled by Silicon-on-Insulator Micromachining," *IEEE Transactions on Antennas and Propagation*, vol. 68, no. 6, pp. 4450–4458, 2020.

[126] J. Xu, Y. Liu, X. Mu, J. T. Zhou, L. Song, H. V. Poor, and L. Hanzo, "Simultaneously Transmitting and Reflecting Intelligent Omni-Surfaces: Modeling and Implementation," *IEEE Vehicular Technology Magazine*, vol. 17, no. 2, pp. 46–54, 2022.

Appendices

Appendix A

Introducción y conclusiones

Este apéndice presenta en español de la parte introductoria de la tesis doctoral así como de las conclusiones obtenidas. Esto complementa el amplio resumen en español que está incluido al inicio del documento de tesis para cumplir la normativa de la Universidad de Granada correspondiente a la redacción de la tesis doctoral en un idioma distinto al español.

Introducción

Desde el 1G de las comunicaciones móviles en los años 80, se han sucedido nuevas generaciones de comunicaciones móviles, cada una de las cuales ha aportado nuevos avances tecnológicos. En la actualidad, nos encontramos ante la llegada de una nueva generación de comunicaciones, el 5G, que se encuentra en sus primeras fases de despliegue. Para el 5G, es necesario mejorar las capacidades ofrecidas por la generación anterior, la 4G. Algunas de estas mejoras están relacionadas con la velocidad máxima de transmisión de datos, la latencia o la densidad de conexiones [1]. En general, hay una mejora de un orden de magnitud en todos estos KPIs en comparación con el 4G. Alcanzar estos KPI es el mayor reto y requiere un gran avance en la tecnología actual. Una de las formas de conseguir estas mejoras es mediante el uso de bandas de frecuencia por encima de los 30 GHz [2], es decir, donde la longitud de onda es del orden de milímetros y, por tanto, también conocidas como frecuencias de ondas milimétricas. En este rango de frecuencias cuyo límite está fijado en 300 GHz, se dispone de más ancho de banda con comunicaciones de menor latencia en comparación con las bandas por debajo de los 6 GHz, donde actualmente el espectro está bastante saturado. Una de las primeras demostraciones experimentales para comprobar la viabilidad de las frecuencias de ondas milimétricas para las comunicaciones 5G se encuentra en [3]. En este trabajo realizado en 2013, los autores prueban un sistema de comunicaciones a 28 GHz y 38 GHz con resultados satisfactorios. Un poco más tarde, se volvió a medir el canal de propagación pero a frecuencias

más altas, concretamente a 73 GHz, y también se demostró su viabilidad [4]. Esto animó a la comunidad científica y de normalización a establecer definitivamente este rango de frecuencias como soporte radioeléctrico de las nuevas tecnologías de comunicación inalámbrica [5, 6]. El 3GPP ha establecido la siguiente división para las bandas de frecuencia 5G, FR1 para las frecuencias en la banda sub-6GHz y FR2 para las frecuencias por encima de 24 GHz, que corresponden a las frecuencias de ondas milimétricas [7]. Para FR1, la tecnología ya está lista para su uso en 5G comercial gracias a los avances heredados de las anteriores generaciones de comunicaciones, mientras que para FR2, la tecnología necesita desarrollarse. Uno de los principales puntos clave para la evolución de la tecnología habilitadora en FR2 está relacionado con los dispositivos de hardware. En las infraestructuras inalámbricas, el hardware para las interfaces de RF son las antenas. Estas son componentes esenciales que permiten una transmisión o recepción eficaz de la señal radiada desde el espacio libre. En el rango de frecuencias de las ondas milimétricas, las pérdidas por propagación son mayores con la distancia según la fórmula de Friis. Por lo tanto, para compensar estas pérdidas no deseadas en el balance del enlace, las antenas deben tener mayor ganancia. Si no se adopta esta solución, la señal llegaría al equipo receptor demasiado atenuada y no sería posible identificarla a partir del ruido de fondo. Esto hace que el uso de antenas de alta ganancia sea crucial para la infraestructura 5G [8, 9]. Para cumplir el requisito anterior (alta ganancia), el sistema radiante debe ser lo más eficiente posible desde el punto de vista energético, es decir, las pérdidas en los componentes de hardware deben ser lo más bajas posible. Este es otro de los objetivos del 5G, ya que se espera un mayor número de antenas en la infraestructura inalámbrica para implementar redes *small cells* [10, 11]. La infraestructura debe ser lo más eficiente posible desde el punto de vista energético. Como consecuencia de tener antenas de alta ganancia, el ancho de haz de estas antenas se reduce directamente [12]. Esto conlleva una reducción del área de conexión inalámbrica en caso de que las antenas se utilicen para cubrir una región específica en lugar de utilizarse para un enlace *backhaul* punto a punto [6, 13]. Esta reducción del área de cobertura puede mitigarse mediante el uso de antenas multihaz con haces fijos o reconfigurables en la dirección de apuntamiento [14]. Estos requisitos presentados para los sistemas radiantes 5G en FR2 son retos que actualmente están abiertos y son foco de atención de la comunidad científica para tratar de resolverlos de la manera más óptima.

En el diseño de dispositivos de RF para frecuencias de ondas milimétricas, la tecnología elegida para su implementación es crucial, ya que determinará sus prestaciones electromagnéticas. Para FR1, una elección común es la tecnología microstrip [15], ya que permite soluciones compactas, planas y de bajo coste debido a que se pueden utilizar técnicas de fabricación convencionales como PCB. En este rango de frecuencias, los factores de pérdidas, como las pérdidas dieléctricas y por radiación, tienen una relevancia limi-

tada. Sin embargo, cuando se necesita un diseño de mayor frecuencia, por ejemplo en las ondas milimétricas, los factores de pérdida mencionados empiezan a ser decisivos para la eficiencia del sistema. De hecho, estos factores de pérdida provocan una reducción de la ganancia realizada (definida en [16]), que incluye todos los factores de eficiencia del sistema. Esta es la razón por la que, a medida que aumenta la banda de frecuencias de funcionamiento, es necesario utilizar otras tecnologías de guiado para el diseño de dispositivos de RF. En la Tabla 1 del trabajo [17], se puede leer una comparación en diferentes puntos de muchas de las tecnologías de líneas de transmisión y estructuras de guías de onda. La que destaca por ser la que menos pérdidas presenta es la guía de onda metálica ya que no utiliza dieléctrico en su estructura y está totalmente apantallada. Por el contrario, la fabricación convencional de guías de onda a frecuencias de ondas milimétricas resulta muy costosa y sensible a las tolerancias ya que debe existir un contacto eléctrico perfecto entre las piezas que forman la guía de onda. Si este contacto eléctrico es imperfecto (algo muy probable debido a las tolerancias de fabricación), se generan fugas de potencia a través de los huecos debido a una discontinuidad de las corrientes eléctricas generadas en las superficies que forman la estructura de la guía de ondas. Como solución al problema descrito anteriormente, se desarrolló la tecnología *gap waveguide* [18], que evita el requisito del contacto eléctrico perfecto. La eliminación de este duro requisito, que debían cumplir las piezas que forman la guía de onda fabricada, se consigue sustituyendo las paredes verticales de la guía de onda por estructuras EBG [19]. Como su nombre indica, estas estructuras periódicas presentan un hueco electromagnético (también llamado *stopband*) en determinadas bandas de frecuencia que impide la propagación de una onda a través de la EBG. Así, al situarlas a ambos lados de la guía de onda, evitan la fuga de campo electromagnético y, por tanto, las pérdidas asociadas. Normalmente, estas EBGs están diseñadas para producir un *stopband* independientemente de si existe o no separación entre las capas que la forman. Esto proporciona robustez en la tolerancia de fabricación y no altera el rendimiento del dispositivo. Este hecho alivia en gran medida las limitaciones de la fabricación de guías de ondas en frecuencias de ondas milimétricas y la convierte en una tecnología prometedora para futuros sistemas de RF.

Como ya se ha mencionado, una de las características deseables para los sistemas radiantes en 5G es la capacidad de orientar la dirección principal de radiación. Con este fin, existen muchas configuraciones de diseño para lograr este requisito. Una de las más populares es la adopción de redes de *beamforming* como la matriz de Butler [20, 21, 22]. Tanto en este tipo de redes *beamforming* como en otras de configuración alternativa [23, 24], para conseguir los requerimientos de fase progresiva deseados en los elementos de antena, se necesitan desfasadores con un rendimiento determinado a lo largo de la frecuencia. Este tipo de redes de *beamforming* realizan la

modificación del apuntamiento del haz principal en función de la selección del puerto de entrada. Esto es debido a que los componentes, que forman la red, no pueden ser sintonizables. Como estrategia de diseño alternativa para lograr la formación de haces, están los *phased array*. Suelen constar de un solo puerto de entrada y desplazadores de fase reconfigurables, que son esenciales entre los componentes que forman la red de formación de haces. Algunos ejemplos de estos *phased array* en tecnología de guía de ondas se presentan en [25, 26, 27, 28, 29]. En todos ellos, los desfasadores reconfigurables se implementan mediante alguna estrategia de diseño en tecnología de guía de ondas. Así pues, tanto los desfasadores fijos como los variables son dispositivos de RF clave para satisfacer las necesidades requeridas por las redes de *beamforming*.

Además de las características para que los sistemas radiantes 5G sean eficientes y puedan realizar *beamforming*, otra característica relevante antes mencionada es que deben proporcionar una alta ganancia lo que implica una alta directividad. Para ello, por razones electromagnéticas, la apertura física del sistema radiante debe ser grande en comparación con la longitud de onda [30], que es del orden de milímetros para frecuencias superiores a 30 GHz. Esto hace que una de las soluciones generalmente adoptadas para conseguir una mayor apertura física sea la implementación de agrupaciones de antenas o *arrays*. Estos *arrays* pueden dividirse en dos grupos. El primer grupo comprende los *arrays* de antenas alimentados mediante estructuras de guiado, como es el caso de las redes *beamforming* o redes corporativas de alimentación [31]; y el segundo grupo es aquel cuyos *arrays* de antenas son alimentados por la radiación de una antena como fuente primaria. Los conjuntos correspondientes a este último grupo se denominan antenas alimentadas espacialmente. En este grupo de arrays de antenas se incluyen las lentes [32], los *transmitarrays* [33] y los *reflectarrays* [34]. Si comparamos ambos grupos de antenas, alimentadas por red o alimentadas espacialmente, ambos tienen sus ventajas e inconvenientes. Por ejemplo, en los arrays de antenas alimentados por redes de alimentación, el diseño con una red sin pérdidas, con componentes sin reflexión que la formen y de gran ancho de banda de operación se convierten en difíciles tareas de diseño. Sin embargo, si se consigue, la eficiencia de apertura del sistema radiante es muy elevada. Por otro lado, las antenas alimentadas espacialmente tienen la ventaja de no tener que lidiar con los problemas de implementación de redes de alimentación pero, a cambio, todo el sistema debe diseñarse con precisión para ser eficiente y evitar la mayor cantidad de pérdidas posible. En el caso de las antenas reflectoras (también puede extenderse al resto de antenas con alimentación espacial), hay que maximizar la eficiencia de iluminación, la eficiencia de desbordamiento, las pérdidas de elementos, la eficiencia de fase, el bloqueo y otros factores de eficiencia. La selección de uno de los dos grupos de antenas depende de los requisitos de ancho de banda, espacio físico disponible, polarización electromagnética deseada, directividad máxima al-

canzable o número de haces radiados necesarios.

Recientemente, ha surgido un nuevo paradigma para complementar la infraestructura de las futuras redes de comunicaciones inalámbricas basado en metasuperficies reconfigurables controladas por *software* [35]. La función principal de estas metasuperficies es mejorar dinámicamente el área de cobertura en situaciones en las que existe NLOS entre las estaciones base y los usuarios. Además de esta funcionalidad, existe un deseo generalizado de ampliar las funcionalidades ofrecidas con el objetivo de controlar el entorno inalámbrico de forma inteligente [36]. La concepción de este nuevo uso de las metasuperficies reconfigurables tiene su origen en el trabajo pionero [37]. Este trabajo presenta por primera vez los metamateriales codificados que se basan en discretizar las respuestas de fase producidas por las celdas unitarias. Estas celdas unitarias componen el metamaterial o metasuperficie. En los resultados experimentales presentados en [37], se emplea una celda unidad controlada por un diodo PIN, que produce dos respuestas de fase con una diferencia entre ellas de 180º. Debido a este comportamiento binario, la celda unitaria se denomina celda unitaria de 1 bit. El número posible de estados de la celda unitaria reconfigurable determina su número de bits. En general, estas metasuperficies se utilizan para reflejar las ondas incidentes en la dirección o direcciones deseadas. La teoría electromagnética para el diseño de estas metasuperficies de reflexión, también llamada RIS, se hereda de la utilizada para reflectarrays con algunas suposiciones para las fases disponibles en los elementos y las características de la onda incidente. Debido a que RIS no hace uso de cadenas de RF en su implementación, se obtiene un menor coste de diseño y un menor consumo de energía en comparación con las futuras estaciones base 5G. De este modo, el uso de RIS es un dispositivo pionero para la sostenibilidad y reconfigurabilidad de las futuras comunicaciones inalámbricas.

Esta tesis está dedicada principalmente a contribuir al diseño de dispositivos de RF en frecuencias de ondas milimétricas para futuras generaciones de comunicaciones. El documento de tesis tiene la siguiente organización. En el Capítulo 1, se inicia con una descripción del papel que tienen los dispositivos de ondas milimétricas en las comunicaciones 5G y las diferentes estrategias de diseño propuestas para obtener estos dispositivos con los requisitos objetivo. En los siguientes subapartados del Capítulo 1, desde el subapartado 1.1.1 hasta el 1.1.6, se realizará una descripción más detallada del estado del arte de los temas más relacionados con las aportaciones presentadas en esta tesis. En el apartado 1.2 se describen los objetivos alcanzados en esta tesis. La metodología de investigación seguida a lo largo de la tesis se describe en la Sección 1.3. La sección 1.4 enumera los resultados producidos por esta tesis tanto en términos de publicaciones como de premios. El Capítulo 2 está dedicado a la presentación de las publicaciones que componen esta tesis, así como a la descripción de las aportaciones realizadas en cada una de ellas. Este capítulo se ha dividido en dos partes, la primera

dedicada a las contribuciones realizadas sobre el tema de los desfasadores en ondas milimétricas. La otra parte del capítulo presenta las publicaciones y contribuciones realizadas sobre el tema de los sistemas radiantes en ondas milimétricas. Finalmente, en el capítulo 4 se enumeran las principales conclusiones de esta tesis y se plantean las futuras líneas de investigación basadas en las aportaciones realizadas.

Conclusiones

A continuación se enumeran las principales conclusiones extraídas de las contribuciones que componen esta tesis:

- A partir de [P1], se demuestra el diseño de un desfasador en guía de onda formado por celda unidad con pines que conservan simetría *glide*. Utilizando este tipo de celda unidad, se consigue un mayor desfase por celda unidad en comparación con la celda unidad que no tiene esta configuración de simetría. Esto permite un diseño más compacto de los desfasadores en guía de ondas para frecuencias milimétricas. Además, como los pines están más separadas en la celda unitaria con simétricas *glide*, la fabricación es menos compleja. En la celda unitaria propuesta no se utiliza material dieléctrico, por lo que se minimizan las pérdidas en este aspecto.

- En [P2] se analizan en detalle los efectos de cargar una guía de ondas rectangular con agujeros periódicos para el rango de frecuencias milimétricas. La disposición espacial de estos agujeros es importante y tiene consecuencias sobre la constante de propagación de la guía de ondas. Si los agujeros mantienen una configuración en simetría *glide*, la celda unitaria resultante proporciona un desfase en un gran ancho de banda. En otro caso, se produce un *stopband* donde ésta es máxima para la configuración en simetría *mirror*. Aprovechando estas dos configuraciones de simetría *glide* y *mirror*, es posible realizar desfasadores y filtros en guía de ondas para frecuencias milimétricas sin complejidad de fabricación ya que consiste en un simple taladrado de las piezas.

- En [P3] se presentan las estructuras periódicas que producen un desfase en una guía de onda *ridge*. Se demuestra que para conseguir un desfase controlado en una celda unitaria en la tecnología de guía de onda *ridge* es necesario incluir medios agujeros a ambos lados de la *ridge*. De este modo, se consigue un mayor desfase por celda unitaria en comparación con la introducción del desfase modulando tanto la altura como la anchura de una guía de onda de *ridge*. Además, la configuración de estos orificios en la celda unitaria debe preservar la simetría *glide* para conseguir el mayor ancho de banda para el modo

fundamental. Basándonos en este tipo de celda unitaria y como prueba de concepto, se presenta un desfasador con una respuesta de fase plana para frecuencias milimétricas cuya referencia es otra guía de onda *ridge* de la misma longitud. Se puede diseñar otro tipo de respuesta en frecuencia para el desfasador mediante la modificación del valor de los agujeros incluidos en la *ridge*.

- En [P4], se detalla el diseño propuesto de un desfasador reconfigurable en tecnología *gap-waveguide*. Aprovechando las ventajas de la tecnología *gap-waveguide*, se demuestran las oportunidades que ofrece para la inclusión relativamente sencilla de elementos reconfigurables dentro de una guías de ondas. En este caso, se utiliza una tira metálica flexible que permite el cambio progresivo de anchura de la guía de ondas por acción mecánica. De este modo, se modifica de forma sencilla la constante de fase a lo largo de la guía de onda y, en consecuencia, el valor de desfase proporcionado por el desfasador.

- En el tema de los dispositivos radiantes, [P5] se propone el uso combinado de la tecnología *gap-waveguide* basada en el diseño de agujeros *glide* y una guía de ondas separada en plano E. Ambas estrategias de diseño ofrecen la posibilidad de dividir el diseño completo en un conjunto de varias piezas para conseguir una fabricación adecuada. Mediante el diseño en guías de ondas divididas en el plano E, y en los casos en los que no se puede conseguir implementando la tecnología *gap-waveguide*, se pueden minimizar las pérdidas por fugas en el ensamblado de las piezas que forman el prototipo fabricado. Con esta división multicapa y un comportamiento robusto frente a las tolerancias de ensamblado, se puede realizar una fabricación de bajo coste de conjuntos multicapa para frecuencias de ondas milimétricas basada en impresión 3D.

- En [P6], se propone una celda unitaria de *reflectarray* metálica con geometría 3D para conseguir una reflexión de bajas pérdidas y un ajuste independiente de la fase reflejada para las polarizaciones lineales ortogonales incidentes. En este trabajo se estudia el efecto de la altura entre las guías de onda de placas paralelas, que forman la celda unitaria. Además, también se analiza la respuesta de fase de la celda unitaria bajo incidencia oblicua. Los resultados muestran una celda unitaria prometedora para el diseño de *reflectarray* sólo metálicos, ya que el nivel de control de fase independiente de cada polarización es elevado, con una respuesta de fase lineal en frecuencia que se mantiene para ángulos oblicuos.

- En [P7], se mejora el diseño de la célula unitaria de [P6] y se propone una nueva célula unitaria reflectora sólo metálica. Esta célula unitaria

tiene un comportamiento lineal en un ancho de banda amplio para la respuesta de fase, así como una gran independencia en el control de la polarización lineal ortogonal reflejada. La celda unitaria propuesta se estudia exhaustivamente para determinar los límites de su rendimiento en ancho de banda. Como esta célula unitaria tiene geometría 3D, la fabricación mediante impresión 3D es sencilla y se demuestra en el artículo con el diseño y prototipo de un reflectarray con gran ancho de banda para ganancia y alta eficiencia de radiación en frecuencias milimétricas. Además, debido al control independiente de la fase reflejada de las polarizaciones ortogonales incidentes, el prototipo también proporciona polarización circular en un gran ancho de banda. Esta polarización conseguida es de especial interés para las comunicaciones, ya que mitiga las pérdidas en el canal de propagación.

- En [P8] se propone una nueva célula unitaria de reflexión-transmisión con prestaciones de banda ancha e independencia de la polarización incidente. Aprovechando las ventajas observadas en [P7], una de las polarizaciones se dedica a ser transmitida en lugar de ser reflejada. Esto se consigue mediante la inclusión de estructuras de onda lenta mediante corrugaciones. Tanto las estructuras que controlan el desfase en transmisión como en reflexión lo hacen sobre un gran ancho de banda por lo que, en consecuencia, el aumento de directividad en ambos modos de operación se produce también sobre un gran ancho de banda. Además, al ser una estructura selectiva de polarización, es posible realizar reflexión completa, transmisión completa o transmisión/reflexión dependiendo del ángulo de la polarización incidente en ϕ.

- Por último, en [P9] se demuestra un diseño de RIS con celdas unitarias que tienen una estructura tridimensional. Esto proporciona un grado adicional de libertad en el control de las polarizaciones recibidas, ya que se pueden controlar de forma independiente. Como elemento reconfigurable, se propone una estructura con grafeno en contacto con los resonadores de anillo partido, que se incluyen en cada una de las paredes laterales de la guía de onda al corte. Debido a la reconfigurabilidad de la resistencia superficial del grafeno a frecuencias inferiores a 100 GHz, se establecen diferentes valores. Éstos provocan un cambio de la frecuencia de resonancia del resonador de anillo partido y, en consecuencia, un cambio de la respuesta de fase reflejada. Dependiendo de la polarización que incida en la RIS, puede producirse un comportamiento diferente de reflexión en la polarización reflejada que dé lugar a situaciones de redirección del haz, división del haz o de haces múltiples. Además, debido a la gama de resistencias superficiales que ofrece el grafeno, la RIS propuesta puede producir un estado

de absorción de la onda incidente que proporciona una funcionalidad avanzada.